The combined solar-photovoltaic electricity and solar-thermal heat application in power-to-chemicals process schemes: Consideration of optimal solar-photovoltaic surface area fractions

By

Maphala Ephraim Llane

(58564144)

Submitted in accordance with the requirements for the degree of

MASTER OF TECHNOLOGY

In the subject

Chemical Engineering

at the

UNIVERSITY OF SOUTH AFRICA

SUPERVISOR: DR BARAKA CELESTIN SEMPUGA

Date submitted September: 2021

Declaration

I the undersigned **Maphala Ephraim Llane (58564144)** hereby declare that the work contained in this dissertation has been produced by me without any collaboration with other students, staff or any third parties aside from those acknowledged. I have not engaged in any acts of plagiarism and to the best of my knowledge, I have recognised all the information obtained from other authors' work. The dissertation is being submitted for the degree of Master of Technology in Chemical Engineering to the University of South Africa, Pretoria. The work has not been submitted before for any degree or examination in any other University.

…… 31-Aug-2021

SIGNATURE DATE

Abstract

Power-to-chemicals processes hold tremendous potential to enable the widespread adoption of renewable sources of energy and to open many avenues to the green hydrogen economy. These processes will play a critical role in reducing mankind reliance on fossil fuels derived energy, thereby helping to abate the harmful emissions concomitant to the use of fossil fuels.

Improving energy efficiency and process economics is key to unlocking the potential of power-to-chemicals processes. This study examines the energy efficiency, cost reduction and environmental benefits, if any, of using the combination of solar photovoltaic and solar thermal heat in power-to-chemicals processes. The power-to-hydrogen, syngas, ammonia, methane, methanol, propane, ethylene, ethanol, and propanol are selected for the analyses.

Thermodynamic analysis using the first and second law of thermodynamics together with the g-h graphical analysis is used to determine the performance limits of processes as well as to set theoretical targets. The theoretical targets of interest are the work storage efficiency and overall system work efficiency. Aspen plus® commercial software is then used to model processes to establish how far the theoretical targets can be met and to also determine the cost of processes.

The analyses revealed that there will always be work efficiency losses when the processes are supplied with solar-photovoltaic electricity alone. The work efficiency is improved when the solar-thermal heat is used to supplement the solar-PV electricity, with maximum work efficiencies achieved at specific solar-photovoltaic area fractions. The analysis further showed the total energy cost of the processes to increase with the solar-PV area fraction, while the area and cost of electrolysis stack decrease with the increasing solar-PV area fraction. The observed trade-off in energy and electrolysis cost suggests that there is an optimal solar-PV area fraction (f_{op}) between the minimum (f_{min}) and f=100% where the cost is minimised.

Aspen simulation showed the overall system work efficiencies of 51.7, 52.7 and 54.3 % for power-to-ammonia, methanol, and methane, respectively. The corresponding Levelized costs of production are 543, 533 and 1158 USD/tonne.

Keywords: Power-to-chemicals; solar-PV electricity; solar-Thermal heat; solar-PV area fraction; thermodynamic analysis; economic analysis.

Acknowledgements

I would first and foremost like to thank my supervisor Doctor Bakaka Celestine Sempuga for the unwavering support he provided during the course this degree. This work would not have been possible had it not been for the long discussions and meetings we held to discuss the concepts and solve complex Engineering problems.

I would also like to extend my gratitude to the process synthesis group at the Institute for Development of Energy for African Sustainability (IDEAS), to both the supervisors and students for insightful meetings where I presented my work and was given positive feedback. Special thanks go to Professor Diane Hildebrandt, Doctor Thomas Neil Stacey, Doctor Ralph Farai Muvhiiwa and Mr. Athi-Enkosi Mavukwana. I would also like to thank the University of South Africa for providing financial assistance which made it possible that I carry out this work.

I would like to thank my family and my spouse Mamakie for the patience and support they showed me during my studies. Finally, I would like to thank God for giving me the strength to start and finish this work.

Table of Contents

Abbreviations and symbols

$\Delta H_R^0 (\frac{kJ}{mol})$ Standard heat of reaction

$\Delta G_R^0(\frac{kJ}{mol})$ Standard Gibbs free energy of reaction

$\Delta H_P(\frac{kJ}{mol})$ Process enthalpy

$\Delta G_P(\frac{kJ}{mol})$ Process Gibbs free energy

$\Delta H_C(\frac{kJ}{mol})$ Enthalpy of combustion

$\Delta S_P(\frac{kJ}{mol.K})$ Process entropy

$S_{gen}(\frac{kJ}{mol.K})$ Entropy generation

$Q(kW)$ Heat

$W(kW)$ Work

$Q_{ST}(kW)$ Solar thermal heat

$W_e(kW)$ Electrical work

$W_{PV}(kW)$ Solar photovoltaic electrical work

f Solar photovoltaic surface area fraction

f_{op} Optimal solar photovoltaic area fraction

f_{min} Minimum solar photovoltaic area fraction

$A_{ST}(m^2)$ Solar thermal heat collection surface area

$A_{PV}(m^2)$ Solar photovoltaic collection surface area

$\eta_{ST}(\%)$ Solar thermal heat collection efficiency

$\eta_{PV}(\%)$ Solar photovoltaic collection efficiency

$\eta_{WS}(\%)$ Work storage efficiency

$\eta_W(\%)$ Overall system work efficiency

$\eta_{optical}(\%)$ Optical efficiency

$G(\frac{W}{m2})$ Global solar irradiation

$T_0(K)$ Ambient temperature

$P_0(atm)$ Ambient pressure

$T^*(°C)$ Reduced tempera

$T_{Carnot}(K)$ Carnot temperature

$T_R(K)$ Reversible temperature

$T_{Comb}(K)$ Combustion temperature

LCOH(USD/kWh) Levelized cost of heat

LCOE (USD/kWh) Levelized cost of electricity

t (hr.) Project lifetime

$EC_T(USD)$ Total energy cost

$A_E(m2)$ Electrolyser active area

I_F (A) Faraday's current

$i(\frac{A}{cm2})$ Current density

$\bar{n}_r$(kmol/s) Number of moles reacting in during electrolysis reaction

n Number of electrons transferred during electrolysis reaction

F(C/mol) Faraday's constant

$V_{op}(V)$ Operating voltage

$V_{rev}(V)$ Reversible voltage

AEC Alkaline electrolytic cells

$ASR(\Omega cm^2)$ Area-specific resistance

PEM Polymer Electrolyte Membrane

PEC (USD) Purchased equipment cost

$PEC_{elec}(USD)$ Purchased equipment cost for the electrolyser

$SC_{elec}(\frac{USD}{m2})$ Specific cost of the electrolyser

CI Cost index

$A_S(m^2)$ Solar collection area

$PEC_T(USD)$ Total purchased cost

RMC (USD) Raw material cost

SOEC Solid oxide electrolytic cells

UC (USD) Utility cost

$S_{BP}(USD)$ By-product cost

m_t (tonne) Total mass of the product produced during the project lifetime

$C_{total}(USD)$ The total cost of producing the chemical

$SC_C(\frac{USD}{tonne})$	Levelized cost of production
$E_{PV\ (in)}$ (kW)	Total energy reaching a solar-PV module
$E_{PV\ (out)}$ (kW)	Total energy leaving a solar-PV module
FPC	Flat plate collector
ETC	Evacuated tube collector
HTF	Heat transfer fluid
Q_g (kW)	Useful heat generated at the solar-T heat absorber
A_C (m^2)	Surface area
A_a (m^2)	Surface area of the aperture in the solar-T collector
CPC	Compound parabolic collector
AC	Alternating current
DC	Direct current
YZS	Zirconia doped Yttria
LSM	Lanthum Strontium Magnanite

List of tables

List of figures

Chapter 1

Introduction and Literature review

1.1 Introduction

The growing global population and subsequent increase in economic activities have led to the use of fossil fuels to meet increasing energy demands. The reliance on fossil fuels has raised the question of long-term sustainability and the concern over environmental degradation due to emissions of carbon dioxide and harmful gases. Global carbon dioxide emissions have been increasing since the industrial revolution and are recently reported to have increased to 33.1 Gt in 2018, up by 1.7% from the previous year. The power sector contributed one-third of the total emissions, with coal-fired power stations contributing 10 Gt in carbon dioxide emissions (IEA, 2019).

The move to include renewable energy in the mix of energy resources around the globe has come as a measure to reduce reliance on fossil fuels and mitigate their effect on climate change. Consequently, the share of renewable energy sources is increasing and is forecast to increase by 50% in the period 2019 to 2024. International Energy Agency reports suggest that solar photovoltaic, wind, and hydropower will contribute to the larger shares of 60, 29, and 10% of the total renewable energy, respectively (IEA, 2019).

Renewable energy sources such as wind and solar are inherently intermittent, their widespread adoption into the electricity grid is problematic because it causes grid instability. Furthermore, there will always be a mismatch between daily and seasonal power demand and supply. Solar energy, for instance, is available in abundance during a sunny day and not available when it is dark or cloudy. Incident solar radiation is not as intense during the winter season as compared to the summer season. Wind energy, on the other hand, is abundant during windy seasons. As a result, there will invariably be excess renewable electricity when solar and wind are in abundance and there will be a shortfall during the periods when they are not enough. These fluctuations in renewable energy can cause instability in the electricity grid.

Countries, where solar and wind energy are extensively used, have had to institute electricity curtailment from these renewable sources as a measure to avoid grid instability. Studies by (Li *et al.*, 2015) that considered the timeframe of 2008 to 2013 showed an increase in curtailed renewable energy with higher renewable electricity production globally. China has particularly experienced serious cases of renewable energy curtailment where 16.23 TWh of wind energy was curtailed in 2013 (Bird *et al.*, 2016). This number was reported to have more than doubled

to 33.9 TWh in 2015, in addition to this 5 TWh of solar energy was also curtailed in the same year (Luo et al., 2018). Other countries that have had to curtail renewable electricity due to the inherent fluctuations of these resources include the United States, Germany, and Italy. Curtailing renewable electricity leads to inefficient use of resources (wind, solar, equipment), and this can have a negative economic impact on renewable energy projects.

Energy storage solutions are necessary to mitigate the problems associated with intermittent power supply. These solutions enable storing renewable energy when the power demand is low and releasing it into the grid when the demand is high. Some of the solutions for renewable energy storage include the use of batteries, pumped hydro, and compressed air storage. The battery technology has attracted much research interest, which led to improvements in charge-discharge efficiency, storage capacity and lifespan from lead-acid to lithium-based batteries (Beaudin et al., 2010). This technology, however, is suitable for short-term energy storage and requires high capital costs for large capacity storage. Pumped hydro and compressed air energy storage schemes are suitable for long-term and large-scale storage, but they both depend primarily on location (Luo et al., 2018). Pumped hydro requires a large area (10-20km^2) to be used for reservoirs(Beaudin et al., 2010), while compressed air energy storage requires large volumes due to its low energy density (Gruber et al., 2018).

Power-to-chemicals energy storage is another solution that holds great potential for seasonal and utility-scale renewable energy storage. There is currently a great deal of research on power-to-chemicals storage, notably on the power-to-hydrogen process. The process collects renewable power from wind or solar and converts it into hydrogen and oxygen using electrolysis technology. The produced hydrogen is then stored and used in applications such as fuel cells. Hydrogen, however, is difficult to contain and its storage could lead to significant losses. Moreover, hydrogen gas has low volumetric density, is highly flammable and thus requires high storage and transport costs (Siddiqui and Dincer, 2020).

Hydrogen is a precursor to many other chemicals that are relatively less expensive to store and transport. These chemicals include methane, methanol, DME, ammonia, and Fischer-Tropsch products(Becker et al., 2012; Cinti et al., 2017; Luo et al., 2018; Zhang, Wang, Van, et al., 2019; Kartohardjono, Adji and Muharam, 2020). The chemicals have a well-developed infrastructure for storage and transportation, as well as well-established markets.

Most research done on solar power-to-chemicals focuses on processes that use renewable electricity alone to meet both work and energy requirements of processes. Electricity is used in

electric heaters to raise the temperature of water/steam fed to electrolysers, where more electricity is used to drive the electrolysis process. Some research has, however, looked at cases where renewable electricity is used together with external heat to supply work and energy demands of processes. Edwin et al (2009) and Rodriguez et al (2019) conducted studies where they used high-temperature heat from nuclear power generation plants together with renewable electricity to produce hydrogen (Harvego et al., 2009; González Rodríguez et al., 2019). (Petrakopoulou, Robinson and Loizidou, 2016) studied a hybrid biomass-to-power and power-to-hydrogen process where low-temperature steam from a biomass-to-power process was used to supplement renewable electricity in the production of hydrogen. Giap, Kang and Ahn studied the use of waste heat to improve the efficiency of a solid-oxide reversible fuel cell. Their work showed that waste heat from steam can improve process efficiency (Giap, Kang and Ahn, 2019). The published literature where renewable electricity is supplemented by heat is notably limited to power-to-hydrogen processes only, hence the current study aims to examine the use of heat and electricity for different process pathways.

Utility-scale solar energy (USSE) requires vast amounts of land together with reduced cost and energy storage to realise its full potential and widespread adoption (Denholm and Margolis, 2008; Hernandez, Hoffacker and Field, 2014). Efficient use of land for solar energy installation can reduce disturbances caused on the natural ecosystem and the environment at large (Hernandez *et al.*, 2015), and reduce the costs associated with the land. Furthermore, the savings in land use make more land available for other essential activities such as agriculture. It is therefore important to find efficient ways of deploying solar energy on large scale for power-to-chemicals applications while also using the land efficiently.

The current research demonstrates the potential of combined renewable electricity and heat in a broad range of power-to-chemicals processes. Solar-photovoltaic and solar-thermal will be used to supply renewable electricity and thermal energy, respectively. The study uses fundamental thermodynamics to determine the heat and work requirements of an ideal process based on its overall mass balance, independent of the specifics of process flow sheeting. Furthermore, the current work aims to use analysis of this type to determine the optimal ways of combining solar-photovoltaic and solar-thermal energy to meet the heat and work requirements of power-to-chemicals processes using a mix of electricity and heat to improve overall efficiency. The improvements in overall efficiency can result in efficient use of land for solar energy and reduced Levelized costs of energy associated with power-to-chemicals.

The study further compares processes that use a mixed energy supply to those using only solar photovoltaic to quantify the potential benefits of the combined approach. Different power-to-chemicals process pathways will be compared based on their overall efficiency, solar area requirements and the associated Levelized costs of energy, to lay the groundwork for the selection of a hydrocarbon as an energy carrier.

1.2. Literature review

1.2.1 Power-to-chemicals processes

The power-to-chemicals process schemes covert electricity, mostly renewable electricity, to chemicals and fuels such as hydrogen, methane, methanol, ammonia, Fischer-Tropsch products etc. The primary goal of electricity or power conversion to chemical fuels is to store the excess renewable energy from intermittent sources of energy.i.e., wind and solar (Jürgensen *et al.*, 2014; Salomone *et al.*, 2019). Power-to-chemicals conversion is not only limited to intermittent renewable sources of energy as shown in the work of (González Rodríguez et al., 2019) where electricity and heat from nuclear power plants were converted to hydrogen. (Petrakopoulou *et al.*, 2016) used the power-to-chemicals process scheme to convert electricity and the low-temperature steam from a biomass power plant to hydrogen gas.

Power-to-chemicals processes are generally divided into two main sub-processes where the first sub-process converts water and electricity to hydrogen in an electrolysis process. The second sub-process comprises synthesis reactors where the hydrogen produced upstream is used to produce a variety of chemicals. Carbon dioxide is used to convert hydrogen to chemicals such as methane and methanol while nitrogen is used to convert hydrogen to ammonia. Water can also be co-electrolyzed with carbon dioxide to form synthesis gas (carbon monoxide and hydrogen) which can be further processed into different chemicals including methanol and Fischer-Tropsch products (Andika et al., 2018).

The next section will discuss the sub-processes of power-to-chemicals process schemes in much more detail starting with water electrolysis technologies and ending with synthesis processes of different chemicals and fuels. The carbon dioxide hydrogenation process alone can produce a myriad of chemicals depending on conditions and catalyst used, this work will therefore limit the in-depth literature discussions to methane, methanol, dimethyl ether, and ammonia. The electrolysis section will discuss electrolysis reaction at different conditions, electrolysis technologies and current developments. The chemicals synthesis sections will discuss important aspects of synthesis reactions such as reactions chemistry, catalyst systems, equilibrium, reactor technologies, operating conditions etc.

1.2.2 Water electrolysis process

The water electrolysis sub-process is used to produce hydrogen from water or steam using electricity and/or heat. The produced hydrogen is then further converted to different chemicals and fuels or be used as a fuel.

1.2.2.1 Electrolysis reactions

Water electrolysis is a reaction that uses electrical power to electrically decompose water molecules into their constituent molecules of hydrogen and oxygen. The electrolysis reaction can occur in both the liquid and the gas phases as shown in Eq. (1) and Eq. (2).

$$H_2O_{(l)} \rightarrow 0.5\ O_{2(g)} + H_{2(g)} \quad (1)$$

$$H_2O_{(g)} \rightarrow 0.5\ O_{2(g)} + H_{2(g)} \quad (2)$$

These reactions are endothermic and require the addition of energy before they can occur, the standard enthalpy of reaction measured at 25℃ and 1 atmosphere is 286 and 241 kJ/mol, with the standard Gibbs free energy of reaction being 237 and 228 kJ/mol for the liquid and gas phase electrolysis, respectively. The total energy requirements of electrolysis (ΔH_r^0) and electricity (ΔG_r^0) consumptions can be represented as functions of the reaction temperature as shown in Fig. (1).

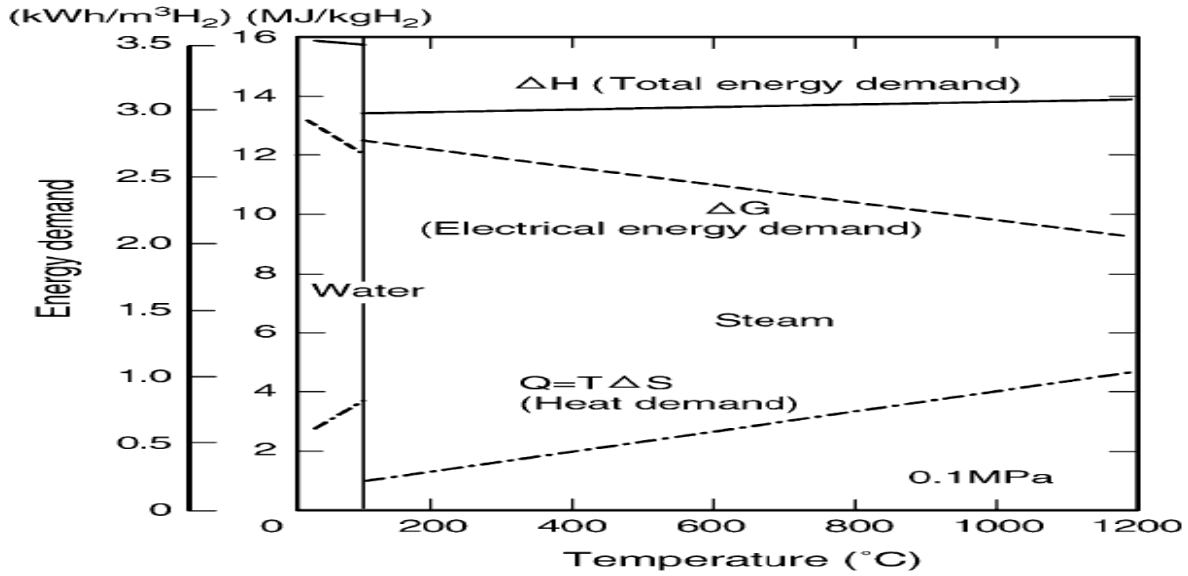

Figure 1: Total energy, electrical and heat demand of electrolysis reaction as functions of temperature at the pressure of 0.1MPa.(Caboche., 2012)

Fig. (1) depicts the energy demand of the electrolysis reaction over the temperature range of 0-1200℃; this temperature range is divided into two segments which are 25-100℃ and 100-1200℃. The first temperature range represents the liquid phase electrolysis while the second

range represents the gas phase electrolysis,100 ℃ is the liquid to gas phase change temperature at the pressure of 1atm, this value is not shown in Fig. (1), but it lies in the middle of 0 and 200℃ on the x-axis. The y-axis represents the energy demand of the electrolysis process reported per volume and mass of produced hydrogen in kWh/m^3H_2 and kWh/kgH_2 respectively at standard pressure and temperature. It is observed that the total energy requirements are higher for the liquid phase electrolysis than the gas phase electrolysis. It can further be seen that the total energy, electricity consumption of liquid phase electrolysis decreases with temperature while the heat demand increases. It is note-worthy that the gas phase electrolysis requires lesser electricity than the liquid phase counterpart. It is also obvious that the electricity consumption decreases with an increase in the reaction temperature while the heat demand increases with the temperature increase.

The electrolysis reaction can be carried out in four different modes depending on the applied voltage. The four different modes occur at equilibrium voltage, thermal neutral voltage, voltages lower than the thermal neutral but higher than the equilibrium voltage and voltage higher than the thermal neutral voltage (Giglio et al., 2015). The equilibrium voltage is defined as the minimum voltage required for electrolysis reaction to occur with the help of heat and it is given by Eq. (3).

$$V_{rev} = \frac{\Delta G_R}{zF} \tag{3}$$

where:

V_{rev} is the equilibrium or reversible voltage (V)

ΔG_R is the Gibbs free energy change of the reaction (J/mol)

F is the Faraday's constant

z is the number of electrons transferred during the reaction.

The thermal neutral or thermo-neutral voltage is the minimum voltage required to split water molecules without the need for heat, Eq. (4) defines the thermo-neutral voltage.

$$V_{tn} = \frac{\Delta H_R}{zF} \tag{4}$$

Where V_{tn} and ΔH_R represent the thermal neutral voltage and the enthalpy of reaction, respectively.

Fig. (1) shows how the electricity consumption and the total energy requirements of the electrolysis reaction vary with the reaction temperature. The electricity consumption can also be related to the over-potentials and the ohmic losses as shown by Eq. (5) (Rashid et al.,2015).

$$V_{cell} = V_{rev} + |\eta_{cathode}| + |\eta_{anode}| + iR_{cell} \quad (5)$$

Where V_{cell}, η_c, η_a and iR_{cell} represent the applied cell voltage (V), cathodic over-potential (V), anodic over-potential (V), and the total cell ohmic losses (V). The over-potentials represent the additional voltage supplied to the electrolysis process to overcome the cell resistances. Cathodic and anodic over-potentials are due to the concentration and activation resistances occurring at the electrodes while the ohmic losses are due to the ohmic resistances within the electrolysis cell (Wang et al.,2021).

The total cell ohmic losses include the losses due to electrolyte resistance and the resistance that migrating ions encounter across the membrane, the schematic diagrams of different electrolysis cells will be provided in the next sections. The type of electrolyte used as well as the properties of the membrane used in the electrolytic cell has an impact on the cell electricity consumption. The over-potentials on cathode and anode depend on the type of metal used as an electrode and metals differ with values of over-potentials. Platinum group metals such as platinum have low over-potentials, while metals such as cobalt have higher over-potentials (Rashid et al., 2015).

1.2.2.2 Electrolysis technologies

There are three different types of available technologies for electrolysis reaction namely, alkaline electrolysis (AEC), polymer electrolyte membrane electrolysis (PEM) and high-temperature solid oxide electrolysis (SOEC). These technologies differ concerning the working principles, the operating conditions (pressure and temperatures), phase of water, maturity of technology and the electricity conversion efficiency.

1.2.2.2.1 Alkaline electrolysis cell technology

Alkaline electrolysis cells (AEC) technology represents the most mature of the electrolysis technologies, this technology is well proven and has been in use to produce hydrogen. The AEC technology is based on the liquid phase electrolysis reaction, and it is typically operated at temperatures of 40-90℃ (Lefebvre et al., 2016). Fig. (2) shows the schematic diagram of the typical alkaline electrolytic cell.

The alkaline electrolytic cell comprises two compartments where the two half-cell reactions occur, one electrode in each compartment, the diaphragm membrane separating the compartments and the electrolyte. Hydrogen gas is produced in the cathode compartment while oxygen gas is produced in the anode compartment. Asbestos has been used as the traditional membrane separating the half-cell compartments, but its use was discontinued due to the associated health problems (Rashid et al., 2015). Zirfon® has also been reported as a good membrane, this membrane only allows the transportation of OH^- ions from one-half cell to the other.

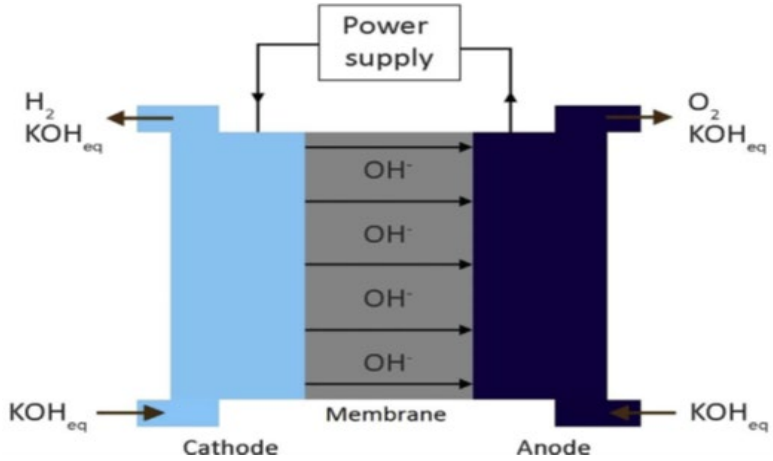

Figure 2: Schematic diagram of an alkaline electrolytic cell using potassium hydroxide as the electrolyte (Ghaib, 2018)

Potassium hydroxide and sodium hydroxide are used as electrolytes, with potassium hydroxide being the most preferred electrolyte because it is less corrosive and offers higher electrical conductivity compared to the sodium hydroxide solution. The electrolyte is typically used in concentrations of 20-40% (Kumar and Himabindu, 2019). The two half-reactions occurring in the cathode and the anode half-cell compartments are represented below.

$$H_2O_{(l)} + 2e^- \rightarrow H_{2(g)} + 2OH^- \quad (6)$$

$$2OH^- \rightarrow H_2O_{(l)} + 0.5O_2 + 2e^- \quad (7)$$

The operating pressures of alkaline electrolyte cells are reported to be in the range of 1-30bar (Bos, Kersten and Brilman, 2020).

The AEC technology is reported to have major drawbacks with regards to the limited current density and low operating pressures. The limited achievable current densities are caused by the ohmic losses on the liquid electrolyte and across the diaphragm (Carmo and Fritz, 2013). Most

conventional AEC cells have a gap between electrodes which is reported to increase the ohmic losses (Rashid et al., 2015) The ohmic losses in turn increase cell power consumption as explained by Eq. (5).

1.2.2.3 Polymer electrolyte electrolysis

Polymer electrolyte membrane (PEM) electrolysis is based on the liquid phase reaction and the typical cell comprises a polymer-based membrane, two electrodes attached on either side of the membrane and an external electricity supply. The PEM is characterised by the compact design where the cathode and anode are pressed onto the membrane forming a membrane-electrodes-assembly MEA(Ghaib, 2018). The anodic and cathodic half-reactions occurring in the PEM electrolysers are given by Eq. (8) and (9) respectively.

$$H_2O_{(l)} \rightarrow 0.5O_{2(g)} + 2e^- + 2H^+_{(aq)} \quad (8)$$

$$2H^+_{(aq)} + 2e^- \rightarrow H_{2(g)} \quad (9)$$

Water is introduced in the anodic chamber where it gets oxidized to oxygen and protons while releasing the electrons to an external source. The protons then migrate through a membrane onto the cathode where they get reduced to hydrogen gas by the electrons drawn from an external source. The working principle of the PEM electrolysis technology is depicted in Fig. (3).

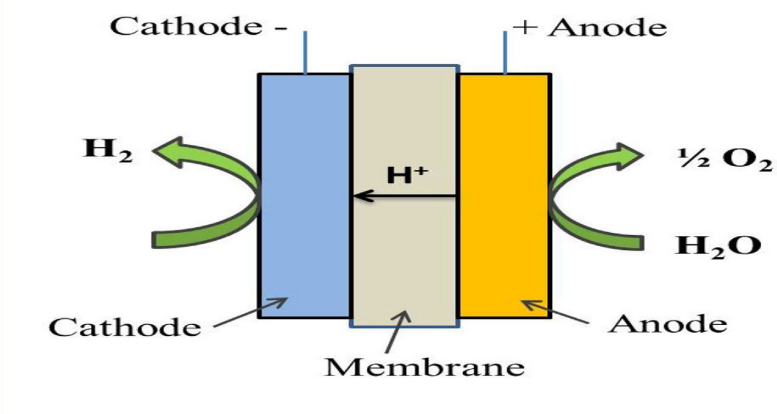

Figure 3: Schematic diagram showing the working principle of polymer electrolyte membrane (Shiva Kumar and Himabindu, 2019)

Perfluorosulphonic acid polymer membranes such as Nafion®, fumapem®, Flemion and aciplex are used as electrolytes and membranes in the PEM cells (Kumar and Himabindu, 2019) These membranes are characterised by low permeability to gases, the toughness allowing for high-pressure operation and high proton conductivity. The thickness of 20-200µm is commonly encountered in literature, with some work reporting membrane thickness of 25µm (Carmo and

Fritz, 2013; Rashid et al., 2015). The advantage of thin membranes is to reduce the ohmic losses across the membranes. The low permeability property of polymer-membranes prevents gases crossover thereby enabling the production of high purity hydrogen. The thin membranes and high proton conductivity result in reduced ohmic resistance losses, this, in turn, reduces electricity consumption as explained by Eq. (5).

Pressures as high as 200 bars have been reported in PEM technology, the high pressures are especially advantageous in the case where hydrogen gas needs to be stored under high pressure. High pressures have also been reported to decrease the ohmic resistances caused by the formation of gas bubbles at the electrodes. The PEM electrolysis cells can operate at the temperature range of 20-100℃ using liquid water as the feed (Lefebvre et al., 2015). This technology allows the use of high current densities, values as high as $10A/cm^2$ have been reported(Villagra and Millet, 2019). High current density values also reduce the electricity consumption of the electrolytic cell. The gap between electrodes in the electrolytic cells like in the case of the AEC is said to contribute to ohmic losses, thus the compact design of PEM further contributes to the lower ohmic losses and consequently the lower electricity consumption (PEM Electrolysis for Hydrogen Production Principles and Applications, 2016).

PEM technology makes use of the platinum group metals as the electrodes, while these metals have low over-potentials, they are costly and render this technology expensive. Platinum and Palladium are mostly used as the cathodes while oxides of Ruthenium and Iridium are mostly used as the anodes.

The properties of PEM cells (thin and tough membranes that are selectively permeable, compact design, high-pressure operation) make this technology to be more energy-efficient and produce hydrogen at higher purity than the AEC technology. The shortfall with this technology is primarily with the costs associated with the use of platinum group metals as electro-catalysts.

1.2.2.3 Solid oxide electrolysis technology

Solid oxide electrolysis cells (SOEC) technology represents the only gas-phase electrolysis technology that operates at high temperatures. The temperatures in the range of 700 – 850℃ are used in the SOEC technology (IRENA, 2020). Fig. (4) shows the working principle of the solid oxide electrolysis cells where steam is electrically decomposed into hydrogen gas and oxygen ions. The formed oxygen ions migrate through a solid electrolyte to the anode where they lose electrons to an external circuit while forming oxygen gas. The cathodic and anodic half-cell reactions are given in Eq. (10) and (11) respectively.

$$H_2O_{(g)} + 2e^- \rightarrow H_{2(g)} + O^{2-} \quad (10)$$

$$O^{2-} \rightarrow 0.5O_{2(g)} + 2e^- \quad (11)$$

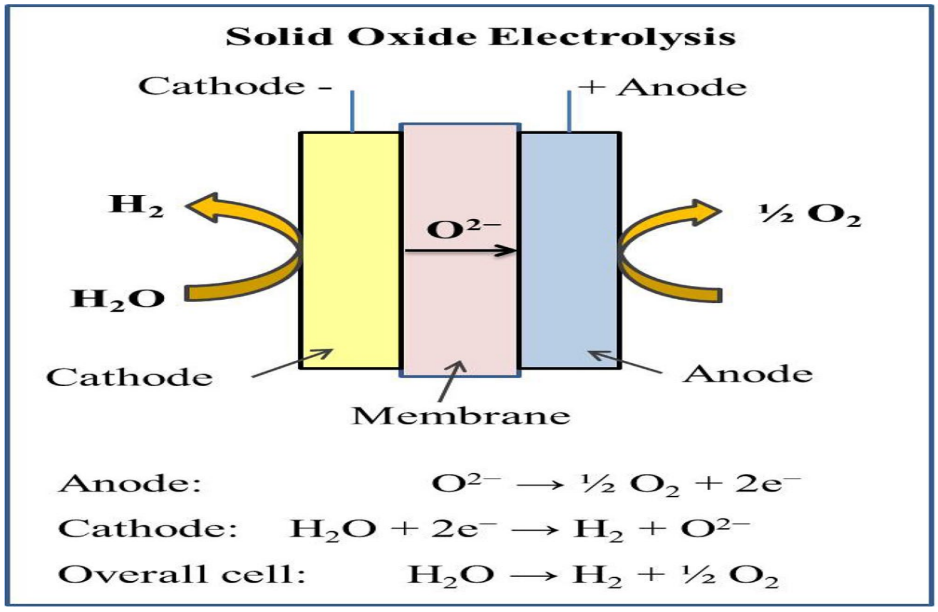

Figure 4: Schematic diagram showing the working principle of high-temperature solid oxide electrolytic cell (Shiva Kumar and Himabindu, 2019)

The SOEC technology employs solid electrolytes that can conduct ions at high temperatures, Zirconia doped with Yttria (YSZ) is the most used solid electrolyte (Laguna-Bercero, 2012; Lefebvre et al., 2015). Other solid electrolytes such as Scandia stabilized Zirconia and Ceria based electrolytes can also be used instead of YSZ. Porous cermet materials made of YSZ and metallic Nickel are usually used as cathodes, other materials such as Sameria doped ceria and Nickel dispersed nanoparticles can also be used. Materials typically used for anode include lanthanum strontium manganite (LSM) and YSZ composite (Laguna-Bercero, 2012).

The electrolysis reaction carried out at high temperatures requires lesser electricity as shown by Fig. (1), this makes the SOEC technology have the lowest electricity consumption and hence the highest energy conversion efficiency as compared to the low-temperature electrolysis technologies. The heat demand of electrolysis reaction has also been shown to increase with the temperature, however, a decrease in the electricity demand is higher than an increase in the heat demand. High temperatures do not only favour the thermodynamics of electrolysis reaction but also improve the reaction kinetics and ion conductivity of the solid electrolyte (Rashid et al., 2015). The improved ion conductivity reduces the ohmic losses and thereby contributes to reduced electricity consumption.

The SOEC technology holds great potential for renewable hydrogen production because of the high electricity conversion efficiency compared to other electrolysis technologies. This technology can also be used to co-electrolyse steam and carbon dioxide to form synthesis gas which is used to synthesise a myriad of fuels and chemicals (Andika et al., 2018; Er-rbib, Kezibri and Bouallou, 2018). The low durability and degradation of materials due to high temperatures present challenges for the commercialization of the SOEC technology.

This section has discussed the electrolysis sub-process which forms an integral part of the overall power-to-chemicals process schemes. The electrolysis sub-process produces hydrogen which can either be used as a fuel or be further processed in the synthesis step to form different chemicals and fuels. The next section will discuss the different synthesis processes and technologies used to produce the considered chemicals and fuels.

1.3 Synthesis processes for different chemicals and fuels

The hydrogen gas produced in the electrolysis sub-process can be catalytically converted to the different carbonaceous chemicals and/or fuels by reactions with carbon dioxide. In the case of non-carbonaceous chemicals like ammonia, the air is used to provide the nitrogen required to react with hydrogen. Extensive studies have been conducted on different power-to-chemicals process schemes, notably on power-to-methane, power-to-methanol, power-to-dimethyl ether, and power-to-Fischer-Tropsch products (Becker et al., 2012; Botta et al., 2015; Luo et al., 2018; Bos, Kersten and Brilman, 2020).

The power-to-chemicals processes can also produce other fuels through the hydrogenation of carbon dioxide using the different catalyst systems. Such chemicals and fuels include ethane, propane, ethanol, methanol, and ethylene. Synthesis gas (carbon monoxide and hydrogen) can also be produced in a power-to-chemicals process through the co-electrolysis of carbon dioxide and water (Er-rbib, Kezibri and Bouallou, 2018).

1.3.1 Methane synthesis

Power-to-methane process pathway produces methane gas from hydrogen and carbon dioxide through the Sabatier reaction as shown in Eq. (12)

$$CO_{2(g)} + 4H_{2(g)} \rightarrow CH_{4(g)} + 2H_2O_{(g)} \quad (12)$$

The Sabatier reaction is highly exothermic and spontaneous with the associated standard enthalpy and Gibbs free energy of reaction of -165 and -131 kJ/mol, respectively. Most reported studies on this process employ the high-temperature SOEC to produce hydrogen. The

heat of the exothermic reaction is used to produce steam that is used in the electrolysis sub-process thereby allowing for heat integration between the two sub-processes. The low-temperature electrolysis processes have also been integrated with the Sabatier reaction; however, such integrations have been reported to cause the overall power-to-methane process to have a low efficiency compared to the high-temperature SOEC electrolysis counterpart.

The Sabatier reaction is reported to be accompanied by other reactions that form by-products such as carbon monoxide and solid carbon. Carbon monoxide is produced by the reverse water gas shift reaction as follows.

$$CO_{2(g)} + H_{2(g)} \leftrightarrow H_2O_{(g)} + CO_{(g)} \quad (13)$$

Carbon can be produced through two different reactions as represented in Eq. (14) and (15)

$$2CO_{(g)} \rightarrow CO_{2(g)} + C_{(s)} \quad (14)$$

$$CO_{(g)} + H_{2(g)} \rightarrow H_2O_{(g)} + C_{(s)} \quad (15)$$

The different catalyst systems have been studied for the Sabatier reaction including nickel, ruthenium and cobalt metals catalysts supported on aluminium dioxide (Gruber et al., 2018). The nickel-based catalyst system is notably preferred for the Sabatier reaction because of its relatively low price, higher activity, and selectivity towards methane (Lefebvre et al., 2016). Nickel, however, forms toxic nickel carbonyl at temperatures below 200℃ and the catalyst sintering occurs at temperatures above 600℃ (Schaaf et al., 2014). The use of a nickel catalyst system, therefore, defines the operating temperature range of methane synthesis reactors.

The operating temperature range not only avoids the formation of nickel carbonyl or prevents catalyst sintering but can also reduce the formation of possible by-products. Nickel catalyst is known to have high activity in promoting the reverse water gas shift reaction, but the thermodynamic analysis by (Schaaf et al., 2014) revealed low to insignificant carbon monoxide within the 200-600℃ range. Carbon formation on the other hand can be impeded by manipulating the ratio of feed carbon dioxide to hydrogen. It has been reported that the stoichiometric ratio of carbon dioxide to the hydrogen of 1:4 prevents the formation of solid carbon (Ghaib, 2018).

The thermodynamic analysis serves as a good starting point to determine reactions conversions at different operating conditions such as the feed concentration, the reaction temperature, and the operating pressures. (Schaaf et al., 2014) studied the two different thermodynamic analyses

on the methanation reaction. The first analysis investigated the effects of the reaction temperature on possible reactions Gibbs free energy, this work determined which products are most likely to form in the considered temperature range. The second analysis was based on determining the equilibrium conversion of carbon dioxide as a function of both the temperature and pressure as shown in Fig. (5).

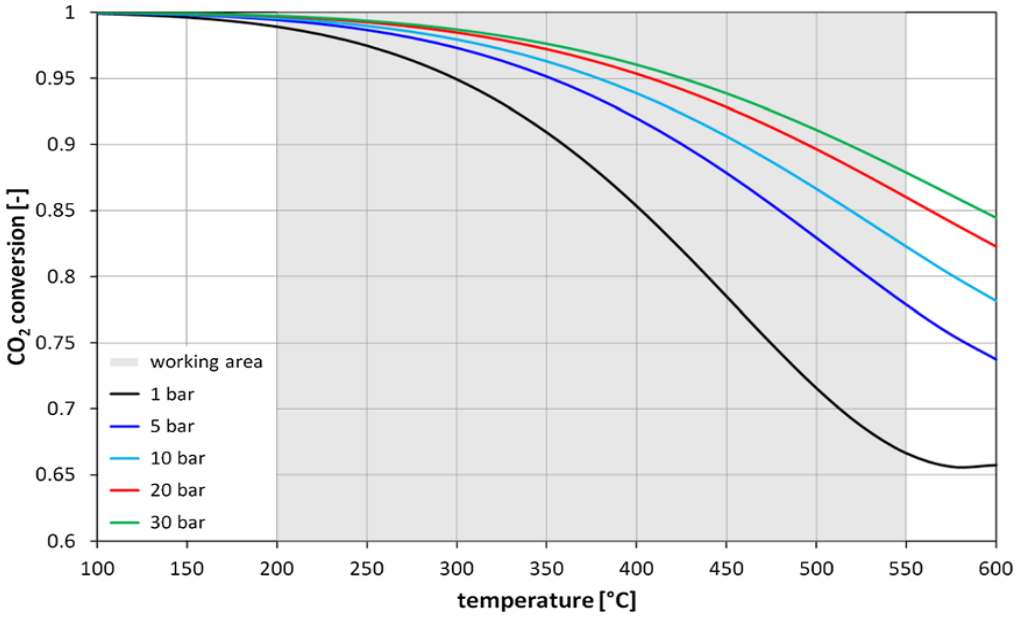

Figure 5: Equilibrium conversion of carbon dioxide as a function of temperature for different reaction pressures(Schaaf et al., 2014)

The equilibrium conversion of carbon dioxide is observed to decrease with an increase in the temperature and a decrease in the operating pressure. The equilibrium conversion value close to 1 is achievable at 200℃ and 30bar, while the conversion close to 65% is achieved at 550℃ and 1 bar. The low temperatures are, however, associated with the slow kinetics which in turn requires enormous amounts of catalyst to achieve reasonable conversions (Gruber et al., 2018).

The different reactor designs and architectures have been used in the different studies; the reactor designs are mostly aimed at optimizing the reactants conversions while also achieving good thermal management to protect the catalysts. It was mentioned that the Sabatier reaction is highly exothermic, therefore a good thermal management strategy is necessary for the reactor designs. Most reported studies employ the fixed bed reactors for methanation synthesis where the adiabatic and cooled fixed bed reactors are mostly used.

The fixed bed reactor design employs a cascade of reactors with the inter-stage cooling systems between the reactors. A cascade of two to four adiabatic reactors is widely reported in the literature, some designs add the water removal units in between the reactors to push the

equilibrium to the right. In some cases, a fraction of the product of the first reactor is recycled back to the inlet to dilute the fresh feed and hence regulate the reactor temperature. (Balan, Buga and Bildea, 2016) investigated the effects of the product of the first reactor recycle ratio on the maximum achievable reaction temperature. They reported the recycle ratio of 0.7 to be optimal for achieving the maximum allowable reactor temperatures. Recycle ratios lower than 0.7 were reported to result in the reaction temperatures being more than what the catalyst can tolerate.

Gruber et al., (2018) performed experimental studies of methanation reaction integrated with high-temperature solid oxide electrolysis stack using the cooled-fixed bed reactors. The reactors architecture comprising two reactors in series, the inter-stage cooling system, and the water removal units were used in the study. This novel architecture produces steam in cooled-fixed bed reactors, the produced steam is then used in the upstream electrolysis sub-processes. Other reactors such as three-phase and membrane reactors can be employed in the methanation synthesis sub-process.

1.3.2 Methanol synthesis

Power-to-methanol process schemes use hydrogen to hydrogenate either carbon monoxide or carbon dioxide to methanol. The produced methanol can be used in fuel application or as a building block to a myriad of other industrial chemicals. In fuel application, methanol can be used to partially replace gasoline, be used in the production of biodiesel and gasoline in methanol-to-gasoline (MTG) processes (Kourkoumpas et al., 2016; Nieminen, Laari and Koiranen, 2019). As a building block, methanol is used to produce important chemicals such as olefins in the methanol-to-olefins (MTO) process, dimethyl ether, methyl amines, methyl acrylates and formaldehyde (Leonzio, 2018; Ouda et al., 2019).

Methanol can be produced from the syngas, or the direct hydrogenation of carbon dioxide as follows.

$$CO_{(g)} + 2H_{2(g)} \rightarrow CH_3OH_{(g)} \quad (16)$$

$$CO_{2(g)} + 3H_{2(g)} \rightarrow CH_3OH_{(g)} + H_2O_{(g)} \quad (17)$$

Carbon monoxide and carbon dioxide hydrogenation reactions are catalysed by copper-based catalyst systems such as Cu/ZnO and CuO/ZnO/Al_3O_2 (Kourkoumpas et al., 2016; Zhang, Wang, Van, et al., 2019). The copper-based catalysts are reported to also activate the water gas shift reaction(Nieminen, Laari and Koiranen, 2019), as represented by Eq. (18)

$$H_2O_{(g)} + CO_{(g)} \rightarrow H_{2(g)} + CO_{2(g)} \quad (18)$$

The associated standard enthalpies of reaction at 25℃ and 1 atmosphere for reactions in Eq. (16-18) are -90, -50 and 41 kJ/mol respectively, this indicates that the heat is given off during the hydrogenation reactions while the WGS reaction absorbs heat. The hydrogenation reactions are thermodynamically favoured at the low temperatures and high pressures, however, the minimum temperature of 200℃ is used because the lower temperatures result in slow kinetics (Nieminen, Laari and Koiranen, 2019). The temperature and pressure ranges used for these reactions are 200-290 ℃ and 50-125bar respectively (Ouda et al., 2019). Carbon monoxide hydrogenation is a well-known and widely used technology in the industry to produce methanol. There are currently two ways in which carbon monoxide hydrogenation can be carried out in the context of the power-to-methanol concept. Carbon dioxide and water co-electrolysis represent the first method in which the syngas is produced during the high-temperature co-electrolysis of steam and carbon dioxide (Andika et al., 2018). The produced syngas is then sent to the methanol synthesis reactor where carbon monoxide hydrogenation is carried out. The second approach constitutes sending carbon dioxide to a water gas shift reactor where it gets converted to carbon monoxide which then goes to a hydrogenation reactor. Carbon monoxide hydrogenation is reported to produce by-products such as higher alcohols, dimethyl ether, oxygenates, acids and aldehydes. Temperature control is one other key issue that needs attention in carbon monoxide hydrogenation (Rivera-Tinoco et al., 2016)

The direct carbon dioxide hydrogenation to methanol represents the alternative pathway, this reaction is said to have slower kinetics, the lower equilibrium conversions and the formation of water are reported to accelerate catalyst deactivation(Nieminen, Laari and Koiranen, 2019). The reaction also requires more hydrogen than its counterpart due to the formation of water. The single-pass conversion as low as 21% has been reported for carbon dioxide hydrogenation technology (Zhang, Wang, Van, et al., 2019).

With all these drawbacks, the direct carbon dioxide hydrogenation reaction results in less to no side products, a feature that carbon monoxide hydrogenation suffers in. Researchers have put efforts to improve the reaction kinetics and conversion of this technology. Technologies such as the membrane reactors, the high pressures to condense formed gases out of the reaction phase, the adsorbents to remove formed products have been used to improve the performance (Bos, Kersten and Brilman, 2020). (Nieminen, Laari and Koiranen, 2019) studied the liquid phase carbon dioxide hydrogenation in their techno-economic analysis of this process. These

researchers proposed the use of the bubble-column reactor operating at the lower temperature of 180 ℃ and the high pressure of 50 bars using 1-butanol and 2-butanol solvents as the medium catalyst, they reported the carbon dioxide single-pass conversion as high as 81%.

The power-to-methanol process schemes using the different electrolysis technologies have been reported in the literature. (Bos, Kersten and Brilman, 2020) used the alkaline electrolysis cells operating at 120℃ and 30 bars to produce hydrogen which was then used in an adiabatic reactor for methanol synthesis. The alkaline electrolysis stacks are also used in a commercial power-to-methanol process used by carbon recycle international plant coupled with the water gas shift reactor and the carbon monoxide hydrogenation synthesis (Harp *et al.*, 2016). (Ouda et al., 2019) used the polymer electrolyte membrane technology in their techno-economic and ecological studies of power-to-methanol.

A novel compact reactor design that combines the solid oxide electrolysis reactor and the methanol synthesis reactor has also been reported. This design allows for the higher operating temperatures for methanol synthesis of above 400℃, which makes it easier to integrate heat with the solid oxide electrolysis operating at 600℃. The technology makes use of ZrO_2 catalyst which allows for the higher temperatures of methanol synthesis. This set-up is reported to result in a well-integrated system with small heat losses and improved overall efficiency (Schwabe et al., 2019).

1.3.2 Dimethyl ether synthesis

Dimethyl ether (DME) is produced in the power-to-DME process schemes using hydrogen produced via electrolysis to catalytically synthesize DME. The produced DME can be used as a fuel where it serves as an alternative to diesel and liquified petroleum gas. This compound burns cleanly with reduced emissions of NO_x and SO_x (Ren et al., 2019; Kartohardjono, Adji and Muharam, 2020). DME can also be used in pesticides, as a replacement of chloro-carbons in aerosols and as a building block in the production of propylene and ethylene (Leonzio, 2018).

Two different methods of DME production can be employed in the power-to-DME process schemes, these methods are the direct and indirect DME syntheses. The direct process uses carbon dioxide and hydrogen as feed materials to the DME synthesis reactor. The following reactions take place during the direct DME synthesis.

$$CO_{2(g)} + 3H_{2(g)} \rightarrow CH_3OH_{(g)} + H_2O_{(g)} \quad (19)$$

$$2CH_3OH_{(g)} \rightarrow CH_3OCH_{3(g)} + H_2O_{(g)} \quad (20)$$

$$CO_{2(g)} + H_{2(g)} \rightarrow CO_{(g)} + H_2O_{(g)} \quad (21)$$

In this reactions scheme, methanol is firstly formed from the carbon dioxide hydrogenation followed by the methanol dehydration to DME, the water gas shift reaction also occurs as a side reaction. These reactions occur in one reactor, hence the direct synthesis, with the use of the by-functional catalyst system. Copper-based catalyst $CuO/ZnO/Al_2O_3$ is used for the methanol synthesis while the acidic γ-alumina and HZM-S are employed for the methanol dehydration reaction (Botta et al., 2015; Ren et al., 2019). Water formation has been reported to pose problems of copper-based catalysts sintering and ultimate deactivation. Since water is an inevitable product in this reactions scheme,(Ren et al., 2019) conducted studies where the by-functional catalyst made of $CuO/ZnO/Al_2O_3$, and HZM-S stability was improved by the method of catalyst preparation. The carbon monoxide hydrogenation to methanol and DME process route is also possible for power-to-DME. (Botta *et al.*, 2015) studies involved the thermodynamic analysis of carbon dioxide and water co-electrolysis to syngas which was then sent to the direct DME synthesis using a by-functional catalyst.

The indirect DME synthesis comprises two sub-processes where the methanol synthesis from carbon dioxide is carried out in one reactor followed by the methanol dehydration in the second reactor. Each reactor uses the catalyst system and the operating conditions suitable for the intended product.

1.3.3 Ammonia synthesis

The power-to-ammonia concept produces hydrogen in the electrolysis sub-process and reacts it with nitrogen to form ammonia in the synthesis step. Nitrogen gas is obtained from the air through the different air separation technologies.

Ammonia represents the second most-produced chemical after sulphuric acid globally with an annual global production of 200 million tonnes/year. Most of the ammonia production technologies use natural gas, coal, and oil as the feedstocks for hydrogen production, resulting in approximately 420 million tons of carbon dioxide emissions per annum (Giddey et al., 2017). The power-to-ammonia concept, which does not involve fossil fuels, holds the potential to greatly reduce carbon dioxide emissions.

Ammonia is used to produce fertilizers, explosives, cleaning chemicals with the potential use as a fuel for fuel cells, internal combustion engines and gas turbines (Giddey et al., 2017;

Pressure et al., 2017). Ammonia is produced from the mixture of nitrogen and hydrogen in the Haber-Bosch synthesis reactor according to Eq. (22).

$$N_{2(g)} + 3H_{2(g)} \leftrightarrow NH_{3(g)} \quad (22)$$

The reaction is exothermic and thermodynamically favourable towards ammonia at high pressures and low temperatures. The operating pressures of up to 200bar and the operating temperatures of 450-500℃ are typically employed with the use of an iron-based catalyst (Giddey et al., 2017). The high equilibrium conversions can be achieved at lower temperatures; however, reaction kinetics are slow at lower temperatures.

Different renewable power-to-ammonia concepts have been investigated where the different electrolysis technologies were used to produce hydrogen gas. (Hasan and Dincer, 2019) studied the production of ammonia using the integrated wind and solar photovoltaic system with the polymer electrolyte membrane used to produce hydrogen. Researchers work compared the energy and exergy efficiency of the integrated system under different solar irradiation and wind velocities. They found that energy and exergy efficiencies were higher when the wind turbines dominated the integrated system, i.e., when the wind velocities were high, and the solar irradiation intensity was low. (Siddiqui and Dincer, 2020) also used the PEM technology to produce hydrogen which was reacted with nitrogen to produce ammonia intended to be used in the fuel cells. (Sánchez and Martín, 2018) used the alkaline electrolysis cells in their study of the optimal renewable (Cinti et al., 2017) considered the use of solid oxide electrolyser in their studies to produce renewable ammonia, their study revealed that the power-to-ammonia using the high-temperature SOEC has higher energy storage efficiency of 62.4% compared to the low-temperature counterparts with a storage efficiency of 36.5%.production of ammonia with the AEC stack operated at the pressure of 5 bar and the temperature of 80℃.

This section has covered the literature on different power-to-chemicals process pathways. The literature highlighted the reactions involved, equilibrium and actual conversions, different reactor set-ups, catalyst systems used, experimental and theoretical work as well as the different electrolysis technologies. Some studies compared the overall storage efficiencies of synthesis processes where different electrolysis modes were used and the results point that the high-temperature electrolysis produces higher efficiencies compared to the low-temperature counterparts.

Now that the power-to-chemicals section has been discussed, the next section will focus on the type of energy source that will be used to provide energy to the power-to-chemicals process schemes. This study proposes to use solar energy to provide the energy required in the power-to-chemicals process schemes, therefore the literature on different types of solar technology, recent developments and the costs associated with producing energy from solar sources will be provided in the next section.

1.4 Solar Energy

Solar represents the most abundant, cleanest, and inexhaustible renewable source of energy; it is estimated that the amount of $1.8x10^{11}$ MW of solar energy intercepts the planet earth (Parida Iniyan and Goic, 2011). This energy is many times over the current global energy demand. Solar energy can be harnessed into useful electrical and thermal energy using solar photovoltaic (PV) and solar thermal technologies, respectively.

1.4.1 Solar photovoltaic technology

Solar PV technology is the most popular of the solar technologies, the PV technology converts the photons in sunlight into electrical energy using the photovoltaic effect. Solar PV technology can be categorised into two main technologies as follows.

- First-generation solar photovoltaic technology
- Second-generation solar photovoltaic technology

First-generation solar photovoltaic technology

The first-generation solar PV cells are constructed from silicon wafers and represent the most popular and the most energy-efficient solar PV technology. The first-generation solar PV cells are manufactured by doping a layer of silicone atoms with five valence electrons atoms such as phosphorous on one side, the phosphorous doped silicon layer is then attached to a layer of pure silicone. The phosphorous atoms have five valence electrons while silicon atoms have four valence electrons, this makes the pure silicon layer of the cell have more affinity to electrons than the phosphorous doped silicon layer. The pure silicone layer is then attached to the boron doped silicone to complete the PV cell. Boron atoms contain three valence electrons and make the boron doped layer have more affinity to electrons than the middle pure silicon layer. The phosphorous doped and boron-doped layers are referred to as N and p-type layers respectively forming what is known to be p-n junction diode (Rathore *et al.*, 2019a). Fig. (6) schematically illustrates the working principle of a typical solar PV cell.

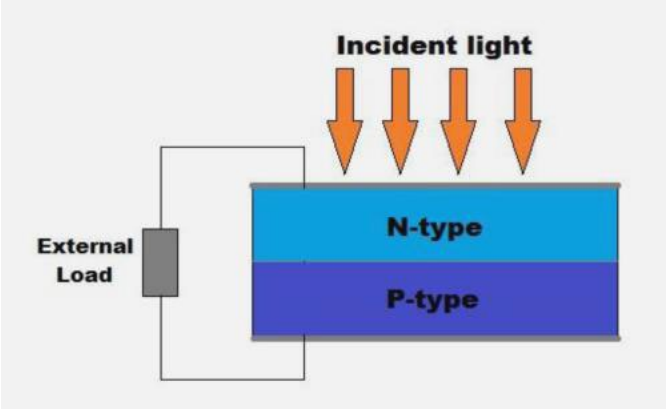

Figure 6: The working principle of a typical solar photovoltaic cell (Hudedmani, Soppimath and Jambotkar, 2017)

Photons present in the incident light transfer the energy to the electrons which then travel from the n-type layer through an external load to the p-type layer, hence creating the current.

The first-generation solar PV can be further categorised into mono-crystalline and poly-crystalline silicon technologies. The mono-crystalline solar PV cells are made up of black octagonally shaped layers and are produced by a complex Czochralski process (Hudedmani, Soppimath and Jambotkar, 2017; Ahmad et al., 2020). This technology is the commercially most efficient solar technology with a panel efficiency range of 16 – 16.9%. The SunPower Corporation reported the highest commercial panel efficiency of 20.4% (Gul, Kotak and Muneer, 2016a; Rathore et al., 2019).

The poly-crystalline solar PV cells are made up of blue rectangularly or squarely shaped layers and are produced by cutting the silicon ingots into thin wafers that are then assembled to form a PV cell (Mughal, Sood and Jarial, 2018; Ahmad et al., 2020). The production process of these solar cells is relatively simple and cheaper compared to the Czochralski process used to manufacture the poly-crystalline solar PV. This renders the poly-crystalline cells cheaper than the mono-crystalline counterparts. The poly-crystalline solar PV cells are more preferred in the industry due to their lower cost but they, however, exhibit lower efficiency compared to the mono-crystalline cells. The efficiency range of 15 – 16.9% has been reported with the highest commercial efficiency of 16.9% reported by the Neo Solar Power Corporation (Gul, Kotak and Muneer, 2016).

Second-generation solar photovoltaic technology

The second-generation solar-PV cells are produced by depositing a thin layer of photovoltaic material on a substrate. The thin nature of these materials makes them cheaper than first-

generation PV cells. Unlike the first-generation solar PV that is dominated by silicon, the second-generation cells are fabricated from different materials such as amorphous silicon (a-Si), cadmium, telluride, and copper. The thin-film solar PV cells are generally lesser efficient as compared to their first-generation counterparts. There are currently three different technologies dominating the thin-film solar photovoltaic market.

- Amorphous silicon (a-Si)
- Cadmium telluride (CdTe)
- Copper indium gallium selenide (CIGS)

The amorphous silicon solar photovoltaics are made up of a non-crystalline allotope of silicon and are said to be absorbing light more efficiently than the thick-film crystalline silicone cells. The a-Si cells command the greatest share amongst the thin-film solar PV with the highest module efficiency of 13.8% (Gul, Kotak and Muneer, 2016). The cadmium telluride solar PV cells have an efficiency range of 9.5 – 11%, these solar cells suffer a drawback of toxicity from the cadmium material (Hudedmani, Soppimath and Jambotkar, 2017b; Mughal, Sood and Jarial, 2018). The copper indium gallium selenide solar photovoltaics have a panel efficiency ranging from 10 to 12% (Rathore et al., 2019).

Solar Photovoltaic performance

The performance of the solar photovoltaic module is evaluated in terms of the solar conversion to electricity. The solar conversion efficiency is defined as the energy output from the solar PV module divided by the total solar energy received by the module (Idoko, Anaya-Lara and McDonald, 2018).

$$\eta_{PV} = \frac{E_{PV(OUT)}}{E_{PV(IN)}} \qquad (23)$$

Where $E_{PV(OUT)}$ and $E_{PV(IN)}$ represent the energy output and the solar energy received by the PV module, respectively.

Eq. (23) can further be simplified to incorporate the solar irradiation and the solar PV modules surface area as shown in Eq. (24)

$$\eta_{PV} = \frac{P}{A_{PV}G} \qquad (24)$$

Where P, A_{PV} and G represents the power output of a solar panel (kW), the surface area of solar panels (m^2) and solar irradiation (kW/m^2), respectively.

Solar photovoltaic cost

The cost of solar photovoltaic is determined by using the Levelized cost of energy (LCOE), the LCOE for a project is defined as the lifetime cost of the project inclusive of the capital, operating & financing costs over the project lifetime (Aldersey-Williams and Rubert, 2019) as shown on Eq. (25)

$$\mathrm{LCOE} = \frac{\sum_{t=1}^{n} \frac{C_t + O_t + V_t}{(1+d)^t}}{\sum_{t=1}^{n} \frac{E_t}{(1+d)^t}} \tag{25}$$

Where $t, C_t\ O_t\ V_t, E_t$ n and d represent time, capital cost, fixed operating cost, variable operating cost, the energy produced, the last year of the project and the discount rate, respectively.

The cost of solar energy has been steadily decreasing to a point where solar energy is becoming more and more cost-competitive compared to fossil fuel-based technologies. Half of the new solar energy installed in Australia, China, Chile, and UAE is reportedly cheaper than fossil fuel-based energy (PV magazine, 2020). International Renewable Energy Agency (IRENA) compiled data on the total installed cost, capacity factor and Levelized cost of electricity as shown in Fig. (7). It is observable that the total installed cost and the LCOE have been steadily decreasing in the period 2010-2019. The LCOE of the solar PV was 0.378 USD/kWh and 0.068 USD/kWh in 2010 and 2019 respectively, this translates to an 82% cost reduction from the year 2010 to the year 2019 (IRENA, 2020).

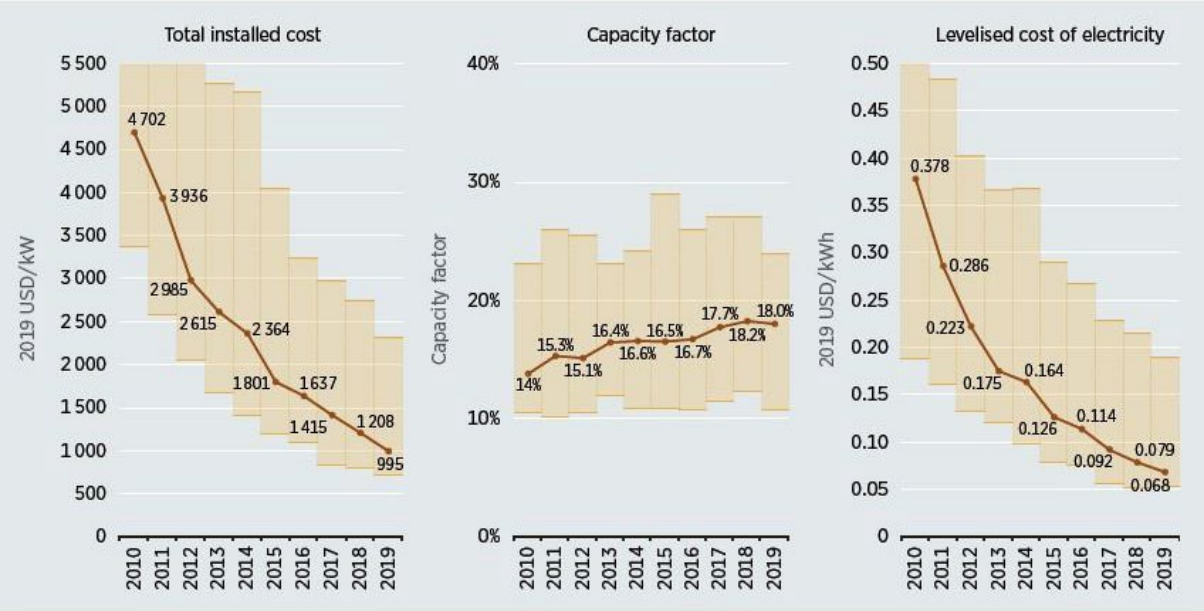

figure 7: The global weighted average total installed costs, capacity factor and LCOE for solar PV, 2010-2019 (IRENA, 2020)

The average weighted LCOE for solar photovoltaics has further dropped from 0.068 USD/kWh to 0.050 USD/kWh in 2020, translating to a further 26.5% in cost reduction. The new solar projects in Australia, China, Chile, and UAE are reported to have the lower LCOE in the range of 0.023-0.029 USD/kWh (PV magazine, 2020).

1.4.2 Solar thermal technology

Solar thermal technologies convert solar energy by absorbing solar radiation and turning it into useful heat. There are three types of solar thermal technologies which can be categorised in terms of the temperature of the working fluid.

- Low-temperature;
- Medium-temperature; and
- High-temperature solar thermal technologies.

Low-temperature solar technology

Low-temperature solar technology is a class of solar collectors operating in the temperature range of 40-100℃. This type of collector is said to be mostly used amongst the solar thermal technologies and can be sub-divided into flat plate collectors (FPC) and evacuated tube collectors (ETC).

The FPC comprise a flat glazed cover, a selectively coated absorber, and tubes with a heat transfer fluid (HTF) flowing inside. The glazed cover is used to reduce the thermal losses by

convection to the environment while a selectively coated absorber is used to improve the absorption of solar rays. The technology mostly uses water and/or air as heat transfer fluid, with improvements in the thermal efficiency brought by using alternative HTF such as methanol, ethanol, and acetone (Gorjian et al., 2020). The FPCs are mostly used in the applications such as domestic and swimming pool water heating.

The ETCs are made of parallel evacuated tubes, selectively coated absorbers, copper tubes, and a heat exchanger. The ETCs use volatile heat transfer fluids such as methanol and ethanol which undergo the evaporation and condensation cycles in the absorber and heat exchanger, respectively. A selectively coated absorber absorbs solar energy and transfers it to the volatile fluid which evaporates and flows to the heat exchanger where it transfers its latent heat to the second fluid. The use of evacuated tubes is meant to greatly reduce the convection heat losses to the environment and renders ETC technology to be more efficient than its FPC counterpart (Gorjian et al., 2020).

The performance of low-temperature solar thermal collectors is best assessed by the solar thermal efficiency which measures how best the absorber works. The solar thermal efficiency is described by Eq. (26)

$$\eta_{ST} = \frac{Q_g}{A_C G} \tag{26}$$

Where η_{ST} , Q_g , A_C and G represents solar thermal efficiency, useful heat generated (W), surface area (m^2) and solar irradiation (W/m^2) respectively. Low-temperature solar thermal collectors perform best with high thermal efficiencies at low temperatures and exhibit low efficiencies when the temperature is greater than 100℃ (Sin et al., 2013; Ferry et al., 2020)

Medium temperature solar thermal technology

The medium-temperature solar thermal collectors operate in the temperature range of 100–300℃. These collectors have potential applications in the fields such as food processing, oil extraction, desalination, methanol-reforming, and process heating (Sin et al., 2013; Bellos et al., 2016). The most common medium-temperature solar thermal collector is based on the stationary compound parabolic concentrators (CPC) that use non-imaging optics to track the sunrays. The compound parabolic concentrators comprise asymmetric parabolic reflectors, evacuated tubes, selectively coated absorbers, and heat transfer fluid inside the tubes.

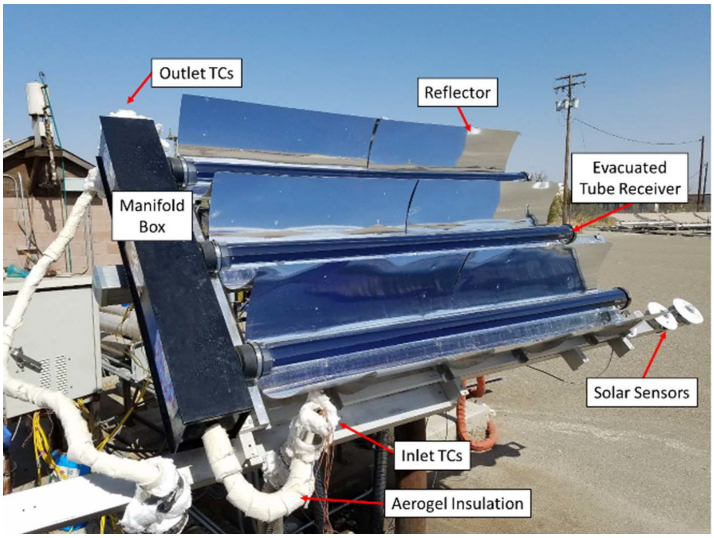

Figure 8: Example of compound parabolic concentrator solar thermal collector (Widyolar et al., 2018)

The parabolic reflectors reflect and concentrate sun rays onto the evacuated tube receiver which contains a selectively coated absorber and a tube containing heat transfer fluid. The reflectors are normally fabricated from aluminium and reflect both the direct and the diffuse sun rays onto the receiver tube.

There are two types of performance metrics that are commonly encountered in the compound parabolic concentrators literature which are the optical and thermal efficiencies. The optical efficiency ($\eta_{optical}$) is defined as the amount of heat the absorber receives from the total solar energy that reaches the collector (Bellos et al., 2016), and is described as:

$$\eta_{optical} = \frac{Q_{abs}}{Q_S} \tag{27}$$

Where $\eta_{optical}$, Q_{abs} and Q_S represent the optical efficiency, amount of heat reaching the absorber and the total solar energy reaching the collector, respectively. Thermal efficiency is the fraction of the total solar energy that is converted to useful heat (Widyolar et al., 2018) and can be described by Eq (28).

$$\eta_{th} = \frac{Q_g}{Q_S} = \frac{\dot{m}C_P\Delta T}{A_a G} \tag{28}$$

Where $\dot{m}$, C_P, ΔT and A_a represent the mass flow rate of heat transfer fluid (kg/s), the specific heat capacity of heat transfer fluid (J/kg. K), changes in temperature of heat transfer fluid (K) and the surface area of the aperture transporting heat transfer fluid (m^2).

Several studies have been conducted aiming at improving the efficiency of compound parabolic concentrators. In general, the performance is improved by increasing the optical and thermal efficiencies (Gorjian et al., 2020). The optical efficiency improvement is achieved by optimizing the geometry of the reflector and thereby improving the amount of the diffuse and direct sun rays reaching the receiver (Bellos et al., 2016) The improvements in the optical efficiency also lead up to increased thermal efficiency. The latter can also be increased by improving the heat transfer using selective coating on the absorber and the more efficient heat transfer fluid. (Hassanzadeh, Jiang and Winston, 2018) reported a thermal efficiency of 50% at 200 ℃ on a novel medium-temperature CPC by optimizing the absorber geometry to a pentagon shape. The same thermal efficiency of 50% at 200 ℃ was obtained in the studies carried out using an external compound parabolic concentrator (XCPC) with the pentagon-shaped absorber (Jiang, Widyolar and Winston, 2015; Widyolar et al., 2018).

High-temperature solar thermal technology

High-temperature solar thermal technology is mostly used for applications that require heat at temperatures higher than 300℃ (Sin et al., 2013; Bellos et al., 2016). The technology makes use of high concentration ratios, highly efficient reflectors, accurate tracking mechanisms and expensive heat transfer fluids to operate at elevated temperatures (Bhusal et al., 2020).

High-temperature solar thermal technology is divided into two main categories which are the line and point focus collectors as shown in Fig. (9). The line focus category is further sub-divided into the parabolic and linear-Fresnel solar thermal collectors. The point focus solar concentrators category consists of the solar tower and parabolic dish concentrators. Both the line and point focus technologies use sun-tracking mechanisms. The line point technology uses a single-axis tracking while the point focus uses a double-axis tracking mechanism (Hachicha et al., 2019).

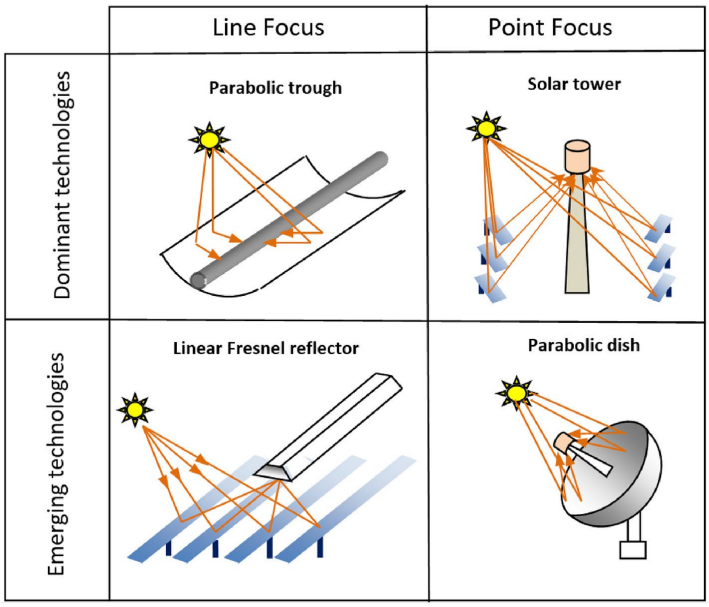

Figure 9: High-temperature solar thermal collectors (Hachicha et al., 2019)

The high-temperature solar thermal technology is mostly used for the power generation application in concentrated solar power plants (CSP). It can, however, also be used in the applications such as process heat generation, space heating, water heating, desalination, and refrigeration (Upadhyay, Patel and Ramana, 2019).

Performance and cost comparisons of solar thermal technologies

Performance comparisons

The performance of different solar thermal technologies in terms of the collection efficiency has been compared as shown in Fig. (10). The collection efficiency is measured as a function of reduced or normalized temperature of the heat transfer / working fluid. The use of normalised temperature is to use the same basis of comparison for different collectors operating under different conditions (temperatures and solar irradiation). The reduced temperature is defined according to Eq. (29).

$$T^* = \frac{T - T_0}{G} \tag{29}$$

Where T^* , T and T_0 are reduced temperature $\left(\frac{m^2 °C}{W}\right)$, the temperature of the working fluid (°C) and the ambient temperature (°C). Many research studies commonly use the solar thermal irradiation of 1000 W/m^2 and the ambient temperature of 10°C. Fig. (10) shows the solar thermal collection efficiency to generally decrease with an increase in the reduced temperature.

The evacuated flat-plate and evacuated tube collector with a round absorber (low-temperature collectors) are observed to exhibit the highest thermal efficiencies at low temperatures. The

external compound parabolic collector is seen to follow the low-temperature collectors with high efficiency at low temperatures.

Medium-temperature collectors, external compound parabolic and novel compound parabolic collectors are seen to have higher efficiencies compared to the low-temperature collectors at medium temperatures. This is of course with an exception to the evacuated flat-plate collector which shows higher thermal efficiency than medium-temperature collectors up to the reduced temperature of $0.21\ \frac{m^2 ℃}{W}$. The reduced temperature of $0.21\frac{m^2 ℃}{W}$ corresponds to the working fluid temperature of 220 ℃, the CPC with pentagon absorber outperforms the evacuated flat plate collector from this temperature upwards.

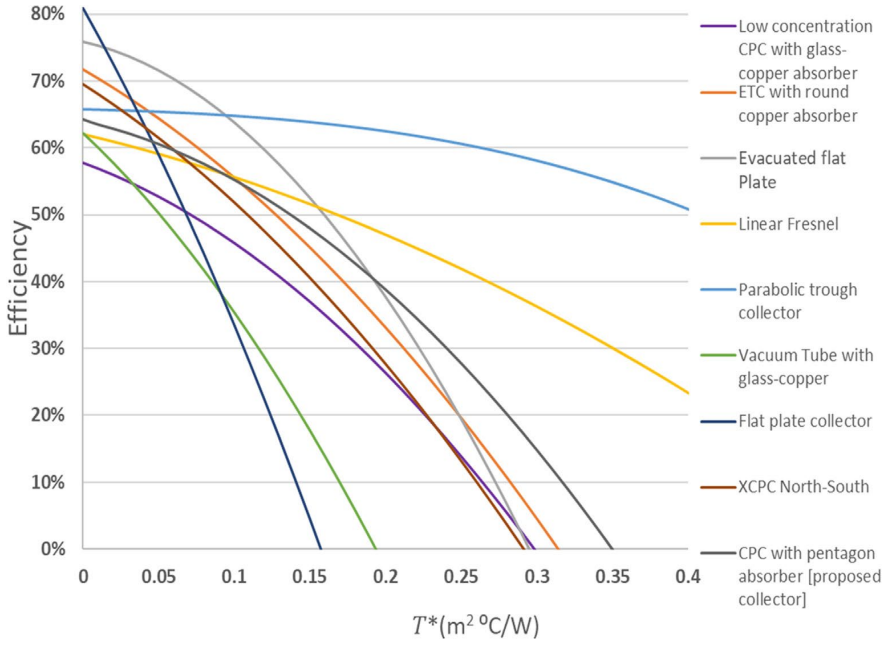

Figure 10: Thermal efficiencies of different solar thermal collectors at different working fluid reduced temperature (Widyolar et al., 2018)

Linear Fresnel and parabolic through collectors, high-temperature thermal collectors, exhibit generally high thermal efficiencies across all the considered temperatures. The parabolic through collector shows a minimum thermal efficiency of 50% at the highest considered reduced temperature, followed by the linear Fresnel collector.

The results from separate studies on the CPC have shown a consistent thermal efficiency of 50% at the working temperature of 200 ℃ (Jiang, Widyolar and Winston, 2015; Hassanzadeh, Jiang and Winston, 2018; Widyolar et al., 2018). Lower thermal efficiencies of 40 and roughly 42% at the same working temperature of 200 ℃ have also been reported for the CPC collectors (Sin et al., 2013; Bhusal et al., 2020).

Cost comparisons of different solar thermal collector technologies

The economic performance of the different solar thermal collectors has been compared for an HTF working temperature of 200 ℃. The Levelized cost of heat (LCOH) is generally used as a universal economic metric for different heat-generating systems including solar thermal collectors and fossil fuels systems. The LCOH covers all the costs incurred in the lifespan of a heat-generating system and it is defined according to Eq. (30)

$$\mathrm{LCOH} = \frac{(\text{installation costs})(\mathrm{FCR}) + \text{annual (O\&M)costs}}{\mathrm{Q_{output}}} \tag{30}$$

Where FCR, O&M and $\mathrm{Q_{output}}$ represent the interest rate, finance, and taxation factor, the operational and maintenance costs, and the annual output heat of the generation system. (Bhusal et al., 2020) compiled a list of some of the commercially available solar thermal collectors to compare the total cost of collector and the resulting LCOH for systems operating at 200℃ as shown in Table (1).

Table 1: Thermal efficiency, total cost and Levelized cost of heat for different solar thermal collectors operating at 200℃ (Bhusal *et al.*, 2020b)

Collector type	Total cost collector $	Thermal efficiency @ 200℃	LCOH $/kWh
Evacuated flat plate collector	430	50%	0.059
Linear fresnel collector	260	50%	0.044
Parabolic through collector	290	63%	0.034
All-glass evacuated collector	247	30%	0.047
External compound parabolic collector	242.5	45%	0.031

Table (1) shows that the costliest technology is the evacuated flat plate collector in terms of both the collector cost and the LCOH. This collector, however, shows a good thermal efficiency of 50% at the considered temperature. The all-glass evacuated collector follows with the second highest LCOH of 0.047 USD/kWh, it should be borne in mind that both technologies belong to the low-temperature class.

The linear Fresnel and the parabolic through collectors follow with the LCOH of 0.044 USD/kWh and 0.034 USD/kWh respectively. These high-temperature collectors show excellent thermal efficiencies of 50 and 63% respectively.

The external compound parabolic collector records the lowest LCOH of 0.031 USD/kWh but with the second-lowest thermal efficiency of 45% at the considered temperature. A study was conducted on the compound parabolic collector where the aim was to reduce the cost while maintaining the thermal performance (Bhusal *et al.*, 2020b). The authors achieved their objective by reducing the collector's material cost thereby reducing the LCOH to 0.029 USD/kWh at the thermal efficiency of 42%. This cost is the same as the current LCOH for natural gas in the United States which means that the solar thermal collector can compete with natural gas for medium-temperature heat applications.

1.3. Research questions

The study aims to answer the following key research questions.

- What is the theoretical overall system efficiency of solar photovoltaic power-to-chemical processes, considering the storage and utilization of hydrogen and hydrogen derived fuels such as methane, methanol etc?
- Can combining solar-photovoltaic with solar-thermal heat improve the overall system efficiency of power-to-chemicals processes?
- How does the performance of processes using solar-photovoltaic alone and processes using the combination of solar-photovoltaic and solar-thermal heat compare in terms of the overall system work efficiency, solar surface area requirements and Levelized cost of production?
- Does the temperature of solar-thermal heat have a significant influence on the process efficiency of the combined solar-photovoltaic and solar-thermal heat systems?

1.4. Research objectives

The objectives of the dissertation are as follows.

- To perform thermodynamic analysis using the ΔG-ΔH graphical tool to determine the most efficient way to store solar energy into chemical fuels, considering solar-photovoltaic and solar-thermal heat.
- To define a thermodynamic performance metric that will be used to assess the power-to-chemicals process pathways performances.
- To compare different power-to-chemicals process pathways using the defined thermodynamics performance indicator, area requirements for solar installation and the associated Levelized costs of production.

- Lastly, Aspen plus software will be used to develop process flowsheets for selected power-to-chemical processes to identify and optimize the most significant parameters to improve the process efficiency and reduce the cost to produce. The simulations consider power-to-hydrogen, power-to-methane, power-to-methanol, and power-to-ammonia process pathways.

1.5 Dissertation outline

Chapter 1: Introduction, literature review and aims of the dissertation.

Chapter 1 provides an outline of the dissertation and presents the executive introduction which discusses the need to carry out this study. The introduction also provides a brief literature review to outline the literature gap that the study aims to address. This chapter also discusses research questions and research objectives.

The literature review covers the subjects on power-to-chemicals schemes, solar-photovoltaic and solar-thermal technologies. It discusses the theoretical concept of electrolysis and the different electrolysis technologies that exist. The literature review further discusses the concept of power-to-chemicals and highlights recent research development and gaps in the field.

Chapter 2: Methodology and results on thermodynamic analysis

This section presents the theory, the tools, and the assumptions used in the development of the new approach to power-to-chemical processes. It introduces a two-dimensional graphical technique that uses the Gibbs free energy and the enthalpy (ΔG-ΔH) of a process to visualize the Thermodynamic analysis, the screening of options, and to set performance targets for a process in terms of the material, energy, and work balances. The discussion uses a hypothetical power-to-chemical process to illustrate the application of the graphical tool in identifying efficient pathways to convert power to chemicals. The methodology also defines the performance indicators to compare different power-to-chemical pathways objectively. Furthermore, the section covers economic analysis which compares the associated Levelized costs of energy for the considered process pathways.

Chapter 3: Case studies on Power-to-hydrogen, power-to-ammonia and power-to-methane and the comparisons between all the selected process schemes.

Chapter 3 uses the theory developed in Chapter 2 to study and compare all selected power-to-chemicals process pathways. Case studies on power-to-hydrogen, power-to-ammonia and power-to-methane are discussed in-depth and compared, followed by comparing with the

remainder of power-to-chemical process schemes. The theoretical targets in thermodynamic performance, optimal solar-PV area fraction and required solar collection area are determined. Comparisons between processes are made to the thermodynamic performance, energy cost and electrolysis costs. The analysis used in this chapter considers the black box approach as used in theoretical development.

Chapter 4: Aspen simulation of power-to-hydrogen process scheme.

Chapter 4 studies the power-to-hydrogen process pathway in the Aspen Plus® simulation software. The goal is to establish if there are any benefits of using the combined solar-PV and solar-T heat to power the process. Two process flowsheets are developed where the first flowsheet includes solar-PV electricity only with the second flowsheet incorporating both solar-PV electricity and solar-T heat. The two process flowsheets are compared in terms of energy performance (work efficiencies defined in Chapter 2), energy cost, electrolyser cost, total cost, and the total solar collection area. Lastly, the Chapter compares results from Aspen Plus® process flowsheets and the theoretical targets determined in Chapter 3.

Chapter 5: Aspen simulation of power-to-ammonia, power-to-methanol, and power-to-methane process schemes.

Chapter 5 examines process flowsheets of power-to-ammonia, power-to-methanol, and power-to-methane in Aspen Plus®. The primary objective is to determine the cost of producing the chemicals considering the process equipment costs and the operating costs. The work and heat flow arrangements, specifically the solar-PV area fractions, determined in Chapter 3 thermodynamic and gh-analyses are used to achieve the performance targets in the Aspen Plus® simulation. Aspen Plus® simulator is used to size and cost all the processing equipment except for the electrolysis stacks for each process and membrane separation system for the power-to-methane. The costs to produce each chemical from the selected power-to-chemicals, overall system work system and solar area collection areas are then compared.

Chapter 6: Conclusions

This chapter provides the summary of the study, considering the objectives, methods used, and results found.

Chapter 2

Thermodynamic analysis: Methodology and results

2.1 Thermodynamic analysis on ΔG-ΔH diagrams

The ΔG-ΔH graphical analysis (gh-diagram) is a process synthesis tool that can be used to determine or set performance targets of processes by using fundamentals of mass, energy, and work balances. The gh-diagram tool is useful in determining the possible performance targets for a process or a reaction. (Fox et al., 2017; Okonye et al., 2012; Muvhiiwa et al., 2018).

The use of the gh-diagram on a process consists of a macroscopic view that considers the interactions between the significant variables in the inlet and outlet material and energy streams across the process; providing insights into the main characteristics of the process and allowing to determine the limit of performance and to set up specific performance targets. Performance targets come mainly in the form of efficiency, which can be further broken down into different categories such as carbon, work, or chemical potential efficiency.

The tool can also assist in simplifying a complex reaction system by visualizing its *attainable region (AR)*, defined as the set of all possible product compositions from a given feed composition to the reactor, on a two-dimensional plot that provides information regarding the material, energy, equilibrium conditions, and possible reaction pathways. For reactive systems, the efficiency can also be based on the maximum possible achievable compositions of the desired products.

A process, defined by its material balance and for which the data of Gibbs free energy and enthalpy of formation of all the chemical components involved in the material balance is known, can be represented on the gh-diagram by a point, which indicates the energy requirement on the ΔH axis and the required energy quality (work) on the ΔG axis (Fox et al.,2017; Sempuga et al., 2010). The quality of energy is the portion of the energy required that must be equivalent to mechanical work, in other words, it is the portion of the energy that must possess the potential to produce work in the quantity given by the value of ΔG. Thus, a point on the gh-diagram provides several significant information concerning the process including the material balance, reflected in the magnitude of ΔG or ΔH, the quantity, the quality, and the direction of the energy required. The information contained on a single point on the gh-diagram can also indicate the feasibility and the subsequent level of the structural complexity of the process.

Thermal energy (heat) transfer is the simplest and most common way of supplying (recovering) energy and work to a process or a reaction. The gh-diagram can visually show how heat can be supplied or removed efficiently from a process. It was established that for heat to meet both energy and work requirements of a process it should be supplied at a special temperature called Carnot temperature as given by eq. (31) (Fox et al.,2017).

$$T_{Carnot} = \frac{T_O}{1-\frac{\Delta G_P(T_O,P_O)}{\Delta H_P(T_O,P_O)}} \tag{31}$$

Where T_{Carnot}, T_O, P_O, ΔH_P and ΔG_P represent the Carnot temperature (K), ambient temperature (K), ambient pressure(atm), process enthalpy, and Gibbs free energy, respectively. Processes occur reversibly when heat is transferred at Carnot temperatures, such processes represent the most thermodynamically efficient and thus represent the limit of performance.

(Sempuga et al., 2010) have classified regions on the gh-diagram into eight distinctive regions according to the signs of enthalpy and Gibbs free energy. Sempuga et al., (2010) further developed and added the Carnot temperature scale showing the thermodynamic feasibility of each region as illustrated in Fig. (11).

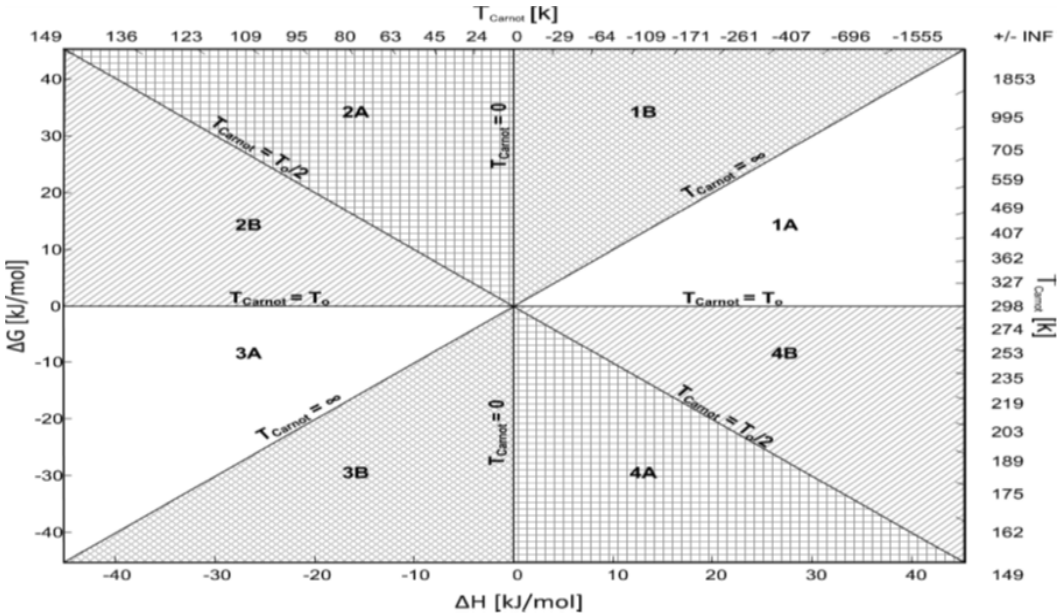

Figure 11: Thermodynamics region on the ΔG-ΔG diagram (Sempuga et al., 2010)

The enthalpy and Gibbs free energy represent the minimum amount of energy and work (work potential) that a process requires before it can proceed. The negative values of enthalpy and Gibbs free energy imply that a process must reject both energy and work, energy can be rejected from the process in the form of heat, work and both work and heat. The positive values of

enthalpy and Gibbs free energy on a gh-diagram imply that a process must be supplied with both the minimum energy and work before it can proceed. The minimum energy and work can be supplied to a process the same way they are rejected from a process.

The eight regions of the gh-diagram are 1A, 1B, 2A, 2B, 3A, 3B, 4A and 4B as shown in Fig. (11). Region 1(A and B) has positive values for both enthalpy and Gibbs free energy, indicating that the processes belonging to this region require energy and work to be added before they can proceed. In 1A, the Carnot temperature ranges from 298 K (25℃) to positive infinity, the amount of minimum energy required is higher than that of the work i.e., $\Delta H_P > \Delta G_P$. Thus, the energy and work requirements for these processes can be satisfied by simply supplying heat at the appropriate temperature (The Carnot temperature) indicated on the temperature scale. Processes belonging to this region are thermodynamically feasible due to the Carnot temperatures being attainable except for the processes that lie very close to the 45° line where the Carnot temperature approaches infinity. Region 1B has the Carnot temperatures ranging from the negative infinity to 0K (-273℃). This region is classified as an infeasible region because the Carnot temperatures are not practical. Processes belonging to region 1B cannot occur if the energy requirements are to be met by thermal energy alone.

Region 2 (A and B) has the negative enthalpy and positive Gibbs free energy, meaning all the processes belonging to this region release heat and require work to proceed. Region 2A has the Carnot temperature range of 0 to 149 K (-273.15 to -124.15℃), these temperatures are not easily attainable with the contemporary technology, indicating that the thermal energy alone cannot feasibly meet the energy requirements of processes belonging to this region. The Carnot temperature range of region 2B is 149 to 298K (-124.15 to 25℃), these temperatures are attainable and thus making region 2B thermodynamically feasible.

Region 3 (A and B) has negative values for both the enthalpy and Gibbs free energy indicating that the processes belonging to the region release both work and heat. The Carnot temperature of region 3A ranges from 298K (25℃) to infinity, while those of region 3B range from infinity to 0k (-273.15 ℃). Region 3A has a similar Carnot temperature range as region 1A, making it thermodynamically feasible when heat alone is used to provide the process energy requirements. All the processes belonging to region 3 are inherently irreversible but can be feasible.

Region 4 (A and B) has positive enthalpy and negative Gibbs free energy, all the processes belonging to this region require heat and have the potential to do work. The Carnot

temperatures of region 4A range from 0 to 149K (-273.15 to 124.15℃), while the Carnot temperatures of region 4B range from 149 to 298K (-124.15 to 25℃). These Carnot temperatures are attainable which makes region 4 a feasible region. The gh-diagram can quickly show if the process is thermodynamically feasible and efficient based on the region to which the process belongs.

Sempuga et al., (2011) showed how processes that inherently belong to the infeasible regions can be moved to the feasible regions by splitting these processes into two sub-processes that belong to the feasible regions. Methods such as chemical looping are an example of splitting an infeasible process into two feasible processes with achievable Carnot temperatures. The above-mentioned researchers showed for example, how work can be reversibly extracted from the combustion reactions by using chemical looping. The use of chemical looping where metals such as zinc oxide are used as intermediates to reversibly extract combustion work has been demonstrated.

The study further showed how work can be used to move processes belonging to the infeasible regions into the feasible regions (Sempuga et al., 2011). The use of work was shown to shift the origin of gh-diagram vertically up or down depending on whether work is injected or rejected from the process as shown in Fig. (12).

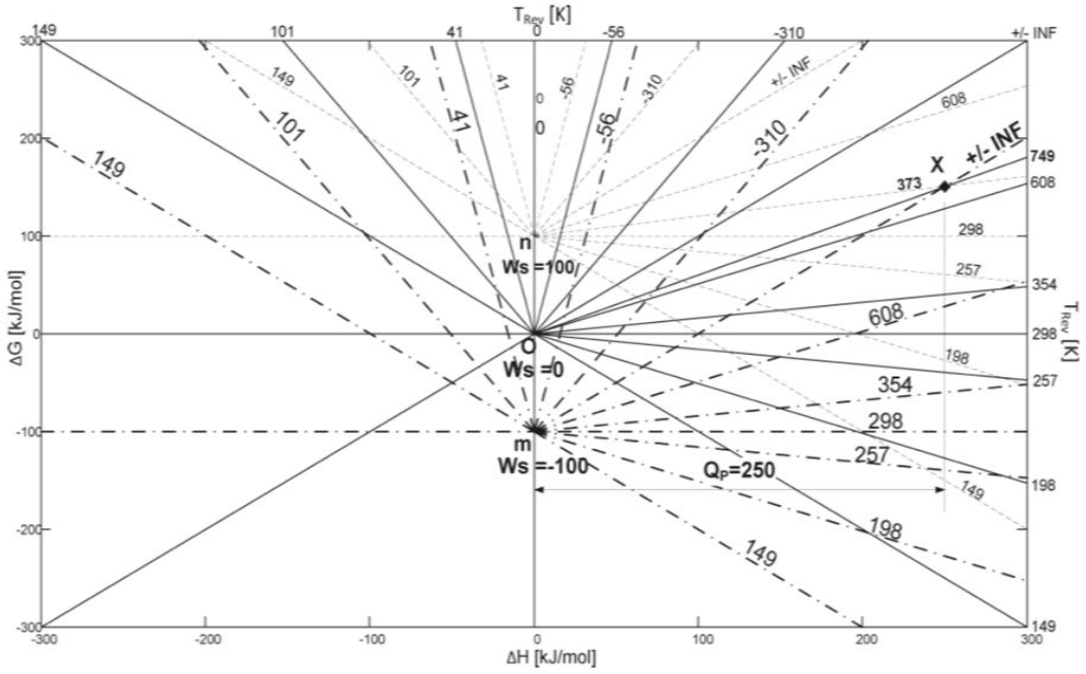

Figure 12: Demonstration of how the addition of work moves the origin of the gh-diagram vertically (Sempuga et al., 2011)

The addition of work to chemical processes can also move the origin of the gh-diagram along the 45° line as shown in Fig. (13). The movement of the origin on the gh-diagram changes the temperature scale and hence the feasibility and efficiency of a process. Succinctly put, the addition of work can move a process with the inherently impractical Carnot temperature to a region where the temperatures are practical.

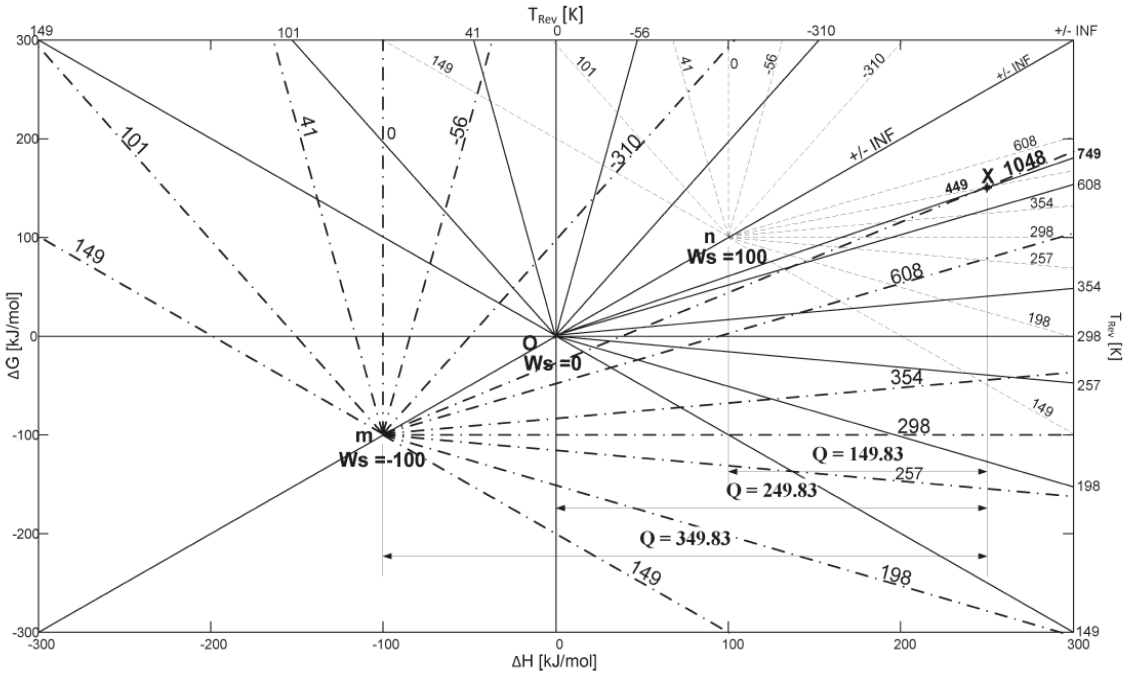

Figure 13: Demonstration of how the addition of work to a process moves the gh-diagram origin along the 45° line (Sempuga et al., 2011)

The temperature at which work is added to supplement heat such that the process is thermodynamically feasible and reversible is called the reversible temperature. The gh-diagrams in Fig. (12) and Fig. (13) has a reversible temperature scale unlike the gh-diagram in Fig. (11) which has the Carnot temperature scale.

The Gibbs free energy, enthalpy, and reversible temperature for the case where shaft work supplements heat to supply the process energy requirements are related by Eq. (32)

$$\Delta G_P(T_O, P_O) = \Delta H_P(T_O, P_O)\left(1 - \frac{T_O}{T_R}\right) + \left(\frac{T_O}{T_R}\right) W_s \tag{32}$$

where T_R is the reversible temperature (K) and W_s is the shaft work (kJ/mol), (eq.32) specifically applies to Fig. (13).

Work can be supplied to the process in the form of shaft work by using a combination of turbines and compressors. In the case of compressors and turbines system, pressure is used to provide work to the processes. However, this requires a change in the number of moles of gas between the feed and the product streams. Sempuga et. al., (2011) have elaborated more on this topic.

This section has provided a brief introduction of what the ΔG-ΔH diagram is and highlighted how this process synthesis tool can be used to give insights on how to provide process energy requirements efficient, comprehensive explanations and examples can be found in the work of Sempuga et., (2010) and Sempuga et., (2011). The section has further illustrated how shaft work can be used to supplement heat such that the processes that would otherwise be infeasible are made to be feasible. Further explanations on how a gh-diagram is constructed, useful information provided by the diagram and how it is used to improve energy efficiency are provided in the proceeding section.

This analysis will be applied to the power-to-chemicals processes where heat and work to the processes are supplied through solar thermal and solar photovoltaics, respectively. The analysis will specifically be used to give insights on the following.

- Whether power-to-chemicals process schemes that use solar-thermal alone or solar-photovoltaic alone are thermodynamically feasible and efficient.
- How the solar-thermal can be used with solar-photovoltaic to efficiently supply the energy requirements of power-to-chemicals process schemes.

2.2 Thermodynamic analysis of the solar PT-chemicals

2.2.1 Solar-thermal heat as the source of energy

Let us consider a power-to-chemical (PT-C) process that converts feed F to product P, both the feed and product are at ambient conditions.

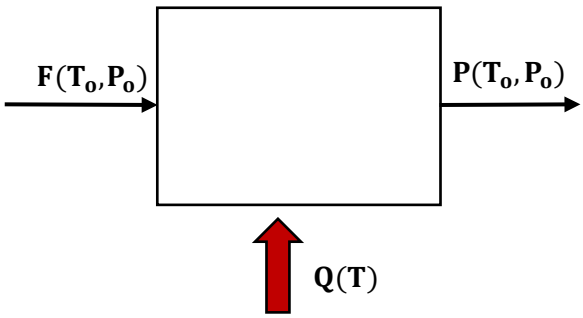

Figure 14: A schematic diagram of the PT-C overall process where heat is provided by the solar-thermal at temperature T.

The energy balance across the process indicates that to supply the minimum amount of energy, the sum of all the energies to the process must be equal to the difference in enthalpy (ΔH) between the feed and the product streams at their respective conditions of temperature and pressure. Thus:

$$Q(T) = \Delta H_P(T_O, P_O) \tag{33}$$

Where $Q(T)$ represents the heat transferred to the process at the temperature T. The temperature at which heat is supplied to the process determines the amount of work potential carried into the process. This work will be referred to as W_Q and is given by:

$$W_{Q(T)} = Q(T)\left(1 - \frac{T_0}{T}\right) \tag{34}$$

The entropy balance around the process is given by Eq. (35)

$$\Delta S_P(T_O, P_O) = \frac{Q(T)}{T} + S_{gen} \tag{35}$$

The entropy is related to the enthalpy and Gibbs free energy according to the relation.

$$\Delta G_P(T_O, P_O) = \Delta H_P(T_O, P_O) - T_O \Delta S_P(T_O, P_O) \tag{36}$$

Eq. (33 – 36) can be solved simultaneously to obtain eq. (37),

$$Q(T)\left(1 - \frac{T_O}{T}\right) = \Delta G_P(T_O, P_O) + T_O S_{gen} \tag{37}$$

The left side of Eq. (37) indicates the amount of energy equivalent to work transferred to the process at temperature T. The right side of the equation represents the total work required by the process. In other words, the right side of the equation indicates the quality of energy needed

to effect the changes in the process. The first term on the right (ΔG) is the minimum work needed, above which the changes in the process will start occurring. $T_O S_{gen}$ is the work above the minimum required to drive finite changes in the process. $T_O S_{gen}$ also includes the work required to overcome internal resistances in the process as well as work losses due to heat losses. The following points can be made regarding the temperature at which heat is provided (T) and the $T_O S_{gen}$ term.

- The term $T_O S_{gen}$=0 when T is equal to the process Carnot temperature, at this point the work carried by the heat provides the minimum energy required by the process.
- At $T < T_{Carnot}$, the term $T_O S_{gen} < 0$, the process does not occur at this point as the minimum energy requirements of the process are not met.
- $T_O S_{gen} \rightarrow \left(W_Q - \Delta G_p(T_o, P_o)\right)$ as $T \rightarrow \infty$, $\left(W_Q - \Delta G_p(T_o, P_o)\right)$ represents the maximum value of $T_O \Delta S_{gen}$

The PT-C process and heat supplied to the process at temperature T can be represented on the gh-diagram as vectors as depicted in Fig. (15). The amount of heat and the minimum work requirements of the process are represented by the ΔH axis and ΔG axis components of vector Op in Fig 15(a).

Fig15(b) shows heat vectors that all start at zero, when the process is not occurring, to a certain point on the gh-diagram. The length of heat vectors indicates the amount of heat provided or removed from the process. When the heat vector has the same direction as the process vector, then heat is supplied to the process, the opposite holds. Vectors Or (OQ(T_1)) and Op (OQ(T_2)) and Oq (OQ(T_3)) represent the same amount of heat supplied to the process at three different temperatures of T_1, T_2 and T_3, respectively. Vector OQ(T_2) is co-linear and has the same magnitude and direction as the process vector Op.

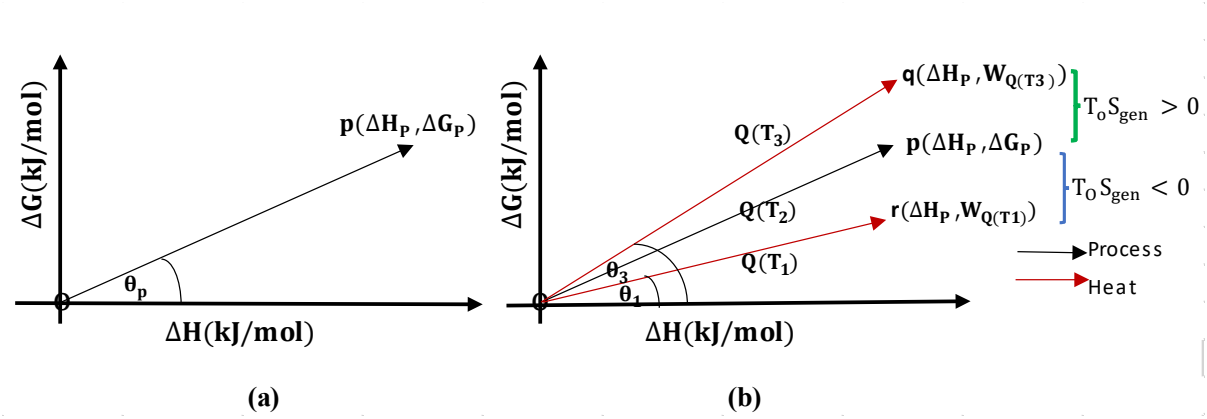

Figure 15: (a) Representation of the PT-C process on a gh-diagram (b) The gh-diagram representation of the PT-C process and heat supplied to the process at different temperatures.

The term $T_O S_{gen}$ can be made a subject of the formular such that it is given by,

$$T_O \Delta S_{gen} = W_Q - \Delta G_P(T_O, P_O)$$

We see that when the process is supplied with heat at T_1 that the $W_{Q(T1)} < \Delta G_P(T_O, P_O)$, which makes $T_O \Delta S_{gen} < 0$, $T_1 < T_{Carnot}$ and the process will not proceed under these conditions. When the heat is supplied at the temperature $T_2 = T_{Carnot}$, we see that $W_{Q(T2)} = \Delta G_P(T_O, P_O)$. The heat carries with it just enough work by its temperature to meet the required work to start the process. When the process is supplied with heat at the temperature T_3, corresponding to the angle θ_3, the heat work potential is greater than the process minimum work requirement [$W_{Q(T3)} > \Delta G_P(T_O, P_O)$] and thus making the term $T_O \Delta S_{gen} > 0$. The temperature at which heat is supplied is greater than the process Carnot temperature under these conditions ($T_3 > T_{Carnot}$). We can infer from the analysis that heat can only meet the process energy needs if supplied to the process at the temperature greater or equal to the process Carnot temperature i.e., $T \geq T_{Carnot}$.

2.2.2. Work (electricity) as the source of energy

Let us now consider a second case where the minimum energy demand is supplied by work only, which could be in the form of shaft work (W_S) or electrical energy (W_e). In this example, we consider electrical work as we intend to analyse the conversion of solar PV to chemicals. We consider the process depicted in Fig (16). where the feed and products are at ambient conditions.

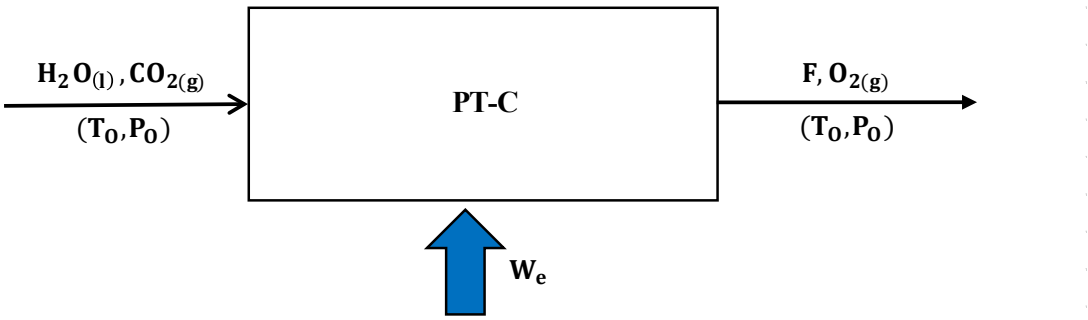

Figure 16: The schematic diagram of a PT-C process where the electrical work is used to supply the process energy needs.

The energy balance for the process is represented by Eq. (38).

$$W_e = \Delta H_p(T_O, P_O) \tag{38}$$

Where W_e represents the electrical work, the entropy balance across this process is given by Eq. (39)

$$\Delta S_P(T_O, P_O) = S_{gen} \tag{39}$$

The eq. (38) and (39) can be used together with the definition of Gibbs free energy in Eq. (36) to relate the $T_O S_{gen}$ term to process energy and work requirements as shown on Eq. (40).

$$T_O S_{gen} = \Delta H_P(T_O, P_O) - \Delta G_P(T_O, P_O) \tag{40}$$

We can see from Eq. (40) that the term $T_O S_{gen}$ can never be equal to zero unless the process minimum energy requirement is the same as the process minimum work requirement i.e., when $\Delta H_P(T_O, P_O) = \Delta G_P(T_O, P_O)$. The negative $T_O S_{gen}$ is only obtainable for the process for which $\Delta H_P(T_O, P_O) < \Delta G_P(T_O, P_O)$, such processes are rare but they do exist. Processes such as the production of formic acid from hydrogen and carbon dioxide and the charging of lead-acid batteries are examples of such processes.

Electrical energy, like mechanical energy, represents a high-quality form of energy. It is equivalent to heat at an infinite temperature. It is, therefore, represented as a 45° vector on the gh-diagram. This is also supported by (Allen, Hammond, and McKenna, 2017) who showed that ΔH=ΔG for electricity. Fig. (17a) shows a PT-C process and work (electricity) on the gh-diagram, electricity is represented by the 45℃ vector OWe. The process minimum energy needs are lower than the minimum work requirements, it, therefore, follows that the $T_O S_{gen} >$

0 and at maximum for this process. The $T_O S_{gen}$ will be zero for the process for which $\Delta H_P(T_O, P_O) = \Delta G_P(T_O, P_O)$ as was mentioned. In this instance, the electricity vector will be the same as the process vector Op.

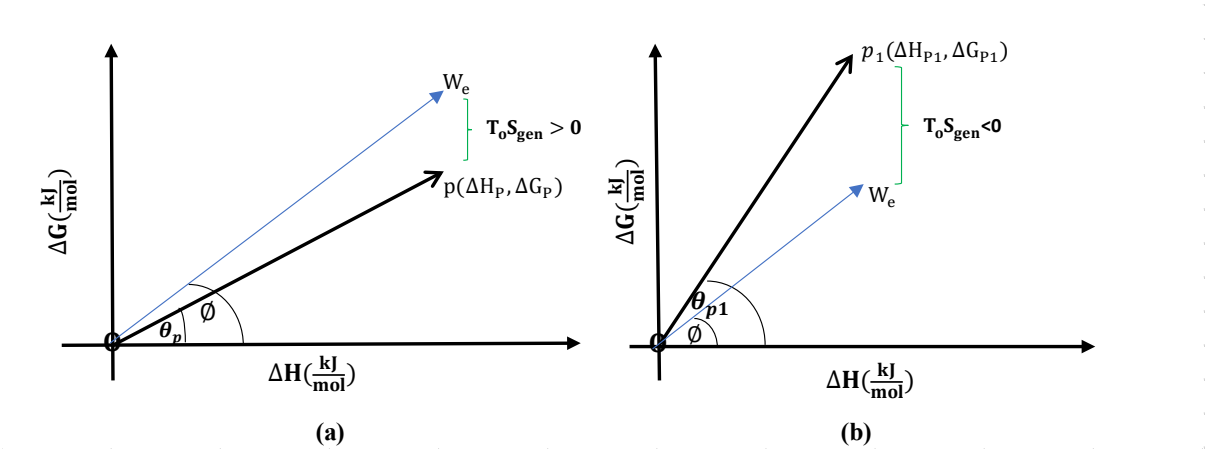

Figure 17: (a) Representation of electricity (work) and a process for which $\Delta H_P > \Delta G_P$ on the gh-diagram (b) The gh-diagram representation of the electricity (work) and the process for which $\Delta H_P < \Delta G_P$.

We can see from Fig 17(b) that when the process minimum energy requirements are lower than the process minimum work requirements ($\Delta H_P < \Delta G_P$) that the term $T_O S_{gen}$ becomes negative, this process will not proceed under the given conditions. The following observations can be made for processes supplied with work (electricity) alone.

- The $T_O S_{gen} > 0$ and at maximum for all the processes for which the process $\Delta H_P > \Delta G_P$.
- The $T_O S_{gen} = 0$ and minimum for the processes for which $\Delta H_P = \Delta G_P$, the work (electricity) provides the minimum work requirements of the processes.
- $T_O S_{gen} < 0$ for all the processes with $\Delta H_P < \Delta G_P$, these processes are thermodynamically infeasible and cannot proceed.

2.2.3 Combination of heat and work(electricity) as the source of energy

Let us consider a case where the minimum energy needs of the process are supplied through the combination of work (electricity) and heat as depicted in Fig. (18).

The sum of heat and work (electricity) supplied to the process must be equal to the change in enthalpy between the product and feed stream as shown on Eq. (41)

$$Q(T) + W_e = \Delta H_P(T_O, P_O) \tag{41}$$

The entropy balance across the process can be described by eq. (35), solving for eq. (35,36 and 41) simultaneously yield Eq. (42) which relates the entropy generation to the process work requirements and the total work supplied to the process.

$$Q(T)\left(1-\frac{T_O}{T}\right)+W_e=\Delta G_P(T_O,P_O)+T_OS_{gen} \quad (42)$$

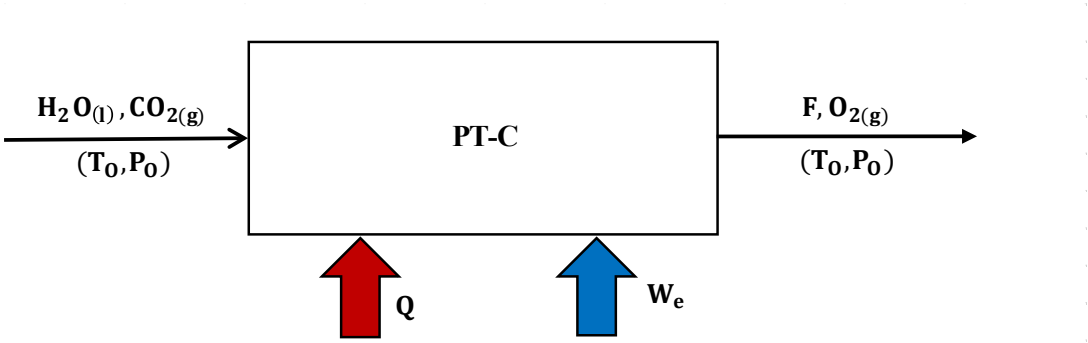

Figure 18: Schematic diagram of PT-C process where the combination of heat and work (electricity) is used to supply the process energy requirements.

The following can be deduced about the entropy generation term on the eq. (42)

- The $T_OS_{gen} < 0$ under the following conditions
  - $W_{Q(T)} + W_e < \Delta G_P(T_O, P_O)$
  - $Q(T) + W_e < \Delta G_P(T_O, P_O)$, for $T \to \infty$ such that $Q \to W_Q$
- The $T_OS_{gen} = 0$ if the following conditions prevail.
  - $W_{Q(T)} + W_e = \Delta G_P(T_O, P_O)$
  - $Q(T) + W_e = \Delta G_P(T_O, P_O)$, for $T \to \infty$ such that $Q \to W_{Q(T)}$
- The $T_OS_{gen} > 0$ under the following conditions
  - $W_{Q(T)} + W_e > \Delta G_P(T_O, P_O)$
  - $Q(T) + W_e > \Delta G_P(T_O, P_O)$, for $T \to \infty$ such that $Q \to W_{Q(T)}$

If we ignore the internal resistance and heat losses to the surroundings, T_OS_{gen} represents the work needed to drive the change at a certain rate. In processes involving chemical reactions, T_OS_{gen} is related to the rate of reaction and thus can be related to the size of a reactor. The larger the value of T_OS_{gen} the faster the reaction and the smaller the volume of the reactor. On

the other hand, the larger the $T_O S_{gen}$ the larger the amount of work above ΔG that must be supplied from external sources such as fossil fuel, solar-PV, or solar-thermal heat. Thus, there is an optimum $T_O S_{gen}$ that minimizes the total cost of the process.

The graphical representation of the process that is supplied by a combination of heat and work on a gh-diagram is represented in Fig. (19). The process represented in Fig.(19a) has the process enthalpy greater than the process Gibbs free energy ($\Delta H_P > \Delta G_P$), which means it belongs to region 1A in Fig. (11). Most of the power-to-chemicals process pathway candidates belong to this region as will be seen later. The process represented in Fig.(19b) has the process enthalpy smaller than the process Gibbs free energy ($\Delta H_P < \Delta G_P$), implying that the process belongs to region 1B on a gh-diagram in Fig. (11).

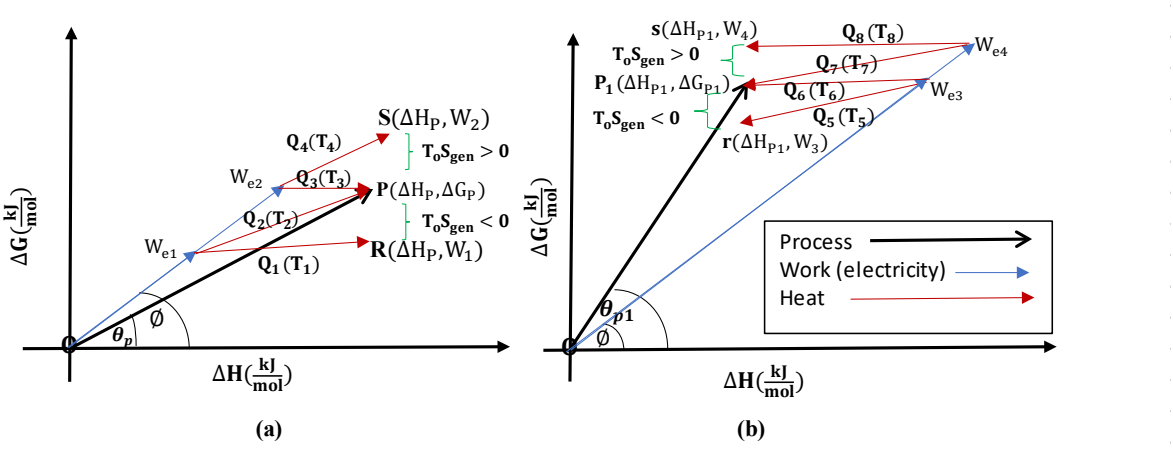

Figure 19: a) The gh-diagram representation of the PT-C process for which $\Delta H_P > \Delta G_P$ together with the different combinations of work (electricity) and heat at different temperatures. b) The gh-diagram representation of the PT-C process for which $\Delta H_P < \Delta G_P$ together with the different combinations of work (electricity) and heat at different temperatures

We can see from Fig.(19a) that there are four different combinations of work (electricity) and heat supplied to the process represented by vector Op. The work and heat combinations considered here are (W_{e1}, $Q(T_1)$), (W_{e1}, $Q(T_2)$), (W_{e2}, $Q(T_3)$) and (W_{e2}, $Q(T_4)$). The amounts of heat $Q(T_1)$, $Q(T_2)$, $Q(T_3)$ and $Q(T_4)$ are supplied to the process at the respective temperatures of T_1, T_2, T_3 and T_4. The following can be deduced from Fig.(19a) about the $T_O S_{gen}$.

- The $T_O S_{gen} < 0$ for the work and heat combination (W_{e1}, $Q(T_1)$), we can see that while the total enthalpy provided by this combination is equal to the process enthalpy, the total work (W_1) is lesser than the minimum energy requirements of the process i.e., $W1 < \Delta G_P$. The process will not proceed under this condition.

- The $T_O S_{gen} = 0$ for the work and heat combination (W_{e1}, $Q(T_2)$), both the process enthalpy (minimum energy required) and the Gibbs free energy (the minimum work required) are met under this condition. The total work input to the process is just enough to get the process going.

- The $T_O S_{gen} = 0$ for the work and heat combination (W_{e2}, $Q(T_3)$), this case is similar to the case of (W_{e1}, $Q(T_1)$) with the only difference in that the electrical energy supplied meets the minimum work requirements but runs short to meet the minimum energy requirements, this is circumvented by adding heat at the ambient temperature ($T_3=T_o$) such that $W_{Q(T3)}=0$, and $Q(T_3)+W_{e2}=\Delta H_P$

- $T_O S_{gen} > 0$ for the work and heat combination (W_{e2}, $Q(T_4)$), the total work supplied to the process is greater than the process minimum work requirements $W_{Q(T4)} + W_{e2} > \Delta H_P$.

The following observations can be made with the processes for which $\Delta H_P < \Delta G_P$ from Fig (19b)

- The amounts of electricity supplied to the process (We_3 and W_{e4}) are both greater than the process minimum energy i.e.., $We_3 > \Delta H_P$ and $We_4 > \Delta H_P$. Heat must be removed from the processes so that the energy balance can be valid. The energy balance for this case is thus given by, $\mathbf{W_e - Q(T) = \Delta H_P(T_O, P_O)}$. The direction of the heat vector for a process that rejects is opposite to the direction of the heat vector when the process is supplied with heat. We have so far been dealing with cases where heat vectors are positive (same direction as process vectors), heat vectors are therefore negative to the processes that reject heat (opposite in direction to the process vector).

- Four combinations of work addition (electricity) and heat removal are seen in the figure.

- Combination (We_3, $Q(T_5)$) has the $T_O S_{gen} < 0$, this process is not thermodynamically feasible and will not process because the total work supplied to the process is lower than the process minimum work requirements.

- The combination (We_3, $Q(T_6)$) has the $T_O S_{gen} = 0$, the nett work supplied to the process is exactly equal to the process minimum work requirements such that, $-W_{Q(T6)} + W_{e1} = \Delta G_P$

- The combination (We_4, $Q(T_7)$) has the $T_O S_{gen} = 0$, the nett work supplied to the process meets the minimum work requirements of the process. The difference between

this case and the previous is that We_4 provides work that is greater than the minimum required by the process, so the heat removed takes with some work such that the nett from exactly matches the process work requirement.

- The combination (W_{e4}, $Q(T_8)$) has the term $T_O S_{gen} > 0$, the temperature at which heat $Q(T_8)$ is removed from the process is such that the nett work ($W_{Q(T8)} + W_{e2} > \Delta H_P$)

We can see from the analysis made that there are two critical parameters that determine if the process is thermodynamically infeasible ($T_O S_{gen} < 0$), if the energy supplied meets the minimum work requirements ($T_O S_{gen} = 0$) or if the process involving reactions proceed at the faster rate ($T_O S_{gen} > 0$). These two critical parameters are the temperature at which heat is added or removed from the process and the ratio of work (electricity) to heat. The work to heat ratio becomes a key variable for processes for which heat is supplied or removed at a constant temperature. The ratio or the proportion of work and heat for the cases where work (electricity) and heat are supplied by solar-PV and solar-T respectively can be represented by the surface area fraction of the solar-PV from the total solar area. In this case, the $T_O S_{gen}$ the term can also be related to the surface area fraction of the solar-PV as will be shown in the next section.

2.3. The solar-PV and solar-T area fractions relations to work (electricity) and solar-T heat.

The surface area required for the installation of solar-PV to supply an amount of electric power W_e can be estimated using (Eq. 24) as follows:

$$A_{PV} = \frac{W_e}{\eta_{PV} G}$$

Where η_{PV} and G are the solar-PV collection efficiency and global solar irradiation, respectively. The surface area required for solar-T collectors is determined according to the relation.

$$A_{ST} = \frac{Q_{ST}}{\eta_{ST} G}$$

Where A_{ST} , η_{ST} and Q_{ST} represents the solar-T surface area, collection efficiency and solar-T heat. The total solar surface area can then be calculated as the sum of solar-PV and solar-T surface areas as given by (Eq.43)

$$A_T = \frac{\eta_{PV} Q_{ST} + \eta_{ST} W_e}{\eta_{ST} \eta_{PV} G} \qquad (43)$$

We can then determine the fraction of the total solar surface area that is occupied by solar-PV modules by solving (Eq.24) and (Eq.44) such that.

$$f = \frac{\eta_{ST} W_e}{\eta_{PV} Q_{ST} + \eta_{ST} W_e} \tag{44}$$

Where *f* represents the surface area fraction of solar-PV modules. The solar-PV electricity (W_e) and solar-T heat (Q_{ST}) can be expressed in terms of the solar-PV surface area fraction by manipulating the energy balance ($\mathbf{\Delta H_P = W_e + Q_{ST}}$) and (eq.44). The expressions for solar-PV work and solar-T heat are thus described by (Eq.45) and (Eq.46) respectively.

$$W_e = \frac{\eta_{PV} \Delta H_P f}{\eta_{ST} + (\eta_{PV} - \eta_{ST}) f} \tag{45}$$

$$Q_{ST} = \frac{\eta_{st} \Delta H_P (1-f)}{\eta_{ST} + (\eta_{PV} - \eta_{ST}) f} \tag{46}$$

The total solar surface area can also be expressed in terms of the solar-PV fraction as shown on (Eq.47)

$$A_T = \frac{\Delta H_P}{G\eta_{ST} + G(\eta_{PV} - \eta_{ST}) f} \tag{47}$$

We can also express the $T_o S_{gen}$ term in terms of the solar-PV fraction by using Eqs.42, 45 and 46.

$$T_O S_{gen} = \frac{T\eta_{ST}\Delta H_P - T_o\eta_{ST}\Delta H_P + (T_o\eta_{ST}\Delta H_P - T\eta_{ST}\Delta H_P + \eta_{PV}\Delta H_P) f}{T\eta_{ST} + T(\eta_{PV} - \eta_{ST}) f} - \Delta G_P(T_O, P_O) \tag{48}$$

2.3. Thermodynamic performance indicators for PT-chemicals pathways

The performance of PT-chemicals process schemes can be evaluated by using different thermodynamic performance indicators. Most researchers have used the following three performance metrics to assess and compare the performance of different PT-chemicals processes.

- Electricity to fuel.
- First law-based; and
- Exergy-based efficiency

These efficiencies are based on high and low heating values of the produced fuels (Rivera-Tinoco *et al.*, 2016b; Luo *et al.*, 2018b; Ancona *et al.*, 2019). While these performance indicators are good, they are not indicative of how much renewable energy stored in chemicals can be

retrieved when the chemicals are used. We will therefore propose to use two thermodynamic indicators which are the work storage and the overall work efficiency in this study.

The work storage efficiency is hereby defined as the amount of work supplied to the process to the process work potential and is described by Eq. (39)

$$\eta_{WS} = \frac{\Delta G_P}{W_T} \tag{49}$$

Where η_{WS} , ΔG_P and W_T represents the work storage efficiency, process Gibbs free energy change (process work potential) and total work supplied to the process. The work storage efficiency can further be expressed in terms of the solar-PV area fraction.

$$\eta_{WS} = \frac{\Delta G_P \eta_{ST} + \Delta G_P(\eta_{PV} - \eta_{ST})f}{\eta_{ST}\Delta H_P - \left[\left(\frac{T_O}{T}\right)\eta_{ST}\Delta H_P - \eta_{ST}\Delta H_P + \eta_{PV}\Delta H_P\right]f} \tag{50}$$

The overall system work efficiency describes the amount of stored work that is recoverable when the product produced in the PT-C process is utilized. This performance metric considers both the storage of work into chemicals and the utilization of the chemicals to produce energy (work). Consider Fig. (20) showing the overall system for the PT-C process scheme, the overall system is divided into energy storage (PT-C) and utilization (C-TP) subsystems. The C-TP subsystem is assumed to be the combustion process, it is further assumed that the are no material losses of the product C between the two sub-processes. The study looks at the situations where solar-T heat is supplied to the process at the temperature of 200℃ with the combustion of considered chemical fuels occurring at the temperature of 1200℃. The choice of solar-T heat is influenced by the fact that the data is available at this temperature, while the combustion temperature was chosen to be close to a typical gas turbine temperature.

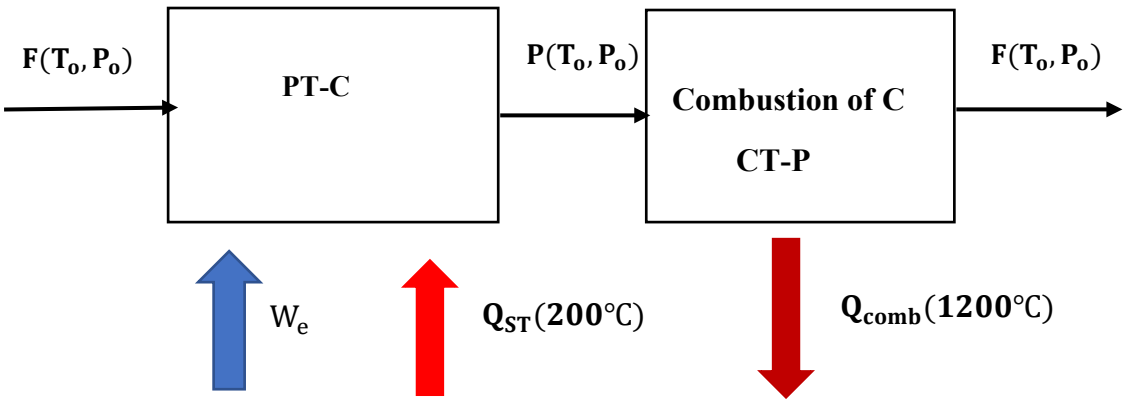

Figure 20: Overall system showing the storage of power into chemical C (PT-C) and the combustion of the product to produce energy (CT-P)

The overall system work efficiency is thus defined as the amount of work obtainable when the fuel is utilized over the total work used to produce the fuel.

$$\eta_w = \frac{W_{comb}}{W_Q + W_e} \tag{51}$$

where η_w and w_c represent the overall system work efficiency and the work of combustion, respectively. The work from combusting the fuels can be expressed in terms of enthalpy and temperature of the combustion reaction, allowing the overall system work efficiency to be expressed in terms of these parameters.

$$\eta_w = \frac{-\Delta H_c\left[1-\frac{T_0}{T_{comb}}\right]}{W_Q + W_e} \tag{52}$$

where T_{comb} and ΔH_c represent the temperature at which the combustion reaction is carried out and the corresponding enthalpy of reaction. The negative sign before the enthalpy of the combustion process is to ensure the positive efficiency since the combustion processes are exothermic ($\Delta H_c < 0$) . The overall system work efficiency can also be expressed in terms of the solar-PV area fraction as shown.

$$\eta_W = \frac{-T\Delta H_C\left(1-\frac{T_0}{T_{comb}}\right)(\eta_{ST}+\eta_{PV}f-\eta_{ST}f)}{T\Delta H_P\eta_{ST}-T_0\Delta H_P\eta_{ST}+(T\eta_{PV}\Delta H_P+T_0\Delta H_P\eta_{ST}-T\Delta H_P\eta_{ST})f} \tag{53}$$

The combustion temperature is important and needs to be known to determine the efficiency of the system.

2.4 Cost analyses of the solar PT-C process schemes.

A comprehensive process cost analysis considers the total capital cost (including equipment purchase costs), the operating costs (inclusive of raw material, production cost, maintenance cost etc) and revenue streams from the sales of the product. The work at hand is to investigate if the use of the combined work (PV electricity) and solar-T heat has any efficiency and most importantly the cost-benefit as compared to the traditional way of supplying pure PV electricity. The process units for processes using only solar-PV or the combined solar-PV and solar-T are the same except for the solar-T field required for the latter case. The differences between these two schemes lie in energy cost and the amounts of electricity used.

We saw from the previous analysis that supplying the process with the combined heat and work generally reduces the amount of work(electricity) consumed by the process. Work (electricity) is generally added to the electrolysis or co-electrolysis sub-process where water and the combination of water and carbon dioxide are electrochemically converted to hydrogen and oxygen or hydrogen, oxygen, and carbon monoxide. The differences in electricity consumption by the electrolyser affect the total electrolyser active area as will be seen later. The total electrolyser active area on the other hand affects the purchased equipment cost of the electrolyser stacks.

The cost analysis considered in this study will therefore account for the total energy costs as the associated capital, running and maintenance costs of the units providing the energy (solar PV and T fields) and the purchased cost of the electrolyser for each process scheme. It is worth mentioning that different process schemes cannot be compared since the process units differ from one process scheme to the other. Only the costs of one process pathway with different arrangements of work (electricity) and heat can be compared.

2.4.1 Process energy cost

The PT-C processes can use the energy in the form of work (electricity) alone or the combination of heat and work. The Levelized cost of electricity (LCOE) and the Levelized cost of heat (LCOH) can be used to determine the energy cost associated with electricity and heat, especially in the case where the electricity and heat are provided by a renewable source such as solar energy. The total energy cost associated with the PT-C process can be described by Eq. (54)

$$EC_T = [(LCOE)(W_e) + (LCOH)(Q)]t \tag{54}$$

Where EC_T, W_e, Q and t represent the total energy cost (USD), amount of electricity (kW) and the operating time (h) respectively, the LCOE and LCOH are reported in USD/kWh. This relation can further be expressed in terms of the solar-PV area fraction.

$$EC_T = \left[\frac{(LCOH)\eta_{ST}\Delta H_P(1-f)+(LCOE)\eta_{PV}\Delta H_P f}{\eta_{ST}+(\eta_{PV}-\eta_{ST})f}\right]t \tag{55}$$

The LCOE from the solar PV and the LCOH from the parabolic trough collector at 200 ℃ were reported to be USD 0.050/kWh and USD 0.034/kWh, respectively.

2.4.2 Electrolyser purchased equipment cost.

The electrolyser capital cost is reported in the literature in terms of the power consumption (cost/kW) and per total electrolysis active area (cost/m^2). We will use the latter convention

where the electrolyser purchase cost is reported per total active area. The total electrolysis active area is calculated according to Eq. (56).

$$A_E = \frac{I_F}{i} \tag{56}$$

Where A_E, I_F and j represent the total electrolysis active area (cm^2), Faraday's current (A) and the current density (A/cm^2) respectively. The total plant Faraday's current is calculated from Faraday's law of electrolysis according to.

$$\bar{n}_r = \frac{I_F}{nF} \tag{57}$$

Where $\bar{n}_r$, n and F represent the number of moles of a feed material that reacts in the electrochemical reaction (kmol/s), the number of electrons being exchanged during the reaction, and the Faraday's constant (96,500/mol), respectively. The current density is on the other hand calculated as follows.

$$i = \frac{V_{op} - V_{rev}}{ASR} \tag{58}$$

Where V_{op}, V_{rev} and ASR represent the operating voltage (V), reversible voltage (V) and the area-specific resistance (Ωcm^2). The operating and reversible voltages are calculated according to Eq. (59) and (60) respectively.

$$V_{op} = I_F W_e \tag{59}$$

$$V_{rev} = \frac{\Delta G_{rxn}}{nF} \tag{60}$$

Where W_e and ΔG_{rxn} represent the electricity(work) supplied to the electrolyser (kW) and the Gibbs free energy of the electrochemical reaction (kJ/mol), respectively. The area-specific resistance (ASR) accounts for all the losses incurred during the electrolysis reaction and it is a function of the geometry of the electrolysis stack, materials used to construct electrodes, electrolyte, and operating conditions of the electrolysis stack (Giglio *et al.*, 2015a). The ASR for the planar geometry high-temperature electrolysis stack operating at the temperature range of 750-850℃ and the pressure of up to 10bar is given by Eq. (61).

$$ASR = De^{(-BT_E)}e^{(-Cp)} \tag{61}$$

Where T_E and p are the electrolyser operating temperature (K) and pressure (bar), the constants B, C and D for the temperature and pressure range of 750-850℃ and 1-10bar are reported in Table 2.

Table 2: Constant values used for the estimation of ASR as a function of pressure and temperature. These values were derived from the interpolation of experimental data available in a temperature range of 750–850°C and for pressure up to 10bar (Giglio *et al.*, 2015a)

	Steam electrolysis	Co-electrolysis
$D[\Omega cm^2]$	35.71	34.22
$B[K^{-1}]$	0.0057	0.0054
$C[bar^{-1}]$	0.0217	0.0217

The value of current density (i) can now be computed for a given work consumption (W_e) in the electrolysis stack operating in the respective temperature and pressure ranges of 750-850°C and 1-10bars. The total electrolysis active area can then be calculated using eq. (56) for a given amount of feed material converted during the electrolysis or the co-electrolysis reaction.

The cost of the electrolyser stack can be computed by multiplying the electrolysis active area by the electrolyser specific cost (SC) given as follows.

$$PEC_{elec} = SC_{elec} \times A_E$$

(Giglio et al., 2015) calculated the specific cost of the planar geometry high-temperature solid oxide electrolysis stack to be USD 3200/m^2. This value considers the factory assembled electrolyser cells cost, the physical enclosure (metallic vessel and ceramic insulation), power conditioning rectifier to convert AC from the solar-PV to the DC, transportation, placement, and foundation costs. The electrolyser specific cost of USD 3200/m^2 was reported in the year 2015, this value can be escalated to the current year by using Eq. (62).

$$\frac{PEC_1}{PEC_2} = \frac{CI_1}{CI_2} \tag{62}$$

Where PEC and CI represent the purchased equipment cost and the cost index respectively, subscripts 1 and 2 represent the current and base years, respectively. The cost index (CI) for each year can be obtained from the chemical engineering plant cost indexes (CEPCI).

Chapter 3

Case studies on PT-H_2 and PT-CH_4, and results of other PT-C process pathways.

Chapter 3 uses the thermodynamic analysis and the gh-diagrams to set the theoretical performance targets in terms of optimal solar-PV area fraction, work storage and overall system efficiencies, total solar area requirements and the major equipment costs. The major equipment cost analysis considers the costliest cost components which are the electrolyzer and energy costs of the PT-C processes. Two case studies investigating PT-H_2 and PT-CH_4 will be studied to illustrate how to use the thermodynamic and gh-diagrams analysis to set theoretical performance targets. The analysis used for these two cases will then be extended to other PT-C processes. Comparisons amongst the considered processes will be made in terms of the thermodynamic performance, solar surface area requirements and the Levelized cost of production. The Levelized cost is calculated based on the total mass in tonnes of the produced chemicals.

The comparisons are based on the output power of 640kW as the basis, this value is the power obtainable when 1 mole/s of methane gas is combusted at 1200℃. Any value can be used as the basis of calculations without altering the results since the cost is reported per mass of the produced chemicals. The following assumptions and process constraints apply for all the PT-C process schemes under consideration.

- Feed and products material from the process are at the ambient conditions.
- The solar-T heat is supplied to the process at 200℃ by parabolic trough collectors at the collection efficiency of 63%
- The efficiency of the solar-PV modules used is 20.4%, the highest reported commercial solar-PV efficiency.
- The solar global irradiation of 1000 W/m^2 is used and assumed to be available for 8 hours per day.
- The plant operates for 300 days per year with the project lasting for 15 years (36,000 h), the latter is a reasonable period for the operational life of the electrolyser.
- The high-temperature planar solid oxide electrolyser is used.

Case studies

3.1 Power-to-H_2 process pathway

The PT-H_2 process forms the heart of the PT-C processes because every PT-C process includes the electrolysis step where renewable electricity is used to produce hydrogen.

The PT-H_2 overall process material balance is described by Eq. (63)

$$H_2O_{(l)} = 1/2\, O_{2(g)} + H_{2(g)} \tag{63}$$

The process minimum energy and minimum work requirements are 286 and 237 kJ per mole of hydrogen gas produced. Fig. (21) depicts a simple process flow diagram of the process where 1 mole/s of liquid water is fed to the process that produces 1mole/s of hydrogen and ½ mole/s of oxygen gas. The process is supplied with solar-T heat and solar-PV electricity (work) to meet the process energy needs. The solar-T heat can be used anywhere within the process while the solar-PV electricity(work) is assumed to be used in the electrolysis stack.

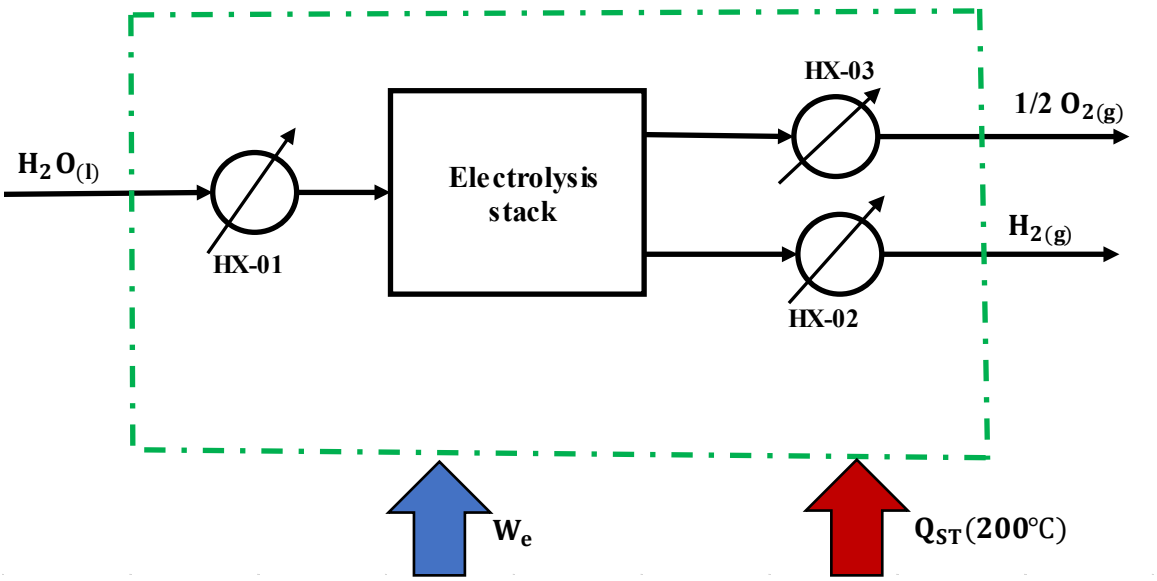

Figure 21: The schematic diagram of the PT-H_2 process powered by the combined solar-PV and solar-T heat to produce Hydrogen.

Water is fed to the process at ambient conditions and pumped to 10atm and fed to a series of heat exchangers (HX-01) where the pressurised steam is produced. The produced steam is then fed into the electrolysis stack where the electrolysis reaction occurs at the temperature of 750°C and 10atm. The produced hydrogen and oxygen gases are passed through a series of heat exchangers (HX-02) and (HX-03), respectively to recover heat. The heat recovered from hydrogen and oxygen streams is used in a series of heat exchangers (HX-01).

The amount of hydrogen gas required to produce 640kW of work when combusted at 1200°C is calculated as follows.

$$W_C = -\dot{n}_{H_{2(g)}} \Delta\hat{H}_C \left[1 - \frac{T_O}{T_C}\right]$$

$$640\ \text{kW} = -\dot{n}_{H_{2(g)}} \left(-241.8 \frac{\text{kJ}}{\text{mol}}\right) \left[1 - \frac{298.15\ \text{K}}{1473.15\ \text{K}}\right]$$

$$\therefore \dot{n}_{H_{2(g)}} = 3.32 \frac{\text{mole}}{\text{s}}$$

The production for the whole project lifetime, after a period of 36,000 h, is thus equal to 433.5 tonnes of hydrogen gas.

3.1.1. Thermodynamic performance of the solar PT-H_2 process

Eq. (48) was used to determine the changes in T_oS_{gen} with variation in the solar-PV area fraction (*f*) which was varied from 0 to 100%. 0% and 100% represent the points where the process is supplied with solar-T heat only and solar-PV only respectively, these points are represented by X and Z respectively in Fig. (22).

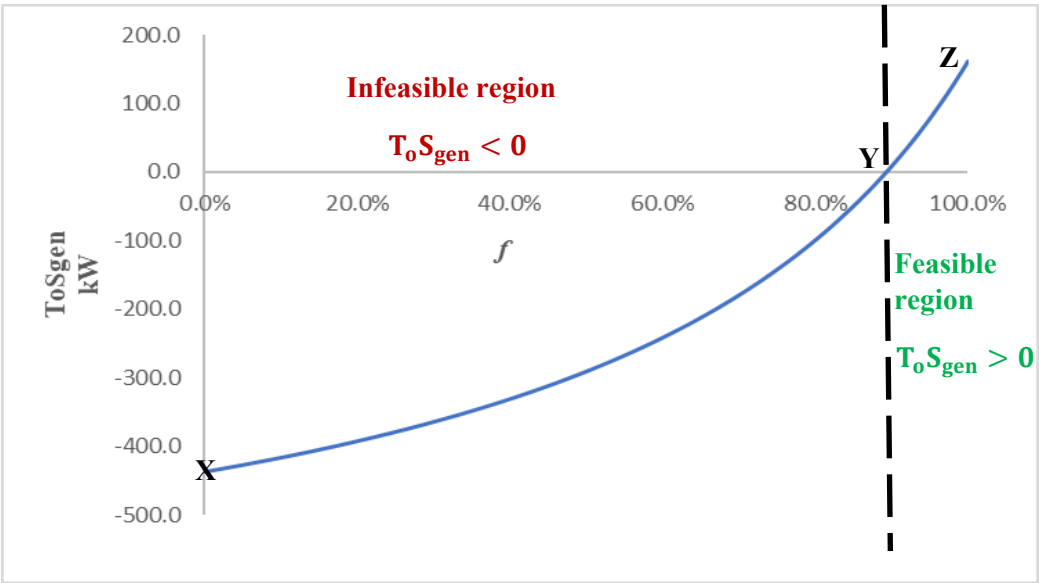

Figure 22: The variation of T_oS_{gen} with the changes in solar-PV area fraction for PT-H_2 process supplied with solar-PV and Solar-T at 200°C

We can see that the value of T_oS_{gen} starts at -436.3 kW at point **X** (*f*=0%), the work supplied by solar-T heat at 200°C is less than the process minimum work requirements ie., $W_{Q(T)} < \Delta G_P$. The process does not occur at this point and the only way heat alone can supply the

process with minimum work requirements is if it is supplied at the process Carnot temperature which is 1480℃. This temperature is out of range of all available solar thermal technologies, which means that the solar-T heat alone cannot be used to supply the PT-H_2 process with the energy. The value of T_oS_{gen} increases as the solar PV area fraction is increased. This implies that the T_oS_{gen} value increases as more electricity (work) is added to the process while the amount of solar-T heat is reduced.

The value of T_oS_{gen} becomes zero at f=89.3% which means that f_{min}=89.3%, the combination of solar-PV and solar-T heat provides the process with the minimum work required $\mathbf{(W_{Q(T)} + W_e = \Delta G_P)}$, the process starts to proceed at this point. T_oS_{gen} continues to increase with the increase in f until it reaches the maximum of 161.3kW at point **Z** when f=100%. It then follows that the value of T_oS_{gen} becomes the highest when solar-PV alone is used as the source of energy to the process. It is worth mentioning that the maximum value of T_oS_{gen} is equal to the difference between the changes in the process enthalpy and Gibbs free energy i.e.., $T_oS_{gen} = \Delta H_P - \Delta G_P = 161.3$ kW. The region to the left of point **Y** represents a thermodynamically infeasible region, and the process does not occur for the solar-PV range of $0\% \leq f < 89.3\%$. Work provided by solar-PV and solar-T heat is less than the work required by the process. The region from point **Y** to the right, $89.29\% \leq f \leq 100\%$, represents the thermodynamically feasible region.

The variation of the overall system work efficiency and work storage efficiency with the changes in solar-PV area fraction are represented in Fig. (23). The efficiencies are plotted for the solar-PV area fraction range of $89.3\% \leq f \leq 100\%$, due to the process being thermodynamically infeasible when the solar-PV are fraction is less than 89.3% as was shown in Fig. (22).

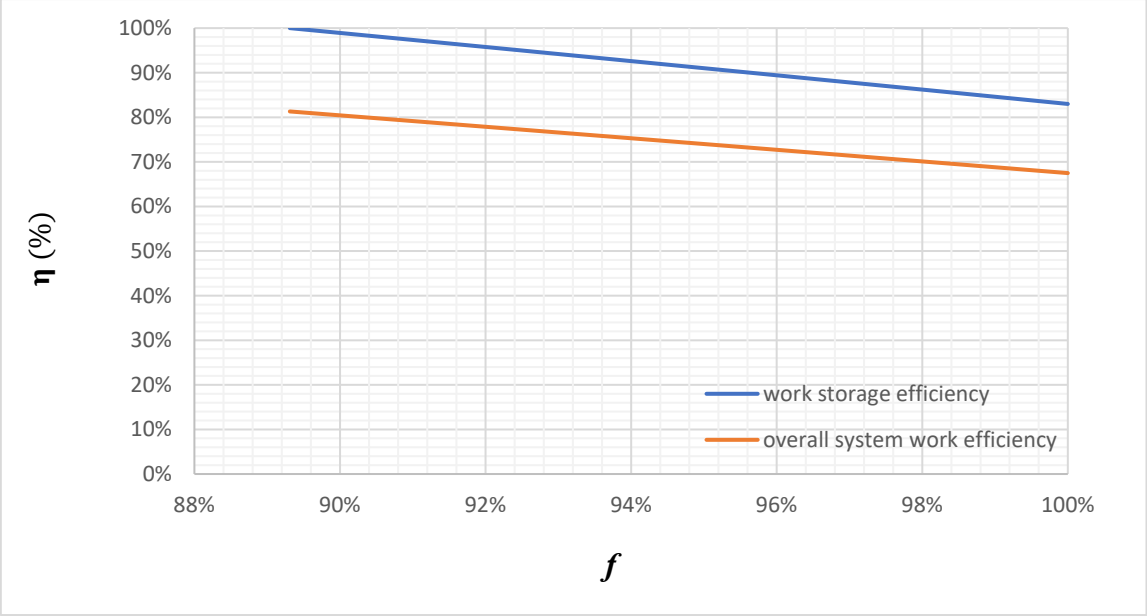

Figure 23: The overall system work and work storage efficiency variations with the solar-PV area fraction

We can see that work efficiencies are maximum at f_{min}=89.3%, the overall system work efficiency and the work storage efficiencies are 81 and 100 % respectively. The work storage efficiency is 100% because the total work supplied by the combination of solar-PV electricity and solar-T heat at the ratio of 89.3% exactly matches both the process minimum energy and work requirements. The overall system work efficiency is not 100% because the combustion of the produced hydrogen gas is not occurring at the Carnot temperature, which represents the temperature at which maximum work can be extracted from the combustion reaction.

The efficiencies are seen to decrease as the solar-PV area fraction is increased from 89.3% to 100%, the values of the overall system work and work storage efficiencies decrease to 67.5 and 83% respectively at f=100%. This behaviour is ascribed to the fact that electricity (work) provides the enthalpy at the same amount as the Gibbs free energy ($\Delta H = \Delta G$). The PT-H_2 minimum energy requirements are higher than the minimum work requirements ($\Delta H > \Delta G$), so for the process to occur electricity must supply the work equivalent to the process minimum energy ($W_e = \Delta H_P$), resulting in the work surplus. The work efficiencies (overall system and storage efficiencies) both decrease as the work surplus increases. It is worth noting that the work surplus is equivalent to the $T_o S_{gen}$ term.

The relationship between an electrolysis stack active area per kW of the work of produced hydrogen combustion at 1200℃ solar-PV collection area fraction was determined and plotted in Fig. (24). The variation in ToSgen with solar-PV surface area fraction was also plotted in the figure.

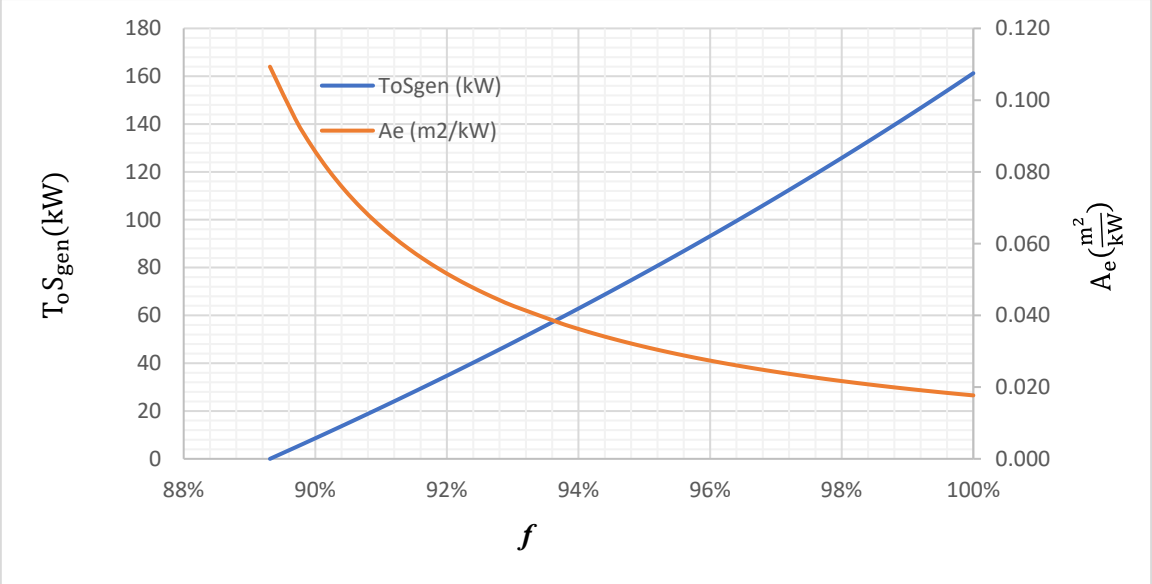

Figure 24:The relationship between the electrolysis active area, ToSgen and solar-PV area fraction

We can see that the electrolysis active area decreases as the solar-PV area is increased from 89.3 to 100%. The electrolysis active area decreases from 0.109 m^2/kW at the solar-PV area fraction and ToSgen values of 89.3% and 0 kW to 0.018 m^2/kW at the solar-PV area fraction and ToSgen value of 100 % and 161.3kW. This constitutes a decrease of 83.8% in the active electrolysis stack area, the results imply that the active area decreases exponentially as the value of T_oSgen increases.

3.1.2 Solar area requirements and the cost implications on PT-H_2 process scheme

The Levelized total solar surface area, the sum of the solar-PV and solar-T surface areas, was determined and plotted against the solar-PV surface area for the feasible region as shown in Fig. (24). We see that the Levelized solar surface area increases when the solar-PV surface area is increased, the minimum value of the solar area fraction of 5.94 m^2/kW is obtained at f_{min}. The highest value of the solar area of 7.26 m^2/kW is found at f=100%, this translates to the area savings of 18.1% if the process is operated at f_{min} instead of f=100%.

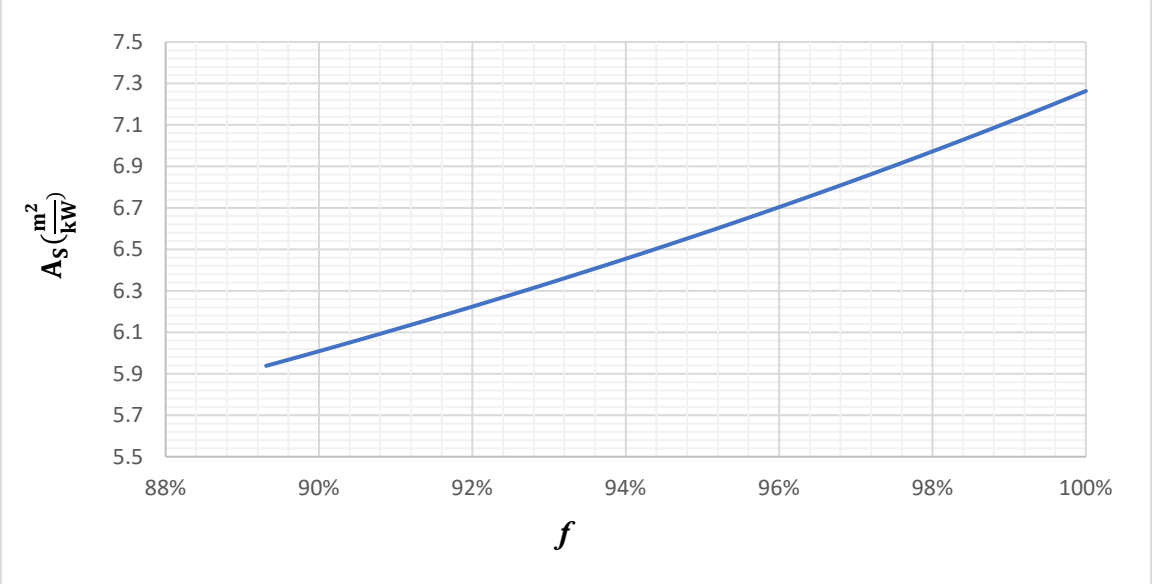

Figure 25: The total solar area per kW of work of combustion as a function of the solar-PV surface area

The Levelized Cost of energy based on work of the combustion reaction (the sum of the Levelized cost of solar-T heat and solar-PV electricity) and the purchased electrolyser cost as functions of the solar-PV area fraction are reported in Fig. (26).

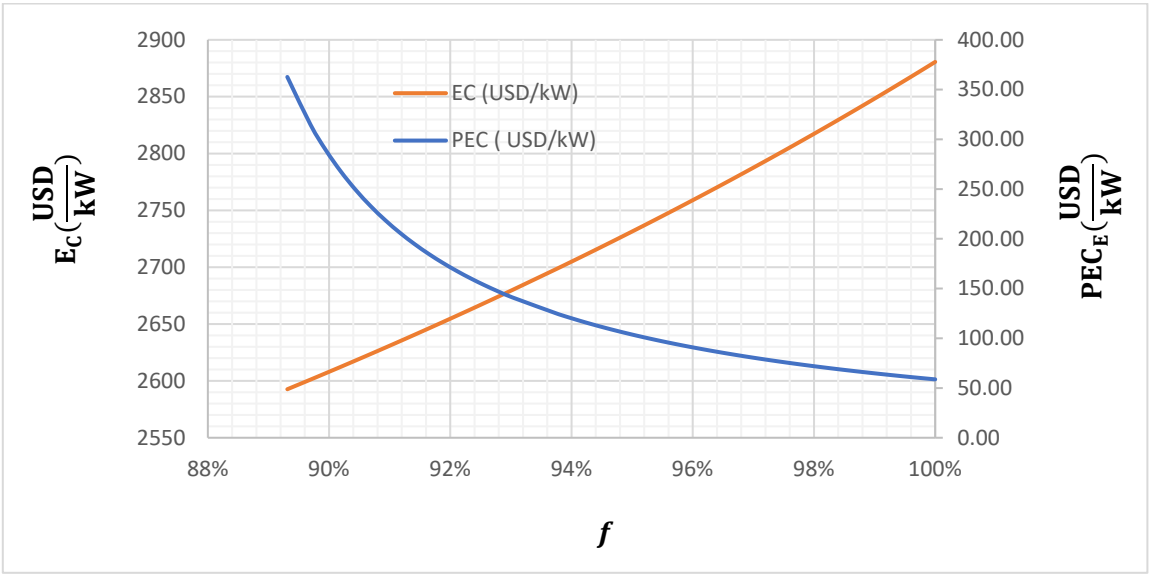

Figure 26:Variation of the total energy cost and the purchased electrolyser cost with the solar-PV area fraction.

We can see that the total energy cost increases while the cost of electrolyser decreases (PEC electrolysis stack) with an increase in solar-PV area fraction. The increase in the total energy cost with increasing solar-PV area is attributable to the increase in solar-PV electricity and a decrease in solar-T heat. The Levelized cost of solar-PV electricity is 0.05 USD/kWh while that of solar-T heat from the parabolic trough collectors is 0.034 USD/kWh, increasing the

fraction of a component with the higher cost increases the total cost of the system. The total energy cost increases from 2,594 USD/kW at *f*=89.3% to 2,881 USD/kW at *f*=100%.

The PEC for the electrolyser is seen to decrease as the solar-PV area fraction is increased, this behaviour is expected since it was shown in Fig. (24) that the size of the electrolyser stack decreases with an increase in the solar-PV surface area fraction. The electrolyser's purchased equipment cost (PEC) per work of combustion decreases from 363 to 59 USD/kW when the solar-PV area fraction is increased from 89.3 to 100%.

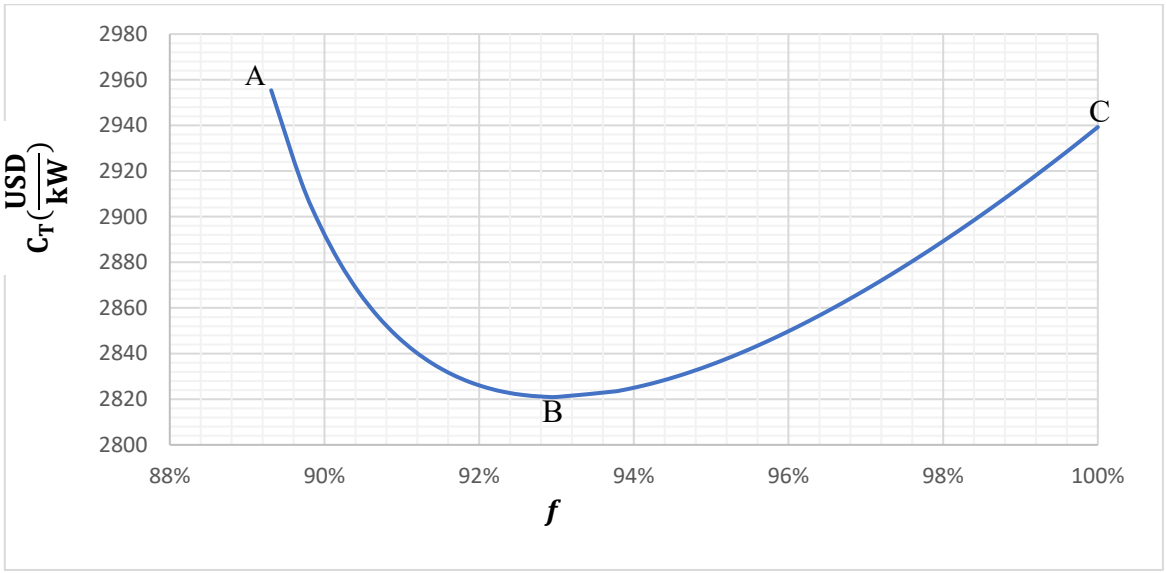

Figure 27: The variance in the total cost with the solar-PV area fraction

The total cost, sum of total energy cost and electrolyser purchased cost, forms a parabolic function ABC in the *f* values ranging from 83.9 to 100%. Point A represents the point where *f*=89.3 %, $T_O S_{gen} = 0$, $A_e = 0.109\ m^2/kW$, A_S=5.94 m^2/kW, $\eta_{ws} = 100\ \%$, $\eta_w = 81\ \%$ with the total levelized cost of 2,957 USD/kW. The properties at point B are as follows: *f*=93%, $T_O S_{gen} = 48.9\ kW$, $A_e = 0.043\ m^2/kW$, A_S= 6.34 m^2/kW, $\eta_{ws} = 94\%$, $\eta_w = 77\%$ with the total cost of 2,821 USD/kW. Point C represent a *f*=100% operating point, $T_O S_{gen} = 161.3\ kW$, $A_e = 0.018\ m^2/kW$, A_S=7.26 m^2/kW, $\eta_{ws} = 83\%$, $\eta_w = 67.5\%$ with the total cost of 2,939 USD/tonne

We see that point A represents the electricity and heat combination that has the highest overall system work and work storage efficiencies than any other point on the curve. This point also represents the highest electrolyser active area per work of combustion and in extension the highest electrolyser purchase cost. Point C (*f*=100%) represents a point where the process is supplied with electricity alone to meet the energy requirements. We noticed that the efficiencies

are the lowest at this point, with the total energy cost being slightly lower than the cost at point A. We can also see that the electrolyser purchased cost is the lowest compared to any other point, this is because the electrolyser active area is the smallest (0.109 m^2/kW), leading to the lowest cost. Point B represents a minimum point of the curve with the lowest total cost of 2,821 USD/kW, this value is 4.5% and 4.02% lower than the total costs at f=89.3 and f=100% respectively. We see that the highest work efficiencies do not necessarily translate to the cheapest cost, this is due to the high capital cost on the electrolyser at f_{min} (f=89.3%).

The optimal point on the total cost curve minimizes the cost, and this point is B with a solar-PV area fraction of 93% i.e., f_{op}=93%. The cost saving of 4.02% is realised when the process is operated at the optimal solar area fraction (f_{op}) instead of f=100%. The work storage and overall work efficiency gain of 11.8% and the solar collection area-saving of 12.7% are achieved when operating the process at optimal solar area fraction instead of f=100%. The sample calculations and the tables with important information are found in appendix B and C rese

3.1.3 Representation of the optimal PT-H_2 process on the gh-diagram

Fig. (28) shows the gh-diagram representation of the PT-H_2 process, the diagram shows the solar-PV electricity (work) and solar-T heat at 200 ℃. The process minimum energy and work requirements, work and heat flows are represented by vectors whereby the black, blue, and red vectors represent the process, electricity (work), and heat flow respectively.

The process enthalpy and Gibbs free energy for a hydrogen production rate of 3.32 mole/s are 948.3 and 787.1 kW respectively. The process vector starts at 0 and ends at the coordinates (ΔH, ΔG) = (948.3 kW, 787.1 kW). The units of enthalpy and Gibbs free energy are in kW since the production is reported in mole/s, this is different from previous cases, Fig (11-12), where the units are based on 1 mole of the product hence the units are reported as kJ/mol.

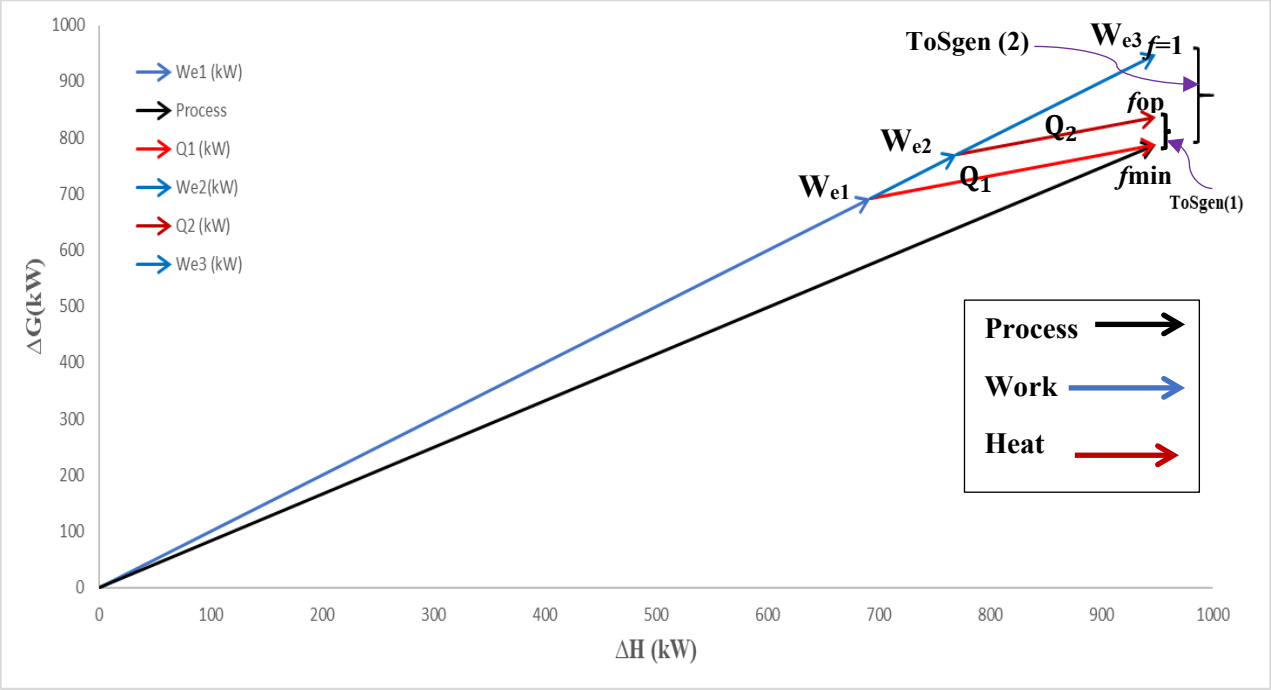

Figure 28: The gh-representation of the PT-H_2 process at f_{min}, f_{op} and f_{max}

Three different arrangements of heat and workflow to the system are illustrated; the first, second and third arrangements are the combinations of W_{e1} and $Q(T_1)$, W_{e2} and $Q(T_2)$ and lastly W_{e3}. The first arrangement represents the point where $f=f_{min}=89.3\%$, the solar-PV electricity and solar-T heat at 200℃ are represented by vectors W_{e1} and $Q(T_1)$, respectively. The f_{min} is found by setting T_oS_{gen} to zero in Eq. (48), the value of $f=f_{min}$ is then substituted in eq. (45) and (46) to determine the corresponding values of W_e and Q_{ST}. The values of W_e and Q_{ST} represent the lengths of electricity and heat vectors on a gh-diagram.

We can see that the magnitudes of vectors W_{e1} and Q_1 are 692.4 and 255.9kW respectively, the $W_{Q(T1)}$ (y-component of vector $Q(T_1)$) is 94.7kW. The total energy supplied to the process is represented by the sum of x-components of vectors W_{e1} and $Q(T_1)$ which are 692.4 and 255.9kW respectively, their sum is equal to 948.3kW which is equivalent to the process minimum energy requirements. The total work supplied to the process is the sum of the y-components of electricity and heat vectors which are 692.4 and 94.7kW, their sum is equal to 787.1kW which is equal to the process work requirements i.e., ΔGp.

The second arrangement represents the $f=f_{op}=93\%$ point and the work and heat flows are represented by W_{e2} and $Q(T_2)$ vectors with magnitudes of 770 and 178.3kW, respectively. The value of f_{op} was determined from Fig. (27) and the work and heat flows were determined according to the procedure used for the f_{min} case. The y-component of the heat vector is equal to the work associated with heat and it is equal to 66 kW. The total energy supplied to the

process by this arrangement is equal to the sum of the x-components of W_{e2} and $Q(T_2)$ which are 770 and 178.3kW, respectively. The corresponding lengths of electricity and heat vectors are, therefore, equal to 770 and 178.3kW respectively. The sum of these components is 948.3kW (equivalent to process enthalpy). The y-components of vectors W_{e2} and $Q(T_2)$ are 770 and 66kW respectively, their sum is equal to 836kW which is greater than the process work requirements (787.1kW) by 48.9kW. The surplus work represents the T_oS_{gen} term, and it is represented by T_oS_{gen} (1) in Fig. (28)

The third arrangement is represented by the point f=100 % where the process is supplied with solar-PV electricity alone. The amount of electricity supplied to the process W_{e3} must meet the minimum process energy requirements (ΔH_P) for the process to occur, the amount of W_{e3} required is thus 948.3kW. The corresponding length of the electricity vector is, thus, equal to 948.3kW. This amount meets the process enthalpy but oversupplies the work with the amount of W_{e3}-ΔH_P, which is equivalent to 161.3kW. This value is represented by T_oS_{gen} (2) in Fig. (28).

The gh-diagram shows that the most energy-efficient way to supply the PT-H_2 process with energy is when the combination of solar-PV and solar-T heat is used at a f_{op} of 89.3%. This is since the surplus work is zero at f_{min} i.e., the end of the combined electricity and heat vectors meet the end of the process vector. The f_{min} point does, however, not represent the cheapest operating point as shown in section 3.1.2 in Fig. (27). The cheapest operating point is represented by f_{op} in Fig. (28).

The theoretical performance targets (optimal operating point) for the PT-H_2 process in terms of solar-PV area fraction, work storage and overall system work efficiency, total solar area and Levelized cost are 93%, 94 and 77%, 6.34m^2/kW, and 2,821 USD/kW.

3.2 PT-CH_4 process scheme

The power-to-methane process pathway produces methane gas (synthetic natural gas) from water and carbon dioxide, the process energy needs are met through solar-PV electricity and solar-T heat. The overall process is divided into two subsections of steam electrolysis and methane synthesis. The hydrogen gas produced by electrolysis reacts with carbon dioxide to produce methane according to the Sabatier reaction. Steam electrolysis, synthesis reaction, the overall process material balance and the accompanying standard enthalpy and Gibbs free energies are provided in Table 3.

Table 3: PT-CH_4 overall process and the two sub-processes material balance and the corresponding standard enthalpy and Gibbs free energy to produce 1mole of methane.

Process	Material balance	$\Delta H_P(\frac{kJ}{mol})$	$\Delta G_P(\frac{kJ}{mol})$
Steam electrolysis	$4H_2O_{(g)} = 4H_{2(g)} + 2O_{2(g)}$	967.3	914.4
Methanation	$4H_{2(g)} + CO_{2(g)} = CH_{4(g)} + 2H_2O_{(g)}$	-165.0	-113.6
Overall	$2H_2O_{(l)} + CO_{2(g)} = CH_{4(g)} + 2O_{2(g)}$	890.3	818

Production of 1 mole of methane is endothermic and work deficient process, 890.3 and 818 kJ/mol_CH_4 of minimum energy and work are required before the process can proceed. This is due to the high endothermicity and work requirements of steam electrolysis, the minimum energy and work requirements of this sub-process are 967.3 and 914.4 kJ/mol of hydrogen produced. The methanation process is exothermic and work-producing with -165 and -113.6 kJ/mol_CH_4 of minimum energy and work required to be rejected by the process. The overall minimum energy and work requirements are the sums of the individual sub-processes. The overall process takes in liquid water while the electrolysis requires steam, therefore the minimum energy and work of vaporisation account for the differences between the sum of sub-processes and overall process enthalpy and Gibbs free energy.

The simplified process flow diagram of the PT-CH_4 process scheme is depicted in Fig. (29), 2 moles of water and 1 mole of carbon dioxide are supplied to the process to produce 2 moles of oxygen and 1 mole of methane gas. The process is supplied with solar-T heat at temperature T (200℃) and solar-PV electricity. The liquid water is vapourised in a series of heat exchangers (HX-01) as in the case of the PT-H_2 process.

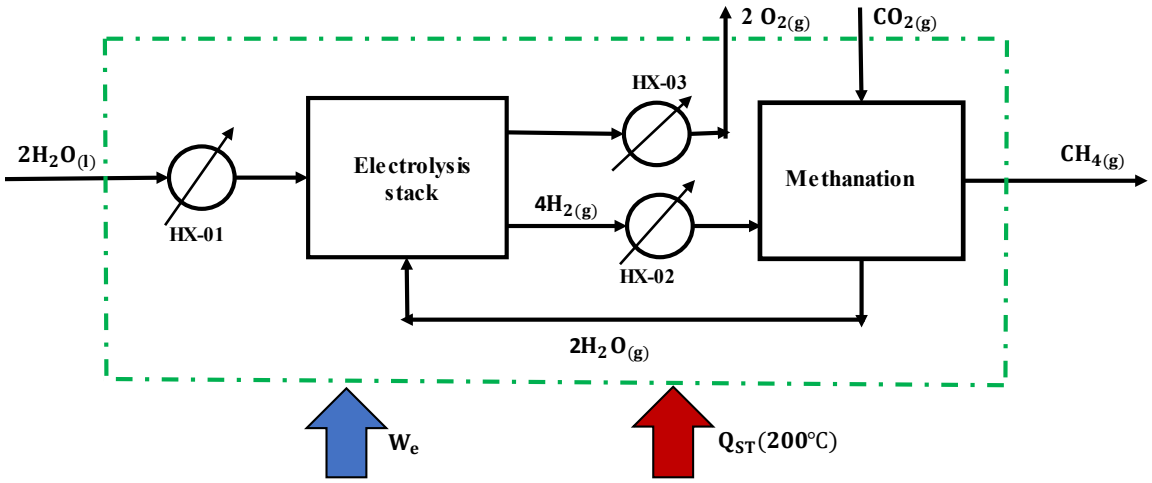

Figure 29: A simplified process flow diagram of PT-CH_4 process scheme

The produced steam is then mixed with the 2 moles of steam produced by the Sabatier reaction downstream and sent to the electrolysis sub-process where 4 moles of steam are converted to 4 and 2 moles of hydrogen and oxygen gases respectively. The produced oxygen leaves the process as a co-product while hydrogen is sent to the methanation sub-process where it is reacted with 1 mole of carbon dioxide to produce 1 mole of methane and 2 moles of water vapour. Water vapour is recycled back to the electrolysis stack while methane exits the process as the main product.

Methane gas production rate of 1 mole/s is required to produce a work output of 640kW from combustion at 1200 ℃, this translates to 2,078.8tonnes for 36,000h (15 years).

3.2.1 Thermodynamic performance

The T_oSg_{en} calculations show the minimum solar-PV (f_{min})area fraction to be 95.4%, therefore the thermodynamic and economic performances are investigated for the range 95.4%≤ f ≤ 100%. The work storage and overall system work efficiencies follow the same trend as in the case of PT-H_2 as shown in Fig. (32)

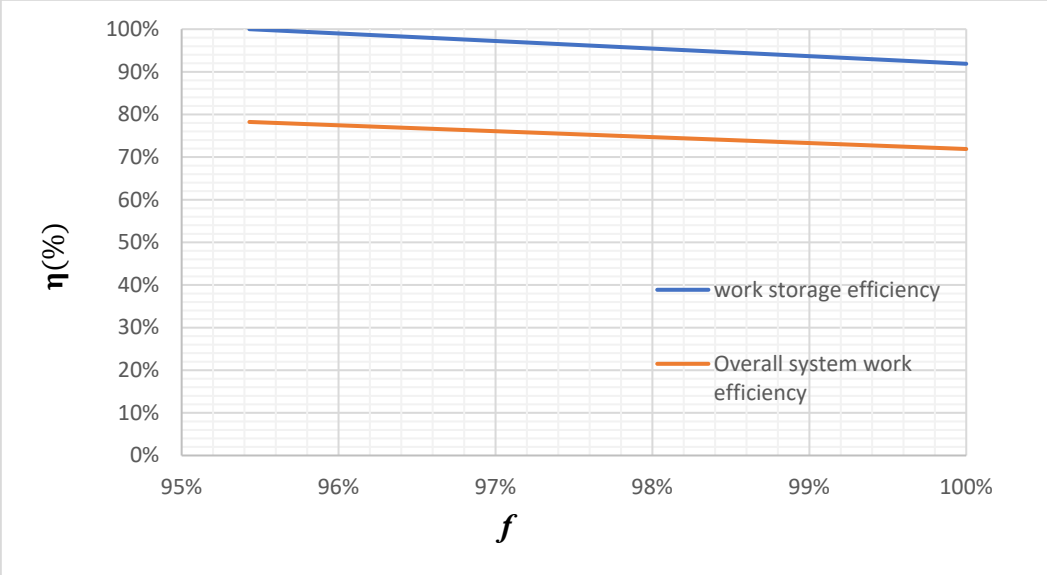

Figure 30: Variation of the overall system work and work storage efficiencies with the solar-PV surface area fraction.

The maximum efficiencies are found at the minimum solar-PV area fraction (f_{min}) where the work storage and overall system work efficiencies are 100 and 78% respectively. The lowest respective values of 92 and 72% are obtained when the process is powered by the solar-PV alone i.e., at f=100 %.

3.2.2 Solar area requirements and the cost implications

The effects of solar-PV surface area fraction on the total solar surface area required per work output were investigated and the results are shown in Fig. (33). We can see that the total solar area increases with an increase in the value of the solar-PV area fraction the same way as in the case of hydrogen. The minimum solar area is 6.22 m^2/kW, and it is found at f_{min}, the highest solar area is 6.82 m^2/kW, and it is found at f=100%.

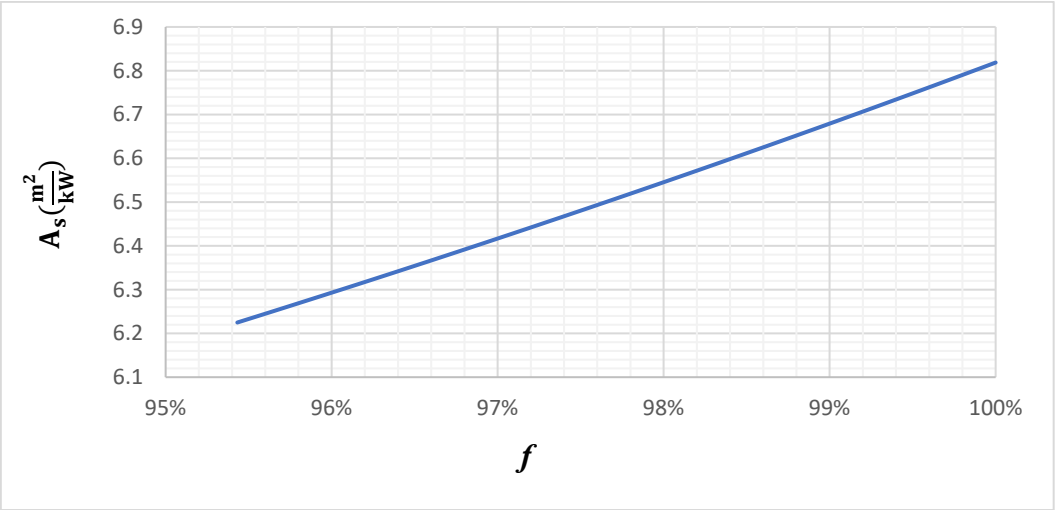

Figure 31: Variation of the total solar surface area with the solar-PV surface area fraction

The results imply that the use of the combined solar-PV and solar-T technologies at the correct solar-PV area fraction reduces the required solar area, this is because the collection efficiency of solar-T (η_{ST} =63%) is higher than that of solar-PV (η_{PV} =20.4%). As a result, supplying a certain amount of work by using the combination of solar-PV and solar-T heat requires a smaller solar area compared to supplying the same amount using solar-PV alone. Operating the process at the minimum solar-PV area fraction of 95.4% instead of 100% (solar-PV only) can reduce the required solar area by 8.7%.

The total solar energy and purchased electrolyser costs for the PT-CH_4 were calculated for the considered solar-PV surface area fraction range of $94.5\% \leq f \leq 100\%$ as shown in Fig. (32). The electrolyser and total energy costs in USD/tonne are represented by curve ACD and line BCE.

We can see that the electrolyser cost decreases while the total energy cost increase with an increase in the value of f. The electrolyser cost at the f_{min} and f=100 % is 59,940 and 226.7 USD/kW. The big value at f_{min} is attributable to the high electrolyser active area of 15,341.9 m^2 which is caused by a very low current density of 0.0050 A/cm^2.

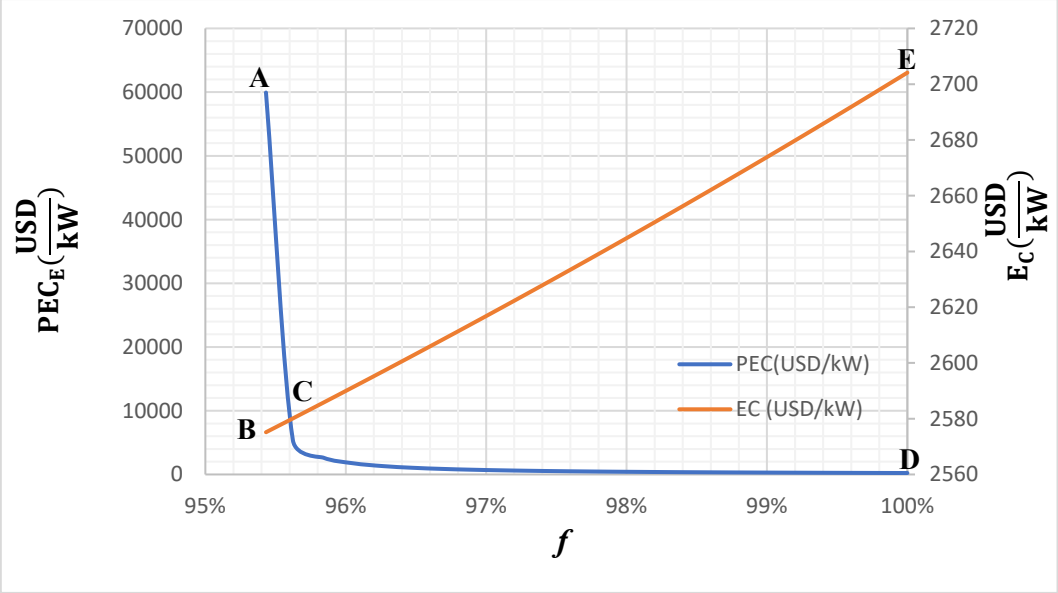

Figure 32: Effects of the solar-PV surface area fraction on the electrolyser and total energy costs

The total solar energy cost, contrary to the electrolyser cost, is minimum at f_{min} and maximum at f=100 %. The respective minimum and maximum values of the total solar energy are found to be 2,575 and 2,704 USD/kW.

The energy and electrolyser costs were then added to give the total cost of the process and plotted against the solar-PV area fraction as shown in Fig. (35).

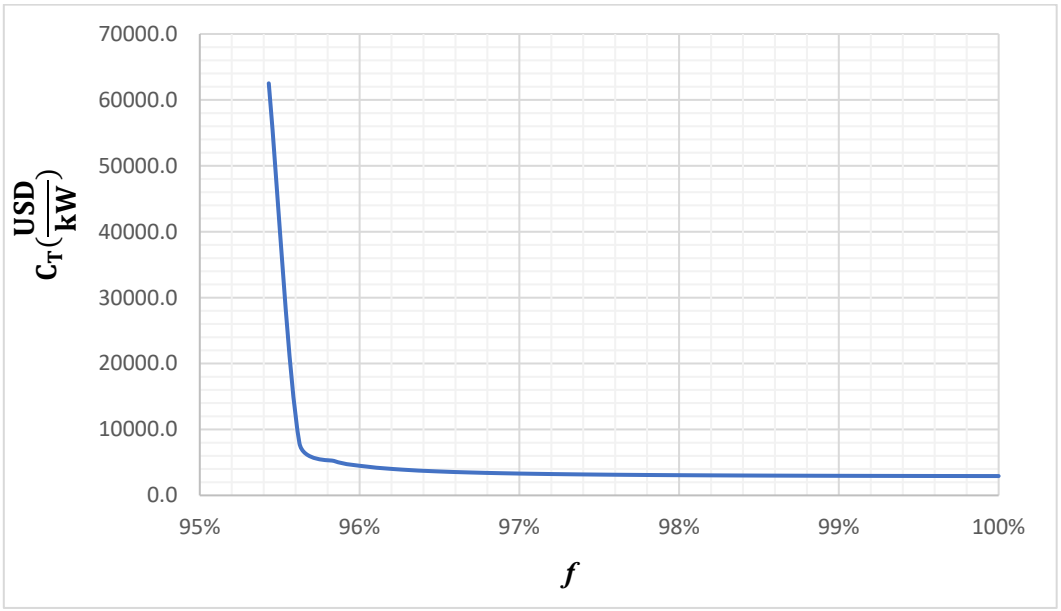

Figure 33: Variation of the total cost with the solar-PV area fraction

We can see that the total cost is the highest at the minimum value f and the lowest when f=100%. The high cost when f_{min} is due to the high electrolyser cost at this point which far

outweighs the low cost of the total energy. The highest and lowest total costs of producing methane for 15 years are 6,2516 and 2,931 USD/kW, respectively. The PT-CH_4, unlike the PT-H_2 process pathways, is less costly when supplied by solar PV only. The thermodynamic performance is the lowest with the highest solar area requirements at this point, however, the cost is the lowest which makes f=100 % an optimal point.

The PT-H_2 process pathway has the f_{op} that lies between f_{min} and f=100 %, we shall call all processes with $f_{min}<f_{op}<f_{max}$ (f=100%) category A processes. PT-CH_4 process scheme has f_{op}=100, we shall call all the processes with $f_{op}=f_{max}$ category B processes.

3.4. Other power-to-chemicals process pathways

The same analysis used for PT-H_2 and PT-CH_4 was extended to PT-Ethane, PT-DME, PT-Ammonia, PT-Ethylene, PT-Syngas, PT-Methanol, PT-Ethanol and PT-Propanol processes. The thermodynamic and economic performance, solar area requirements, Levelized costs, efficiency gains and costs savings for all the considered process schemes are reported in Table 4. We see that category A processes are predominant, with only three processes belonging to category B. PT-Hydrogen, Syngas, DME, Ammonia, Ethylene, Methanol and Ethanol are all category A processes. Power-to-alkanes, PT-Methane and PT-Ethane, and PT-Propanol form category B processes.

Table 4: Results for other PT-C process pathways.

Process pathway	Category	f_{op}	Performance					% Gains/losses			
			η_{WS}	η_W	$A_S(\frac{m^2}{kW})$	$C_T(\frac{USD}{kW})$	$C_T(\frac{USD}{tonne})$	η_{WS}	η_W	A_S	C_T
PT-Hydrogen	A	93.0%	94.3%	76.6%	6.34	2821.0	2098.1	11.8%	11.8%	12.7%	4.0%
PT-Syngas	A	93.2%	96.8%	81.0%	6.00	2664.0	418.9	11.2%	9.4%	12.4%	3.9%
PT-DME	A	98.4%	98.0%	74.8%	6.54	2787.1	494.6	5.0%	5.0%	5.3%	0.4%
PT-Ammonia	A	96.8%	94.2%	70.1%	6.96	3008.6	344.1	11.3%	11.3%	12.1%	4.4%
PT-Ethylene	A	99.6%	95.1%	75.4%	6.50	2741.0	359.6	5.6%	5.6%	6.0%	2.2%
PT-Methanol	A	99.2%	98.3%	71.2%	6.87	2691.9	330.2	1.6%	1.1%	1.7%	0.1%
PT-Ethanol	A	98.4%	98.6%	71.0%	6.89	2933.1	329.7	2.9%	2.1%	3.1%	0.4%
PT-Methane	B	100.0%	91.9%	71.9%	6.82	2930.3	902.2	-8.1%	-8.1%	-8.7%	95.3%
PT-Ethane	B	100.0%	94.0%	80.0%	6.13	2630.6	842.6	-14.4%	-12.0%	-15.4%	8.4%
PT-Propanol	B	100.0%	97.0%	72.8%	6.29	2876.4	543.50	-3.0%	-3.0%	-3.2%	2.1%

PT-Ethanol, Methanol and DME have the highest work storage efficiencies of 98.6, 98.3 and 98.0% respectively, followed by PT-Propanol and Syngas at respective efficiencies of 97 and 96.8%. The lowest work storage efficiency is reported for the PT-Methane process pathway at 91.9%. PT-Syngas, Ethane and Hydrogen have the highest overall system work efficiencies of 81, 80 and 76.6% respectively. The lowest overall system work efficiencies are recorded for PT-Ammonia, Ethanol and Methanol at respective values of 70.1, 71.0 and 71.2%.

PT-Syngas shows the lowest solar area requirements at 6.00 m^2/kW, followed by PT-Ethane, Propanol and Hydrogen at 6.13, 6.29 and 6.34 m^2/kW, respectively. The highest solar area requirements are recorded by the PT-Ammonia process pathway at 6.96 m^2/kW, followed by PT-Ethanol and Methanol at respective values of 6.89 and 6.87 m^2/kW. PT-Ammonia records the highest Levelized cost at 3,009 USD/kW. PT-Ethanol and Methane follow at 2,933 and 2,930 USD/kW, respectively. PT-Ethane and Syngas record the lowest Levelized costs of 2,631 and 2,664 USD/kW.

PT-Hydrogen, PT-Ammonia and PT-Syngas processes register the highest work storage and overall work system efficiency gains of 11.8 and 11.3 and 11.2% as respective work storage gains, and 11.8,11.3 and 9.4% as the overall system work efficiency gains respectively. PT-Methanol registers the lowest work storage and overall system work efficiency gains of 1.6 and 1.1% respectively. The highest solar area savings of 12.7% are realised for PT-Hydrogen when operating the process at f_{op} instead of f=100 %. PT-Methanol records the lowest solar area requirements savings of 1.7%.

PT-Methane and Ethane process showed the highest costs saving of 94 and 16.4% made when operating at f=100 % instead of f_{min}. PT-Syngas, propanol and Hydrogen follow with cost savings of 8.4,4.8 and 4.0%, respectively when operated at $f$op instead of f=100%. PT-Methanol, DME and Ethanol register the lowest cost savings of 0.1, 0.4 and 0.4% respectively.

Chapter 4

Flow sheeting and process modelling for PT-H_2.

4.1 Basis of design and assumptions for PT-$H_{2(g)}$ process simulation

This chapter looks at simulating a PT-H_2 process scheme on Aspen Plus® software to determine the benefit of using the combined solar-T heat and solar-PV system to supply the process energy needs. This process was looked at in the previous chapter, section 3.1, where the thermodynamic and gh-diagram analyses showed the theoretical performance targets in terms of the optimal solar-PV area fraction, overall system work efficiency, total solar area requirements and the Levelized Cost of production of 93%,76.6%,6.32m^2/kW, and 2,821 USD/kW (2,098 USD/tonne) respectively. The analyses showed that using the combined solar-PV and solar-T heat at the correct or optimal ratio offers a better process and economic performance compared to using solar-PV electricity alone to power the process. The process was assumed to be ideal in the sense that the feed and products streams were at ambient conditions with the assumption of complete heat integration within the system. The simulation takes away these assumptions and introduces an element of complexity. The objectives of this chapter are two-folds and are as follows

- To develop two process flowsheets of PT-H_2 process pathways where one flowsheet assumes the use of solar-PV only to supply the process energy needs. The second flowsheet uses the combination of solar-PV and solar-T heat at 200℃ to meet theoretical performance targets set in section 3.1.
- The second objective compares two cases to establish if there are benefits of using the combination of solar-PV and solar-T heat at the determined solar-PV area fraction. The gains or losses obtained will, therefore, be compared to the gains or losses obtained in section 3.1. it is also the goal of this chapter to meet the performance targets set in section 3.1.

Two process flow diagrams are developed where in the first case the process is powered by solar-PV only (f=100%) and in the second case, the process is powered by the combined solar-T and solar-PV.

The production of hydrogen is kept the same at 3.32 mole/s (11.95 kmol/h) with water at ambient conditions fed at 3.32 mole/s on both process flow diagrams for a fair comparison. The following assumptions and design constraints apply to both process flow diagrams.

- The processes are assumed to be operating at a steady state.

- The cold water (utility) stream amount fed to both processes are the same with quantities (mole flow rates) and the process conditions (temperature and pressure), this is to ensure a fair comparison between the process flow sheets.
- The electrolyser is assumed to operate at a thermal-neutral voltage and the pressure and temperature of 10atm and 750℃ on both the process flow diagrams.
- The electrolyser geometry and material of construction, solar global irradiance, solar-T heat, and solar-PV collection efficiency are assumed to be the same as the ones used in section 3.1.

The process flow diagram of the proposed PT-H_2 process is represented in Fig. (36). The process takes in water (3.32 mole/s) at 1 atm and 25℃ as the feed.

4.2. Process description

Water is fed to the process and transferred to the feed water pump (P-01) where the pressure is raised to 10atm as required by the electrolyser. The pump discharge is sent to a cascade of heat exchanges (HX-01, HX-02, HX-03, HX-04) where water is pre-heated and partially vapourised at the temperature of 180.9 ℃ in stream 5. The goal of the heat exchangers system is to recover as much heat as possible from the electrolysis product streams. HX-04 and HX-02 recover heat from the cathode stream by exchanging heat with heat exchangers HX-05 and HX-06. HX-01 and HX-03 recover heat from the anode stream by exchanging heat with HX-06 and HX-07. This set-up reduces the anode and cathode streams temperatures to 30℃, reducing the number of heat exchangers on water stream from 4 will lead to the reduced temperature of stream number 5, which will, in turn, result in higher electrical heater load. It is therefore only reasonable to recover as much heat to reduce the workload of the electrical heater and the electricity consumption thereof. Adding more exchangers to further reduce cathode and anode stream temperatures to below 30℃ will not be economical, the cost of more exchangers will outweigh the benefit from recovering heat since heat at low temperatures has little value.

Stream 5 is sent to the electric heater (EL-HE) where the temperature is further raised to the electrolysis stack operating temperature of 750℃. The product of EL-HE (stream 6) is mixed with the recycled hydrogen to produce a composition of 10% mole of hydrogen, hydrogen is recycled to maintain a reducing atmosphere on the cathode. The composition of 10% mole and 90% mole for hydrogen and water is recommended (Harvego *et al.*, 2009). The outlet stream of the electrolyser comprises a mixture of hydrogen and oxygen at the temperature of 750 ℃. The stoichiometric reactor (Stack) with the input of electrolysis reaction, temperature, and

pressure of 750℃ and 10atm is used to simulate the electrolyser in Aspen Plus®. It is imperative to note that the outlet of a stoichiometric reactor has one material stream, so the separator was used in the Aspen simulation to separate hydrogen from oxygen. This arrangement is not shown in Fig. (36). Please refer to Appendix D in Table D2 for the Aspen Plus® flowsheet.

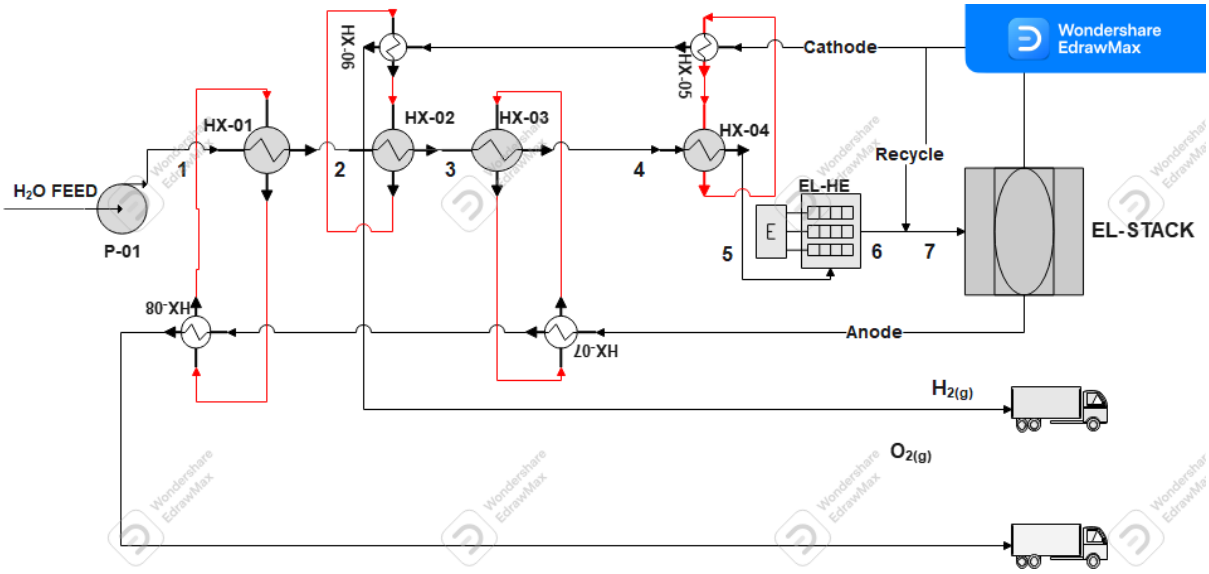

Figure 36: Process flow diagram of PT-H_2 powered by solar-PV only system

The anodic product, oxygen, is sent to heat exchangers (HX-03 and HX-01) where the heat of the stream is recovered by the feedwater. The cathode stream is split into two streams where 10% of the stream is recycled while 90% is sent to heat exchangers HX-05 and HX-06 where heat is recovered.

The solar-PV and solar-T heat system includes the solar-T field represented by ST-field in Fig. (37). The exit stream of HX-03 is sent to the solar-T field where the temperature is raised to 200℃ before being sent to HX-04. Please refer to Appendix D, Table D3 for complete streams properties.

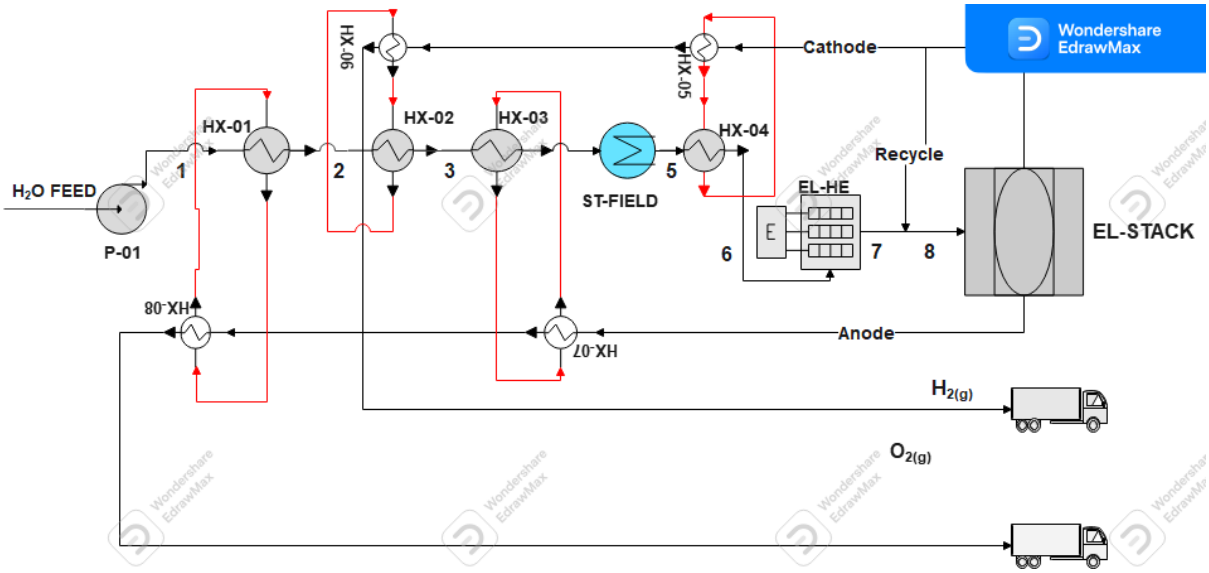

Figure 37: Process flow diagram for the combined solar-T heat and solar-PV system

4.3. Economic analysis methodology

The processing units and utility costs are determined from the economic analysis module of Aspen Plus® version 10 with an exception to the costs of electrolyser, solar-PV electricity, and solar-T heat. The costs of these components are determined by using a similar approach adopted in chapter 3. The costs of raw materials, namely carbon dioxide, nitrogen and process water are taken from the literature. These costs are then escalated to 2021 by using eq. (62) and chemical engineering index for the current year. The total cost of the process for the project lifetime is therefore estimated according to Eq. (64)

$$C_{total} = PEC_T + RMC + UC + EC_T - S_{BP} \quad (64)$$

Where C_{total} , RMC, UC, EC_T and S_{BP} represent the total, raw material, utility, total energy costs and the sales from by-products in USD, respectively. The specific cost for each product is thus calculated by diving the total cost of the process by the total amount of the chemical produced in a project lifetime.

$$SC_C = \frac{C_{total}}{m_n} \quad (65)$$

Where SC_C and m_n represent the specific cost (USD/tonne) and the total amount of the chemical (tonne) produced in the project lifetime, respectively.

The Levelized cost of producing a chemical can also be expressed in terms of the power output when the chemical is combusted at 1200°C as follows.

$$LC = \frac{C_{total}}{W_c}$$

(66)

Where LC and W_c represent the Levelized cost (USD/kW) and work of combustion (kW) respectively.

4.4. Simulation results and discussions

This section reports mainly the energy, heat and work, flow without delving deep into the stream's material flows and other properties such as the temperature. Please refer to appendix D for complete streams information.

4.4.1. Thermodynamic performance and solar area requirements

The thermodynamic performance is reported in terms of the overall system work efficiency as defined in section 2 as the ratio of work out-put to work input. The work output from combusting 3.33 mole/s of hydrogen at 1200℃ was calculated to be 640kW, which was the basis of comparing different processes. The work input, in this case, will be the sum of solar-PV electricity and work brought by the solar-T heat at 200 ℃. Solar-PV electricity is used to power the feed water pump (P-01), electric heater (EL-HE) and electrolysis stack (EL-STACK). The electrical load and the corresponding share for each processing unit are reported in Table 10.

Table 10: Work and heat flows into the PT-H_2 process

Component	**Solar-PV**		**Solar-PV +solar-T heat**	
	Electrical load (kW)	Percentage share (%)	Electrical load (kW)	Percentage share (%)
P-01	0.18	0.0%	0.2	0.0%
EL-HE	131.9	13.8%	31.5	3.7%
Electrolysis stack	823.8	86.2%	823.8	96.3%
Total	955.9	100%	855.5	100%

We can see from Table 10 that the electrolysis stack takes up the biggest share of electricity for both the solar-PV only process and the combined solar-PV and solar-T heat process scheme. The total electricity share of the electrolysis stack in solar-PV and the combined solar-PV and solar-T heat processes are 86.2 and 96.3% respectively. The actual amount of electricity consumption in the electrolysis stack is 823.8kW for both processes, this value is constant due to the same operating conditions in both cases. The feed water pump commands the lowest electricity share of 0.019 and 0.021% for the solar-PV only and the combined process respectively. Electric heater consumes 131.9 and 31.5kW of electricity for the respective

processes. The electrical load of an electric heater for the combined solar-PV and solar-T heat process is significantly lower compared to the electric heater load for the solar-PV only process. The reason for this observation is that the solar-T field in the combined process completes water vaporization and raises the steam temperature to 200℃ followed by HX-04 raising the temperature further to 513 ℃. The inlet temperature to the electrical heater in the solar-PV only process is 180.4℃ which is significantly lower than 513℃. The electric heater in the case of solar PV only thus requires supplying more work to raise the temperature to 750℃ as compared to the combined system.

The solar area requirements, workflows, and the corresponding overall system work efficiencies of the solar-PV only and the combined solar-PV and solar-T heat processes are reported in Table 11. We see that the combined system requires heat at the rate of 100.4kW to raise the temperature of stream 4 (Fig. 37) to 200 ℃. The solar-PV surface area fraction required to achieve this was found to be 96.3%, this value is higher than 93% found for theoretical calculations in section 3.1 of chapter 3. The total work for the f=100% and f=96.3% were found to be 955.9 and 855.5 kW respectively.

Table 11: The energy flows, solar surface area requirements and the associated costs for each process flow sheet

Process	f	W_{PV} kW	Q_{ST} kW	W_{ST} kW	W_T kW	A_S m^2/tonne	η_W %
Solar PV only process	100%	955.9	0	0	955.9	5.5	67.0%
Combined solar PV and solar-T process	96.3%	855.5	100.4	37.1	892.6	5.1	71.7%

The overall system work efficiency for the solar-PV and the combined system are 67.0 and 71.7% respectively. The combined system shows a higher thermodynamic performance than the solar-PV only system with an efficiency gain of 4.7%. The total solar surface area is lower (5.1 m^2/tonne) for the combined solar-T heat and solar-PV arrangement compared to (5.5 m^2/tonne) for the f=100% arrangement. The solar area savings of 7.5% can be achieved when operating the process at f= 96.3% compared to f=100%.

It is worth noting and discussing that the efficiency values are lower while the solar area requirements are higher for the Aspen Plus® simulation than for the theoretical calculations in section 3.1. The overall system work efficiency and the solar area requirements were found to be 76.6% and 4.7 m^2/tonne (6.34 m^2/kW) for the combined system at f_{op}= 93% in the theoretical section. These values were found to be 67.5% and 5.4m^2/tonne for the f=100% case. The

differences in Aspen Plus® modelling values and the target values (theoretical values) can be ascribed to the following points.

- The heat integration is not ideal (complete) for the Aspen simulation
- The temperature of streams leaving the process is not ambient temperature like in the case of the theoretical calculations.
- Some of the electricity supplied to the process is used to heat the electrolyser feed, whereas all the electricity supplied to the ideal process is assumed to be utilized in the electrolyser.

It is, however, interesting to mention that the theoretical values at 96.3% are very close to the Aspen Plus® values at the same area fraction. The theoretical overall system work efficiency and solar area requirements at f=96.3 % are found to be 72.3 % and 5.0 m^2/tonne respectively, these values are close to 71.7 % and 5.1 m^2/tonne reported for Aspen Plus® models.

4.4.3. Cost analysis

The costs of the two process flowsheets were determined as per the methodology outlined in section 4.3.

Solar PV only (f=100%)

The operating costs of the process consist of raw material (feed water), energy cost (solar-PV electricity) and utilities. The cost of process water is given as 0.000467 USD/kg (Zhang, Wang, Van Herle, et al., 2020), this value was used with the total amount of water used per project lifetime to determine the feed water cost. The utility costs per hour were taken from Aspen Plus® as 0.267 USD/h, the total number of hours (36,000 h) were used to determine the cost of utilities. The Levelized cost of solar-PV electricity of 0.05 USD/kWh was used together with the total electricity requirements to determine the cost of energy for the project lifetime. The costs of processing units, with an exception to the electrolyser, were determined using Aspen Plus® while the cost of the electrolyser was determined the same way as in Chapter 3.

The operating and equipment costs for the process are provided in Tables 12 and 13, we see from Table 12 that the energy cost contributes the highest with the share of 99.3 % while feed water constitutes the lowest share of 0.19%. The total operating cost of the process is found to be USD 1,871,458.

Table 12: Process operating costs

Component	Cost USD	Share %
Raw material	$ 3,619.94	0.19%
Utility	$ 9,633.60	0.51%
Energy	$1,858,204.64	99.29%
Total	$1,871,458.18	100%

The electrolysis stack commands the biggest share of the total equipment cost of 48.2% at the cost of UDS 673,312. The electric heater and feed water pump have the lowest costs shares of 0.8 and 2.8% respectively. The total purchase equipment cost of the process was calculated to be USD 1,403,355.

Table 13: Process equipment cost

Equipment	Cost USD	Share %
HX-8	$ 83,400.00	5.9%
HX-7	$ 99,100.00	7.1%
HX-5	$ 69,400.00	4.9%
STACK	$ 676,312.44	48.2%
HX-1	$ 74,500.00	5.3%
P-1	$ 39,000.00	2.8%
HX-6	$ 69,300.00	4.9%
HX-2	$ 55,300.00	3.9%
EL-HE	$ 11,542.74	0.8%
MIX	$ 64,800.00	4.6%
HX-4	$ 66,000.00	4.7%
HX-3	$ 94,700.00	6.7%
Total	$1,403,355.18	100.0%

The process produces 3.32 mole/s of hydrogen gas, which translates to 867.3 tonnes for 15 years (36,000 h). The Levelized cost of hydrogen gas, without sales of by-product, was thus found to be 3,775.5 USD/tonne or 5,116.9 USD/kW. This cost is within the reported green hydrogen cost range of 2-5 USD/kg (IRENA, 2020). The cost becomes lower when the sale of oxygen is considered, the sales of oxygen gas are found to be 1,412.5 USD/tonne when using the cost per kg of 0.0017 USD/kg. The Levelized cost of hydrogen becomes 2,363 USD/tonne with the sales of oxygen.

Solar-PV and solar-T heat @ *f*=96.3%

The operating and purchased equipment cost of the combined process are reported in Tables 14 and 15, the raw material and utility costs are the same as in the case of solar-PV only. The energy cost, however, is lower for the combined cost at USD 1,799,162 which makes the total operating costs to be USD 1,799,163.

Table 14: Operating costs of the process

Component	Cost USD	Share %
Raw material	$ 3,619.94	0.20%
Utility	$ 9,633.60	0.54%
Energy	$ 1,785,909.24	99.26%
Total	$ 1,799,162.78	100%

The total equipment costs of the process were found to be slightly lower compared to the solar-PV only case at USD 1,390,702.

Table 15: Equipment cost of the process

Equipment	Cost USD	Share %
HX-8	$ 83,400.00	6.0%
HX-7	$ 99,100.00	7.1%
HX-5	$ 69,400.00	5.0%
STACK	$ 676,312.44	48.5%
HX-1	$ 74,500.00	5.3%
P-1	$ 39,000.00	2.8%
HX-6	$ 69,300.00	5.0%
HX-2	$ 55,300.00	4.0%
EL-HE	$ 2,756.85	0.2%
HX-3	$ 64,800.00	4.6%
HX-4	$ 66,000.00	4.7%
HX-03	$ 94,700.00	6.8%
Total	$ 1,394,569.30	100.0%

The lower reported cost for the combined system is due to a lower electric heater and HX-4 costs which are in turn due to the lower electricity and heat loads caused by the presence of the solar-T field. The Levelized cost of hydrogen when oxygen sales are not considered was found to be 3,682 USD/tonne (4,990 USD/kW) and 2,277 USD/tonne when the oxygen sales are considered. This hydrogen cost is lower than the cost found for the solar-PV only process by 2.4%.

The Levelized cost of hydrogen of 3,086 USD/tonne (4,990 USD/kW) at the f_{op} is greater than the costs of hydrogen obtained in Chapter.3 (section 3.1). The theoretical cost of 2,098 USD/tonne (2,821 USD/kW) was obtained for f_{op} in Chapter 3. The primary reason for this discrepancy is that only the energy and electrolyser costs were considered in Chapter 3, whereas the raw material, other equipment such as heat exchangers and pumps are considered in this Chapter. The other reason is that the theoretical f_{op}=93% is lesser than the f_{op}=96.3% obtained in Aspen Plus® modelling. The assumptions, such as complete heat integration, made in theoretical calculations also contribute to the observed discrepancy in the Levelized cost of hydrogen.

In summary, the Aspen Plus® modelling of the solar-PV only and the combined solar-PV and solar-T heat system showed consistent results with the theoretical analysis. The models have shown that using the combined system improves the overall system work efficiency, reduces the solar area requirements and the Levelized cost of hydrogen. The theoretical targets for the combined solar-PV and solar-T heat system set in Chapter 3.1 were not achieved in Aspen Plus®. The simulation results are, however, observed to be close to the theoretical targets. The theoretical targets and simulations results for the optimal solar-PV area fraction, solar area requirements and the costs were found to be 93%,76.6**%,** 6.34 m^2/kW and 2,821 USD/kW (theoretical targets) compared to 96%, 71.7% ,6.9 m^2/kW and 3,682 USD/kW.

Chapter 5

Process modelling for selected PT-C process schemes.

This chapter looks at the complete process simulations for power-to-ammonia, power-to-methane, and power-to-methanol process schemes. It extends from Chapter 3 where the black-box approach considering the feed and product streams at ambient conditions and the complete heat integration was assumed. The process costs considered in chapter 3 were limited to only the energy (solar PV electricity and solar T heat) and electrolyser costs. Chapter 5 aims to meet the theoretical targets found in Chapter 3 by using the heat and workflow arrangements determined in Chapter 3 (theoretical analyses). The Aspen Plus® simulation software is used to develop the process flowsheets of selected process pathways considering the heat and flow arrangements determined in the previous chapter and all the necessary processing units. The assumptions of feed and product stream being at the ambient conditions and the complete heat integration will be relaxed in process simulations.

Thermodynamic efficiencies will be limited to the overall system work efficiency. The total cost inclusive of the raw materials, utilities, and all processing units' costs will be determined for each selected power-to-chemical process scheme. The total cost will thus be used to estimate the Levelized cost of producing each considered chemical.

The following design basis and assumptions will apply for all the considered processes pathways.

- **Basis:** 10 MW of electricity is consumed in the electrolysis stack, resulting in the hydrogen production rate of 146 kmol/h. The electrolysis electrical load of 10MW and more have been reported to be reasonably economical and has indeed been used extensively in the literature (Giglio *et al.*, 2015b).
- The steam conversion of 100% is assumed in the electrolysis stack.
- Electrolysis reaction is assumed to occur isothermally at 750℃.
- Cooling water is available at 25℃ and 1atm.
- The project lifetime is 15years, with each process operating for 300days per annum and thus resulting in 36,000 hours in the project lifetime.
- The global solar irradiation of 1000W/m^2 is assumed for all the processes.
- Pressure drop is assumed to be negligible in process lines.
- The raw material cost and by-product selling prices are assumed to be constant in the project lifetime, this assumption is made to simplify the calculations

5.1. Power-to-ammonia process

The power-to-ammonia process produces ammonia from the feedstock of water and nitrogen, water is used to produce hydrogen in a steam electrolyser operated at 750℃ and 10atm. The produced hydrogen is then sent to the synthesis loop where it is reacted with nitrogen. The theoretical analysis revealed that the process performs better when the energy requirements are met through combining solar-PV and solar-T at the theoretical solar-PV area fraction of 96.8%. The performance targets at the theoretically optimal conditions in terms of the solar area requirements, overall system work efficiency and the Levelized cost were determined to be 6.96 m^2/kW (0.8m^2/tonne),70% and 3,009 USD/kW (344 USD/kW) respectively.

This section aims to use the work and heat flow arrangements determined in Chapter 3 together with Aspen Plus® simulation to meet the theoretical performance targets set. The work and heat flow arrangement determined in Chapter 3 comprises combining solar-PV electricity and solar-T heat at the solar-PV area fraction of 96.8%. The thermodynamic model used in the Aspen Plus® simulator is the Peng-Robinson equation of state. The electrolysis sub-process is modelled the same way as in Chapter 4 where the electrolysis stack is represented by a stoichiometric reactor and the separator to separate hydrogen from oxygen.

5.1.1. Process description

The power-to-ammonia process pathway can be divided into two major sub-processes of steam electrolysis and ammonia synthesis. The process flow diagram of this process scheme is represented in Fig. (38). Liquid water (145.1 kmol/h) at ambient conditions is supplied to the process and sent to pump P-01 where pressure is raised to 10atm. The pressurised water is then sent to a series of four heat exchangers (HX-01, HX-02, HX-03, and HX-04) where it gets pre-heated and partly vapourised. The saturated steam is sent to a solar thermal field where complete vaporisation is achieved. Steam at 200℃ emerges from the solar thermal field and is sent to the electric heater where the temperature is raised to 750℃. Steam at 750℃ is then mixed with recycled hydrogen gas before being sent to a 10 MW electrolyser. The electrolysis plant layout is the same as the one in Fig. (36).

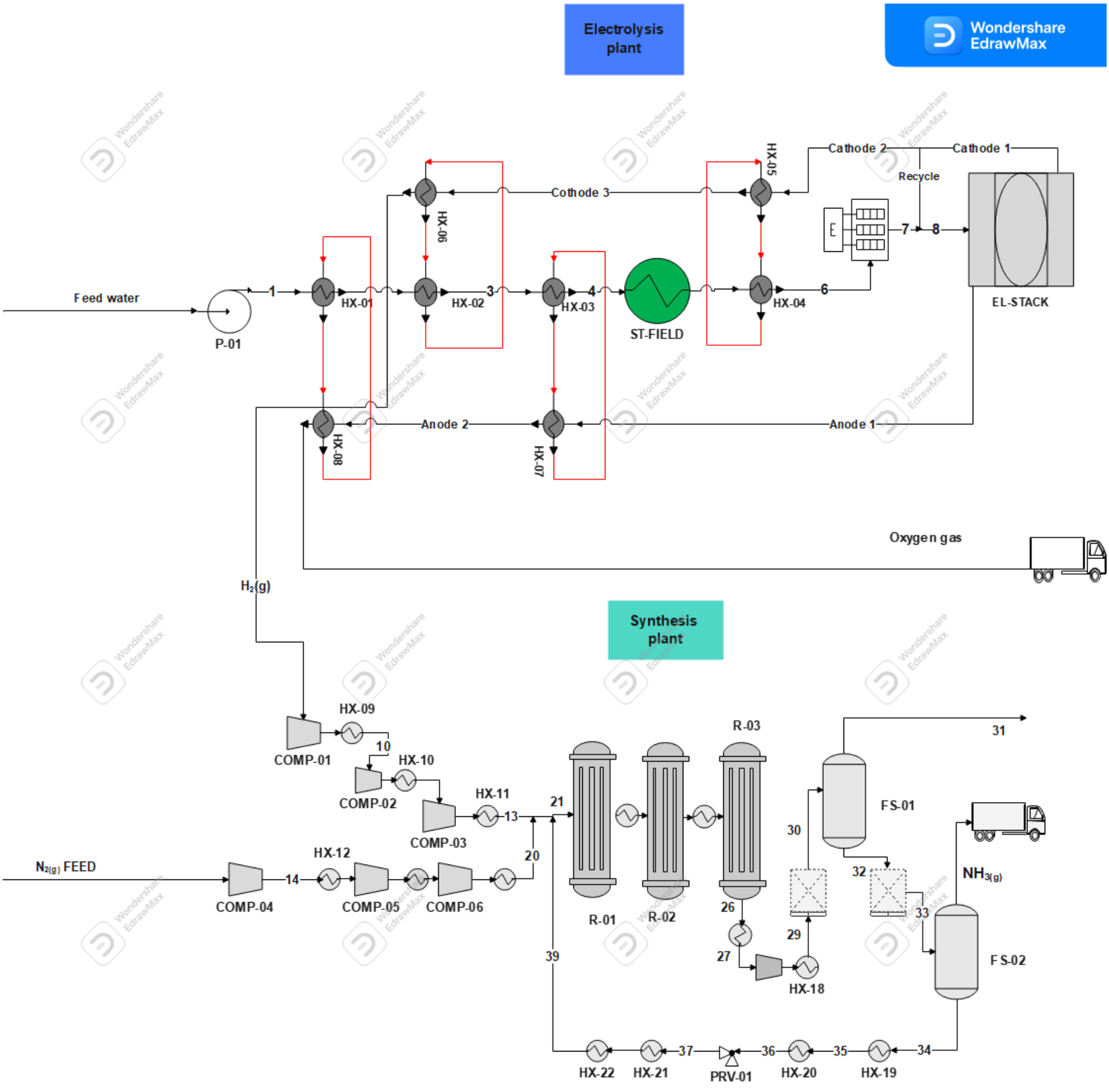

Figure 38: Plant wide process flow diagram of PT-NH_3 process

Nitrogen gas supplied to the process at ambient conditions is sent to three compressors COMP-04,05 and 06 where the pressure is raised to 98.7atm. The nitrogen stream is then mixed with hydrogen at the ratio of N_2:H_2 is 1/3. The combined stream is mixed with the recycle stream containing unreacted hydrogen and nitrogen to form synthesis feed stream 21. Stream 21 at 470℃ is sent to a cascade of adiabatic reactors with an interstage coolers system where ammonia is produced. The conversions and temperature of the reactor and heat exchanger loop are reported in Table 48. The product stream from the reaction loop is sent to HX-17 where the temperature is reduced before being sent to the COMP-07 where the pressure is increased to 132.2atm. The stream is then sent to HX-18 and refrigerator (REF-01) where the temperature is reduced to -3℃ before being sent to a flash separator FS-01. The conditions of 132.2atm and -5℃ are used to liquefy ammonia and thus aid the separation as shown by (Zhang, Wang, Van Herle, *et al.*, 2020). The gas product from FS-01 is sent to a refrigerator (REF-02) where the temperature is further reduced to -5℃ before being sent to a second flash separator where the composition of 99.9% wt of ammonia is achieved. The unreacted components are

sent back as stream 34 to be mixed with the fresh nitrogen and hydrogen. The process produces 97.3 kmol/h of ammonia and 72.6 kmol/h of oxygen from the feed of 145.1 and 48.4 kmol/h of liquid water and nitrogen, respectively. The important streams information is found in appendix D, in Table D3.

5.1.2. Reactor design

5.1.2.1 Theoretical calculations for the reactor/s conversion.

Ammonia synthesis is industrially carried out by reacting nitrogen with hydrogen in the temperature and pressure ranges of 450-600℃ and 100-250 bars, respectively(Zhang, Wang, Van Herle, *et al.*, 2020). The reaction kinetics of ammonia synthesis is given by Eq. (67) as follows.

$$r_{NH_3} = \frac{9.5}{\rho_{cat}}\left(k_1 \frac{p_{N_2} p_{H_2}^{1.5}}{p_{NH_3}} - k_{-1} \frac{p_{NH_3}}{p_{H_2}^{1.5}}\right) \quad (67)$$

Where r_{NH_3} , ρ_{cat} , p_{N_2}, p_{H_2}, p_{NH_3}, k_1 and k_{-1} represent the reaction rate (kmol/kg cat h), the density of the catalyst (kg/m^3), partial pressures of nitrogen, hydrogen, ammonia (Pa), forward and reverse reaction kinetic factors (kmol/kg cat h) respectively. The kinetic factors are given by eq. (68) and eq. (69)

$$k_1 = 1.79 \times 10^4 e^{\frac{-87090}{RT}} \quad (68)$$

$$k_{-1} = 2.75 \times 10^{16} e^{\frac{-198464}{RT}} \quad (69)$$

Where T and R represent the temperature (K) and the universal gas constant (kJ/mol. K) respectively. The kinetic model is then used to generate the plots of constant reactions rates determining theoretical conversions. The plots show how a reactor conversion changes with temperature assuming a constant reaction rate throughout a reactor. The method is used to estimate the number of catalyst beds or reactors required to achieve the conversion of a certain reactant. The tool is especially useful for exothermic reactions carried out in the adiabatic reactors.

.

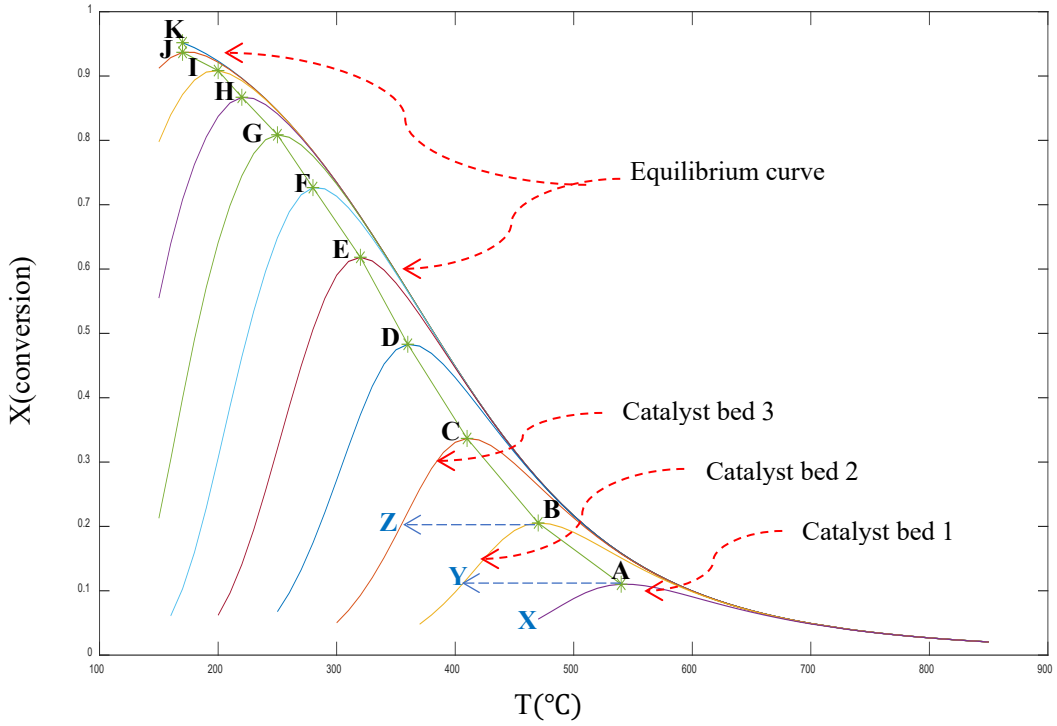

Figure 39: Reactor evolution for ammonia synthesis from nitrogen and hydrogen gases at the pressure of 98.7atm

We can see that there are eleven curves with each curve starting at low conversion and rising with the temperature until the maximum point is reached, then drops with a further increase in temperature. We can also observe that all the curves converge outwards one curve, this curve represents the equilibrium curve as marked in Fig (39). Each curve represents the conversion of each catalyst bed with variation with the bed's temperature. We will assume that one catalyst bed is placed in one reactor. The optimal reactor architecture is the one that comprises a set of reactors that are operated at the maximum conversion point for each reactor, this would be represented by points A to K for ammonia synthesis.

We see that the feed at 470℃ (point X) is sent to the first reactor, marked in Fig (39), where the conversion increases to the maximum point (point A). The temperature and conversion at point A are 540℃ and 11.02% respectively. The product is then withdrawn from the adiabatic reactor and cooled along line AY until the temperature is 410℃, the reaction mix is then sent to reactor number two where the conversion is further raised to 22% at point B, the temperature at this point is 470℃. The reaction mixture is again withdrawn from the second reactor at this point and cooled along line BZ to the temperature of 350℃. The third reactor is then used to

further raise the conversion to 33.6 % at point C where the temperature is 410℃. The cascade of reactors is stopped at this point because using the fourth reactor will require working temperatures that are way outside the industrially used temperature range. The maximum point in reactor number four (point D) is 360℃ which is 90℃ lower than the minimum temperature of 450℃ employed industrially. Operating the reactor at this temperature might affect the catalyst and reaction rate, hence the fourth reactor will not be deployed.

5.1.2.2 Reactor design and modelling in Aspen Plus®

The conversions and corresponding process conditions obtained from Fig. (39) are used as the targets that should be met by the Aspen Plus® model. The model will further aim at determining the reactors' dimensions required to meet the set conversion, temperature, and pressure targets.

It was shown in Fig. (39) that a cascade of three adiabatic reactors with an interstage cooling system can achieve cumulative conversions of 11.02, 22, and 33.6% for each reactor. Three plug flow reactors with interstage coolers operated adiabatically are used to model the system in Aspen Plus®. The process flowsheet of reactors and heat exchangers loop is represented by Fig. (40). The feed (S-FEED) to this system comprising nitrogen and hydrogen at the operating pressure of 100 bar is sent to HX-R1 where the temperature is raised to 470℃ (inlet to the first reactor of Fig. (39)) before being sent to the first reactor, R-01. The reaction mixture is then withdrawn from the reactor when the temperature is approximately 540℃, the maximum temperature of R-01. The reaction mixture is then cooled to 410℃ in HX-R2 before being sent to reactor R-02 where conversion is further increased. The product of R-02 is at approximately 470℃ and gets cooled to 350℃ in HX-R3 before being sent to reactor R-03 where the reaction proceeds until the temperature is approximately 410℃. The pressure is assumed to be constant throughout the system.

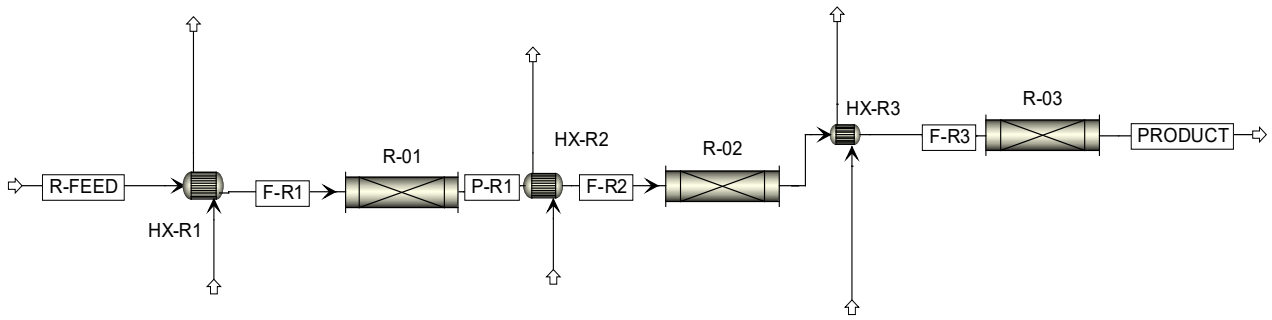

Figure 40: Ammonia synthesis reactors and heat exchangers loop.

The Aspen Plus® model results of the system are reported in Table 11, results include each reactors maximum temperature, the length and diameter of each reactor and the corresponding conversions of nitrogen gas.

Table 16: The single-pass (SP), cumulative (CUM) conversions for three reactors with the corresponding reactor dimensions and temperatures.

Reactor	T_{min} (°C)	T_{max} (°C)	D(m)	L(m)	X_{N_2}(SP)	X_{N_2}(CUM)
Reactor 1	470	549.5	0.10	3	10%	10%
Reactor 2	410	473.2	0.15	12	9%	18%
Reactor 3	350	409.3	0.50	7	9%	26%

We can see from Table.16 that the single-pass conversion in reactors 1, 2 and 3 are 10, 9 and 9 % respectively. This single-pass (SP) conversions correspond to the cumulative conversions of 10, 18 and 26% respectively for reactors 1, 2 and 3. The cumulative conversions of nitrogen for the theoretical calculations and the Aspen Plus® model are compared in Table.17.

Table 17: Comparisons in cumulative conversions obtained in theoretical calculations and Aspen plus® models.

	Cumulative conversion		
Model	R-01	R-02	R-03
Theoretical calculation	11%	22%	33%
Aspen Plus®	10%	18%	26%

We see that the theoretical conversion values are higher as compared to the values obtained from the Aspen model, the differences are, however, small and can be attributed to factors such as constant reaction rates assumed in the theoretical calculations.

5.1.3. Process energy requirements and thermodynamic performance.

The process is supplied with solar energy in the form of solar-PV electricity and solar-T heat at 200 ℃. The solar-PV electricity is used to run the pump, electric heater, electrolysis stack, compressors, and refrigeration units. Solar-T heat, on the other hand, is used to provide heat to the process which is then used to heat water to 200℃.

The process units that use electricity and their corresponding electrical loads are provided in Table 18.

Table 18: Electricity consumption of different process units.

Unit	Electrical load kW	Electricity share %
Comp-1	212.8	1.67%
Comp-2	120.9	0.95%
Comp-3	90.5	0.71%
Comp-4	223.3	1.75%
Comp-5	71.6	0.56%
Comp-6	48.8	0.38%
Comp-7	374.1	2.93%
Refrigeration-1	699.9	5.48%
Refrigeration-2	65.6	0.51%
Pump-01	2.3	0.02%
EL-HE	861.5	6.74%
Stack	10001.8	78.30%
Total	**12773**	**100%**

We see that the total electricity consumption of the process is 12,773kW with the electrolysis stack commanding the bigger share of 78.3% (10,000kW). The electric heater EL-01 comes second with an electrical load of 862kW which corresponds to 6.7%. The pump P-01 consumes the least electricity at 2.3kW (0.02%). The solar-T heat required to raise the temperature of saturated steam (stream 5) to 200℃ is found to be 780.7kW, the work carried by this heat is equal to 288.8kW.

The thermodynamic performance of the process reported as the overall system work efficiency is given in Table 19.

Table 19: Thermodynamic performance of the PT-NH_3 process

W_{PV} kW	Q_{ST} kW	W_{ST} kW	W_T kW	W_{comb} kW	η_w %
12773	780.7	288.8	13062	6758	51.7%

We see that the work obtainable when the produced ammonia (96.4 kmol/h) is combusted at 1200℃ is 6,758kW. The total solar-PV electricity and solar-T work supplied to the process were found to be 12,773 and 288.8kW respectively, making the total work provided to the process to be 13,062kW. The solar-PV area fraction is calculated as 98.1%, this value is 1.3% higher than the 96.8% target determined in Chapter 3 (section 3.3). The resulting overall system work efficiency, which is the ratio of work out-put to the work input, is calculated to be 51.7%.

This value is lower than the target value of 70% obtained in Chapter 3. The Aspen Plus® simulation includes seven compressors, two refrigeration units and an electric heater while the calculations in Chapter 3 did not have these units. Again, the analysis in Chapter 3 assumed a fully heat integrated process which means the total energy requirement were reduced. All these factors are attributable to the observed discrepancy in the overall system work efficiency.

The solar-PV (A_{PV}) and solar-T heat (A_{ST}) required areas were found to be 62,613 and 1,239m^2 respectively, resulting in the total area requirements of 63,852m^2. The total specific solar area requirements of 9.4m^2/kW. These specific solar area requirements are higher than the target of 6.9m^2/kW found in Chapter 3. Higher solar-PV electricity per kW of work from combusting ammonia directly results in a higher solar-PV area and in extension a total specific solar area requirement.

5.1.4. Cost analysis of PT-NH_3 process

The total cost of production for the PT-NH_3 process with a project lifetime of 15 years is discussed in this section. The total cost is given by Eq. (65) and it is used together with the production rate of methanol to estimate the specific cost according to Eq. (66).

Purchased equipment costs.

The purchased equipment cost of each process unit and the total capital cost are reported in Table 20. We see that the total equipment cost is USD 18,841,462 with the electrolysis stack commanding a biggest of 44% of the total cost. Compressors follow at the combined total cost of USD 6,172,500. Heat exchangers and reactors follow the compressors at the respective costs of USD 1,960,200 and USD 1,010,300. Pump P-01 registers the lowest cost share of 0.2% at the cost of USD 43,700.

Table 20: Purchased equipment cost of each process unit and the total equipment cost.

Equipment		Cost USD	cost share %
P-01	$	43,700.0	0.2%
HX-1	$	54,900.0	0.3%
HX-2	$	66,000.0	0.4%
HX-3	$	80,400.0	0.4%
HX-4	$	129,700.0	0.7%
HX-5	$	62,500.0	0.3%
HX-6	$	101,500.0	0.5%
HX-7	$	63,800.0	0.3%
HX-8	$	101,700.0	0.5%
HX-9	$	59,300.0	0.3%
HX-10	$	130,200.0	0.7%
HX-11	$	134,800.0	0.7%
HX-12	$	174,700.0	0.9%
HX-13	$	119,800.0	0.6%
HX-14	$	82,000.0	0.4%
HX-15	$	127,400.0	0.7%
HX-16	$	290,900.0	1.5%
HX-17	$	180,600.0	1.0%
EL-HE	$	75,382.6	0.4%
Electrolysis stack	$	8,294,979.8	44.0%
Comp-1	$	1,583,400.0	8.4%
Comp-2	$	811,900.0	4.3%
Comp-3	$	761,700.0	4.0%
Comp-4	$	1,434,200.0	7.6%
Comp-5	$	1,342,000.0	7.1%
Comp-6	$	128,600.0	0.7%
Comp-7	$	110,700.0	0.6%
R-01	$	126,900.0	0.7%
R-02	$	509,100.0	2.7%
R-03	$	374,300.0	2.0%
FSP-1	$	950,000.0	5.0%
FSP-2	$	136,400.0	0.7%
REF-1	$	117,800.0	0.6%
REF-2	$	80,200.0	0.4%
Total	**$**	**18,841,462.4**	**100%**

Operating costs and by-product sales.

Energy costs

The energy cost, solar-PV electricity and solar-T heat are reported in Table 21. The total electricity and solar-T heat consumed by the process are 459,832 and 28,106 MWh respectively for 15 years.

Table 21: Solar-PV electricity and solar-T heat cost for the project lifetime (n=15years)

Solar PV electricity costs USD	Solar T heat costs USD
$ 22,991,611	$ 955,596

The total energy cost (EC_T), which is the sum of solar-PV electricity and solar-T heat costs for the process is USD 23,947,207.

Utility and catalyst costs.

The utility costs are estimated by Aspen Plus® economic module, the process utilizes cooling water and refrigerant - Freon 12 to cool process streams. The heating of process streams is achieved by integrating cold streams with hot streams, hence there is no need for external heat. The costs of cooling water and the refrigerant are found to be 16.8 and 3.2 USD/h respectively, these costs translate to USD 606,446 and USD 115,382 for 15 years (36,000 h). The total utility cost (UC) is thus calculated to be USD 721,828.

The catalyst cost and the lifetime are adopted from (Zhang, Wang, Van Herle, et al., 2020) where they are reported to be 23 USD/kg and 14 years, respectively. The process requires 5.99 tones at the cost of USD 137,728.

Raw material costs and by-product revenue.

The process uses water and nitrogen gas as feedstocks to produce ammonia and oxygen as a by-product. Water and nitrogen are fed at 145.1 and 48.4 kmol/h respectively to produce ammonia and oxygen at the respective rates of 96.4 and 72.5 kmol/h. The total amounts of water and nitrogen are 94,109.2 and 48,779.4 tonnes respectively for 15 years. The total amounts of oxygen and ammonia produced are found to be 83,578.5 and 59,108.8 tonnes, respectively. (Zhang, Wang, van Herle, et al., 2020)give the costs of process water, nitrogen, and oxygen as 0.467, 50 and 177 USD/tonne, respectively. The total raw material cost and by-product sales can be calculated using the assumption that these values do not change throughout the project lifetime and that the selling price of oxygen is equal to its cost. The raw material cost and oxygen sales are thus found to be USD 2,482,920 and 14,793,394, respectively.

The operating cost for the project lifetime is calculated to be USD 28,083,182 making the total cost (operating cost + equipment cost) to be USD 46,924,645.

5.1.3.3. Levelized cost of ammonia

The Levelized cost of ammonia is calculated for two cases, the first case is when the produced oxygen is not sold with the second case considering the additional revenue stream from oxygen sale. The corresponding Levelized costs of ammonia production for case 1 and case 2 are found

to be 793.4 and 543.6 USD/tonne, respectively. The theoretical Levelized cost of ammonia production was found to be 344 USD/tonne, with oxygen sales not considered. This value is significantly lower than 793 USD/tonne mainly because the theoretical analysis considered only the energy and electrolysis cost. The purchased equipment costs of other processing units, including compressors, heat exchangers, compressors, increase the total cost per tonne of production. Furthermore, the operation of compressors and refrigeration processing units require electricity, which in turn increases the electricity consumption of the process resulting in higher energy cost per tonne.

5.2. Power-to-methanol process scheme, PT-CH_3OH

The power-to-methanol process scheme produces methanol from a feedstock of water and carbon dioxide. The process is divided into two sub-processes of electrolysis and synthesis sub-processes just like the power-to-ammonia process. Water is used to produce hydrogen in the electrolysis section which is then reacted with carbon dioxide downstream to produce methanol. The theoretical analysis of the process revealed that the process operates optimally when the solar-PV electricity is completed with solar-T at the optimal solar-PV area fraction of 99.2%. The performance targets in terms of the overall system work efficiency, solar area requirements and the Levelized Cost of production were found to be 71.2%, 6.9m^2/kW, and 330 USD/tonne (2,692 USD/kW).

The process modelling of this process will also be carried out on Aspen Plus® V10 to achieve performance that is as close to the performance targets as possible. The combination of solar-PV electricity and solar-T heat at the solar-PV area fraction of or close to 99.2% is targeted in the simulation. The methanol process occurs at high pressures (49.3atm), the property method used will therefore be the SRK equation of state. The electrolysis stack will be modelled the same way as in the case of PT-NH_3 and the plug flow adiabatic reactor will be used to model reactor/s.

5.2.1. Process description

The process is supplied with water and carbon dioxide at the ambient conditions with the respective flow rates of 145.1 and 48.4 kmol/h. Water flow rate is dictated by the basis of 10MW electricity supplied to the electrolyser to produce 145.1 kmol/h of hydrogen gas. The carbon dioxide flow rate is determined by the ratio of hydrogen to carbon dioxide of 3 required in the synthesis step.

The process flow diagram of the process is represented in Fig. (40), water is supplied through an H_2O-feed stream where it undergoes the same steps as in the case of PT-NH_3. The produced hydrogen gas is sent to compressors COMP-01,02 and 03 where the pressure is raised from 10atm (operating pressure of the electrolyser) to the operating pressure of methanol synthesis of 74atm.

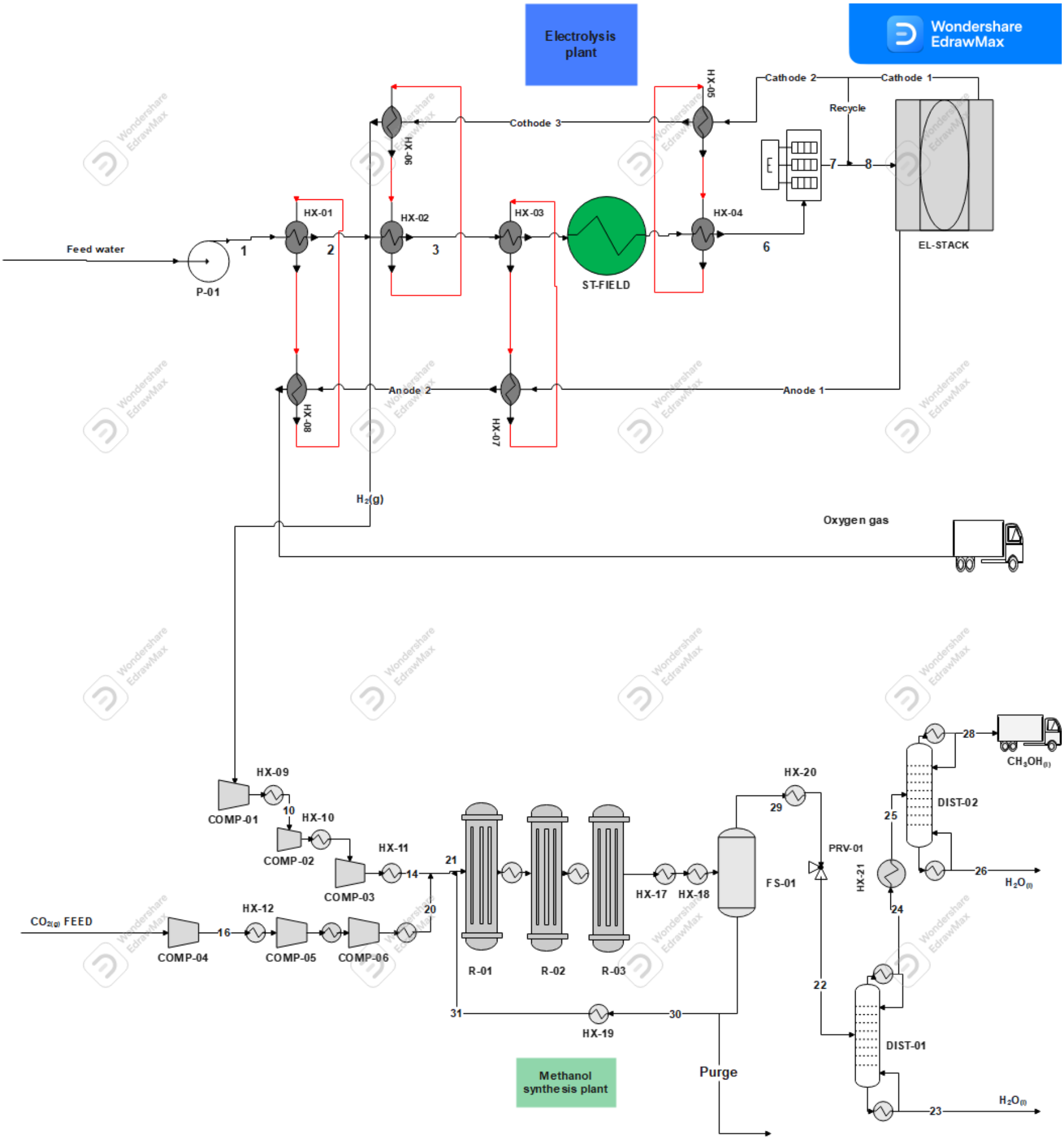

Figure 40: Process flow diagram of PT-CH_3OH

The carbon dioxide feed stream is also fed to a multi-stage compressor with interstage cooling where pressure is raised from 1 to 74atm (the operating pressure of the synthesis loop). Carbon dioxide and hydrogen at 200℃ and 74atm are mixed and sent to the synthesis loop where the stream (stream 20) is mixed with the recycle stream (stream 31) before being sent to a cascade of three adiabatic reactors with interstage coolers. The product of reactor 3 (R-03) is sent to two heat exchangers (HX-17 and 18) where the temperature is reduced and methanol together with water are liquefied before

being sent to a flash separator (FS-01). The gaseous stream comprising mostly the unreacted hydrogen and carbon dioxide as well traces of methanol and water vapour is recycled back to the reactors. The liquid stream from FS-01 is sent to HX-21 where the temperature is further reduced before being sent to two distillation columns operating at the atmospheric pressure. The first distillation column (DIST-01) achieves 90% wt of methanol with the second distillation column (DIST-02) achieving 99% wt of methanol liquid. The rad-frac column is used to model both distillation columns. The recycle stream is purged to remove formed carbon monoxide, the purge split fraction of 2% was selected. The production rate of methanol product was found to be 42.9kmol/h

5.2.2. Reactor design

Methanol synthesis occurs according to reaction represented by eq. (17), with reverse water-gas shift occurring in parallel. The synthesis step is industrially carried out at the temperature and pressure ranges of 200-300℃ and 49.3-80atm respectively (Portha *et al.*, 2017). Reaction kinetics for methanol reaction (eq. (18)) and reverse water gas shift reactions as represented by eq. (70) and eq. (71) respectively.

$$r_{CH_3OH} = \frac{1.07\times10^{-13}e^{\left(\frac{-4\,413.76}{T}\right)}p_{CO_2}p_{H_2} - 4.182\times10^{7}e^{\left(\frac{-2645.966}{T}\right)}\frac{p_{CH_3OH}p_{H_2O}}{p_{H_2}^{2}}}{\left[1+3453.38\left(p_{H_2O}p_{H_2}^{-1}\right)+1.578\times e^{\left(\frac{2068.44}{T}\right)}p_{H_2}^{0.5}+6.62\times10^{-16}e^{\left(\frac{14928.95}{T}\right)}p_{H_2O}\right]^{3}} \quad (70)$$

$$r_{RWGS} = \frac{1.22e^{\left(\frac{-11398.24}{T}\right)}p_{CO_2} - 1.1412e^{\left(\frac{-6624.98}{T}\right)}\frac{p_{CO}p_{H_2O}}{p_{H_2}^{1}}}{\left[1+3453.38\left(p_{H_2O}p_{H_2}^{-1}\right)+1.578\times e^{\left(\frac{2068.44}{T}\right)}p_{H_2}^{0.5}+6.62\times10^{-16}e^{\left(\frac{14928.95}{T}\right)}p_{H_2O}\right]^{1}} \quad (71)$$

The feed stream to the reactors synthesis loop is at 74atm and 200℃ with a ratio of hydrogen to carbon dioxide of 3. The reaction mixture is sent to R-01 where a single-pass conversion of 16.8% is achieved, the mixture is then withdrawn from the reactor and cooled to 250℃ before being sent to R-02 and R-03 where single-pass conversions of 6.0% and 5.0% are achieved. The cumulative conversion of 25.6% is achieved by this cascade of reactors.

5.2.3 Energy requirements and thermodynamic performance

Table.30 shows electrical load and the corresponding percentage share of the electricity for all the units that utilize electricity. We see that the electrolysis stack consumes the greatest share of electricity like in the case of the PT-NH_3 process. The electric heater EL-01 comes next as

the processing unit consuming the most electricity. Water feed pump P-01 consumes the least amount of electricity of 2.3kW.

Table 30: Electricity consumption of the process

Unit	Electrical load kW	Electricity share %
Comp-1	155.9	1.36%
Comp-2	116.4	1.01%
Comp-3	74.2	0.65%
Comp-4	176.6	1.54%
Comp-5	54.6	0.48%
Comp-6	30.0	0.26%
Pump-01	2.3	0.02%
EL-HE	861.5	7.51%
Stack	10001.8	87.17%
Total	**11473**	**100%**

The total amount of electricity that the process requires is 11,473kW, which is just slightly lower than the electricity requirement of the PT-NH_3 process pathway.

Table.31 shows the thermodynamic performance of the process, the process produces 44.4 kmol/h of methanol which produces 6,200kW of work when combusted at 1200℃. The solar-T heat of 780.7kW brings in work of 288.8kW by its temperature of 200℃.

Table 31: Thermodynamic performance of the process

W_{PV} kW	Q_{ST} kW	W_{ST} kW	W_T kW	W_{Comb} kW	η_W %
11473	780.7	288.8	11762	6200	52.7%

The sum of electrical work and the work brought in by the solar thermal heat is 11,762 kW which result in an overall system work efficiency of 52.7%. This value is higher than the value of 51.7% obtained for the PT-NH_3 process pathway. The optimal solar-PV area fraction for the process is 97.9%, this value is 1.3% lower than the target of 99.2% determined in the theoretical analysis.

The solar-PV and solar-T heat collection area requirements of 56,240 and 1,239m^2 respectively. The total solar collection area requirements and the corresponding specific area were found to be 57,479m^2 and 8.5m^2/kW. The specific area requirements of 8.5m^2/kW are higher than the targeted 6.9m^2/kW as expected. The reasons provided for PT-ammonia also

apply for the discrepancies observed in the reported simulation performance and the theoretical performance targets set in Chapter 3.

5.2.4 Purchased equipment costs.

Table.32 gives the purchased equipment cost of all the process units and their corresponding share of the total cost. We see that the electrolysis stack commands the biggest share of equipment costs followed by compressors like in the case of the PT-NH_3 process scheme. Pump P-01 records the lowest cost percentage share of 0.2% at the cost of USD 43,700.

Table 32: Purchased equipment cost for all process units.

Equipment		Cost USD	cost share %
P-01	$	43,700.00	0.2%
HX-1	$	66,000.00	0.4%
HX-2	$	80,300.00	0.4%
HX-3	$	121,000.00	0.7%
HX-4	$	134,900.00	0.8%
HX-5	$	62,500.00	0.3%
HX-6	$	101,500.00	0.6%
HX-8	$	101,700.00	0.6%
HX-9	$	47,800.00	0.3%
HX-10	$	49,100.00	0.3%
HX-11	$	69,500.00	0.4%
HX-12	$	47,100.00	0.3%
HX-13	$	47,700.00	0.3%
HX-14	$	69,000.00	0.4%
HX-15	$	66,400.00	0.4%
HX-16	$	65,700.00	0.4%
HX-17	$	70,500.00	0.4%
HX-18	$	89,300.00	0.5%
HX-19	$	88,600.00	0.5%
HX-20	$	60,700.00	0.3%
EL-HE	$	75,382.58	0.4%
Electrolys	$	8,294,979.79	46.2%
Comp-1	$	1,548,100.00	8.6%
Comp-2	$	1,161,075.00	6.5%
Comp-3	$	1,005,607.00	5.6%
Comp-4	$	1,275,400.00	7.1%
Comp-5	$	1,161,500.00	6.5%
Comp-6	$	990,750.00	5.5%
R-01	$	107,300.00	0.6%
R-02	$	119,200.00	0.7%
R-03	$	114,000.00	0.6%
DIST-1	$	265,700.00	1.5%
DIST-2	$	252,000.00	1.4%
FSP-1	$	113,200.00	0.6%
Total	**$**	**17,967,194.37**	**100%**

The total equipment cost of the process is found to be USD 17,967,194, this value is slightly lower than the value of USD 18,841,462.4 reported for the PT-NH_3 process.

5.2.4. Operating costs

Energy costs

The energy costs associated with the process are recorded in Table.32, we can see that the solar-PV electricity and solar-T heat costs are USD 20,651,839 and USD 955,596, respectively. The total energy costs, a sum of solar-PV electricity and solar-T heat cost, is found to be USD 21,607,435.27.

Table 32: The energy costs of the PT-CH_3OH process.

Solar PV electricity USD		Solar T heat USD	
$	20,651,838.98	$	955,596.30

Raw material cost and by-product sales.

The power-to-methanol process uses water and carbon dioxide as raw material, the cost of carbon dioxide is reported as 0.035 USD/kg by(Atsbha *et al.*, 2021). The process uses a total amount of 76,633.6tonnes of carbon dioxide for the project lifetime, this translates to a total cost of USD 2,682,174.62. The total cost of process water used is the same as in the case of PT-NH_3 at USD 43,949. The total cost of raw material is, therefore, USD 2,726,124. The amount of oxygen produced by the process is the same as in the previous case of PT-NH_3 with total revenue of USD 14,793,394.

Utility and catalyst costs

The process uses cooling water as the only external utility apart from the solar-PV electricity, the process streams heating is achieved by a heat integration between cold and hot streams. Aspen Plus® estimates the cooling cost rate of PT-CH_3OH at 10.1 USD/h which is equal to USD 364,366 for the project lifetime.

The methanol synthesis catalyst cost and the catalyst lifetime are reported to be 21.36 USD/kg and 4 years respectively (Zhang, Wang, Van Herle, *et al.*, 2019) The total catalyst mass and cost for the project lifetime were found to be 4.9tonnes and USD 104,264.

The operating cost and the total cost for the project lifetime are respectively USD 25,212,520.7 and USD 43,179,715.

Levelized cost of methanol

The total amount of methanol of 50,554.2tonnes is produced during the project lifetime at the total cost (C_{total}) of USD 43,179,715. This results in the Levelized Cost of 854.1 and 561.5 USD/tonne for cases when the oxygen by-product is not sold and when it is sold, respectively.

The value of 854.1 USD/tonne is greater than 330.2 USD/tonne (theoretical value), the theoretical analysis considers only the energy and electrolyzer costs and this causes a huge discrepancy between the Aspen plus® and theoretical results. The other processing units such as the heat exchangers, compressors, distillation columns are not considered in the theoretical analysis costing.

5.3. Power-to-methane (PT-CH_4) process modelling.

The power-to-methane process produces synthetic natural gas, a mixture of methane, carbon dioxide and hydrogen, from a feedstock of liquid water and carbon dioxide. The overall process is divided into two sub-processes of steam electrolysis and methanation. The electrolysis sub-process produces hydrogen and oxygen gases using solar-PV electricity. The methanation section produces methane gas from by hydrogenation of carbon dioxide.

The theoretical analysis revealed the process to operate at the lowest cost (optimally) when the process energy needs are met through solar-PV electricity alone. The optimal solar-PV area fraction was thus found to be 100%, with the performance targets of 71.9%, 6.82 m^2/kW (2.1 m^2/tonne) and 2,930 USD/kW (902 USD/kW). This section will simulate the PT-CH_4 with the input from the theoretical analysis results of using f_{op}=100% which represents an optimal work and heat flow arrangement.

The process is modelled in the Aspen Plus® simulator where the mass and energy balances, process units sizing, and costing are carried out. The method used is the SRK equation of state because the process pressure ranges from 10 to 98.7atm. The electrolysis stack and catalytical reactors are modelled as in the cases of ammonia and methanol.

5.3.1. Process description.

The plant-wide process flow diagram of the process is represented in Fig. (41), the process is supplied with liquid water and carbon dioxide at the respective flow rates of 145.1 and 36.3 kmol/h, respectively. Water goes through the electrolysis sub-process where it gets converted to hydrogen. Carbon dioxide gas at ambient conditions is sent to a compressor (COMP-01) where the pressure is raised to 10atm before being mixed with hydrogen gas to make a synthesis feed stream with an H_2/CO_2 ratio of 4.

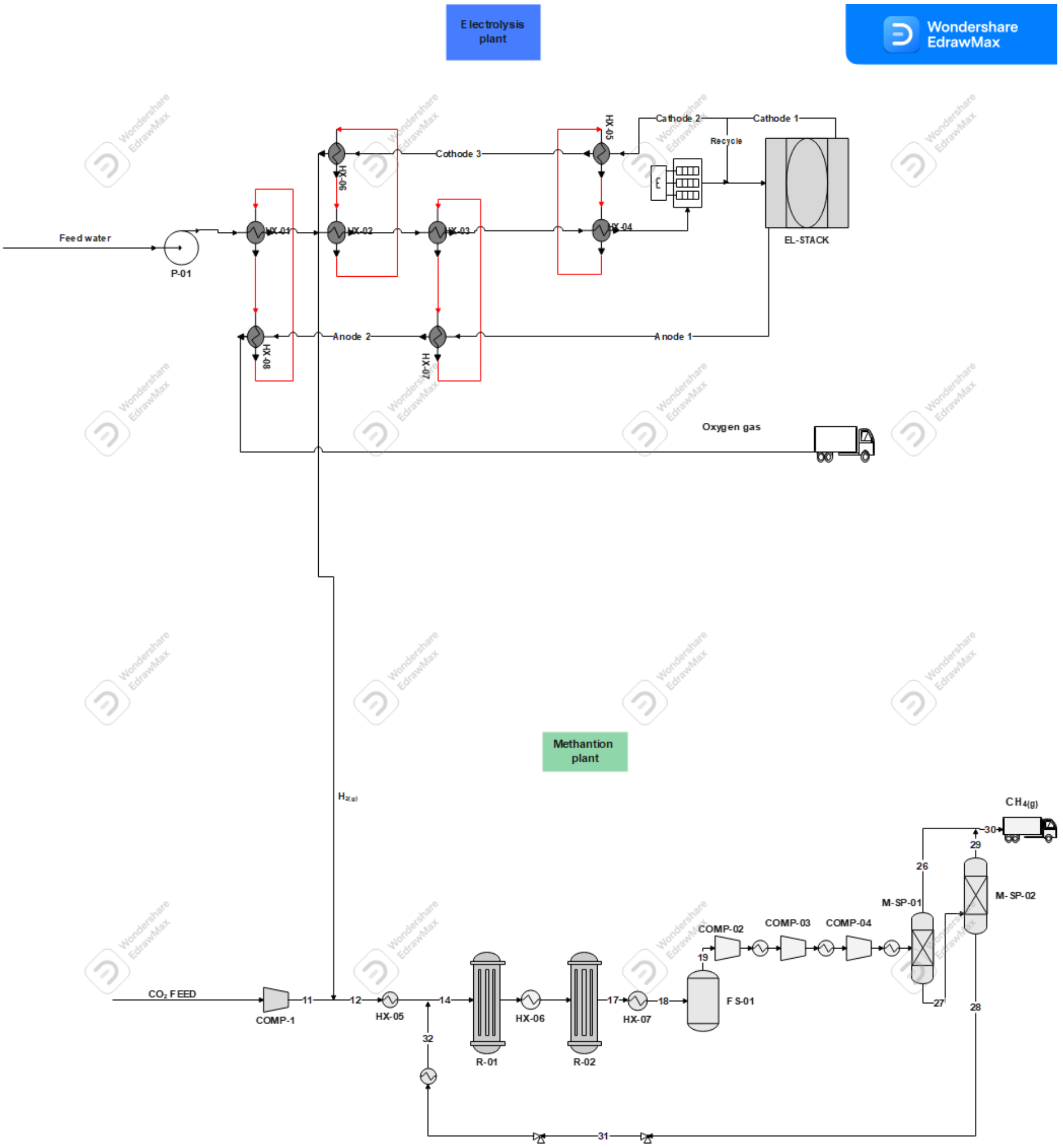

Figure 41: Plant-wide process flow diagram of PT-CH_4 process pathway

The mixed stream (stream 12) is sent to HX-05 where the temperature is raised to 250℃. The product of HX-05 is mixed with unconverted hydrogen and carbon dioxide (recycle stream 32) before being sent to reactors R-01 and R-02. The reactors operate adiabatically with an inter-stage cooling system. The product of R-02 is sent to HX-07 where it gets cooled to 50℃ before being sent into the flash separator (FS-01) where liquid water is separated from the crude synthetic natural gas. The crude natural gas is then sent to a multi-stage compression with an inter-cooling system where the pressure is raised to 98.7atm required by the membrane separation system. Heat exchanger HX-10 is used to reduce the temperature of the synthetic natural gas to 40℃ before being sent to a double-stage membrane system to achieve an 85% recovery of methane gas. The membrane separation configuration is the same as the one used by (Ahmad *et al.*, 2012). Synthetic natural gas leaves the first and second membranes as the permeate stream while the unreacted hydrogen and carbon dioxide are recycled back to the reaction loop. The process produces synthetic natural gas and oxygen at 36.2 and 72.6 kmol/h which translate to mass flow rates of 578.3 and 2,321.6 kg/h, respectively. The composition of the produced synthetic natural gas is provided in Table 33.

Table 33: Composition of synthetic natural gas

Compounds	Wt %
Methane	99.80%
Carbon dioxide	0.12%
Hydrogen	0.08%

We see that the synthetic natural gas produced is predominately methane at 99.8% with traces of carbon dioxide and hydrogen gases.

5.3.2. Reactor design.

Reactor design for methanation reactors was carried out in Aspen Plus® where plug flow reactors with an inter-stage cooling system were used. The methanation reaction is represented by the Sabatier reaction as follows.

$$CO_{2(g)} + 4H_{2(g)} \leftrightarrow CH_{4(g)} + 2H_2O_{(g)}$$

The reaction kinetics governing this reaction is adopted from (Falbo *et al.*, 2018)as represented by Eq. (72)

$$r_{CO_2} = \frac{k}{1+0.91p_{H_2O}}\left\{p_{CO_2}^{0.14}p_{H_2}^{0.56} - \frac{p_{CH_4}^{0.14}p_{H_2O}^{0.28}}{K_{eq}^{0.14}}\right\} \quad (72)$$

Where r_{co2}, k, p_i and K_{eq} represent the rate of reaction, kinetic constant, partial pressure of individual components and the equilibrium constant, respectively. The kinetic constant and equilibrium constant are represented by eq. (73) and (74) respectively.

$$k = k_O e^{\left(\frac{-E_A}{RT}\right)} \quad (73)$$

Where k_o (95.43mol/s/cat), E_A (75.3 kJ/mol), R (8.314) and T (K) represent the Arrhenius equation constant, activation energy, universal gas constant, and the temperature, respectively.

$$K_{eq}(T) = e^{\left[\left(\frac{1}{1.987}\right)\left(\frac{56000}{T^2}+\frac{34633}{T}-16.4\ln T+0.00557T+33.165\right)\right]} \quad (74)$$

The reaction kinetic represented by Eq. (72) is for the 0.5wt% Ru/Al2O3 catalyst system which is reported to impede the water-gas shift reaction that occurs in parallel to Sabatier reaction in nickel-based catalyst systems (Falbo *et al.*, 2018).

The feed to the first reactor (R-01) is at the temperature and pressure of 250℃ and 10atm, the reaction mixture is withdrawn from the reactor at 550℃ from R-01. The conversion of carbon dioxide from R-01 is found to be 27.4%. The product of R-01 is cooled to 250℃ before being sent to the R-02 where the conversion is raised to 97.8%. The two reactors with an inter-stage cooler achieve a cumulative conversion of 98.7%. The streams information of the process is reported in Table D3 of appendix D

5.3.3. Energy requirements and thermodynamic performance.

It was shown in chapter 3 that the power-to-methane process, unlike the power-to-methanol and power-to-ammonia, has the optimal solar-PV area fraction of 100%. The process, therefore, uses only solar-PV electricity as the source of energy, the process units and their corresponding electrical loads are provided in Table 34.

Table 34: Electrical consumption of different process units in the process

Process unit	**Electrical load kW**	**Electricity share %**
Comp-1	86.5	0.73%
Comp-2	64.3	0.54%
Comp-3	28.1	0.24%
Comp-4	18.0	0.15%
Pump-01	2.3	0.02%
EL-HE	1656.1	14.0%
Stack	10001.8	84.4%
Total	**11857**	**100%**

We see that the electrolysis stack has the highest contribution of 84.4% at 10MW as expected, an electric heater EL-HE follows at an electric load share of 14%. The electric load of EL-HE is higher than the ones reported for PT-NH_3 and PT-CH_3OH processes, this observation is due to the PT-NH_3 process not including solar-T heat which is responsible for reducing the electric heater load in previous cases. The pump consumes the least electricity at 2.3kW which translates to 0.02%. The PT-CH_4 process consumes 11,857kW in total. The overall system work efficiency of 54.3% was calculated for the process, this value is lower than the 71.9% theoretical target for the same reasons provided for power-to-ammonia and power-to-methanol processes.

The process is supplied with solar-PV electricity alone, the solar-PV area requirements and the corresponding specific area requirements were determined to be 58,123m^2 and 8.6m^2/kW

respectively. The specific solar area requirements are higher than 6.8m^2/kW obtained as the target. The expected higher simulations area requirements can be contributed to a higher electricity consumption per ton as compared to the electricity consumption in the theoretical analysis.

5.3.4. Purchased equipment costs.

The cost of each process equipment and the corresponding total equipment investment cost are shown in Table 34. We see that the electrolysis stack, as in the case of PT-CH_3OH and PT-NH_3, commands the biggest share of 57.2% at USD 8,294,980.

Table 34: Process equipment and the corresponding cost

Equipment		Cost USD	cost share %
P-01	$	43,800.00	0.3%
HX-1	$	54,900.00	0.4%
HX-2	$	66,000.00	0.5%
HX-3	$	80,300.00	0.6%
HX-4	$	129,700.00	0.9%
HX-5	$	101,500.00	0.7%
HX-6	$	49,900.00	0.3%
HX-7	$	62,500.00	0.4%
HX-8	$	101,700.00	0.7%
HX-9	$	63,900.00	0.4%
HX-10	$	88,100.00	0.6%
HX-11	$	74,400.00	0.5%
HX-12	$	46,400.00	0.3%
HX-13	$	46,500.00	0.3%
HX-14	$	68,400.00	0.5%
EL-HE	$	75,382.58	0.5%
Electrolysis stack	$	8,294,979.79	57.3%
Comp-1	$	1,000,800.00	6.9%
Comp-2	$	1,138,100.00	7.9%
Comp-3	$	1,000,606.00	6.9%
Comp-4	$	950,700.00	6.6%
R-01	$	223,440.00	1.5%
R-02	$	235,200.00	1.6%
MB-S	$	390,000.00	2.7%
F-S	$	90,700.00	0.6%
Total	**$**	**14,477,908.37**	**100%**

The compressors come second at the total cost of USD 4,090,206 with the heat exchangers sitting at the total cost of USD 1,034,200. The reactors and membrane costs are USD 458,640

and USD 390,000 respectively, with the pump being the least costly processing unit at USD 43,800. The total purchased equipment cost was found to be USD 14,477,908.

5.3.5. Operating costs.

Energy costs.

The process consumes 11,857 kW as shown in section 5.3.3., this corresponds to 426,853,667 kWh (426.9MWh) for 15 years (36,000 h). The corresponding total solar-PV electricity cost is found to be USD 21,342,683.

Raw material costs and by-product revenues.

Power-to-methane process scheme uses water and carbon dioxide at the respective rates of 2,614.14 and 1,596.53kg/h which translate to 94,109,157 and 57,475,250 tonnes for 15 years. The corresponding costs for processing water and carbon dioxide are found to be USD 43,949 and USD 1,724,258 respectively, with the total raw material cost of USD 1,768,207. The revenues from the sale of oxygen by-product are the same as in the cases of PT-NH_3 and PT-CH_3OH at USD 14,793,394.

Utility and catalyst costs.

The process uses cooling water as the only utility apart from the solar-PV electricity, the utility cost was found to be 10.8 USD/h which equates to USD 388,203.8 for the project lifetime. The catalysts cost was calculated by using the specific cost (17.4 USD/kg) and catalyst lifetime (4 years) for methanation provided by (Zhang, Wang, van herle, *et al.*, 2020). The total mass and cost of the catalyst are calculated to be 3.14tonnes and USD 54,522.

The total operating cost is found to be USD 22,947,168, which makes the total cost to be USD 37,425,077.

5.3.6. Levelized cost of methane production.

The process produces 578.3 kg/h of synthetic natural gas which translates to 20,819.7 tonnes for 15 years. The Levelized Cost of production when the by-product sales are not considered and when sales are considered is thus found to be 1,798 and 1,087 USD/tonne, respectively. The theoretical cost was determined to be 902 USD/tonne when the oxygen sales are not considered. This value is almost half the actual cost of 1,798 USD/tonne obtained when all the processing units costing, and operating costs are considered.

5.4. Comparisons between the selected process pathways

The solar-PV electricity requirements of PT-NH_3, PT-CH_3OH and PT-CH_4 were determined to be 12,773, 11,473, 11,857kW, respectively. The PT-NH_3 consumes more electricity than the other processes with PT-CH_3OH consuming the least amount of electricity. This is attributed to many compressors (7 compressors) in PT-NH_3 that is required to raise the process pressure to 98.7atm and the refrigeration unit required to liquefy ammonia. PT-CH_3OH process pathway uses 6 compressors to raise the process pressure to 74atm. The PT-CH_4 process employs 4 compressors, 1 of the compressors raises the pressure of feed to 10atm while there other 3 raise the pressure of the membranes separation system to 100atm. The reason why PT-CH_4 consumes more electricity than the PT-CH_3OH even though there are fewer compressors in the process is due to the higher electricity load of 1,656.1 kW for the electrical heater. The solar-T heat requirements of PT-NH_3 and PT-CH_3OH are the same at 780.7 kW while the PT-CH_4 does not require any solar-T heat.

The overall system work efficiency for the PT-NH_3, PT-CH_3OH and PT-CH_4 were found to be 51.7, 52.7 and 54.3% respectively. The methane process registers the highest work efficiency followed by the methanol process with the ammonia process being the least work efficient process. The theoretical overall work efficiencies at optimal solar-PV area fractions were found to be 70.1, 71.2 and 71.9% for PT-NH_3, PT-CH_3OH and PT-CH_4 respectively, the ammonia process has the lowest theoretical efficiency target which may explain why the simulation efficiency is the lowest. PT-CH_3OH and PT-CH_4 have the same efficiency targets, however, the former process uses more electricity to raise the process pressure. Higher electricity consumption increases the total work input to the process which decreases the overall work efficiency. The simulation results for the overall work process efficiencies are lower than the target(theoretical) efficiencies mainly due to the relaxed assumptions of fully heat integrated processes the product streams being at ambient conditions. Moreover, the Aspen Simulation included more processing units that do not operate at 100% efficiency, and this also contribute to the drop in work efficiency.

The solar-PV collection areas of 62,613, 56,240 and 58,123m^2 were recorded for the PT-NH_3, PT-CH_3OH and PT-CH_4 process schemes. The solar-T heat collection area for both PT-NH_3 and PT-CH_3OH was found to be 1,239m^2 resulting in the total solar collection areas of 63,852 and 57,497m^2 for PT-NH_3 and PT-CH_3OH. The ammonia process recorded the lowest theoretical solar area of 1,734m^2 compared to 3,447 and 4,364 m^2 for PT-CH_3OH and PT-CH_4.

The reason why simulation results show higher solar area requirements for the ammonia process can be ascribed to the higher solar-PV area fraction of 98.6% as compared to the target of 96%. The optimal solar-PV area fraction for the PT-CH_3OH found in the simulation study is 97.7% which is closer to the target of 98.4%.

The electricity costs for processes were found to be USD 22,991,611, 19,101,112 and 19,101,112 for the PT-NH_3, PT-CH_3OH and PT-CH_4 processes, respectively. The solar-T heat costs for PT-NH3 and PT-CH3OH were found to be USD 955,596 for each process. The total costs for the process pathways were found USD 46,924,645, USD 43,179,715, and USD 37,425,077 for respective processes. The corresponding Levelized costs of production of 544, 562 and 1,087 USD/tonne were determined for the respective processes. The PT-NH_3 produces the least costly product followed the PT-CH_3OH process pathway. The PT-CH_4 process pathway produces the costliest product albeit the process registered the lowest total cost. The reason for the lowest cost is ascribed to the lowest mass flow rate of 578.3 kg/h compared to 1,641.9 and 1,404.3 kg/h registered for PT-NH_3 and PT-CH_3OH, respectively.

Chapter 6

Conclusion

The work studied the application of the combined solar-PV electricity and solar-T heat in different power-to-chemicals process schemes. The primary aim was to establish if there will be any benefit of using the combined system instead of just solar-PV as it is done in most power-to-chemicals studies. The study aimed at answering the following specific questions.

- Does using the solar-T heat to supplement solar-PV electricity improve the process energy efficiency?
- What are the economic and environmental benefits of using the combined solar-PV electricity and solar-T heat in the power-to-chemicals processes?

Background

To thoroughly address the posed questions, the study looked at the comprehensive literature review in chapter 1 to establish the gaps and the work that has been done by other researchers. The methodology and theoretical development were addressed in chapter 2. Process synthesis tool of the graphical G-H analysis was used to analyze the hypothetical processes that use electricity and heat as sources of energy. The methodology included defining the thermodynamic performance metrics as well as the procedure to calculate the process costs.

Chapter 3 looked at the case studies for power-to-hydrogen, power-to-methane, and power-to-ammonia process schemes. The chapter determined the theoretical targets in the form of thermodynamic performance as well as the energy and selected equipment costs. All the considered power-to-chemicals process pathways were then compared in terms of the thermodynamic performance and cost at the theoretical level.

Chapters 4 and 5 looked at the Aspen plus® simulations where some of the assumptions made in the theoretical analysis in chapter 3 were relaxed. Chapter 4 studied the power-to-hydrogen process pathway where the production rate of 1 mol/s of hydrogen gas was considered, the results of the process thermodynamic performance and the basic costs were determined and compared to the theoretical targets. Chapter 5 looked at the Aspen plus simulation of power-to-ammonia, and power-to-methane (synthetic natural gas) where the basis of 10MW electricity consumption by the electrolysis stack was used as the basis. The thermodynamic performance and specific cost of products (ammonia, methanol, and methane) were determined and compared.

The theoretical analysis in chapter 2 looked at the work and energy deficient hypothetical processes that belong to regions 1A and 1B of the G-H diagram. The reason for this choice is that the candidate power-to-chemicals processes belong to those regions. The theoretical analysis was divided into three scenarios, where the hypothetical process was supplied by electricity alone, heat alone and the combination thereof.

Thermodynamic and graphical analysis using gh-diagrams

The graphical analysis looked at three types of processes depending on the direction and magnitude of their heat and work requirements as well as the form of energy used to meet these requirements. The analysis revealed that when electrical energy (work) alone is used to meet the process requirements, the following scenarios can be identified:

- Processes with $\Delta H_P > \Delta G_P$ (region 1A processes) will always result in work over-supply since $\Delta H = \Delta G$ for electricity. This will result in work potential losses.
- Processes with $\Delta H_P < \Delta G_P$ will require the electricity to be supplied by more than the process enthalpy, therefore the excess electrical energy will be removed from the process in the form of waste heat The excess work can be quantified by $W_{excess} = \Delta H_P - \Delta G_P$.

Therefore, using electricity alone to meet the energy demand of the processes will always result in the loss of energy and work potential and thus in loss of efficiency.

The analysis also showed that when heat alone supplies the process energy needs, the process can only be efficient when the heat is supplied at the process Carnot temperature. The Carnot temperatures for all power-to-chemicals process candidates have high Carnot temperatures that are in fact way higher than the temperatures that solar-T heat can be produced. The results simply imply that the solar-T heat alone cannot be used to supply process energy needs of power-to-chemicals candidate processes.

Lastly, the analysis revealed that it is possible to prevent electricity (work) losses when the candidate processes are supplied with electricity and heat at a certain temperature. It was revealed that the electricity and heat must be supplied at a certain proportion for each temperature at which heat is supplied. The results showed that electricity must be supplied at a rate lesser than process work requirements (ΔG_P) and be supplemented by heat at the appropriate temperature for processes for which $\Delta H_P > \Delta G_P$. The alternative is to supply electrical work at a rate equal to the process work requirement and supplement it with heat at

the ambient temperature. In general, heat needs to be supplied at the appropriate temperature such that the combination of electricity and heat meets both the process minimum energy requirements (energy balance) and the minimum work potential requirement indicated by ΔG_P. The temperature at which heat is provided to the process should be such that the sum of electrical work and the work brought in by heat by the virtue of its temperature is equal to the process work potential (work balance). The analysis of the three scenarios thus led to the conclusion that process energy efficiency is the highest when the process is supplied with a combination of heat and electricity.

The gh-graphical analysis was extended to the cases where electricity and heat are supplied by solar-PV and solar-T. It was shown in the previous analysis that heat and electricity must be supplied at a unique proportion for a given amount of electricity and the temperature at which heat is provided. This unique proportion in the context of solar-PV electricity and solar-T heat is described by the fraction of the total collection area occupied by solar-PV electricity (f). This fraction is 100% for cases when the process is supplied with electricity alone and 50% when half of the total solar collection area is occupied by solar-T collectors.

Case studies

The theoretical analysis conducted in chapter 3 considered two case studies notably power-to-hydrogen and power-to-methane. The black box approach was adopted where the streams into and out of the processes were assumed to be at the ambient temperature and pressure with complete heat integration within the system boundaries. The analysis considered a project lifetime of 15 years with 36,000 operational hours. The basis of comparison on the different processes was set to be 640kW of work output when the chemicals in consideration are combusted at the temperature of 1200℃. Furthermore, the analysis included the entropy balance across the system boundaries to determine the extent of irreversibility on each process pathway. The reason to include the concept of irreversibility, represented by the T_oS_{gen} term, is because irreversible processes have the highest thermodynamic inefficiency and at the same time require the smallest equipment surface areas which in turn affect process economics.

The power-to-hydrogen case study revealed that the term T_oS_{gen} increases with the increase in solar-PV area fraction, with the highest value recorded at f=100%. These results imply that the process is mostly irreversible when the solar PV alone is used to provide the process with energy. The minimum solar-PV area fraction was determined to be 89.3% (f_{min}=89.3%), the minimum solar-PV area fraction represents a point where the work and energy supplied to the

process exactly match the process work and energy requirements. The process is thermodynamically reversible at this point and all the energy supplied to the process is stored.

The working storage and overall system work efficiencies were found to be 100 and 80% at the minimum solar-PV area fraction and 83 and 67.5% at f=100%. The electrolyser active area was found to be 0.11 and 0.018 m^2/kW respectively at f=89.3 and 100%. The corresponding electrolysis equipment costs were calculated to be 362.7 and 58.7 USD/kW for f_{min} and f=100 % respectively. This shows that while the efficiencies are the highest at the f_{min}, the cost of electrolysis equipment is also the highest at this solar-PV area fraction.

The total energy costs, sum solar-PV electricity and solar-T heat, were found to be 1,928 USD/tonne (2,592.7 USD/kW) and 2,142 USD/tonne (2,880.6 USD/kW) for f_{min} and f=100% respectively. The results revealed that the total energy cost increases with an increase in the solar-PV area fraction while the equipment costs decrease with an increasing solar-PV area fraction.

This trade-off implies that there is a point between f_{min} and f=100% where the total cost, the sum of energy and equipment cost, is minimum. Such a point is the optimum point with the optimal solar-PV area fraction (f_{op}). The f_{op} for the power-to-hydrogen process was found to be 93 %. The total cost at this point is found to be 2,098 USD/tonne (2,679.9 USD/kW) which is indeed lesser than the total costs of 2,198 and 2,186 USD/tonne at f_{min} and f=100%. The cost saving of 4.02% is realized when operating the process at f_{op} than when operating at f=100%.

The work storage and overall system work efficiencies at the optimal point were found to be 94 and 77% respectively. This translates to efficiency gains of 11.2 and 9.1% for work storage and overall system work efficiencies respectively. The total solar surface area requirements for f_{op} and f=100% were found to be 6.34 and 7.26 m^2/kW respectively, which translates to an area savings of 12.7%.

The results for power-to-hydrogen answered the questions of the study of whether using the combined solar-PV electricity and solar-T heat have energy efficiency, cost, and environmental benefits. The energy efficiency is higher, the total cost and the total solar collection area are lower for the combined system compared to the solar-PV system alone. The environmental benefits are realized in collection area savings for the combined system at the optimal solar-PV surface area. This observation was made for power-to-syngas, power-to-methanol, power-to-ethylene, power-to-ethanol, and power-to-DME.

Power-to-methane and power-to-ethane process pathways revealed a different trend when it comes to the total cost of the process. This category (category B) of power-to-chemicals processes showed the optimal solar-PV area fraction to be f=100 %. In answering the questions posed by the study, it can be concluded that using the combined solar-PV electricity and solar-T heat have efficiency, cost, and environmental benefits for certain processes, notably category A processes. There are, however, no benefits realized for processes belonging to category B.

Power-to-ethanol, power-to-methanol, power-to-DME and power-to-ethylene record the highest work storage efficiencies of 98.6, 98.3, 98 and 95% respectively, with power-to-methane registering the lowest work storage efficiency of 92%. Power-to-syngas, power-to-ethane and power-to-hydrogen show the highest overall system work efficiencies of 81, 80 and 76.6% respectively. The power-to-methane process recorded the lowest overall system work efficiency of 72%. The costliest process scheme in terms of electrolysis cost and total energy cost is power-to-ammonia at 3,008.9 USD/kW followed by power-to-methane at 2,930.3 USD/kW. The cheapest processes are power-to-ethane and power-to-syngas at 2,630.6 and 2,664 USD/kW respectively. The power-to-syngas and power-to-methane require the lowest solar collection area of 6.00 and 6.13 m^2/kW. The highest solar collection areas are recorded for power-to-ammonia, power-to-ethanol, and power-to-methanol at 6.96, 6.89 and 6.87 m^2/kW, respectively.

Power-to-hydrogen, power-to-ammonia, and power-to-syngas recorded the highest work storage efficiency gains of 11.8, 11.3 and 11.2% respectively when the process is operated at f_{op} instead of f=100%. The lowest work storage efficiency gains are reported for the power-to-methanol and power-to-ethanol processes at 1.6 and 2.9%. Power-to-hydrogen, power-to-ammonia and power-to-syngas record the highest overall work storage efficiencies of 11.8,11.3 and 9.4% respectively. The lowest overall system work efficiency is observed for power-to-methanol at 1.1%.

The highest cost savings are realized for category B processes, power-to-methane, and power-to-ethane at the savings of 95 and 8.4% when the process is operated at f=100%. These results simply mean that it will not be a good idea to combine electricity and heat to power category B processes. Power-to-ammonia, power-to-hydrogen and power-to-syngas recorded the cost savings of 4.4, 4.0 and 3.9%, respectively when the processes are operated at f_{op} instead of f=100%. Power-to-methanol and power-to-ethanol register the respective lowest cost savings of 0.1 and 0.4%. The power-to-hydrogen process shows the highest area savings of 12.7%,

followed by power-to-syngas and power-to-ammonia at the solar area savings of 12.4 and 12.1 % respectively. The power-to-methanol and power-to-ethanol registered the lowest solar collection area savings of 1.7 and 3.1% respectively.

Aspen Plus® simulation of the PT-H_2 process

The assumptions of complete heat integration and products being at ambient conditions made on the theoretical analysis (Chapter 3) were relaxed for the power-to-hydrogen process pathway in chapter 4, and the process was modelled in Aspen Plus®. Two process flowsheets were developed where the first case looked at a solar-PV only system with the second flowsheet on the combined system. The aim was to establish how far the theoretical targets could be reached when the process is modelled in Aspen Plus®.

The optimal solar-PV area fraction of 96.3% was found, which is different from 93% obtained on the theoretical analysis. The total solar collection area and total cost (energy cost + electrolysis stack purchased cost) were found to be 5.06 m^2/tonne and 3,694 USD/tonne. The Levelized cost of hydrogen decreased to 2,289 USD/tonne when oxygen sales revenue stream is accounted for. The values for f=100 % were found to be 5.47 m^2/tonne and 3,768 USD/tonne, the Levelized cost of hydrogen of 2,363 USD/tonne was obtained when considering oxygen sales. This confirms the theoretical analysis findings that the combined solar-PV electricity and solar-T heat at 200℃ system requires a lesser solar collection area with the lower Levelized cost of hydrogen as compared to the f=100% process. The overall system work efficiency was found to be 71.7 and 67% for the combined and solar-PV only systems, respectively. This translates to the efficiency gain of 2.9% when using the combined system at f_{op}.

The solar area and cost savings of 7.5 and 2.0% are realized for f_{op}=96.3%, these values are notably lower than the targets of 12.7 and 4.0%. The overall system work efficiencies of 71.7and 67% are also lower than the theoretical targets of 78 and 67.5% for f_{op} and f=100 %. These differences are ascribed to the fact that the heat is not fully integrated in the Aspen model, and that the products are not at 25℃ like they were assumed to be in the theoretical analysis. Chapter 4 concludes that there are solar energy collection area savings, work efficiency gains and cost savings when supplying the power-to-hydrogen process with the combined solar-PV electricity and solar-T heat.

Ammonia, methanol, and methane process simulations in Aspen Plus®

The process modelling and costing in chapter 5 for power-to-ammonia, power-to-methanol and power-to-methane considered total costs of production that included all process units and all operating expenses. The results revealed the cost of production of ammonia, methanol, and methane (synthetic natural gas) to be 544, 562 and 1,087 USD/tonne, respectively. The overall system work efficiencies for these respective processes are found to be 51.7, 52.7 and 57%. The power-to-methanol process appears to be the cheapest option of the selected processes with the second-highest work efficiency. The power-to-methane process pathway is the most expensive notwithstanding the highest overall system work efficiency.

References

Ahmad, F. *et al.* (2012) "Process simulation and optimal design of membrane separation system for CO 2 capture from natural gas," *Computers and Chemical Engineering*, 36(1), pp. 119–128. doi:10.1016/j.compchemeng.2011.08.002.

Ahmad, L. *et al.* (2020) "Recent advances and applications of solar photovoltaics and thermal technologies," *Energy*, 207, p. 118254. doi:10.1016/j.energy.2020.118254.

Aldersey-Williams, J. and Rubert, T. (2019) "Levelised cost of energy – A theoretical justification and critical assessment," *Energy Policy*, 124(February 2018), pp. 169–179. doi:10.1016/j.enpol.2018.10.004.

Allen, S.R., Hammond, G.P. and McKenna, R.C. (2017) “The thermodynamic implications of electricity end-use for heat and power,” *Proceedings of the Institution of Mechanical Engineers, Part A: Journal of Power and Energy*, 231(6), pp. 508–525. doi:10.1177/0957650917693483.

Ancona, M.A. *et al.* (2019) “Thermal integration of a high-temperature co-electrolyzer and experimental methanator for Power-to-Gas energy storage system,” *Energy Conversion and Management*, 186, pp. 140–155. doi:10.1016/j.enconman.2019.02.057.

Andika, R. *et al.* (2018) “Co-electrolysis for power-to-methanol applications,” *Renewable and Sustainable Energy Reviews*, 95(December 2017), pp. 227–241. doi:10.1016/j.rser.2018.07.030.

Atsbha, T.A. *et al.* (2021) “Techno-economic and environmental analysis for direct catalytic conversion of co2 to methanol and liquid/high-calorie-sng fuels,” *Catalysts*, 11(6). doi:10.3390/catal11060687.

Balan, O.M., Buga, M.R. and Bildea, C.S. (2016) “Conceptual design, performance and economic evaluation of carbon dioxide methanation plant,” *Revista de Chimie*, 67(11), pp. 2237–2242.

Beaudin, M. *et al.* (2010) “Energy for Sustainable Development Energy storage for mitigating the variability of renewable electricity sources : An updated review,” *Energy for Sustainable Development*, 14(4), pp. 302–314. doi:10.1016/j.esd.2010.09.007.

Becker, W. L. *et al.* (2012) “Production of Fischer-Tropsch liquid fuels from high-temperature solid oxide co-electrolysis units,” *Energy*, 47(1), pp. 99–115. doi:10.1016/j.energy.2012.08.047.

Bellos, E. *et al.* (2016) “Design, simulation and optimization of a compound parabolic collector,” *Sustainable Energy Technologies and Assessments*, 16, pp. 53–63. doi:10.1016/j.seta.2016.04.005.

Bhusal, Y. *et al.* (2020) “Technical and economic analysis of a novel low-cost concentrated medium-temperature solar collector,” *Renewable Energy*, 146, pp. 968–985. doi:10.1016/j.renene.2019.07.032.

Bird, L. *et al.* (2016) “Wind and solar energy curtailment: A review of international experience,” *Renewable and Sustainable Energy Reviews*, 65, pp. 577–586. doi:10.1016/j.rser.2016.06.082.

Bos, M.J., Kersten, S.R.A. and Brilman, D.W.F. (2020) “Wind power to methanol : Renewable methanol production using electricity, electrolysis of water and CO 2 air capture,” *Applied Energy*, 264(February), p. 114672. doi:10.1016/j.apenergy.2020.114672.

Botta, G. *et al.* (2015) “Thermodynamic analysis of coupling a SOEC in co-electrolysis mode with the dimethyl ether synthesis,” *Fuel Cells*, 15(5), pp. 669–681. doi:10.1002/fuce.201500016.

Carmo, M. and Fritz, D.L. (2013) “A comprehensive review on PEM water electrolysis,” 8(1). doi:10.1016/j.ijhydene.2013.01.151.

Cinti, G. *et al.* (2017) “Coupling Solid Oxide Electrolyser (SOE) and ammonia production plant,” *Applied Energy*, 192, pp. 466–476. doi:10.1016/j.apenergy.2016.09.026.

Denholm, P. and Margolis, R.M. (2008) “Land-use requirements and the per-capita solar footprint for photovoltaic generation in the United States,” *Energy Policy*, 36(9), pp. 3531–3543. doi:10.1016/j.enpol.2008.05.035.

Dean, John A. (1979).”Lange’s Handbook of Chemistry, 12th ed.; Mcraw-Hill: New York,pp9-94

Er-rbib, H., Kezibri, N. and Bouallou, C. (2018) “Performance assessment of a power-to-gas process based on reversible solid oxide cell,” *Frontiers of Chemical Science and Engineering*, 12(4), pp. 697–707. doi:10.1007/s11705-018-1774-z.

Falbo, L. *et al.* (2018) “Kinetics of CO2 methanation on a Ru-based catalyst at process conditions relevant for Power-to-Gas applications,” *Applied Catalysis B: Environmental*, 225, pp. 354–363. doi:10.1016/j.apcatb.2017.11.066.

Ferry, J. *et al.* (2020) “Solar thermal wastewater evaporation for brine management and low-pressure steam using the XCPC,” *Applied Energy*, 265(March), p. 114746. doi:10.1016/j.apenergy.2020.114746.

Fox, J.A. (2017) “Process Flow-Sheet Synthesis : Systems-Level Design applied to Synthetic Crude Production,” pp. 1–55. doi:10.1002/aic.

Ghaib, K. (2018) “Power-to-Methane : A state-of-the-art review,” 81(August 2017), pp. 433–446. doi:10.1016/j.rser.2017.08.004.

Giap, V.T., Kang, S. and Ahn, K.Y. (2019) “HIGH-EFFICIENT reversible solid oxide fuel cell coupled with waste steam for the distributed electrical energy storage system,” *Renewable Energy*, 144, pp. 129–138. doi:10.1016/j.renene.2018.10.112.

Giddey, S. *et al.* (2017) “Ammonia as a Renewable Energy Transportation Media,” *ACS Sustainable Chemistry and Engineering*, 5(11), pp. 10231–10239. doi:10.1021/acssuschemeng.7b02219.

Giglio, E. *et al.* (2015) “Synthetic natural gas via integrated high-temperature electrolysis and methanation: Part I-Energy performance,” *Journal of Energy Storage*, 1(1), pp. 22–37. doi:10.1016/j.est.2015.04.002.

Giglio, E. *et al.* (2015) “Synthetic natural gas via integrated high-temperature electrolysis and methanation: Part I-Energy performance,” *Journal of Energy Storage*, 1(1), pp. 22–37. doi:10.1016/j.est.2015.04.002.

Gilles CABOCHE, M. and Olivier LOTTIN, M. (2012) *Spécialité : Ingénierie-Matériaux Mécanique Énergétique Environnement Procédés Production Modélisation et Validation Expérimentale de la Co-Électrolyse de la Vapeur d’Eau et du Dioxyde de Carbone à Haute Température Mme. Sandra CAPELA*.

González Rodríguez, D. *et al.* (2019) “Hydrogen production methods efficiency coupled to an advanced high-temperature accelerator-driven system,” *International Journal of Hydrogen Energy*, 44(3), pp. 1392–1408. doi:10.1016/j.ijhydene.2018.11.083.

Gorjian, S. *et al.* (2020) “A review on recent advancements in performance enhancement techniques for low-temperature solar collectors,” *Energy Conversion and Management*, 222(May), p. 113246. doi:10.1016/j.enconman.2020.113246.

Gruber, M. *et al.* (2018) “Power-to-Gas through thermal integration of high-temperature steam electrolysis and carbon dioxide methanation - Experimental results,” *Fuel Processing Technology*, 181(September), pp. 61–74. doi:10.1016/j.fuproc.2018.09.003.

Gul, M., Kotak, Y. and Muneer, T. (2016) *Review on the recent trend of solar photovoltaic technology*, *Energy Exploration and Exploitation*. doi:10.1177/0144598716650552.

Hachicha, A.A. *et al.* (2019) “A review study on the modelling of high-temperature solar thermal collector systems,” *Renewable and Sustainable Energy Reviews*, 112(January), pp. 280–298. doi:10.1016/j.rser.2019.05.056.

Harp, G. *et al.* (2016) “Application of Power to Methanol Technology to Integrated Steelworks for Profitability, Conversion Efficiency, and CO 2 Reduction. Contact : The Power to Methanol (PtMeOH) Concept CRI ’ s Production of Methanol,” *METEC & 2nd ESTAD, Düsseldorf, Germany*, (June), pp. 15–19.

Harvego, E.A. *et al.* (2009) “Parametric evaluation of large-scale high-temperature electrolysis hydrogen production using different advanced nuclear reactor heat sources,” 239, pp. 1571–1580. doi:10.1016/j.nucengdes.2009.03.003.

Hasan, A. and Dincer, I. (2019) “Development of an integrated wind and PV system for ammonia and power production for a sustainable community,” *Journal of Cleaner Production*, 231, pp. 1515–1525. doi:10.1016/j.jclepro.2019.05.110.

Hassanzadeh, A., Jiang, L. and Winston, R. (2018) “Coupled optical-thermal modelling, design and experimental testing of a novel medium-temperature solar thermal collector with pentagon absorber,” *Solar Energy*, 173(April), pp. 1248–1261. doi:10.1016/j.solener.2018.08.022.

Hernandez, R.R. *et al.* (2015) “Solar energy development impacts on land cover change and protected areas,” *Proceedings of the National Academy of Sciences of the United States of America*, 112(44), pp. 13579–13584. doi:10.1073/pnas.1517656112.

Hernandez, R.R., Hoffacker, M.K. and Field, C.B. (2014) “Land-use efficiency of big solar,” *Environmental Science and Technology*, 48(2), pp. 1315–1323. doi:10.1021/es4043726.

Hudedmani, M.G., Soppimath, V. and Jambotkar, C. (2017) “A Study of Materials for Solar PV Technology and Challenges Scholars Research Library,” *Scholars Research Library*, 5(1), pp. 1–13.

Idoko, L., Anaya-Lara, O. and McDonald, A. (2018) “Enhancing PV modules efficiency and power output using a multi-concept cooling technique,” *Energy Reports*, 4, pp. 357–369. doi:10.1016/j.egyr.2018.05.004.

IRENA, T. (2020), Green Hydrogen Cost Reduction: Scaling up electrolyzers to meet the 1.5°C climate goal, Internation Renewable Energy Agency. Available at: www.irena.org/publications.

IRENA(2020), Renewable Power Generation Cost in 2019, Internationa Renewable Energy Agency, Abu Dabhi.

Jiang, L., Widyolar, B. and Winston, R. (2015) "Characterization of Novel Mid-temperature CPC Solar Thermal Collectors," *Energy Procedia*, 70, pp. 65–70. doi:10.1016/j.egypro.2015.02.098.

Jürgensen, L. *et al.* (2014) "Utilization of surplus electricity from wind power for dynamic biogas upgrading: Northern Germany case study," *Biomass and Bioenergy*, 66, pp. 126–132. doi:10.1016/j.biombioe.2014.02.032.

Kartohardjono, S., Adji, B.S. and Muharam, Y. (2020) "CO2 Utilization Process Simulation for Enhancing Production of Dimethyl Ether (DME)," *International Journal of Chemical Engineering*, 2020, pp. 16–19. doi:10.1155/2020/9716417.

Kourkoumpas, D.S. *et al.* (2016) "Implementation of the Power to Methanol concept by using CO2 from lignite power plants: Techno-economic investigation," *International Journal of Hydrogen Energy*, 41(38), pp. 16674–16687. doi:10.1016/j.ijhydene.2016.07.100.

Kumar, S.S. and Himabindu, V. (2019) "Materials Science for Energy Technologies Hydrogen production by PEM water electrolysis – A review," *Materials Science for Energy Technologies*, 2(3), pp. 442–454. doi:10.1016/j.mset.2019.03.002.

Laguna-Bercero, M.A. (2012) "Recent advances in high-temperature electrolysis using solid oxide fuel cells: A review," *Journal of Power Sources*, 203, pp. 4–16. doi:10.1016/j.jpowsour.2011.12.019.

Lefebvre, J. *et al.* (2015) "Renewable Power-to-Gas : A technological and economic review." doi:10.1016/j.renene.2015.07.066.

Lefebvre, J. *et al.* (2016) "Renewable Power-to-Gas : A technological and economic review," 85. doi:10.1016/j.renene.2015.07.066.

Leonzio, G. (2018) "State of art and perspectives about the production of methanol, dimethyl ether and syngas by carbon dioxide hydrogenation," *Journal of CO2 Utilization*, 27(July), pp. 326–354. doi:10.1016/j.jcou.2018.08.005.

Li, C. *et al.* (2015) "Comprehensive review of renewable energy curtailment and avoidance: A specific example in China," *Renewable and Sustainable Energy Reviews*, 41, pp. 1067–1079. doi:10.1016/j.rser.2014.09.009.

Luo, Y. *et al.* (2018) "Exergy analysis of an integrated solid oxide electrolysis cell-methanation reactor for renewable energy storage," *Applied Energy*, 215(November 2017), pp. 371–383. doi:10.1016/j.apenergy.2018.02.022.

Mughal, S., Sood, Y.R. and Jarial, R.K. (2018) "A Review on Solar Photovoltaic Technology and Future Trends," *NCRACIT) International Journal of Scientific Research in Computer Science, Engineering, and Information Technology © 2018 IJSRCSEIT*, 1(4), pp. 227–235.

Muvhiiwa, R.F. *et al.* (2018) "Applying thermodynamics to digestion/gasification processes: the Attainable Region approach," *Journal of Thermal Analysis and Calorimetry*, 131(1), pp. 25–36. doi:10.1007/s10973-016-6063-9.

Nieminen, H., Laari, A. and Koiranen, T. (2019) “CO2 hydrogenation to methanol by a liquid-phase process with alcoholic solvents: A techno-economic analysis,” *Processes*, 7(7), pp. 1–24. doi:10.3390/pr7070405.

Okonye, L.U. *et al.* (2012) “Attainable regions for a reactor: Application of ΔH-ΔG plot,” *Chemical Engineering Research and Design*, 90(10), pp. 1590–1609. doi:10.1016/j.cherd.2012.02.006.

Ouda, M. *et al.* (2019) *Zukünftige Kraftstoffe*, *Zukünftige Kraftstoffe*. Springer Berlin Heidelberg. doi:10.1007/978-3-662-58006-6.

Parida, B., Iniyan, S. and Goic, R. (2011) “A review of solar photovoltaic technologies,” *Renewable and Sustainable Energy Reviews*, 15(3), pp. 1625–1636. doi:10.1016/j.rser.2010.11.032.

PEM Electrolysis for Hydrogen Production Principles and Applications (2016).

Petrakopoulou, F. *et al.* (2016) “Exergetic analysis of hybrid power plants with biomass and photovoltaics coupled with a solid-oxide electrolysis system,” *Energy*, 94, pp. 304–315. doi:10.1016/j.energy.2015.10.118.

Petrakopoulou, F., Robinson, A. and Loizidou, M. (2016) “Exergetic analysis and dynamic simulation of a solar-wind power plant with electricity storage and hydrogen generation,” *Journal of Cleaner Production*, 113, pp. 450–458. doi:10.1016/j.jclepro.2015.11.074.

Portha, J.F. *et al.* (2017) “Kinetics of Methanol Synthesis from Carbon Dioxide Hydrogenation over Copper-Zinc Oxide Catalysts,” *Industrial and Engineering Chemistry Research*, 56(45), pp. 13133–13145. doi:10.1021/acs.iecr.7b01323.

Pressure, D. *et al.* (2017) “Exergy Assessment of Single and Dual Pressure Abstract :” doi:10.1016/j.energy.2017.06.139.

Rashid, M.M. *et al.* (2015) “Hydrogen Production by Water Electrolysis: A Review of Alkaline Water Electrolysis, PEM Water Electrolysis and High-Temperature Water Electrolysis,” *International Journal of Engineering and Advanced Technology*, (3), pp. 2249–8958.

Rathore, N. *et al.* (2019) “A comprehensive review of different types of solar photovoltaic cells and their applications,” *International Journal of Ambient Energy*, 0(0), pp. 1–18. doi:10.1080/01430750.2019.1592774.

Ren, S. *et al.* (2019) “Effects of mixing methods of bifunctional catalysts on catalyst stability of DME synthesis via CO2 hydrogenation,” *Carbon Resources Conversion*, 2(1), pp. 85–94. doi:10.1016/j.crcon.2019.03.002.

Rivera-Tinoco, R. *et al.* (2016) “Investigation of power-to-methanol processes coupling electrolytic hydrogen production and catalytic CO2 reduction,” *International Journal of Hydrogen Energy*, 41(8), pp. 4546–4559. doi:10.1016/j.ijhydene.2016.01.059.

Salomone, F. *et al.* (2019) “Techno-economic modelling of a Power-to-Gas system based on SOEC electrolysis and CO2 methanation in a RES-based electric grid,” *Chemical Engineering Journal*, 377(xxxx), pp. 1–20. doi:10.1016/j.cej.2018.10.170.

Sánchez, A. and Martín, M. (2018) “Optimal renewable production of ammonia from water and air,” *Journal of Cleaner Production*, 178, pp. 325–342. doi:10.1016/j.jclepro.2017.12.279.

Schaaf, T. *et al.* (2014) “Methanation of CO 2 - storage of renewable energy in a gas distribution system,” pp. 1–14. doi:10.1186/s13705-014-0029-1.

Schwabe, F. *et al.* (2019) “Concept, design, and energy analysis of an integrated power-to-methanol process utilizing a tubular proton-conducting solid oxide electrolysis cell,” *International Journal of Hydrogen Energy*, 44(25), pp. 12566–12575. doi:10.1016/j.ijhydene.2018.11.133.

Sempuga, B.C. *et al.* (2010) “Classification of chemical processes: A graphical approach to process synthesis to improve reactive process work efficiency,” *Industrial and Engineering Chemistry Research*, 49(17), pp. 8227–8237. doi:10.1021/ie100288h.

Sempuga, B.C. *et al.* (2011) “Work to chemical processes: The relationship between heat, temperature, pressure, and process complexity,” *Industrial and Engineering Chemistry Research*, 50(14), pp. 8603–8619. doi:10.1021/ie2004785.

Sempuga, B.C. *et al.* (2012) “Efficient combustion: A process synthesis approach to improve the efficiency of coal-fired power stations,” *Industrial and Engineering Chemistry Research*, 51(26), pp. 9061–9077. doi:10.1021/ie201433k.

Sempuga, B.C. and Yao, Y. (2017) “CO 2 hydrogenation from a process synthesis perspective : Setting up process targets,” *Journal of CO2 Utilization*, 20(April), pp. 34–42. doi:10.1016/j.jcou.2017.05.004.

Shiva Kumar, S. and Himabindu, V. (2019) “Hydrogen production by PEM water electrolysis – A review,” *Materials Science for Energy Technologies*, 2(3), pp. 442–454. doi:10.1016/j.mset.2019.03.002.

Siddiqui, O. and Dincer, I. (2020) “A new solar energy system for ammonia production and utilization in fuel cells,” *Energy Conversion and Management*, 208(February), p. 112590. doi:10.1016/j.enconman.2020.112590.

Sin, Y. *et al.* (2013) “Efficient stationary solar thermal collector systems operating at a medium-temperature range,” *Applied Energy*, 111, pp. 1071–1079. doi:10.1016/j.apenergy.2013.06.051.

Upadhyay, B.H., Patel, A.J. and Ramana, P. V. (2019) “A detailed review on solar parabolic trough collector,” *International Journal of Ambient Energy*, 0(0), pp. 1–21. doi:10.1080/01430750.2019.1636869.

Villagra, A. and Millet, P. (2019) “An analysis of PEM water electrolysis cells operating at elevated current densities,” *International Journal of Hydrogen Energy*, 44(20), pp. 9708–9717. doi:10.1016/j.ijhydene.2018.11.179.

Widyolar, B. *et al.* (2018) “Non-tracking East-West XCPC solar thermal collector for 200-celsius applications,” *Applied Energy*, 216(November 2017), pp. 521–533. doi:10.1016/j.apenergy.2018.02.031.

Zhang, H., Wang, L., van Herle, J., *et al.* (2019) "Techno-economic optimization of CO2-to-methanol with a solid-oxide electrolyzer," *Energies*, 12(19). doi:10.3390/en12193742.

Zhang, H., Wang, L., Van, J., *et al.* (2019) "with Solid-Oxide Electrolyzer."

Zhang, H., Wang, L., van herle, J., *et al.* (2020) "Techno-economic comparison of green ammonia production processes," *Applied Energy*, 259. doi:10.1016/j.apenergy.2019.114135.

Appendices:

Appendix A: Thermodynamic information of selected PT-C process pathways

Table A1: Standard enthalpy of formation and Gibbs free energy for compounds considered in the study(Dean, John A, 1979)

Compound	State	$\Delta\hat{H}_f^0(\frac{kJ}{mol})$	$\Delta\hat{G}_f^0(\frac{kJ}{mol})$
Water	liquid	-285.8	-237.2
Water	gas	-241.8	-228.6
Hydrogen	gas	0.0	0.0
Oxygen	gas	0.0	0.0
Methane	gas	-74.9	-50.8
Ethane	gas	-84.7	-32.8
Propane	gas	-103.8	-23.6
Methanol	liquid	-239.0	-166.8
Ethanol	liquid	-277.0	-174.2
Propanol	liquid	-304.0	-170.6
Dimethyl ether	gas	-184.1	-112.9
Ethylene	gas	52.5	68.0
Carbon monoxide	gas	-110.5	-137.3
Carbon dioxide	gas	-393.5	-394.4
Nitrogen	gas	0.0	0.0
Ammonia	gas	-46.1	-16.5

Sample calculation of process (mass balance) enthalpy and Gibbs free energy

Example: Process splitting liquid water to hydrogen and oxygen gases where the feed and products are at ambient conditions (T=298.15 K and P=1 atm)

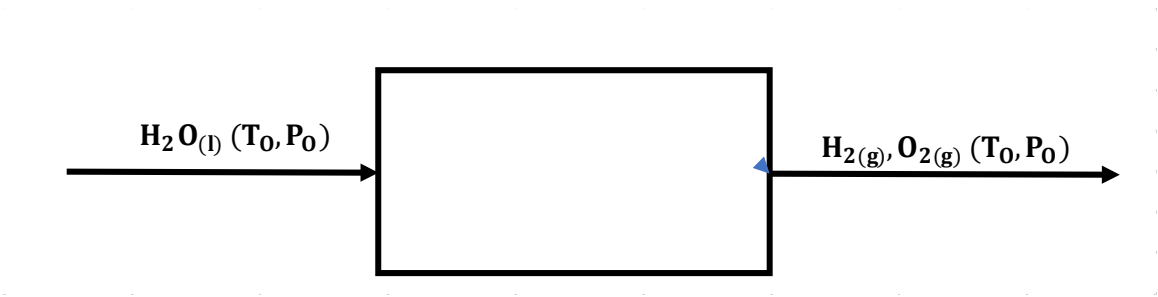

Figure A1: Schematic diagram of water splitting process, demonstration of how to calculate the process enthalpy and Gibbs free energy.

Process enthalpy:

$$\Delta\hat{H}_P = 0.5\Delta\hat{H}^o_{f,O_{2(g)}} + \Delta\hat{H}^o_{f,H_{2(g)}} - \Delta\hat{H}^o_{f,H_2O_{(l)}}$$

$$\therefore \Delta\hat{H}_P = 0 + 0 - (-285.8) = 285.8\ kJ/mol$$

Process Gibbs free energy:

$$\Delta\widehat{G}_P = 0.5\Delta\widehat{G}^o_{f,O_{2(g)}} + \Delta\widehat{G}^o_{f,H_{2(g)}} - \Delta\widehat{G}^o_{f,H_2O_{(l)}}$$

$$\therefore \Delta\widehat{G}_P = 0 + 0 - (-237.2) = 237.2\ \text{kJ/mol}$$

Appendix B: Theoretical development calculations on g-h diagrams

Illustration of representing a process on a G-H diagram

Consider the process of water splitting represented in Table A1:

The enthalpy and Gibbs free energy for the splitting of 1 mole of liquid water are 285.8 and 237.2 kJ/mol as shown in Appendix A. The processed vector, where x and y-axis are represented by enthalpy and Gibbs free energy, starts at the origin where there is no reaction yet and ends when 1 mole of water has reacted. Figure B1 illustrates the process on a g-h diagram

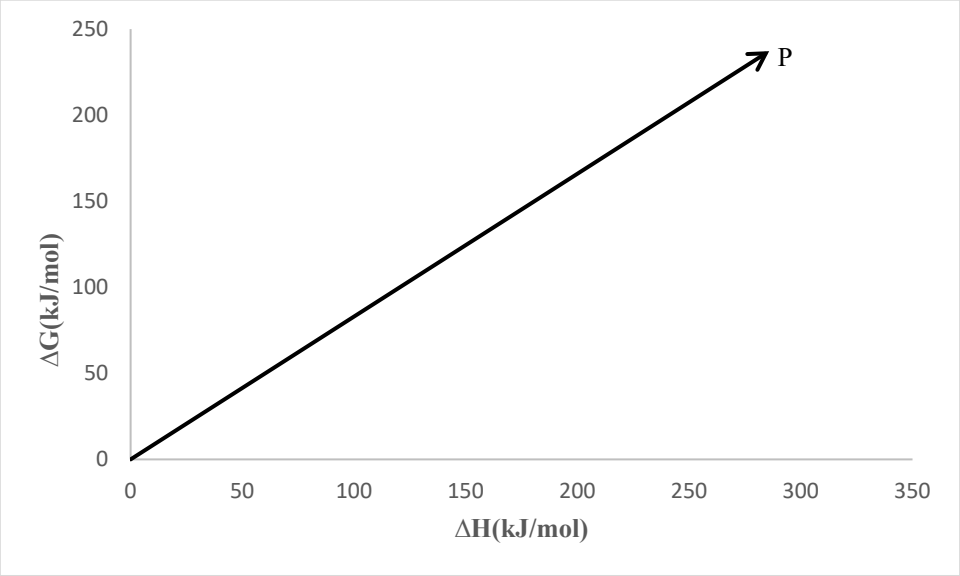

Figure B1: Illustration of plotting water splitting process vector on the gh diagram

The length of vector 0P is determined by the $(\Delta H_P, \Delta G_P)$ coordinates, starting from the origin. The total enthalpy and Gibbs free energy of the system are determined by the x and y components of vector 0P. The direction is the process vector is determined by the signs of enthalpy and Gibbs free energy

Derivation of the equation to calculate ToSgen term

Consider Fig B2 representing a hypothetical process

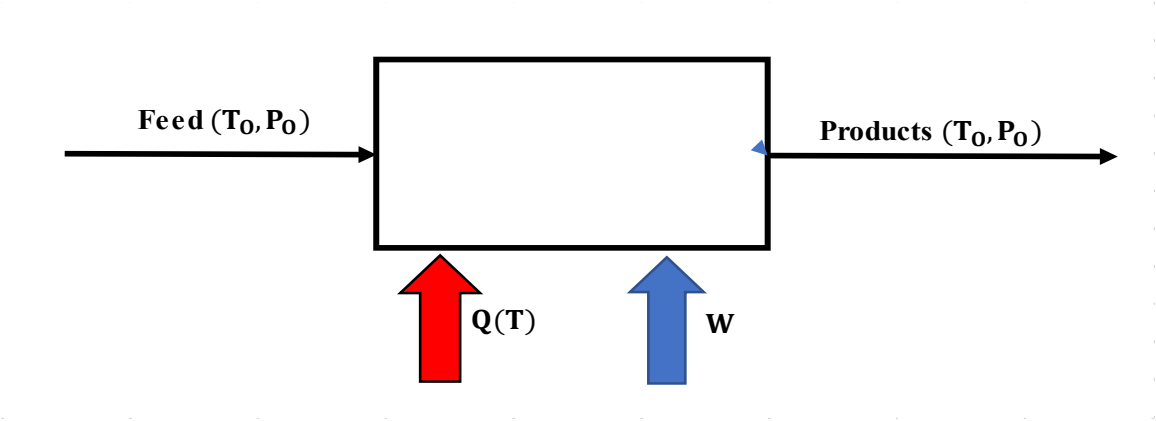

Figure B2: Hypothetical process with the feed and products at ambient temperature, supplied with heat at temperature T and work.

Equations derivation:

Case 1(Process powered by heat only)

Energy balance around the process: (1^{ST} law of thermodynamics)

$$\Delta H_P(T_O, P_O) = Q(T) \qquad \text{B1}$$

Entropy balance around the process: (2^{nd} law of thermodynamics)

$$\Delta S_P(T_O, P_O) = \frac{Q(T)}{T} + S_{gen} \qquad \text{B2}$$

Definition of enthalpy:

$$\Delta H_P = \Delta G_P(T_O, P_O) + T_O \Delta S_P \qquad \text{B3}$$

Solving eq (B1, B2 and B3) simultaneously yields eq.(B4)

$$T_O S_{gen} = \Delta H_P(T_O, P_O)\left[1 - \frac{T_O}{T}\right] - \Delta G_P(T_O, P_O) \qquad \text{B4}$$

But, $$\Delta H_P(T_O, P_O) = Q(T)$$

Therefore: $$T_O S_{gen} = Q(T)\left[1 - \frac{T_O}{T}\right] - \Delta G_P(T_O, P_O) \qquad \text{B5}$$

Case 2: Process supplied with work only

Energy balance around the process: (1^{ST} law of thermodynamics)

$$\Delta H_P(T_O, P_O) = W \qquad \text{B1}$$

Entropy balance around the process: (2^{nd} law of thermodynamics)

$$\Delta S_P(T_O, P_O) = \frac{Q(T)}{T} + S_{gen} \qquad \text{B2}$$

Definition of enthalpy:

$$\Delta H_P = \Delta G_P(T_O, P_O) + T_O \Delta S_P \qquad \text{B3}$$

Solving eq (B1, B2 and B3) simultaneously yields eq.(B4)

$$T_O S_{gen} = W - \Delta G_P(T_O, P_O) \qquad \text{B4}$$

Case 3 (Process powered by a combination of heat and work)

Energy balance around the process: (1^{ST} law of thermodynamics)

$$\Delta H_P(T_O, P_O) = Q(T) + W \qquad \text{C1}$$

Entropy balance around the process: (2^{nd} law of thermodynamics)

$$\Delta S_P(T_O, P_O) = \frac{Q(T)}{T} + S_{gen} \qquad \text{C2}$$

Definition of enthalpy:

$$\Delta H_P = \Delta G_P(T_O, P_O) + T_O \Delta S_P \qquad \text{C3}$$

Solving Eq. (C1, C2 and C3) simultaneously yields eq.(B4)

$$T_O S_{gen} = \Delta H_P(T_O, P_O)\left[1 - \frac{T_O}{T}\right] + \left(\frac{T_O}{T}\right) W - \Delta G_P(T_O, P_O) \qquad \text{C4}$$

Appendix C: Case studies and other PT-C process pathways sample calculations and data

Example: Power-to-hydrogen case study

Table C1: Data relevant to electrolysis calculations

Z	$\mathbf{v_{rev}}$	$\mathbf{v_{tn}}$	**F**	**D**	**B**	**C**	**t**	$\mathbf{PEC_{ELEC}}$
	v	**v**	**C/mol**	**Ω**	$\mathbf{K^{-1}}$	$\mathbf{bar^{-1}}$	**yr**	$\mathrm{USD/m^2}$
2	1.004	1.228	96487	35.71	0.0057	0.0217	15	3317.4

Table C2: Additional data including the work of combustion at 1200℃

$\mathbf{T_{Q_{st}}}$	$\mathbf{T_{Q_{st}}}$	$\mathbf{T_{ELEC}}$	$\mathbf{T_{ELEC}}$	$\mathbf{p_{ELEC}}$	$\mathbf{\bar{n}_{H_2}}$	$\mathbf{\bar{n}_{H_2}}$	$\mathbf{W_c}$
℃	**K**	℃	**K**	**bar**	**mol/s**	**kmol/s**	**kW**
200	473.15	750	1023.15	10	1.00	0.001	192.9

Calculations for work of combustion: (1mole/s of hydrogen is a basis of calculations)

$$\mathrm{W_c} = \dot{\mathrm{n}}_{\mathrm{H_{2(g)}}} \Delta\hat{\mathrm{H}}_{\mathrm{c}} \left[1 - \frac{\mathrm{T_O}}{\mathrm{T_C}}\right]$$

$$\therefore \mathrm{W_C} = \left(1\frac{\mathrm{mol}}{\mathrm{s}}\right) \times \left(-241.8\frac{\mathrm{kJ}}{\mathrm{mol}}\right)\left[1 - \frac{298.15}{1473.15}\right] = -192.9\ \mathrm{kW}$$

Table C3: Calculated data for PT-H_2 process case study

W_e	Q_{ST}	$W_{Q_{st}}$	T_OS_{gen}	I_F	V_{OP}	ASR	j	A	f	EC_T	PEC_{ELEC}	C_T	η_{WS}	η_W	A_S
kW	kW	kW	kW	kA	V	Ω m²	A/m^2	m²		USD/t	USD	USD	%	%	m²
0	285.8	105.7	-131.5	193.0	0.00	0.08	-11.91	-1.62	0.0%	349819.2	-5373.1	344446.1	224.4%	182.5%	453.65
25	260.8	96.5	-115.7		0.13		-10.38	-1.86	22.8%	367819.2	-6169.0	361650.2	195.3%	158.8%	536.52
50	235.8	87.2	-100.0		0.26		-8.84	-2.18	39.6%	385819.2	-7241.5	378577.7	172.9%	140.6%	619.38
75	210.8	78.0	-84.2		0.39		-7.30	-2.64	52.4%	403819.2	-8765.6	395053.6	155.1%	126.1%	702.25
100	185.8	68.7	-68.5		0.52		-5.77	-3.35	62.4%	421819.2	-11102.1	410717.1	140.6%	114.3%	785.12
125	160.8	59.5	-52.7		0.65		-4.23	-4.56	70.6%	439819.2	-15136.9	424682.3	128.6%	104.6%	867.98
208.7	77.1	28.5	0.0		1.08		0.92	21.09	89.3%	500064.5	69955.9	570020.4	100.0%	81.3%	1145.33
210	75.8	28.0	0.8		1.09		1.00	19.36	89.5%	501019.2	64233.9	565253.1	99.6%	81.0%	1149.73
215	70.8	26.2	4.0		1.11		1.30	14.80	90.4%	504619.2	49091.8	553711.0	98.3%	80.0%	1166.30
220	65.8	24.3	7.1		1.14		1.61	11.98	91.2%	508219.2	39726.9	547946.1	97.1%	78.9%	1182.88
225	60.8	22.5	10.3		1.17		1.92	10.06	92.0%	511819.2	33362.5	545181.7	95.8%	77.9%	1199.45
230	55.8	20.6	13.4		1.19		2.23	8.67	92.7%	515419.2	28755.8	544175.0	94.6%	77.0%	1216.02
236	49.8	18.4	17.2		1.22		2.60	7.44	93.6%	519739.2	24668.3	544407.5	93.2%	75.8%	1235.91
240	45.8	16.9	19.7		1.24		2.84	6.79	94.2%	522619.2	22533.0	545152.2	92.3%	75.1%	1249.17
245	40.8	15.1	22.9		1.27		3.15	6.13	94.9%	526219.2	20332.9	546552.1	91.2%	74.2%	1265.74
250	35.8	13.2	26.0		1.30		3.46	5.58	95.6%	529819.2	18524.3	548343.5	90.1%	73.3%	1282.32
264.30	21.50	8.0	35.1		1.37		4.34	4.45	97.4%	540118.7	14766.4	554885.1	87.1%	70.8%	1329.73
268	17.8	6.6	37.4		1.39		4.56	4.23	97.9%	542779.2	14031.2	556810.4	86.4%	70.2%	1341.98
270	15.8	5.8	38.6		1.40		4.69	4.12	98.1%	544219.2	13662.9	557882.1	86.0%	69.9%	1348.61
273	12.8	4.7	40.5		1.41		4.87	3.96	98.5%	546379.2	13145.5	559524.7	85.4%	69.4%	1358.55
275	10.8	4.0	41.8		1.43		4.99	3.86	98.7%	547819.2	12821.7	560640.9	85.0%	69.1%	1365.18
280	5.8	2.1	44.9		1.45		5.30	3.64	99.3%	551419.2	12078.1	563497.3	84.1%	68.4%	1381.76
276.3	9.5	3.5	42.6		1.43		5.07	3.81	98.9%	548736.3	12623.7	561360.0	84.8%	68.9%	1369.40
285.8	0	0.0	48.6		1.48		5.66	3.41	100.0%	555595.2	11316.7	566911.9	83.0%	67.5%	1400.98
1490	-1204	-445.4	807.4		7.72		79.69	0.24	135.4%	1422619.2	803.3	1423422.5	22.7%	18.5%	807.41

Procedure: Electrical work is varied from 0 kW to 1490 kW, solar thermal heat and the ToSgen term are then calculated for each value of solar-PV work. Energy balance is used to calculate the solar-T heat for each value of solar-PV work.

-Consider the first value of We=0 kW

$$\dot{n}_{H_{2(g)}}\Delta\widehat{H}_P = W_e + Q_{ST}$$

$$\left(1\frac{\text{mol}}{\text{s}}\right)\left(285.8\frac{\text{kJ}}{\text{mol}}\right) = 0\ \text{kW} + Q_{ST}$$

$$\therefore Q_{ST} = 285.8\ \text{kW}$$

-ToSgen value is then calculated using eq.(B4), again considering the first value of We=0 kW.

$$T_OS_{gen} = \dot{n}_{H_{2(g)}}\Delta\widehat{H}_P(T_O, P_O)\left[1 - \frac{T_O}{T}\right] + \left(\frac{T_O}{T}\right)W - \dot{n}_{H_2}\Delta\widehat{G}_P(T_O, P_O)$$

$$T_OS_{gen} = \left(1\frac{\text{mole}}{\text{s}}\right)\left(285.8\frac{\text{kJ}}{\text{mol}}\right)\left[1 - \frac{298.15\ \text{K}}{472.15\ \text{K}}\right] + \left(\frac{298.15\ \text{K}}{472.15\ \text{K}}\right)(0\ \text{kW}) - (1\frac{\text{mole}}{\text{s}})(237.2\frac{\text{kJ}}{\text{mol}})$$

$$\therefore T_O S_{gen} = -131.5\ \text{kW}$$

The process is thermodynamically infeasible at the T_oS_{gen} values that are lower than zero, hence the process only occurs from the W_e value of 208.7 kW where ToSgen=0 kW.

Electrolysis calculations:

(i) Faradic current

$$\dot{n}_{H_{2(g)}/\text{formed}} = \frac{I_F}{zF} \qquad \text{(Faraday's law of electrolysis)}$$

$$\left(0.001\frac{\text{kmol}}{\text{s}}\right) = \frac{I_F}{(2)(96487\frac{\text{C}}{\text{mol}})}$$

$$\therefore I_f = 193.0\ \text{kA}$$

(ii) Area-specific resistance

$$\text{ASR} = De^{(-BT)}e^{(-Cp)}$$

$$\therefore \text{ASR} = (35.7\Omega\text{m}^2)e^{(-0.0057\text{K}^{-1}\times 1023.15\ \text{K})}e^{(-0.0217\text{bar}^{-1}\times 10\ \text{bar})} = 0.084\Omega\text{m}^2$$

(iii) Operating voltage

$$W_e = I_F V_{op}$$

$$0\ \text{kW} = 193.0\ \text{kA} \times V_{op}$$

$$\therefore V_{op} = 0\ \text{V}$$

(iv) Operating current

$$V_{op} = V_{rev} + i\text{ASR}$$

$$0\ \text{V} = 1.004\ \text{V} + i \times 0.084\ \Omega\text{m}^2$$

$$\therefore i = -11.9\ \text{A/cm}^2$$

Derivation of solar-PV area fraction equation

$$W_e = \eta_{PV} G A_{PV}$$

$$Q_{ST} = \eta_{ST} G A_{ST}$$

Total solar collection surface area

$$A_{PV} + A_{ST} = A_T$$

$$\frac{W_e}{\eta_{PV} G} + \frac{Q_{ST}}{\eta_{ST} G} = A_T$$

$$\therefore A_T = \frac{\eta_{ST} W_e + \eta_{PV} Q_{ST}}{\eta_{PV} \eta_{ST} G}$$

Solar-PV area fraction

$$f = \frac{A_{PV}}{A_T} = \frac{\frac{W_e}{\eta_{PV} G}}{\frac{\eta_{ST} W_e + \eta_{PV} Q_{ST}}{\eta_{PV} \eta_{ST} G}}$$

$$\therefore f = \frac{\eta_{ST} W_e}{\eta_{ST} W_e + \eta_{PV} Q_{ST}}$$

Calculations for f @ W_e= 208.7 kW and Q_{ST}= 77.1 kW.

$$f = \frac{(63\%)(208.7\ \text{kW})}{(63\%)(208.7\ \text{kW}) + (20.4\%)(77.1\ \text{kW})}$$

$$\therefore f = 89.3\ \%$$

Total area requirements @ f=89.3 %

$$A_T = \frac{\eta_{ST} W_e + \eta_{PV} Q_{ST}}{\eta_{PV} \eta_{ST} G}$$

$$A_T = \frac{(63\ \%)(208.7\ \text{kW}) + (20.4\ \%)(77.1\ \text{kW})}{(20.4\ \%)(63\ \%)(\ 1 \frac{\text{kW}}{\text{m}^2})}$$

$$\therefore A_T = 1145\ \text{m}^2$$

Cost calculations @ f=89.3 %

- Energy cost

$$E_C = C_{PV} + C_{ST}$$

$$E_C = \left(0.05\frac{\text{USD}}{\text{kWh}}\right)(208.7\text{ kW})(36{,}000\text{h}) + (0.034\frac{\text{USD}}{\text{kWh}})(77.1\text{ kW})(36{,}000\text{h})$$

$$\therefore E_C = \text{USD } 500{,}064$$

- Purchase electrolysis stack cost

$$PEC_E = (3{,}317.4\frac{\text{USD}}{\text{m}^2})A_{AE}$$

$$PEC_E = (3{,}317.4\frac{\text{USD}}{\text{m}^2})(21.09\text{ m}^2)$$

$$\therefore PEC_E = \text{USD } 69\,956$$

- Total cost

$$C_T = E_C + PEC_E$$

$$\therefore C_T = \text{USD } 500{,}064 + \text{USD}69{,}956 = \text{USD } 520{,}020$$

Data for PT-C processes with a basis of 640 kW output power from combustion.

PT-$H_{2(g)}$ example:

$$W_{Comb} = -\dot{n}_{H_{2(g)}}\Delta\widehat{H}_C\left[1 - \frac{T_O}{T_C}\right]$$

$$640\text{ kW} = -\dot{n}_{H_{2(g)}}(-241.8\frac{\text{kJ}}{\text{mol}})\left[1 - \frac{298.15\text{ K}}{1{,}473.15\text{ K}}\right]$$

$$\therefore \dot{n}_{H_{2(g)}} = 3.32\frac{\text{mole}}{\text{s}}$$

Appendix C: Calculation's data table for case studies, theoretical analysis and setting of performance targets

Table C4: Data for PT-H2 process

W_e kW	Q_{ST} kW	$W_{Q_{st}}$ kW	T_0S_{gen} kW	I_F kA	V_{OP} v	ASR Ω cm2	j A/cm2	Ae cm2	Ae m2	f	EC_T USD/yr	EC_T USD/t	PEC_{ELEC} USD	C_T USD	η_{WS} %	η_W %	A_S m^2
0.0	948.3	350.8	-436.3	640.323	0.000	0.084	-11.914	-53743.961	-5.374	0%	77384.296	1160764.439	-17829.055	1142935.385	224%	182%	1505.30
5.0	943.3	348.9	-433.2		0.008		-11.822	-54165.133	-5.417	2%	77624.296	1164364.439	-17968.774	1146395.665	222%	181%	1521.87
10.0	938.3	347.1	-430.0		0.016		-11.729	-54592.957	-5.459	3%	77864.296	1167964.439	-18110.701	1149853.738	220%	179%	1538.44
15.0	933.3	345.2	-426.9		0.023		-11.636	-55027.594	-5.503	5%	78104.296	1171564.439	-18254.888	1153309.551	219%	178%	1555.02
20.0	928.3	343.4	-423.7		0.031		-11.544	-55469.207	-5.547	6%	78344.296	1175164.439	-18401.389	1156763.050	217%	176%	1571.59
25.0	923.3	341.5	-420.6		0.039		-11.451	-55917.966	-5.592	8%	78584.296	1178764.439	-18550.260	1160214.179	215%	175%	1588.16
30.0	918.3	339.7	-417.4		0.047		-11.358	-56374.045	-5.637	9%	78824.296	1182364.439	-18701.560	1163662.879	213%	173%	1604.74
35.0	913.3	337.8	-414.3		0.055		-11.266	-56837.625	-5.684	11%	79064.296	1185964.439	-18855.349	1167109.091	211%	172%	1621.31
40.0	908.3	336.0	-411.1		0.062		-11.173	-57308.892	-5.731	12%	79304.296	1189564.439	-19011.687	1170552.752	209%	170%	1637.88
45.0	903.3	334.1	-408.0		0.070		-11.081	-57788.040	-5.779	13%	79544.296	1193164.439	-19170.640	1173993.800	208%	169%	1654.46
50.0	898.3	332.3	-404.8		0.078		-10.988	-58275.267	-5.828	15%	79784.296	1196764.439	-19332.273	1177432.166	206%	167%	1671.03
55.0	893.3	330.4	-401.7		0.086		-10.895	-58770.780	-5.877	16%	80024.296	1200364.439	-19496.655	1180867.785	204%	166%	1687.60
60.0	888.3	328.6	-398.5		0.094		-10.803	-59274.792	-5.927	17%	80264.296	1203964.439	-19663.856	1184300.583	203%	165%	1704.18
65.0	883.3	326.7	-395.4		0.102		-10.710	-59787.524	-5.979	19%	80504.296	1207564.439	-19833.950	1187730.490	201%	163%	1720.75
70.0	878.3	324.9	-392.2		0.109		-10.617	-60309.203	-6.031	20%	80744.296	1211164.439	-20007.012	1191157.427	199%	162%	1737.32
75.0	873.3	323.0	-389.1		0.117		-10.525	-60840.066	-6.084	21%	80984.296	1214764.439	-20183.121	1194581.318	198%	161%	1753.90
80.0	868.3	321.2	-385.9		0.125		-10.432	-61380.358	-6.138	22%	81224.296	1218364.439	-20362.358	1198002.082	196%	160%	1770.47
85.0	863.3	319.3	-382.8		0.133		-10.339	-61930.333	-6.193	23%	81464.296	1221964.439	-20544.807	1201419.633	195%	158%	1787.04
90.0	858.3	317.5	-379.6		0.141		-10.247	-62490.251	-6.249	24%	81704.296	1225564.439	-20730.554	1204833.885	193%	157%	1803.62
95.0	853.3	315.6	-376.5		0.148		-10.154	-63060.387	-6.306	26%	81944.296	1229164.439	-20919.692	1208244.748	192%	156%	1820.19
100.0	848.3	313.8	-373.3		0.156		-10.061	-63641.022	-6.364	27%	82184.296	1232764.439	-21112.312	1211652.128	190%	155%	1836.76
105.0	843.3	311.9	-370.2		0.164		-9.969	-64232.449	-6.423	28%	82424.296	1236364.439	-21308.512	1215055.927	189%	154%	1853.34
110.0	838.3	310.1	-367.0		0.172		-9.876	-64834.972	-6.483	29%	82664.296	1239964.439	-21508.393	1218456.046	187%	152%	1869.91
115.0	833.3	308.2	-363.9		0.180		-9.784	-65448.905	-6.545	30%	82904.296	1243564.439	-21712.060	1221852.380	186%	151%	1886.48
685	263.34	97.40	-4.68		1.070		0.778	823410.629	82.341	88.9%	110264.296	1653964.439	273158.748	1927123.187	100.6%	81.8%	3775.838
690	258.34	95.55	-1.52		1.078		0.870	735758.731	73.576	89.2%	110504.296	1657564.439	244081.053	1901645.493	100.2%	81.5%	3792.412
692.42	255.92	94.65	0.00		1.081		0.915	699722.611	69.972	89.3%	110620.408	1659306.125	232126.409	1891432.534	100.0%	81.3%	3800.430
700	248.34	91.85	4.78		1.093		1.056	606611.404	60.661	89.7%	110984.296	1664764.439	201237.640	1866002.079	99.4%	80.8%	3825.558
910	38.3	14.2	137.1		1.421		4.947	129448.584	12.945	98.7%	121064.296	1815964.439	42943.353	1858907.792	85.2%	69.3%	4521.637
915	33.3	12.3	140.3		1.429		5.039	127068.756	12.707	98.8%	121304.296	1819564.439	42153.867	1861718.307	84.9%	69.0%	4538.210
920	28.3	10.5	143.4		1.437		5.132	124774.852	12.477	99.0%	121544.296	1823164.439	41392.886	1864557.326	84.6%	68.8%	4554.783
925	23.3	8.6	146.6		1.445		5.224	122562.301	12.256	99.2%	121784.296	1826764.439	40658.893	1867423.332	84.3%	68.5%	4571.357
930	18.3	6.8	149.7		1.452		5.317	120426.849	12.043	99.4%	122024.296	1830364.439	39950.477	1870314.916	84.0%	68.3%	4587.930
935	13.3	4.9	152.9		1.460		5.410	118364.537	11.836	99.5%	122264.296	1833964.439	39266.324	1873230.764	83.7%	68.1%	4604.503
940	8.3	3.1	156.0		1.468		5.502	116371.670	11.637	99.7%	122504.296	1837564.439	38605.209	1876169.649	83.5%	67.9%	4621.076
948.337	0.0	0.0	161.3		1.481		5.657	113193.936	11.319	100.0%	122904.470	1843567.051	37551.026	1881118.077	83.0%	67.5%	4648.711

Table C5: Data for PT-CH_4

W_e kW	Q_{ST} kW	$W_{Q_{st}}$ kW	T_0S_{gen} kW	I_F kA	V_{OP} v	ASR Ω cm2	j A/cm2	Ae cm2	Ae m2	f	EC_T USD/yr	EC_T USD/t	PEC_{ELEC} USD	C_T USD	η_{WS} %	η_W %	A_S m^2
0	890.25	329.3	-488.7	771.896	0	0.084287	-11.91	-64787.20	-6.48	0.0%	72644.40	1089666.00	-21492.55	1068173.45	2.48	1.94	1413.10
100	790.25	292.3	-425.7		0.130		-10.38	-74383.05	-7.44	28.1%	77444.40	1161666.00	-24675.88	1136990.12	2.09	1.63	1744.56
200	690.25	255.3	-362.7		0.259		-8.84	-87315.67	-8.73	47.2%	82244.40	1233666.00	-28966.16	1204699.84	1.80	1.41	2076.03
300	590.25	218.3	-299.7		0.389		-7.30	-105691.79	-10.57	61.1%	87044.40	1305666.00	-35062.26	1270603.74	1.58	1.23	2407.49
400	490.25	181.3	-236.7		0.518		-5.77	-133864.38	-13.39	71.6%	91844.40	1377666.00	-44408.25	1333257.75	1.41	1.10	2738.96
500	390.25	144.3	-173.7		0.648		-4.23	-182514.31	-18.25	79.8%	96644.40	1449666.00	-60547.41	1389118.59	1.27	0.99	3070.42
600	290.25	107.4	-110.6		0.777		-2.69	-286713.91	-28.67	86.5%	101444.40	1521666.00	-95114.65	1426551.35	1.16	0.90	3401.89
700	190.25	70.4	-47.6		0.907		-1.16	-668193.62	-66.82	91.9%	106244.40	1593666.00	-221666.96	1371999.04	1.06	0.83	3733.36
775.6	114.6573	42.4	0.0		1.005		0.01	115638169.21	11563.82	95.4%	109872.85	1648092.71	38361877.30	40009970.01	1.00	0.78	3983.92
780	110.25	40.8	2.8		1.010		0.07	10372601.78	1037.26	95.6%	110084.40	1651266.00	3441013.29	5092279.29	1.00	0.78	3998.53
785	105.25	38.9	5.9		1.017		0.15	5102845.83	510.28	95.8%	110324.40	1654866.00	1692821.21	3347687.21	0.99	0.78	4015.10
790	100.25	37.1	9.1		1.023		0.23	3383747.42	338.37	96.1%	110564.40	1658466.00	1122526.45	2780992.45	0.99	0.77	4031.68
795	95.25	35.2	12.2		1.030		0.30	2531058.72	253.11	96.3%	110804.40	1662066.00	839654.97	2501720.97	0.99	0.77	4048.25
800	90.25	33.4	15.4		1.036		0.38	2021619.86	202.16	96.5%	111044.40	1665666.00	670653.42	2336319.42	0.98	0.77	4064.82
805	85.25	31.5	18.5		1.043		0.46	1682895.13	168.29	96.7%	111284.40	1669266.00	558284.67	2227550.67	0.98	0.77	4081.40
810	80.25	29.7	21.7		1.049		0.54	1441388.79	144.14	96.9%	111524.40	1672866.00	478167.20	2151033.20	0.97	0.76	4097.97
815	75.25	27.8	24.8		1.056		0.61	1260499.02	126.05	97.1%	111764.40	1676466.00	418158.72	2094624.72	0.97	0.76	4114.54
820	70.25	26.0	28.0		1.062		0.69	1119948.94	111.99	97.3%	112004.40	1680066.00	371532.55	2051598.55	0.97	0.76	4131.12
825	65.25	24.1	31.1		1.069		0.77	1007598.20	100.76	97.5%	112244.40	1683666.00	334261.25	2017927.25	0.96	0.75	4147.69
830	60.25	22.3	34.3		1.075		0.84	915733.85	91.57	97.7%	112484.40	1687266.00	303786.11	1991052.11	0.96	0.75	4164.26
835	55.25	20.4	37.4		1.082		0.92	839220.74	83.92	97.9%	112724.40	1690866.00	278403.61	1969269.61	0.96	0.75	4180.84
840	50.25	18.6	40.6		1.088		1.00	774507.63	77.45	98.1%	112964.40	1694466.00	256935.64	1951401.64	0.95	0.75	4197.41
845	45.25	16.7	43.7		1.095		1.07	719060.22	71.91	98.3%	113204.40	1698066.00	238541.48	1936607.48	0.95	0.74	4213.98
850	40.25	14.9	46.9		1.101		1.15	671021.43	67.10	98.5%	113444.40	1701666.00	222605.06	1924271.06	0.95	0.74	4230.56
855	35.25	13.0	50.0		1.108		1.23	628999.41	62.90	98.7%	113684.40	1705266.00	208664.65	1913930.65	0.94	0.74	4247.13
860	30.25	11.2	53.2		1.114		1.30	591930.38	59.19	98.9%	113924.40	1708866.00	196367.35	1905233.35	0.94	0.73	4263.70
865	25.25	9.3	56.3		1.121		1.38	558987.39	55.90	99.1%	114164.40	1712466.00	185438.82	1897904.82	0.94	0.73	4280.28
870	20.25	7.5	59.5		1.127		1.46	529517.88	52.95	99.3%	114404.40	1716066.00	175662.59	1891728.59	0.93	0.73	4296.85
875	15.25	5.6	62.6		1.134		1.53	502999.99	50.30	99.4%	114644.40	1719666.00	166865.52	1886531.52	0.93	0.73	4313.42
880	10.25	3.8	65.8		1.140		1.61	479011.43	47.90	99.6%	114884.40	1723266.00	158907.54	1882173.54	0.93	0.72	4330.00
885	5.25	1.9	68.9		1.147		1.69	457206.79	45.72	99.8%	115124.40	1726866.00	151674.06	1878540.06	0.92	0.72	4346.57
890	0.25	0.1	72.1		1.153		1.77	437300.82	43.73	100.0%	115364.40	1730466.00	145070.44	1875536.44	0.92	0.72	4363.14
890.25	0	0	72.25		1.153		1.77	436350.92	43.64	100.0%	115376.40	1730646.00	144755.32	1875401.32	0.92	0.72	4363.97

Table C5: Data for PT-NH_3

W_e	Q_{ST}	$W_{Q_{st}}$	T_0S_{gen}	I_F	V_{OP}	ASR	j	Ae	Ae	f	EC_T	EC_T	PEC_{ELEC}	C_T	η_{WS}	η_W	A_S
kW	kW	kW	kW	kA	v	Ω cm2	A/cm2	cm2	m2		USD/yr	USD/t	USD	USD	%	%	m^2
0	969.633	358.6	-501.7	733.761	0	0.084287	-11.91	-61600.33	-6.16	0.0%	79122.05	1186830.80	-20435.33	1166395.47	2.40	1.78	1539.10
50	919.633	340.1	-470.2		0.068		-11.10	-66085.59	-6.61	14.4%	81522.05	1222830.80	-21923.28	1200907.52	2.21	1.64	1704.83
100	869.633	321.6	-438.7		0.136		-10.29	-71275.32	-7.13	26.2%	83922.05	1258830.80	-23644.92	1235185.88	2.04	1.52	1870.57
150	819.633	303.2	-407.2		0.204		-9.49	-77349.62	-7.73	36.1%	86322.05	1294830.80	-25660.01	1269170.79	1.90	1.41	2036.30
200	769.633	284.7	-375.7		0.273		-8.68	-84555.71	-8.46	44.5%	88722.05	1330830.80	-28050.56	1302780.23	1.78	1.32	2202.03
250	719.633	266.2	-344.2		0.341		-7.87	-93242.42	-9.32	51.8%	91122.05	1366830.80	-30932.30	1335898.50	1.67	1.24	2367.76
300	669.633	247.7	-312.7		0.409		-7.06	-103918.31	-10.39	58.0%	93522.05	1402830.80	-34473.92	1368356.87	1.57	1.17	2533.50
310	659.633	244.0	-306.4		0.422		-6.90	-106353.73	-10.64	59.2%	94002.05	1410030.80	-35281.85	1374748.94	1.55	1.16	2566.64
796.2	173.423	64.1	0.0		1.085		0.96	762522.67	76.25	93.4%	117340.13	1760102.01	252959.74	2013061.75	1.00	0.74	4178.26
800	169.633	62.7	2.4		1.090		1.02	716870.75	71.69	93.6%	117522.05	1762830.80	237815.14	2000645.94	1.00	0.74	4190.83
810	159.633	59.0	8.7		1.104		1.19	619076.41	61.91	94.0%	118002.05	1770030.80	205372.79	1975403.58	0.99	0.74	4223.97
820	149.633	55.3	15.0		1.118		1.35	544761.00	54.48	94.4%	118482.05	1777230.80	180719.35	1957950.14	0.98	0.73	4257.12
830	139.633	51.6	21.3		1.131		1.51	486375.34	48.64	94.8%	118962.05	1784430.80	161350.45	1945781.25	0.98	0.73	4290.27
840	129.633	47.9	27.6		1.145		1.67	439293.35	43.93	95.2%	119442.05	1791630.80	145731.45	1937362.24	0.97	0.72	4323.41
850	119.633	44.2	33.9		1.158		1.83	400522.11	40.05	95.6%	119922.05	1798830.80	132869.45	1931700.25	0.96	0.72	4356.56
860	109.633	40.5	40.2		1.172		1.99	368039.59	36.80	96.0%	120402.05	1806030.80	122093.68	1928124.48	0.96	0.71	4389.71
870	99.633	36.9	46.5		1.186		2.16	340430.53	34.04	96.4%	120882.05	1813230.80	112934.63	1926165.43	0.95	0.71	4422.85
880	89.633	33.2	52.8		1.199		2.32	316674.69	31.67	96.8%	121362.05	1820430.80	105053.85	1925484.65	0.94	0.70	4456.00
890	79.633	29.5	59.1		1.213		2.48	296018.02	29.60	97.2%	121842.05	1827630.80	98201.20	1925832.00	0.94	0.70	4489.15
900	69.633	25.8	65.4		1.227		2.64	277891.21	27.79	97.6%	122322.05	1834830.80	92187.80	1927018.59	0.93	0.69	4522.29
910	59.633	22.1	71.7		1.240		2.80	261856.30	26.19	97.9%	122802.05	1842030.80	86868.37	1928899.16	0.92	0.69	4555.44
920	49.633	18.4	78.0		1.254		2.96	247570.94	24.76	98.3%	123282.05	1849230.80	82129.33	1931360.13	0.92	0.68	4588.59
969.633	0	0.0	109.3		1.321		3.77	194819.79	19.48	100.0%	125664.44	1884966.56	64629.64	1949596.19	0.89	0.66	4753.10

Table C6: PT-Syngas data

W_e	Q_{ST}	$W_{Q_{st}}$	T_0S_{gen}	I_F	V_{OP}	ASR	j	Ae	Ae	f	EC_T	EC_T	PEC_{ELEC}	C_T	η_{WS}	η_W	A_S
kW	kW	kW	kW	kA	v	Ω cm2	A/cm2	cm2	m2		USD/yr	USD/t	USD	USD	%	%	m^2
0	894.5	330.8	-434.9	606.0	0.00	0.08	-11.91	-50859.61	-5.09	0.00	72988.64	1094829.54	-16872.20	1077957.34	231.5%	193.5%	1419.79
100	794.5	293.8	-371.9		0.17		-9.96	-60861.12	-6.09	0.28	77788.64	1166829.54	-20190.11	1146639.44	194.4%	162.5%	1751.26
200	694.5	256.9	-308.9		0.33		-8.00	-75759.11	-7.58	0.47	82588.64	1238829.54	-25132.37	1213697.17	167.6%	140.1%	2082.72
300	594.5	219.9	-245.9		0.50		-6.04	-100314.83	-10.03	0.61	87388.64	1310829.54	-33278.50	1277551.04	147.3%	123.1%	2414.19
400	494.5	182.9	-182.9		0.66		-4.08	-148423.05	-14.84	0.71	92188.64	1382829.54	-49237.95	1333591.59	131.4%	109.8%	2745.66
450.7	443.7	164.1	-150.9		0.74		-3.09	-196171.88	-19.62	0.76	94624.84	1419372.55	-65078.18	1354294.37	124.5%	104.1%	2913.89
462	432.5	160.0	-143.8		0.76		-2.87	-211228.70	-21.12	0.77	95164.64	1427469.54	-70073.14	1357396.40	123.1%	102.9%	2951.16
690.2	204.2	75.5	0.0		1.14		1.60	378790.38	37.88	0.91	106119.39	1591790.86	125660.15	1717451.02	100.0%	83.6%	3707.65
700	194.5	71.9	6.2		1.16		1.79	338311.62	33.83	0.92	106588.64	1598829.54	112231.71	1711061.25	99.2%	82.9%	3740.05
705	189.5	70.1	9.3		1.16		1.89	320779.05	32.08	0.92	106828.64	1602429.54	106415.44	1708844.98	98.8%	82.6%	3756.63
710	184.5	68.2	12.5		1.17		1.99	304974.15	30.50	0.92	107068.64	1606029.54	101172.31	1707201.85	98.4%	82.2%	3773.20
715	179.5	66.4	15.6		1.18		2.08	290653.54	29.07	0.92	107308.64	1609629.54	96421.58	1706051.12	98.0%	81.9%	3789.77
720	174.5	64.5	18.8		1.19		2.18	277617.51	27.76	0.93	107548.64	1613229.54	92097.00	1705326.55	97.6%	81.6%	3806.35
725	169.5	62.7	21.9		1.20		2.28	265700.64	26.57	0.93	107788.64	1616829.54	88143.69	1704973.24	97.2%	81.3%	3822.92
730	164.5	60.8	25.1		1.20		2.38	254764.74	25.48	0.93	108028.64	1620429.54	84515.81	1704945.35	96.8%	80.9%	3839.49
735	159.5	59.0	28.2		1.21		2.48	244693.46	24.47	0.93	108268.64	1624029.54	81174.76	1705204.30	96.4%	80.6%	3856.07
740	154.5	57.1	31.4		1.22		2.57	235388.18	23.54	0.94	108508.64	1627629.54	78087.82	1705717.36	96.1%	80.3%	3872.64
745	149.5	55.3	34.5		1.23		2.67	226764.69	22.68	0.94	108748.64	1631229.54	75227.06	1706456.60	95.7%	80.0%	3889.21
750	144.5	53.4	37.7		1.24		2.77	218750.72	21.88	0.94	108988.64	1634829.54	72568.50	1707398.04	95.3%	79.7%	3905.79
755	139.5	51.6	40.8		1.25		2.87	211283.85	21.13	0.94	109228.64	1638429.54	70091.43	1708520.98	94.9%	79.3%	3922.36
760	134.5	49.7	44.0		1.25		2.97	204309.91	20.43	0.95	109468.64	1642029.54	67777.89	1709807.43	94.6%	79.0%	3938.93
765	129.5	47.9	47.1		1.26		3.06	197781.64	19.78	0.95	109708.64	1645629.54	65612.20	1711241.74	94.2%	78.7%	3955.51
770	124.5	46.0	50.3		1.27		3.16	191657.64	19.17	0.95	109948.64	1649229.54	63580.62	1712810.16	93.8%	78.4%	3972.08
775	119.5	44.2	53.4		1.28		3.26	185901.49	18.59	0.95	110188.64	1652829.54	61671.08	1714500.62	93.5%	78.1%	3988.65
780	114.5	42.3	56.6		1.29		3.36	180481.02	18.05	0.95	110428.64	1656429.54	59872.89	1716302.43	93.1%	77.8%	4005.23
785	109.5	40.5	59.7		1.30		3.46	175367.69	17.54	0.96	110668.64	1660029.54	58176.59	1718206.13	92.8%	77.5%	4021.80
894.5	0.0	0.0	128.7		1.48		5.60	108232.57	10.82	1.00	115923.13	1738846.92	35905.14	1774752.06	85.6%	71.6%	4384.65

Table C7: PT-Methanol data

W_e kW	Q_{ST} kW	W_{Qst} kW	T_0S_{gen} kW	I_F kA	V_{OP} v	ASR Ω cm2	j A/cm2	Ae cm2	Ae m2	f	EC_T USD/yr	EC_T USD/t	PEC_{ELEC} USD	C_T USD	η_{WS} %	η_W %	A_S m^2
0.00	912.93	337.66	-545.24	727.5	0.0	0.084	-11.9	-61073.4	-6.1	0.0%	74495.4	1117431.0	-20260.5	1097170.5	261.5%	189.5%	1449.1
100.00	812.93	300.67	-482.23		0.1		-10.3	-70761.5	-7.1	27.5%	78335.4	1175031.0	-23474.5	1151556.6	220.4%	159.7%	1780.6
200.00	712.93	263.69	-419.21		0.3		-8.6	-84102.8	-8.4	46.4%	82175.4	1232631.0	-27900.3	1204730.7	190.4%	138.0%	2112.0
300.00	612.93	226.70	-356.20		0.4		-7.0	-103643.7	-10.4	60.2%	86015.4	1290231.0	-34382.8	1255848.2	167.6%	121.5%	2443.5
400.00	512.93	189.71	-293.19		0.5		-5.4	-135013.4	-13.5	70.7%	89855.4	1347831.0	-44789.4	1303041.6	149.7%	108.5%	2775.0
500.00	412.93	152.73	-230.17		0.7		-3.8	-193614.4	-19.4	78.9%	93695.4	1405431.0	-64229.7	1341201.3	135.3%	98.0%	3106.4
865.27	47.66	17.63	0.00		1.2		2.2	330725.7	33.1	98.2%	107721.9	1615828.0	109715.2	1725543.2	100.0%	72.5%	4317.2
870.00	42.93	15.88	2.98		1.2		2.3	319526.5	32.0	98.4%	107903.4	1618551.0	105999.9	1724550.9	99.7%	72.2%	4332.9
875.00	37.93	14.03	6.13		1.2		2.4	308478.3	30.8	98.6%	108095.4	1621431.0	102334.8	1723765.8	99.3%	72.0%	4349.4
880.00	32.93	12.18	9.28		1.2		2.4	298168.5	29.8	98.8%	108287.4	1624311.0	98914.6	1723225.6	99.0%	71.7%	4366.0
885.00	27.93	10.33	12.43		1.2		2.5	288525.7	28.9	99.0%	108479.4	1627191.0	95715.7	1722906.7	98.6%	71.5%	4382.6
890.00	22.93	8.48	15.58		1.2		2.6	279487.0	27.9	99.2%	108671.4	1630071.0	92717.2	1722788.2	98.3%	71.2%	4399.1
895.00	17.93	6.63	18.73		1.2		2.7	270997.4	27.1	99.4%	108863.4	1632951.0	89900.8	1722851.9	97.9%	71.0%	4415.7
900.00	12.93	4.78	21.88		1.2		2.8	263008.3	26.3	99.5%	109055.4	1635831.0	87250.5	1723081.6	97.6%	70.7%	4432.3
905.00	7.93	2.93	25.03		1.2		2.8	255476.8	25.5	99.7%	109247.4	1638711.0	84752.0	1723463.1	97.2%	70.5%	4448.9
910.00	2.93	1.09	28.18		1.3		2.9	248364.6	24.8	99.9%	109439.4	1641591.0	82392.6	1723983.7	96.9%	70.2%	4465.4
912.93	0.00	0.00	30.03		1.3		3.0	244372.8	24.4	100.0%	109552.1	1643280.9	81068.4	1724349.3	96.7%	70.1%	4475.2

Table C8: Data from PT-DME

W_e kW	Q_{ST} kW	W_{Qst} kW	T_0S_{gen} kW	I_F kA	V_{OP} v	ASR Ω cm2	j A/cm2	Ae cm2	Ae m2	f	EC_T USD/yr	EC_T USD/t	PEC_{ELEC} USD	C_T USD	η_{WS} %	η_W %	A_S m^2
0.00	882.10	326.25	-511.87	699.4	0.0	0.084	-11.9	-58715.6	-5.9	0.0%	71979.3	1079689.2	-19478.4	1060210.8	256.9%	196.2%	1400.2
50.00	832.10	307.76	-480.36		0.1		-11.1	-63217.0	-6.3	15.7%	74379.3	1115689.2	-20971.6	1094717.5	234.3%	178.9%	1565.9
100.00	782.10	289.27	-448.86		0.1		-10.2	-68465.9	-6.8	28.3%	76779.3	1151689.2	-22712.9	1128976.3	215.3%	164.4%	1731.6
150.00	732.10	270.78	-417.35		0.2		-9.4	-74665.3	-7.5	38.8%	79179.3	1187689.2	-24769.5	1162919.7	199.2%	152.1%	1897.4
200.00	682.10	252.28	-385.84		0.3		-8.5	-82099.1	-8.2	47.5%	81579.3	1223689.2	-27235.6	1196453.6	185.3%	141.5%	2063.1
250.00	632.10	233.79	-354.33		0.4		-7.7	-91176.9	-9.1	55.0%	83979.3	1259689.2	-30247.1	1229442.1	173.2%	132.3%	2228.8
300.00	582.10	215.30	-322.83		0.4		-6.8	-102511.8	-10.3	61.4%	86379.3	1295689.2	-34007.3	1261681.9	162.6%	124.2%	2394.6
310.00	572.10	211.60	-316.53		0.4		-6.7	-105125.6	-10.5	62.6%	86859.3	1302889.2	-34874.4	1268014.8	160.7%	122.7%	2427.7
812.31	69.79	25.81	0.00		1.2		1.9	374424.2	37.4	97.3%	110970.3	1664554.3	124211.7	1788766.0	100.0%	76.4%	4092.7
814.00	68.10	25.19	1.06		1.2		1.9	368773.3	36.9	97.4%	111051.3	1665769.2	122337.1	1788106.3	99.9%	76.3%	4098.3
816.00	66.10	24.45	2.32		1.2		1.9	362292.4	36.2	97.4%	111147.3	1667209.2	120187.1	1787396.3	99.7%	76.1%	4104.9
818.00	64.10	23.71	3.58		1.2		2.0	356035.3	35.6	97.5%	111243.3	1668649.2	118111.4	1786760.6	99.6%	76.0%	4111.5
820.00	62.10	22.97	4.84		1.2		2.0	349990.8	35.0	97.6%	111339.3	1670089.2	116106.1	1786195.3	99.4%	75.9%	4118.2
822.00	60.10	22.23	6.10		1.2		2.0	344148.0	34.4	97.7%	111435.3	1671529.2	114167.9	1785697.1	99.3%	75.8%	4124.8
824.00	58.10	21.49	7.36		1.2		2.1	338497.1	33.8	97.8%	111531.3	1672969.2	112293.2	1785262.4	99.1%	75.7%	4131.4
826.00	56.10	20.75	8.62		1.2		2.1	333028.8	33.3	97.8%	111627.3	1674409.2	110479.2	1784888.4	99.0%	75.6%	4138.1
828.00	54.10	20.01	9.89		1.2		2.1	327734.3	32.8	97.9%	111723.3	1675849.2	108722.8	1784572.0	98.8%	75.5%	4144.7
830.00	52.10	19.27	11.15		1.2		2.2	322605.6	32.3	98.0%	111819.3	1677289.2	107021.4	1784310.6	98.7%	75.4%	4151.3
832.00	50.10	18.53	12.41		1.2		2.2	317634.9	31.8	98.1%	111915.3	1678729.2	105372.4	1784101.6	98.5%	75.2%	4158.0
834.00	48.10	17.79	13.67		1.2		2.2	312815.0	31.3	98.2%	112011.3	1680169.2	103773.4	1783942.6	98.4%	75.1%	4164.6
836.00	46.10	17.05	14.93		1.2		2.3	308139.3	30.8	98.2%	112107.3	1681609.2	102222.3	1783831.5	98.3%	75.0%	4171.2
838.00	44.10	16.31	16.19		1.2		2.3	303601.2	30.4	98.3%	112203.3	1683049.2	100716.9	1783766.0	98.1%	74.9%	4177.8
840.00	42.10	15.57	17.45		1.2		2.3	299194.9	29.9	98.4%	112299.3	1684489.2	99255.1	1783744.3	98.0%	74.8%	4184.5
842.00	40.10	14.83	18.71		1.2		2.4	294914.7	29.5	98.5%	112395.3	1685929.2	97835.2	1783764.4	97.8%	74.7%	4191.1
844.00	38.10	14.09	19.97		1.2		2.4	290755.2	29.1	98.6%	112491.3	1687369.2	96455.3	1783824.5	97.7%	74.6%	4197.7
846.00	36.10	13.35	21.23		1.2		2.4	286711.4	28.7	98.6%	112587.3	1688809.2	95113.8	1783923.0	97.5%	74.5%	4204.4
848.00	34.10	12.61	22.49		1.2		2.5	282778.5	28.3	98.7%	112683.3	1690249.2	93809.1	1784058.3	97.4%	74.4%	4211.0
850.00	32.10	11.87	23.75		1.2		2.5	278952.1	27.9	98.8%	112779.3	1691689.2	92539.7	1784228.9	97.2%	74.3%	4217.6
852.00	30.10	11.13	25.01		1.2		2.5	275227.8	27.5	98.9%	112875.3	1693129.2	91304.3	1784433.4	97.1%	74.1%	4224.2
854.00	28.10	10.39	26.27		1.2		2.6	271601.7	27.2	98.9%	112971.3	1694569.2	90101.3	1784670.5	97.0%	74.0%	4230.9
856.00	26.10	9.65	27.53		1.2		2.6	268069.9	26.8	99.0%	113067.3	1696009.2	88929.7	1784938.9	96.8%	73.9%	4237.5
858.00	24.10	8.91	28.79		1.2		2.6	264628.8	26.5	99.1%	113163.3	1697449.2	87788.1	1785237.3	96.7%	73.8%	4244.1
860.00	22.10	8.17	30.05		1.2		2.7	261274.8	26.1	99.2%	113259.3	1698889.2	86675.5	1785564.7	96.5%	73.7%	4250.8
862.00	20.10	7.43	31.31		1.2		2.7	258004.9	25.8	99.3%	113355.3	1700329.2	85590.7	1785919.9	96.4%	73.6%	4257.4
864.00	18.10	6.69	32.57		1.2		2.7	254815.8	25.5	99.3%	113451.3	1701769.2	84532.7	1786301.9	96.3%	73.5%	4264.0
882.10	0.00	0.00	43.98		1.3		3.1	229180.1	22.9	100.0%	114320.0	1714800.5	76028.3	1790828.8	95.0%	72.6%	4324.0

Table C9: PT-Ethylene

W_e kW	Q_{ST} kW	$W_{Q_{st}}$ kW	T_0S_{gen} kW	I_F kA	V_{OP} v	ASR Ω cm2	j A/cm2	Ae cm2	Ae m2	f	EC_T USD/yr	EC_T USD/t	PEC_{ELEC} USD	C_T USD	η_{WS} %	η_W %	A_S m^2
0.00	855.74	316.51	-491.02	702.14	0.00	0.084	-11.91	-58945.84	-5.89	0.00%	69828.37	1047425.61	-19554.73	1027870.88	255.1%	202.2%	1358.32
50.00	805.74	298.01	-459.52		0.07		-11.07	-63445.86	-6.34	16.08%	72228.37	1083425.61	-21047.57	1062378.04	232.0%	183.9%	1524.05
100.00	755.74	279.52	-428.01		0.14		-10.22	-68689.75	-6.87	29.01%	74628.37	1119425.61	-22787.18	1096638.43	212.8%	168.6%	1689.78
150.00	705.74	261.03	-396.50		0.21		-9.38	-74878.57	-7.49	39.63%	77028.37	1155425.61	-24840.26	1130585.34	196.5%	155.7%	1855.52
200.00	655.74	242.53	-365.00		0.28		-8.53	-82293.02	-8.23	48.50%	79428.37	1191425.61	-27299.94	1164125.67	182.5%	144.6%	2021.25
250.00	605.74	224.04	-333.49		0.36		-7.69	-91337.20	-9.13	56.04%	81828.37	1227425.61	-30300.26	1197125.35	170.4%	135.0%	2186.98
300.00	555.74	205.55	-301.98		0.43		-6.84	-102614.78	-10.26	62.51%	84228.37	1263425.61	-34041.49	1229384.12	159.7%	126.6%	2352.72
310.00	545.74	201.85	-295.68		0.44		-6.67	-105212.95	-10.52	63.69%	84708.37	1270625.61	-34903.41	1235722.20	157.8%	125.0%	2385.86
779.23	76.51	28.30	0.00		1.11		1.26	559409.26	55.94	96.92%	107231.51	1608472.68	185578.77	1794051.45	100.0%	79.3%	3941.21
800.00	55.74	20.62	13.09		1.14		1.61	437180.68	43.72	97.79%	108228.37	1623425.61	145030.59	1768456.20	98.4%	78.0%	4010.04
805.00	50.74	18.77	16.24		1.15		1.69	415332.51	41.53	98.00%	108468.37	1627025.61	137782.66	1764808.27	98.0%	77.7%	4026.62
810.00	45.74	16.92	19.39		1.15		1.78	395564.12	39.56	98.20%	108708.37	1630625.61	131224.68	1761850.29	97.7%	77.4%	4043.19
815.00	40.74	15.07	22.54		1.16		1.86	377592.05	37.76	98.41%	108948.37	1634225.61	125262.62	1759488.23	97.3%	77.1%	4059.76
820.00	35.74	13.22	25.69		1.17		1.94	361182.10	36.12	98.61%	109188.37	1637825.61	119818.77	1757644.38	96.9%	76.8%	4076.34
825.00	30.74	11.37	28.84		1.17		2.03	346139.07	34.61	98.81%	109428.37	1641425.61	114828.39	1756254.00	96.6%	76.5%	4092.91
830.00	25.74	9.52	31.99		1.18		2.11	332299.01	33.23	99.01%	109668.37	1645025.61	110237.08	1755262.69	96.2%	76.2%	4109.48
835.00	20.74	7.67	35.14		1.19		2.20	319523.16	31.95	99.20%	109908.37	1648625.61	105998.81	1754624.42	95.8%	75.9%	4126.06
840.00	15.74	5.82	38.29		1.20		2.28	307693.33	30.77	99.40%	110148.37	1652225.61	102074.37	1754299.98	95.5%	75.7%	4142.63
845.00	10.74	3.97	41.44		1.20		2.37	296708.18	29.67	99.59%	110388.37	1655825.61	98430.15	1754255.76	95.1%	75.4%	4159.20
846.00	9.74	3.60	42.07		1.20		2.38	294604.60	29.46	99.63%	110436.37	1656545.61	97732.31	1754277.92	95.0%	75.3%	4162.52
847.00	8.74	3.23	42.70		1.21		2.40	292530.65	29.25	99.67%	110484.37	1657265.61	97044.30	1754309.91	95.0%	75.3%	4165.83
848.00	7.74	2.86	43.33		1.21		2.42	290485.69	29.05	99.71%	110532.37	1657985.61	96365.90	1754351.51	94.9%	75.2%	4169.15
849.00	6.74	2.49	43.96		1.21		2.43	288469.13	28.85	99.74%	110580.37	1658705.61	95696.93	1754402.53	94.8%	75.2%	4172.46
850.00	5.74	2.12	44.59		1.21		2.45	286480.37	28.65	99.78%	110628.37	1659425.61	95037.17	1754462.78	94.8%	75.1%	4175.78
855.74	0.00	0.00	48.21		1.22		2.55	275575.36	27.56	100.00%	110903.89	1663558.32	91419.54	1754977.86	94.4%	74.8%	4194.80

Table C10: PT-Ethane

W_e	Q_{ST}	$W_{Q_{st}}$	T_0S_{gen}	I_F	V_{OP}	ASR	j	Ae	Ae	f	EC_T	EC_T	PEC_{ELEC}	C_T	η_{WS}	η_W	A_S
kW	kW	kW	kW	kA	v	Ω cm2	A/cm2	cm2	m2		USD/yr	USD/t	USD	USD	%	%	m^2
0.0	800.2	296.0	-456.5	692.590	0.000	0.084	-11.912	-58143.929	-5.814	0.00%	65294.24	979413.55	-19288.70	960124.85	254.2%	216.2%	1270.12
25.0	775.2	286.7	-440.7		0.036		-11.483	-60312.313	-6.031	9.06%	66494.24	997413.55	-20008.04	977405.51	241.4%	205.3%	1352.98
50.0	750.2	277.5	-425.0		0.072		-11.055	-62648.696	-6.265	17.07%	67694.24	1015413.55	-20783.12	994630.44	229.8%	195.4%	1435.85
75.0	725.2	268.2	-409.2		0.108		-10.627	-65173.387	-6.517	24.21%	68894.24	1033413.55	-21620.66	1011792.90	219.2%	186.5%	1518.72
100.0	700.2	259.0	-393.4		0.144		-10.199	-67910.108	-6.791	30.61%	70094.24	1051413.55	-22528.54	1028885.01	209.6%	178.3%	1601.58
25.0	775.2	286.7	-440.7		0.036		-11.483	-60312.313	-6.031	9.06%	66494.24	997413.55	-20008.04	977405.51	241.4%	205.3%	1352.98
50.0	750.2	277.5	-425.0		0.072		-11.055	-62648.696	-6.265	17.07%	67694.24	1015413.55	-20783.12	994630.44	229.8%	195.4%	1435.85
75.0	725.2	268.2	-409.2		0.108		-10.627	-65173.387	-6.517	24.21%	68894.24	1033413.55	-21620.66	1011792.90	219.2%	186.5%	1518.72
706.4	93.8	34.7	-11.3		1.020		0.189	3658039.156	365.804	95.88%	99202.05	1488030.68	1213520.16	2701550.83	101.5%	86.4%	3611.64
707.5	92.7	34.3	-10.6		1.022		0.208	3330402.542	333.040	95.93%	99254.24	1488813.55	1104829.79	2593643.34	101.4%	86.3%	3615.24
710.0	90.2	33.4	-9.1		1.025		0.251	2761684.834	276.168	96.05%	99374.24	1490613.55	916163.02	2406776.58	101.2%	86.1%	3623.53
712.5	87.7	32.4	-7.5		1.029		0.294	2358871.130	235.887	96.17%	99494.24	1492413.55	782533.36	2274946.91	101.0%	85.9%	3631.81
715.0	85.2	31.5	-5.9		1.032		0.336	2058606.932	205.861	96.29%	99614.24	1494213.55	682923.53	2177137.08	100.8%	85.7%	3640.10
717.5	82.7	30.6	-4.3		1.036		0.379	1826153.189	182.615	96.40%	99734.24	1496013.55	605809.18	2101822.74	100.6%	85.6%	3648.39
720.0	80.2	29.7	-2.8		1.040		0.422	1640869.513	164.087	96.52%	99854.24	1497813.55	544343.06	2042156.61	100.4%	85.4%	3656.67
722.5	77.7	28.7	-1.2		1.043		0.465	1489720.680	148.972	96.64%	99974.24	1499613.55	494200.85	1993814.41	100.2%	85.2%	3664.96
724.4	75.8	28.0	0.0		1.046		0.497	1393116.017	139.312	96.72%	100064.57	1500968.60	462153.16	1963121.76	100.0%	85.1%	3671.20
727.5	72.7	26.9	2.0		1.050		0.551	1257965.486	125.797	96.87%	100214.24	1503213.55	417318.24	1920531.80	99.7%	84.8%	3681.53
730.0	70.2	26.0	3.5		1.054		0.593	1167176.888	116.718	96.98%	100334.24	1505013.55	387199.98	1892213.53	99.5%	84.7%	3689.82
732.5	67.7	25.0	5.1		1.058		0.636	1088610.784	108.861	97.10%	100454.24	1506813.55	361136.41	1867949.96	99.3%	84.5%	3698.11
735.0	65.2	24.1	6.7		1.061		0.679	1019954.641	101.995	97.21%	100574.24	1508613.55	338360.38	1846973.93	99.1%	84.3%	3706.39
737.5	62.7	23.2	8.3		1.065		0.722	959444.703	95.944	97.32%	100694.24	1510413.55	318286.78	1828700.33	98.9%	84.1%	3714.68
740.0	60.2	22.3	9.8		1.068		0.765	905712.316	90.571	97.43%	100814.24	1512213.55	300461.56	1812675.11	98.7%	84.0%	3722.97
742.5	57.7	21.3	11.4		1.072		0.808	857679.169	85.768	97.55%	100934.24	1514013.55	284527.01	1798540.57	98.5%	83.8%	3731.25
745.0	55.2	20.4	13.0		1.076		0.850	814484.175	81.448	97.66%	101054.24	1515813.55	270197.48	1786011.04	98.3%	83.6%	3739.54
747.5	52.7	19.5	14.6		1.079		0.893	775431.396	77.543	97.77%	101174.24	1517613.55	257242.09	1774855.64	98.1%	83.4%	3747.83
750.0	50.2	18.6	16.1		1.083		0.936	739952.264	73.995	97.88%	101294.24	1519413.55	245472.22	1764885.77	97.9%	83.3%	3756.11
752.5	47.7	17.6	17.7		1.087		0.979	707577.713	70.758	97.99%	101414.24	1521213.55	234732.27	1755945.82	97.7%	83.1%	3764.40
755.0	45.2	16.7	19.3		1.090		1.022	677917.328	67.792	98.10%	101534.24	1523013.55	224892.71	1747906.27	97.5%	82.9%	3772.69
757.5	42.7	15.8	20.9		1.094		1.064	650643.521	65.064	98.21%	101654.24	1524813.55	215844.88	1740658.44	97.3%	82.8%	3780.97
760.0	40.2	14.9	22.4		1.097		1.107	625479.386	62.548	98.32%	101774.24	1526613.55	207496.92	1734110.47	97.1%	82.6%	3789.26
762.5	37.7	13.9	24.0		1.101		1.150	602189.256	60.219	98.43%	101894.24	1528413.55	199770.63	1728184.19	96.9%	82.4%	3797.55
765.0	35.2	13.0	25.6		1.105		1.193	580571.307	58.057	98.53%	102014.24	1530213.55	192599.08	1722812.64	96.7%	82.3%	3805.83
767.5	32.7	12.1	27.2		1.108		1.236	560451.693	56.045	98.64%	102134.24	1532013.55	185924.59	1717938.14	96.5%	82.1%	3814.12
770.0	30.2	11.2	28.7		1.112		1.279	541679.856	54.168	98.75%	102254.24	1533813.55	179697.21	1713510.76	96.3%	81.9%	3822.41
772.5	27.7	10.2	30.3		1.115		1.321	524124.757	52.412	98.85%	102374.24	1535613.55	173873.47	1709487.02	96.1%	81.8%	3830.69
775.0	25.2	9.3	31.9		1.119		1.364	507671.813	50.767	98.96%	102494.24	1537413.55	168415.36	1705828.91	95.9%	81.6%	3838.98
800.1	0.1	0.0	47.7		1.155		1.794	386113.690	38.611	100.00%	103697.72	1555465.85	128089.59	1683555.44	94.0%	80.0%	3922.09

Table C11: PT-Ethanol data

W_e	Q_{ST}	W_{Qst}	T_0S_{gen}	I_F	V_{OP}	ASR	j	Ae	Ae	f	EC_T	EC_T	PEC_{ELEC}	C_T	η_{WS}	η_W	A_S
kW	kW	kW	kW	kA	v	Ω cm2	A/cm2	cm2	m2		USD/yr	USD/t	USD	USD	%	%	m^2
0.0	928.2	343.3	-544.8	736.15	0.00	0.08	-11.91	-61801.28	-6.18	0.0%	75743.82	1136157.28	-20501.99	1115655.28	258.7%	186.4%	1473.39
50.0	878.2	324.8	-513.3		0.07		-11.11	-66285.49	-6.63	15.0%	78143.82	1172157.28	-21989.59	1150167.69	236.9%	170.7%	1639.12
100.0	828.2	306.3	-481.8		0.14		-10.30	-71471.34	-7.15	27.2%	80543.82	1208157.28	-23709.95	1184447.33	218.6%	157.5%	1804.85
150.0	778.2	287.8	-450.2		0.20		-9.49	-77537.49	-7.75	37.3%	82943.82	1244157.28	-25722.33	1218434.94	202.8%	146.2%	1970.58
200.0	728.2	269.3	-418.7		0.27		-8.69	-84728.88	-8.47	45.9%	85343.82	1280157.28	-28108.01	1252049.27	189.2%	136.4%	2136.32
250.0	678.2	250.9	-387.2		0.34		-7.88	-93390.61	-9.34	53.2%	87743.82	1316157.28	-30981.46	1285175.82	177.3%	127.8%	2302.05
300.0	628.2	232.4	-355.7		0.41		-7.08	-104024.94	-10.40	59.6%	90143.82	1352157.28	-34509.30	1317647.98	166.8%	120.2%	2467.78
310.0	618.2	228.7	-349.4		0.42		-6.92	-106449.21	-10.64	60.8%	90623.82	1359357.28	-35313.53	1324043.75	164.9%	118.8%	2500.93
864.5	63.7	23.6	0.0		1.17		2.02	364204.57	36.42	97.7%	117240.58	1758608.73	120821.45	1879430.18	100.0%	72.1%	4338.96
870.0	58.2	21.5	3.5		1.18		2.11	348946.19	34.89	97.9%	117503.82	1762557.28	115759.62	1878316.90	99.6%	71.8%	4357.14
875.0	53.2	19.7	6.6		1.19		2.19	336107.91	33.61	98.1%	117743.82	1766157.28	111500.64	1877657.92	99.3%	71.5%	4373.71
880.0	48.2	17.8	9.8		1.20		2.27	324180.78	32.42	98.3%	117983.82	1769757.28	107543.93	1877301.21	98.9%	71.3%	4390.29
885.0	43.2	16.0	12.9		1.20		2.35	313071.14	31.31	98.4%	118223.82	1773357.28	103858.41	1877215.69	98.6%	71.0%	4406.86
890.0	38.2	14.1	16.1		1.21		2.43	302697.72	30.27	98.6%	118463.82	1776957.28	100417.13	1877374.41	98.2%	70.8%	4423.43
895.0	33.2	12.3	19.2		1.22		2.51	292989.69	29.30	98.8%	118703.82	1780557.28	97196.58	1877753.86	97.9%	70.5%	4440.01
900.0	28.2	10.4	22.4		1.22		2.59	283885.01	28.39	99.0%	118943.82	1784157.28	94176.19	1878333.47	97.5%	70.3%	4456.58
905.0	23.2	8.6	25.5		1.23		2.67	275329.14	27.53	99.2%	119183.82	1787757.28	91337.86	1879095.14	97.2%	70.1%	4473.15
910.0	18.2	6.7	28.7		1.24		2.75	267273.90	26.73	99.4%	119423.82	1791357.28	88665.61	1880022.89	96.9%	69.8%	4489.73
915.0	13.2	4.9	31.8		1.24		2.83	259676.60	25.97	99.5%	119663.82	1794957.28	86145.28	1881102.55	96.5%	69.6%	4506.30
920.0	8.2	3.0	35.0		1.25		2.92	252499.28	25.25	99.7%	119903.82	1798557.28	83764.27	1882321.54	96.2%	69.3%	4522.87
925.0	3.2	1.2	38.1		1.26		3.00	245708.03	24.57	99.9%	120143.82	1802157.28	81511.33	1883668.61	95.9%	69.1%	4539.45
928.2	0.0	0.0	40.2		1.26		3.05	241507.88	24.15	100.0%	120299.01	1804485.09	80117.97	1884603.06	95.7%	68.9%	4550.16

Table C12: PT-Propanol data

W_e	Q_{ST}	W_{Qst}	T_0S_{gen}	I_F	V_{OP}	ASR	j	Ae	Ae	f	EC_T	EC_T	PEC_{ELEC}	C_T	η_{WS}	η_W	A_S
kW	kW	kW	kW	kA	v	Ω cm2	A/cm2	cm2	m2		USD/yr	USD/t	USD	USD	%	%	m^2
0	878.9053	325.0733	-527.608	755.30	0.00	0.084	-11.91	-63408.20	-6.34	0.00%	71718.67	1075780.06	-21035.08	1054744.99	262.3%	196.9%	1395.09
50	828.9053	306.5802	-496.101		0.07		-11.13	-67884.18	-6.79	15.70%	74118.67	1111780.06	-22519.94	1089260.12	239.1%	179.5%	1560.82
100	778.9053	288.0871	-464.595		0.13		-10.34	-73040.07	-7.30	28.39%	76518.67	1147780.06	-24230.36	1123549.70	219.7%	164.9%	1726.55
150	728.9053	269.594	-433.088		0.20		-9.56	-79043.52	-7.90	38.86%	78918.67	1183780.06	-26221.95	1157558.12	203.2%	152.5%	1892.29
200	678.9053	251.101	-401.581		0.26		-8.77	-86122.25	-8.61	47.64%	81318.67	1219780.06	-28570.25	1191209.81	189.0%	141.9%	2058.02
250	628.9053	232.6079	-370.074		0.33		-7.98	-94593.56	-9.46	55.11%	83718.67	1255780.06	-31380.53	1224399.53	176.7%	132.6%	2223.75
300	578.9053	214.1148	-338.567		0.40		-7.20	-104913.23	-10.49	61.54%	86118.67	1291780.06	-34803.98	1256976.08	165.9%	124.5%	2389.49
310	568.9053	210.4162	-332.265		0.41		-7.04	-107253.39	-10.73	62.73%	86598.67	1298980.06	-35580.30	1263399.76	163.8%	123.0%	2422.63
837.2896	41.61569	15.39204	0		1.11		1.24	608863.20	60.89	98.42%	111908.57	1678628.56	201984.65	1880613.22	100.0%	75.1%	4170.42
840	38.90528	14.38957	1.707935		1.11		1.28	588659.86	58.87	98.52%	112038.67	1680580.06	195282.38	1875862.44	99.8%	74.9%	4179.40
842.5	36.40528	13.46491	3.283281		1.12		1.32	571178.31	57.12	98.62%	112158.67	1682380.06	189483.04	1871863.10	99.6%	74.8%	4187.69
845	33.90528	12.54026	4.858627		1.12		1.36	554705.12	55.47	98.72%	112278.67	1684180.06	184018.22	1868198.28	99.4%	74.6%	4195.97
847.5	31.40528	11.61561	6.433973		1.12		1.40	539155.49	53.92	98.81%	112398.67	1685980.06	178859.77	1864839.83	99.3%	74.5%	4204.26
850	28.90528	10.69095	8.009319		1.13		1.44	524453.87	52.45	98.91%	112518.67	1687780.06	173982.65	1861762.71	99.1%	74.4%	4212.55
852.5	26.40528	9.766298	9.584665		1.13		1.48	510532.74	51.05	99.01%	112638.67	1689580.06	169364.44	1858944.50	98.9%	74.2%	4220.83
855	23.90528	8.841644	11.16001		1.13		1.52	497331.54	49.73	99.10%	112758.67	1691380.06	164985.07	1856365.13	98.7%	74.1%	4229.12
857.5	21.40528	7.91699	12.73536		1.14		1.56	484795.83	48.48	99.20%	112878.67	1693180.06	160826.47	1854006.53	98.5%	74.0%	4237.41
860	18.90528	6.992336	14.3107		1.14		1.60	472876.54	47.29	99.29%	112998.67	1694980.06	156872.35	1851852.42	98.3%	73.8%	4245.69
862.5	16.40528	6.067682	15.88605		1.14		1.64	461529.29	46.15	99.39%	113118.67	1696780.06	153108.01	1849888.07	98.2%	73.7%	4253.98
865	13.90528	5.143028	17.4614		1.15		1.68	450713.85	45.07	99.48%	113238.67	1698580.06	149520.09	1848100.15	98.0%	73.6%	4262.27
867.5	11.40528	4.218374	19.03674		1.15		1.72	440393.71	44.04	99.58%	113358.67	1700380.06	146096.48	1846476.54	97.8%	73.4%	4270.55
870	8.905278	3.29372	20.61209		1.15		1.75	430535.59	43.05	99.67%	113478.67	1702180.06	142826.14	1845006.20	97.6%	73.3%	4278.84
878.9053	0	0	26.22365		1.16		1.89	398741.13	39.87	100.00%	113906.12	1708591.86	132278.63	1840870.49	97.0%	72.8%	4308.36

Appendix D: Aspen Plus® streams data

Table D1: Streams information for the PT-H_2 process powered by solar-PV only (f=100%)

									Material									
Stream Name	**Units**	**1**	**2**	**3**	**4**	**5**	**R-F**	**15**	**CATHODE3**	**ANODE2**	**CATHODE2**	**26**	**RECYCLE**	**ANODE1**	**CATHODE1**	**FEED**	**H2**	**O2**
Description																		
From		P-01	HX-1	HX-2	HX-3	HX-4	MIXER	B9	HX-5	HX-7	SPLITTER	EL-STACK	SPLITTER	SP	SP		HX-6	HX-8
To		HX-1	HX-2	HX-3	HX-4	EL-STACK	B9	SP	HX-6	HX-8	HX-5	MIXER	MIXER	HX-7	SPLITTER	P-01		
Stream Class		CONVEN	CONVEN	CONVEN	CONVEN	CONVEN	CONVEN	CONVEN	CONVEN	CONVEN	CONVEN	CONVEN	CONVEN	CONVEN	CONVEN	CONVEN	CONVEN	CONVEN
MIXED Substream																		
Phase		Liquid Phase	Liquid Phase	Liquid Phase			Vapor Phase	Vapor Phase	Vapor Phase	Vapor Phase	Vapor Phase	Vapor Phase	Vapor Phase	Vapor Phase	Vapor Phase	Liquid Phase	Vapor Phase	Vapor Phase
Temperature	C	25.4952	76.4265	169.94	180.968	180.968	749.661	750	300	300	750	750	750	750	750	25	30	30
Pressure	bar	10.1325	10.1325	10.1325	10.1325	10.1325	10.1325	10.1325	10.1325	10.1325	10.1325	10.1325	10.1325	10.1325	10.1325	1.01325	10.1325	10.1325
Molar Vapor Fraction		0	0	0	0.174249	0.52676	1	1	1	1	1	1	1	1	1	0	1	1
Molar Liquid Fraction		1	1	1	0.825751	0.47324	0	0	0	0	0	0	0	0	0	1	0	0
Molar Solid Fraction		0	0	0	0	0	0	0	0	0	0	0	0	0	0	0	0	0
Mass Vapor Fraction		0	0	0	0.174249	0.52676	1	1	1	1	1	1	1	1	1	0	1	1
Mass Liquid Fraction		1	1	1	0.825751	0.47324	0	0	0	0	0	0	0	0	0	1	0	0
Mass Solid Fraction		0	0	0	0	0	0	0	0	0	0	0	0	0	0	0	0	0
Molar Enthalpy	cal/mol	-68712.5	-67719.7	-65834.8	-64036.3	-60870.9	-45703.4	5266.45	1920.79	1996.73	5108.12	-51349.1	5108.12	5616.1	5108.12	-68725.8	35.8219	13.0581
Mass Enthalpy	cal/gm	-3814.12	-3759.01	-3654.39	-3554.55	-3378.85	-2784.19	465.196	952.829	62.4001	2533.94	-2850.31	2533.94	175.51	2533.94	-3814.86	17.7699	0.408081
Molar Entropy	cal/mol-K	-40.0906	-37.0214	-32.25	-28.2831	-21.3126	-2.99475	5.53003	-0.0199038	0.151058	4.07829	-4.49667	4.07829	4.79157	4.07829	-40.1199	-4.46309	-4.51132
Mass Entropy	cal/gm-K	-2.22536	-2.055	-1.79015	-1.56995	-1.18303	-0.182436	0.488479	-0.00987348	0.00472075	2.02308	-0.249603	2.02308	0.149742	2.02308	-2.22699	-2.21396	-0.140984
Molar Density	mol/cc	0.0551465	0.0523364	0.0466164	0.00157949	0.00053481	0.000119359	0.000118889	0.000212007	0.000212285	0.000118925	0.000119439	0.000118925	0.000118864	0.000118925	0.055173	0.000400064	0.00040547
Mass Density	gm/cc	0.993479	0.942855	0.839807	0.028455	0.00963474	0.00195931	0.00134594	0.000427381	0.00679288	0.000239738	0.00215172	0.000239738	0.00380352	0.000239738	0.993957	0.000806481	0.0129745
Enthalpy Flow	cal/sec	-228125	-224829	-218572	-212601	-202091	-168595	28169.7	6377.02	3314.57	16959	-170479	1884.33	9322.72	18843.3	-228170	118.929	21.6764
Average MW		18.0153	18.0153	18.0153	18.0153	18.0153	16.4153	11.3209	2.01588	31.9988	2.01588	18.0153	2.01588	31.9988	2.01588	18.0153	2.01588	31.9988
Mole Flows	kmol/hr	11.952	11.952	11.952	11.952	11.952	13.28	19.256	11.952	5.976	11.952	11.952	1.328	5.976	13.28	11.952	11.952	5.976
WATER	kmol/hr	11.952	11.952	11.952	11.952	11.952	11.952	0	0	0	0	11.952	0	0	0	11.952	0	0
HYDROGEN	kmol/hr	0	0	0	0	0	1.328	13.28	11.952	0	11.952	0	1.328	0	13.28	0	11.952	0
OXYGEN	kmol/hr	0	0	0	0	0	0	5.976	0	5.976	0	0	0	5.976	0	0	0	5.976
Mole Fractions																		
WATER		1	1	1	1	1	0.9	0	0	0	0	1	0	0	0	1	0	0
HYDROGEN		0	0	0	0	0	0.1	0.689655	1	0	1	0	1	0	1	0	1	0
OXYGEN		0	0	0	0	0	0	0.310345	0	1	0	0	0	1	0	0	0	1
Mass Flows	kg/hr	215.319	215.319	215.319	215.319	215.319	217.996	217.996	24.0938	191.225	24.0938	215.319	2.67709	191.225	26.7709	215.319	24.0938	191.225
WATER	kg/hr	215.319	215.319	215.319	215.319	215.319	215.319	0	0	0	0	215.319	0	0	0	215.319	0	0
HYDROGEN	kg/hr	0	0	0	0	0	2.67709	26.7709	24.0938	0	24.0938	0	2.67709	0	26.7709	0	24.0938	0
OXYGEN	kg/hr	0	0	0	0	0	0	191.225	0	191.225	0	0	0	191.225	0	0	0	191.225
Mass Fractions																		
WATER		1	1	1	1	1	0.98772	0	0	0	0	1	0	0	0	1	0	0
HYDROGEN		0	0	0	0	0	0.0122805	0.122805	1	0	1	0	1	0	1	0	1	0
OXYGEN		0	0	0	0	0	0	0.877195	0	1	0	0	0	1	0	0	0	1

Table D2: Streams information for the PT-H_2 process powered by solar-PV only (f_{OP}=96%)

										Material									
Stream Name	**Units**	**1**	**2**	**3**	**4**	**6**	**7**	**8**	**9**	**ANODE**	**ANODE1**	**CATHODE**	**CATHODE1**	**CATHODE2**	**H2-PROD**	**H2-RECY**	**H2O-S**	**H2OFEED**	**O2-PROD**	**5**
Description																				
From		P-1	HX-1	HX-2	HX-3	HX-4	EL-HE	STACK	MX-01	SP-ELEC	HX-5	SP-ELEC	SPLT-01	HX-7	HX-8	SPLT-01			HX-6	ST-FIELD
To		HX-1	HX-2	HX-3	ST-FIELD	EL-HE	MX-01	SP-ELEC	STACK	HX-5	HX-6	SPLT-01	HX-7	HX-8		MX-01		P-1		HX-4
Stream Class		CONVEN	CONVEN	CONVEN	CONVEN	CONVEN	CONVEN	CONVEN	CONVEN	CONVEN	CONVEN	CONVEN	CONVEN	CONVEN	CONVEN	CONVEN		CONVEN	CONVEN	CONVEN
MIXED Substream																				
Phase		Liquid Phase	Liquid Phase			Vapor Phase	Vapor Phase	Vapor Phase	Vapor Phase	Vapor Phase	Vapor Phase	Vapor Phase	Vapor Phase	Vapor Phase	Vapor Phase	Vapor Phase		Liquid Phase	Vapor Phase	Vapor Phase
Temperature	C	25.4612	82.5978	179.946	179.946	514.884	750	750	749.709	750	350	750	750	350	35	750		25	30	200
Pressure	bar	10	10	10	10	10	10	10	10	10	10	10	10	10	10	10		1.01325	10	10.1325
Molar Vapor Fraction		0	0	0.0145726	0.192589	1	1	1	1	1	1	1	1	1	1	1		0	1	1
Molar Liquid Fraction		1	1	0.985427	0.807411	0	0	0	0	0	0	0	0	0	0	0		1	0	0
Molar Solid Fraction		0	0	0	0	0	0	0	0	0	0	0	0	0	0	0		0	0	0
Mass Vapor Fraction		0	0	0.0145726	0.192589	1	1	1	1	1	1	1	1	1	1	1		0	1	1
Mass Liquid Fraction		1	1	0.985427	0.807411	0	0	0	0	0	0	0	0	0	0	0		1	0	0
Mass Solid Fraction		0	0	0	0	0	0	0	0	0	0	0	0	0	0	0		0	0	0
Molar Enthalpy	cal/mol	-68979.8	-67796	-65579.8	-63962.6	-53616.3	-51345.8	5266.43	-45700.4	5618.11	2383.73	5107.85	5107.85	2270.99	70.9866	5107.85		-68993.4	16.1409	-56453.1
Mass Enthalpy	cal/gm	-3828.96	-3763.25	-3640.23	-3550.47	-2976.15	-2850.12	465.195	-2784.01	175.573	74.4945	2533.8	2533.8	1126.55	35.2137	2533.8		-3829.72	0.504423	-3133.62
Molar Entropy	cal/mol-K	-38.9407	-35.7899	-31.0593	-27.607	-6.98689	-4.46919	5.55596	-2.96707	4.81876	0.821959	4.10393	4.10393	0.59196	-4.32249	4.10393		-38.9675	-4.48234	-11.5965
Mass Entropy	cal/gm-K	-2.16154	-1.98664	-1.72405	-1.53242	-0.387832	-0.248078	0.490769	-0.18075	0.150592	0.0256872	2.0358	2.0358	0.293648	-2.14422	2.0358		-2.16302	-0.140078	-0.643701
Molar Density	mol/cc	0.0533351	0.0503711	0.0133998	0.00141317	0.000153745	0.000117762	0.000117324	0.00011771	0.000117256	0.000192415	0.000117356	0.000117356	0.000192482	0.00038833	0.000117356		0.0533478	0.000398698	0.000269527
Mass Density	gm/cc	0.960847	0.90745	0.241402	0.0254587	0.00276976	0.00212151	0.00132821	0.00193225	0.00375205	0.00615706	0.000236576	0.000236576	0.000388021	0.000782827	0.000236576		0.961076	0.0127579	0.00485561
Enthalpy Flow	cal/sec	-229013	-225083	-217725	-212356	-178006	-170468	28169.6	-168584	9326.06	3957	18842.3	16958	7539.69	235.676	1884.23		-229058	26.7939	-187424
Average MW		18.0153	18.0153	18.0153	18.0153	18.0153	18.0153	11.3209	16.4153	31.9988	31.9988	2.01588	2.01588	2.01588	2.01588	2.01588		18.0153	31.9988	18.0153
Mole Flows	kmol/hr	11.952	11.952	11.952	11.952	11.952	11.952	19.256	13.28	5.976	5.976	13.28	11.952	11.952	11.952	1.328		11.952	5.976	11.952
H2	kmol/hr	0	0	0	0	0	0	13.28	1.328	0	0	13.28	11.952	11.952	11.952	1.328		0	0	0
O2	kmol/hr	0	0	0	0	0	0	5.976	0	5.976	5.976	0	0	0	0	0		0	5.976	0
H2O	kmol/hr	11.952	11.952	11.952	11.952	11.952	11.952	0	11.952	0	0	0	0	0	0	0		11.952	0	11.952
Mole Fractions																				
H2		0	0	0	0	0	0	0.689655	0.1	0	0	1	1	1	1	1		0	0	0
O2		0	0	0	0	0	0	0.310345	0	1	1	0	0	0	0	0		0	1	0
H2O		1	1	1	1	1	1	0	0.9	0	0	0	0	0	0	0		1	0	1
Mass Flows	kg/hr	215.319	215.319	215.319	215.319	215.319	215.319	217.996	217.996	191.225	191.225	26.7709	24.0938	24.0938	24.0938	2.67709		215.319	191.225	215.319
H2	kg/hr	0	0	0	0	0	0	26.7709	2.67709	0	0	26.7709	24.0938	24.0938	24.0938	2.67709		0	0	0
O2	kg/hr	0	0	0	0	0	0	191.225	0	191.225	191.225	0	0	0	0	0		0	191.225	0
H2O	kg/hr	215.319	215.319	215.319	215.319	215.319	215.319	0	215.319	0	0	0	0	0	0	0		215.319	0	215.319
Mass Fractions																				
H2		0	0	0	0	0	0	0.122805	0.0122805	0	0	1	1	1	1	1		0	0	0
O2		0	0	0	0	0	0	0.877195	0	1	1	0	0	0	0	0		0	1	0
H2O		1	1	1	1	1	1	0	0.98772	0	0	0	0	0	0	0		1	0	1

Table D3: Streams information for the PT-NH_3 process

Material																						
Stream Name	**Units**	**1**	**2**	**3**	**5**	**5**	**6**	**7**	**8**	**15**	**ANODE1**	**ANODE2**	**CATHODE1**	**CATHODE2**	**CATHODE3**	**H2-PRO**	**H2-R**	**H2O-FEED**	**N2-FEED**	**NH3-PROD**	**O2-PROD**	**RECYCLE**
Description																						
From		P-1	HX-1	HX-2	STACK	ST-FIELD	HX-04	EL-HE	MIX-01	HX-3	EL-SP	HX-07	EL-SP	SPLIT-01	HX-05	HX-06	SPLIT-01			MX-3	HX-08	HX-19
To		HX-1	HX-2	HX-3	EL-SP	HX-04	EL-HE	MIX-01	STACK	ST-FIELD	HX-07	HX-08	SPLIT-01	HX-05	HX-06	CPMP-1	MIX-01	P-1	COMP-4			MX-2
Stream Class		CONVEN	CONVEN	CONVEN	CONVEN	CONVEN	CONVEN	CONVEN	CONVEN	CONVEN	CONVEN	CONVEN	CONVEN	CONVEN	CONVEN	CONVEN	CONVEN	CONVEN	CONVEN	CONVEN	CONVEN	CONVEN
MIXED Substream																						
Phase		Liquid Phase	Liquid Phase	Liquid Phase	Vapor Phase	Vapor Phase	Vapor Phase	Vapor Phase	Vapor Phase		Vapor Phase	Vapor Phase	Vapor Phase	Vapor Phase	Vapor Phase	Vapor Phase	Vapor Phase	Liquid Phase	Vapor Phase		Vapor Phase	Vapor Phase
Temperature	C	25.4952	76.4757	169.899	750	200	552.483	750	749.661	180.404	750	300	750	750	300	30	750	25	25	-5.28939	30	295.344
Pressure	bar	10.1325	5	10.1325	10.1325	10.1325	10.1325	10.1325	10.1325	10	10.1325	10.1325	10.1325	10.1325	10.1325	10.1325	10.1325	1.01325	1.01325	135	10.1325	100
Molar Vapor Fraction		0	0	0	1	1	1	1	1	0.176563	1	1	1	1	1	1	1	0	1	9.59E-07	1	1
Molar Liquid Fraction		1	1	1	0	0	0	0	0	0.823437	0	0	0	0	0	0	0	1	0	0.999999	0	0
Molar Solid Fraction		0	0	0	0	0	0	0	0	0	0	0	0	0	0	0	0	0	0	0	0	0
Mass Vapor Fraction		0	0	0	1	1	1	1	1	0.176563	1	1	1	1	1	1	1	0	1	5.02E-07	1	1
Mass Liquid Fraction		1	1	1	0	0	0	0	0	0.823437	0	0	0	0	0	0	0	1	0	0.999999	0	0
Mass Solid Fraction		0	0	0	0	0	0	0	0	0	0	0	0	0	0	0	0	0	0	0	0	0
Molar Enthalpy	cal/mol	-68712.5	-67720.7	-65835.7	5266.45	-56454.1	-53266.8	-51349.1	-45703.4	-64026	5616.1	1996.73	5108.12	5108.12	1920.79	35.8219	5108.12	-68725.8	-1.84543	-16448.5	13.0581	1565.95
Mass Enthalpy	cal/gm	-3814.12	-3759.07	-3654.44	465.196	-3133.68	-2956.76	-2850.31	-2784.19	-3553.98	175.51	62.4001	2533.94	2533.94	952.829	17.7699	2533.94	-3814.86	-0.0658764	-968.533	0.408081	177.325
Molar Entropy	cal/mol-K	-40.0906	-37.0164	-32.2519	5.53003	-11.5941	-6.577	-4.49667	-2.99475	-28.256	4.79157	0.151058	4.07829	4.07829	-0.0199038	-4.46309	4.07829	-40.1199	-0.00532922	-46.9034	-4.51132	-4.00861
Mass Entropy	cal/gm-K	-2.22536	-2.05472	-1.79025	0.488479	-0.643572	-0.365079	-0.249603	-0.182436	-1.56845	0.149742	0.00472075	2.02308	2.02308	-0.00987348	-2.21396	2.02308	-2.22699	-0.000190238	-2.76181	-0.140984	-0.453927
Molar Density	mol/cc	0.0551465	0.0523336	0.0466191	0.000118889	0.000270159	0.000148692	0.000119439	0.000119359	0.00154073	0.000118864	0.000212285	0.000118925	0.000118925	0.000212007	0.000400064	0.000118925	0.055173	4.09E-05	0.0377061	0.00040547	0.00204734
Mass Density	gm/cc	0.993479	0.942804	0.839856	0.00134594	0.00486699	0.00267874	0.00215172	0.00195931	0.0277566	0.00380352	0.00679288	0.000239738	0.000239738	0.000427381	0.000806481	0.000239738	0.993957	0.00114554	0.640359	0.0129745	0.0180799
Enthalpy Flow	cal/sec	-2.77E+06	-2.73E+06	-2.65E+06	341751	-2.27E+06	-2.15E+06	-2.07E+06	-2.05E+06	-2.58E+06	113102	40211.9	228604	205744	77365.1	1442.83	22860.4	-2.77E+06	-24.7948	-443142	262.976	341016
Average MW		18.0153	18.0153	18.0153	11.3209	18.0153	18.0153	18.0153	16.4153	18.0153	31.9988	31.9988	2.01588	2.01588	2.01588	2.01588	2.01588	18.0153	28.0135	16.9829	31.9988	8.83096
Mole Flows	kmol/hr	145	145	145	233.611	145	145	145	161.111	145	72.5	72.5	161.111	145	145	145	16.1111	145	48.369	96.9883	72.5	783.973
H2O	kmol/hr	145	145	145	0	145	145	145	145	145	0	0	0	0	0	0	0	145	0	0	0	0
O2	kmol/hr	0	0	0	72.5	0	0	0	0	0	72.5	72.5	0	0	0	0	0	0	0	0	72.5	0
H2	kmol/hr	0	0	0	161.111	0	0	0	16.1111	0	0	0	161.111	145	145	145	16.1111	0	0	0.433095	0	567.19
N2	kmol/hr	0	0	0	0	0	0	0	0	0	0	0	0	0	0	0	0	0	48.369	0.171083	0	190.105
NH3	kmol/hr	0	0	0	0	0	0	0	0	0	0	0	0	0	0	0	0	0	0	96.3841	0	26.6779
Mole Fractions																						
H2O		1	1	1	0	1	1	1	0.9	1	0	0	0	0	0	0	0	1	0	0	0	0
O2		0	0	0	0.310345	0	0	0	0	0	1	1	0	0	0	0	0	0	0	0	1	0
H2		0	0	0	0.689655	0	0	0	0.1	0	0	0	1	1	1	1	1	0	0	0.00446544	0	0.723482
N2		0	0	0	0	0	0	0	0	0	0	0	0	0	0	0	0	0	1	0.00176396	0	0.242489
NH3		0	0	0	0	0	0	0	0	0	0	0	0	0	0	0	0	0	0	0.993771	0	0.0340291
Mass Flows	kg/hr	2612.22	2612.22	2612.22	2644.69	2612.22	2612.22	2612.22	2644.69	2612.22	2319.91	2319.91	324.781	292.303	292.303	292.303	32.4781	2612.22	1354.98	1647.14	2319.91	6923.23
H2O	kg/hr	2612.22	2612.22	2612.22	0	2612.22	2612.22	2612.22	2612.22	2612.22	0	0	0	0	0	0	0	2612.22	0	0	0	0
O2	kg/hr	0	0	0	2319.91	0	0	0	0	0	2319.91	2319.91	0	0	0	0	0	0	0	0	2319.91	0
H2	kg/hr	0	0	0	324.781	0	0	0	32.4781	0	0	0	324.781	292.303	292.303	292.303	32.4781	0	0	0.873068	0	1143.39
N2	kg/hr	0	0	0	0	0	0	0	0	0	0	0	0	0	0	0	0	0	1354.98	4.79264	0	5325.51
NH3	kg/hr	0	0	0	0	0	0	0	0	0	0	0	0	0	0	0	0	0	0	1641.48	0	454.339
Mass Fractions																						
H2O		1	1	1	0	1	1	1	0.98772	1	0	0	0	0	0	0	0	1	0	0	0	0
O2		0	0	0	0.877195	0	0	0	0	0	1	1	0	0	0	0	0	0	0	0	1	0
H2		0	0	0	0.122805	0	0	0	0.0122805	0	0	0	1	1	1	1	1	0	0	0.00053005	0	0.165152
N2		0	0	0	0	0	0	0	0	0	0	0	0	0	0	0	0	0	1	0.00290967	0	0.769223
NH3		0	0	0	0	0	0	0	0	0	0	0	0	0	0	0	0	0	0	0.99656	0	0.0656253

Table D4: Aspen model stream information for PT-CH_4

Material												
Stream Name	**Units**	**1**	**2**	**3**	**4**	**5**	**6**	**7**	**8**	**9**	**10**	**11**
Description												
From		HX-09	HX-11	P-01	HX-10	EL-H1	HX-3	HX-2	HX-1	HX-5	COMP-4	HX-8
To		R-01	F-SP	HX-1	R-02	B5	HX-4	HX-3	HX-2	HX-7	HX-14	HX-9
Stream Class		CONVEN	CONVEN	CONVEN	CONVEN	CONVEN	CONVEN	CONVEN	CONVEN	CONVEN	CONVEN	CONVEN
MIXED Substream												
Phase		Vapor Phase		Liquid Phase	Vapor Phase	Vapor Phase		Liquid Phase	Liquid Phase	Vapor Phase	Vapor Phase	Vapor Phase
Temperature	C	250	50	25.468	250	750	180.504	159.883	72.4991	300	156.531	300
Pressure	bar	10.1325	10.1325	10.1325	10.1325	10.1325	10.1325	10.1325	10.1325	10.1325	100	10.1325
Molar Vapor Fraction		1	0.387253	0	1	1	0.149107	0	0	1	1	1
Molar Liquid Fraction		0	0.612747	1	0	0	0.850893	1	1	0	0	0
Molar Solid Fraction		0	0	0	0	0	0	0	0	0	0	0
Mass Vapor Fraction		1	0.35681	0	1	1	0.149107	0	0	1	1	1
Mass Liquid Fraction		0	0.64319	1	0	0	0.850893	1	1	0	0	0
Mass Solid Fraction		0	0	0	0	0	0	0	0	0	0	0
Molar Enthalpy	cal/mol	-17218.4	-49010.3	-68979.6	-21736.9	-51346.1	-64346.5	-66155.9	-68005.7	1999.38	-17596.8	1920.8
Mass Enthalpy	cal/gm	-1614.67	-2854.04	-3828.95	-1823.44	-2850.14	-3571.78	-3672.21	-3774.89	62.483	-1112.15	952.834
Molar Entropy	cal/mol-K	0.496395	-31.1212	-38.9403	-1.06495	-4.49563	-28.4332	-32.1932	-36.3092	0.152858	-23.3164	-0.0200542
Mass Entropy	cal/gm-K	0.04655	-1.8123	-2.16151	-0.0893348	-0.249546	-1.57828	-1.787	-2.01547	0.004777	-1.47364	-0.00994813
Molar Density	mol/cc	0.000231074	0.000974139	0.0533349	0.000231909	0.000119325	0.00183008	0.04538	0.0509343	0.000211986	0.00281043	0.000211989
Mass Density	gm/cc	0.00246411	0.0167282	0.960844	0.00276455	0.00214967	0.0329694	0.817533	0.917595	0.00678329	0.0444676	0.000427345
Enthalpy Flow	cal/sec	-914006	-1.62E+06	-2.78E+06	-1.03E+06	-2.07E+06	-2.59E+06	-2.67E+06	-2.74E+06	40295	-224629	77422.6
Average MW		10.6637	17.1723	18.0153	11.9208	18.0153	18.0153	18.0153	18.0153	31.9988	15.8223	2.01588
Mole Flows	kmol/hr	191.1	118.67	145.107	170.947	145.107	145.107	145.107	145.107	72.5535	45.9552	145.107
CH4	kmol/hr	6.34956	42.5645	0	16.426	0	0	0	0	0	42.3265	0
CO2	kmol/hr	37.0314	0.816433	0	26.9549	0	0	0	0	0	0.769972	0
H2	kmol/hr	147.191	2.3316	0	106.885	0	0	0	0	0	2.33152	145.107
O2	kmol/hr	0	0	0	0	0	0	0	0	72.5535	0	0
H2O	kmol/hr	0.527237	72.9571	145.107	20.6802	145.107	145.107	145.107	145.107	0	0.527211	0
N2	kmol/hr	0	0	0	0	0	0	0	0	0	0	0
AIR	kmol/hr	0	0	0	0	0	0	0	0	0	0	0
Mole Fractions												
CH4		0.0332264	0.358681	0	0.0960887	0	0	0	0	0	0.921038	0
CO2		0.193781	0.00687988	0	0.15768	0	0	0	0	0	0.0167549	0
H2		0.770234	0.0196478	0	0.625256	0	0	0	0	0	0.0507347	1
O2		0	0	0	0	0	0	0	0	1	0	0
H2O		0.00275897	0.614792	1	0.120975	1	1	1	1	0	0.0114723	0
N2		0	0	0	0	0	0	0	0	0	0	0
AIR		0	0	0	0	0	0	0	0	0	0	0
Mass Flows	kg/hr	2037.83	2037.83	2614.14	2037.83	2614.14	2614.14	2614.14	2614.14	2321.62	727.117	292.518
CH4	kg/hr	101.864	682.852	0	263.519	0	0	0	0	0	679.033	0
CO2	kg/hr	1629.74	35.9311	0	1186.28	0	0	0	0	0	33.8863	0
H2	kg/hr	296.72	4.70022	0	215.468	0	0	0	0	0	4.70007	292.518
O2	kg/hr	0	0	0	0	0	0	0	0	2321.62	0	0
H2O	kg/hr	9.49832	1314.34	2614.14	372.56	2614.14	2614.14	2614.14	2614.14	0	9.49785	0
N2	kg/hr	0	0	0	0	0	0	0	0	0	0	0
AIR	kg/hr	0	0	0	0	0	0	0	0	0	0	0
Mass Fractions												
CH4		0.0499868	0.335088	0	0.129314	0	0	0	0	0	0.93387	0
CO2		0.799746	0.017632	0	0.58213	0	0	0	0	0	0.0466036	0
H2		0.145606	0.00230649	0	0.105734	0	0	0	0	0	0.00646397	1
O2		0	0	0	0	0	0	0	0	1	0	0
H2O		0.00466101	0.644973	1	0.182822	1	1	1	1	0	0.0130623	0
N2		0	0	0	0	0	0	0	0	0	0	0
AIR		0	0	0	0	0	0	0	0	0	0	0

12	21	22	23	24	25	26	29	CH4PROD	CO2FEED	H2+CO2	H2-P	H2O	H2OFEED	H2RECYCL	OXYGEN	RECYCLE
F-SP	COMP-2	HX-12	COMP-3	HX-13	V-1	V-2	R-01	M-SP		MX-03	HX-9	F-SP		SPL-01	HX-7	M-SP
COMP-2	HX-12	COMP-3	HX-13	COMP-4	V-2	B2	HX-10		COMP-1	MX-4	MX-03		P-01	B5		V-1
CONVEN	CONVEN	CONVEN	CONVEN	CONVEN	CONVEN	CONVEN	CONVEN	CONVEN	CONVEN	CONVEN	CONVEN	CONVEN	CONVEN	CONVEN	CONVEN	CONVEN
Vapor Phase	Vapor Phase	Vapor Phase	Vapor Phase	Vapor Phase			Vapor Phase	Vapor Phase	Vapor Phase	Vapor Phase	Vapor Phase	Liquid Phase	Liquid Phase	Vapor Phase	Vapor Phase	
50	180.658	110	166.551	120	34.5219	27.1354	540.567	40	25	79.2243	35	50	25	750	35	40
10.1325	40	40	70	70	50	10.1325	10.1325	100	1.01325	10.1325	10.1325	10.1325	1.01325	10.1325	10.1325	100
1	1	1	1	1	0.945506	0.94838	1	1	1	1	1	0	0	1	1	0.943798
0	0	0	0	0	0.0544944	0.0516199	0	0	0	0	0	1	1	0	0	0.0562021
0	0	0	0	0	0	0	0	0	0	0	0	0	0	0	0	0
1	1	1	1	1	0.933656	0.93877	1	1	1	1	1	0	0	1	1	0.929188
0	0	0	0	0	0.0663441	0.0612299	0	0	0	0	0	1	1	0	0	0.0708117
0	0	0	0	0	0	0	0	0	0	0	0	0	0	0	0	0
-18450.7	-17248.2	-17970.4	-17443.7	-17933.1	-22606.3	-22606.3	-19248.2	-17937.7	-93997.9	-18332.5	71.0157	-68323.7	-68993.4	5107.89	51.6318	-22606.3
-1166.12	-1090.12	-1135.76	-1102.48	-1133.41	-1478.17	-1478.17	-1614.67	-1123.61	-2135.84	-1760.26	35.2281	-3790.41	-3829.72	2533.83	1.61355	-1478.17
-21.1168	-20.7116	-22.4397	-22.2585	-23.4345	-20.2959	-17.3154	2.70586	-28.6076	0.666516	-2.08243	-4.34867	-37.444	-38.9675	4.07779	-4.39224	-21.5841
-1.33462	-1.30901	-1.41823	-1.40678	-1.4811	-1.3271	-1.13221	0.226985	-1.79197	0.0151447	-0.199951	-2.15721	-2.07729	-2.16302	2.02283	-0.137263	-1.41133
0.000381624	0.00106133	0.00127664	0.00192051	0.00218429	0.00208051	0.000429237	0.00014939	0.00427663	4.11E-05	0.000336121	0.000393449	0.0519365	0.0533478	0.000118908	0.00039725	0.00406365
0.00603818	0.0167928	0.0201995	0.030387	0.0345605	0.0318181	0.0065645	0.00178085	0.0682737	0.00180795	0.00350059	0.000793146	0.936178	0.961076	0.000239705	0.0127115	0.0621471
-235529	-220179	-229398	-222675	-228922	-61094.2	-61094.2	-914006	-180504	-947206	-923673	2862.46	-1.38E+06	-2.78E+06	22876.3	1040.57	-61094.2
15.8223	15.8223	15.8223	15.8223	15.8223	15.2934	15.2934	11.9208	15.9644	44.0098	10.4147	2.01588	18.0254	18.0153	2.01588	31.9988	15.2934
45.9552	45.9552	45.9552	45.9552	45.9552	9.72912	9.72912	170.947	36.226	36.2768	181.384	145.107	72.7145	145.107	16.123	72.5535	9.72912
42.3265	42.3265	42.3265	42.3265	42.3265	6.34897	6.34897	16.426	35.9775	0	0	0	0.238047	0	0	0	6.34897
0.769972	0.769972	0.769972	0.769972	0.769972	0.754572	0.754572	26.9549	0.0153994	36.2768	36.2768	0	0.0464612	0	0	0	0.754572
2.33152	2.33152	2.33152	2.33152	2.33152	2.09837	2.09837	106.885	0.233152	0	145.107	145.107	7.78E-05	0	16.123	0	2.09837
0	0	0	0	0	0	0	0	0	0	0	0	0	0	0	72.5535	0
0.527211	0.527211	0.527211	0.527211	0.527211	0.527211	0.527211	20.6802	0	0	0	0	72.4299	145.107	0	0	0.527211
0	0	0	0	0	0	0	0	0	0	0	0	0	0	0	0	0
0	0	0	0	0	0	0	0	0	0	0	0	0	0	0	0	0
0.921038	0.921038	0.921038	0.921038	0.921038	0.652574	0.652574	0.0960887	0.993139	0	0	0	0.00327372	0	0	0	0.652574
0.0167549	0.0167549	0.0167549	0.0167549	0.0167549	0.0775581	0.0775581	0.15768	0.000425093	1	0.2	0	0.000638954	0	0	0	0.0775581
0.0507347	0.0507347	0.0507347	0.0507347	0.0507347	0.215679	0.215679	0.625256	0.00643604	0	0.8	1	1.07E-06	0	1	0	0.215679
0	0	0	0	0	0	0	0	0	0	0	0	0	0	0	1	0
0.0114723	0.0114723	0.0114723	0.0114723	0.0114723	0.0541889	0.0541889	0.120975	0	0	0	0	0.996086	1	0	0	0.0541889
0	0	0	0	0	0	0	0	0	0	0	0	0	0	0	0	0
0	0	0	0	0	0	0	0	0	0	0	0	0	0	0	0	0
727.117	727.117	727.117	727.117	727.117	148.791	148.791	2037.83	578.326	1596.53	1889.05	292.518	1310.71	2614.14	32.502	2321.62	148.791
679.033	679.033	679.033	679.033	679.033	101.855	101.855	263.519	577.178	0	0	0	3.81893	0	0	0	101.855
33.8863	33.8863	33.8863	33.8863	33.8863	33.2086	33.2086	1186.28	0.677726	1596.53	1596.53	0	2.04475	0	0	0	33.2086
4.70007	4.70007	4.70007	4.70007	4.70007	4.23006	4.23006	215.468	0.470007	0	292.518	292.518	0.00015675	0	32.502	0	4.23006
0	0	0	0	0	0	0	0	0	0	0	0	0	0	0	2321.62	0
9.49785	9.49785	9.49785	9.49785	9.49785	9.49785	9.49785	372.56	0	0	0	0	1304.85	2614.14	0	0	9.49785
0	0	0	0	0	0	0	0	0	0	0	0	0	0	0	0	0
0	0	0	0	0	0	0	0	0	0	0	0	0	0	0	0	0
0.93387	0.93387	0.93387	0.93387	0.93387	0.684549	0.684549	0.129314	0.998015	0	0	0	0.00291364	0	0	0	0.684549
0.0466036	0.0466036	0.0466036	0.0466036	0.0466036	0.223189	0.223189	0.58213	0.00117188	1	0.845151	0	0.00156003	0	0	0	0.223189
0.00646397	0.00646397	0.00646397	0.00646397	0.00646397	0.0284295	0.0284295	0.105734	0.000812702	0	0.154849	1	1.20E-07	0	1	0	0.0284295
0	0	0	0	0	0	0	0	0	0	0	0	0	0	0	1	0
0.0130623	0.0130623	0.0130623	0.0130623	0.0130623	0.0638333	0.0638333	0.182822	0	0	0	0	0.995526	1	0	0	0.0638333
0	0	0	0	0	0	0	0	0	0	0	0	0	0	0	0	0
0	0	0	0	0	0	0	0	0	0	0	0	0	0	0	0	0